# MONITORING OF THE CHEMICAL COMPOSITION OF COMETS IN THE FRAMEWORK OF THE TRAPPIST SURVEY

Presented on September 23, 2016 at University of Liège
For the degree of Doctor of Science
Specialisation in Space Sciences

Under the direction of Dr. Emmanuel Jehin
by

**Cyrielle Opitom**

Université de Liège

Jury members:

Pr. Denis GRODENT, President of the Jury
Dr. Damien HUTSEMÉKERS, Secretary of the Jury
Dr. Emmanuel JEHIN, Supervisor
Dr. Benoît HUBERT, Member of the Jury
Dr. Colin SNODGRASS, Member of the Jury
Dr. Matthew KNIGHT, Member of the Jury
Dr. Philippe ROUSSELOT, Member of the Jury
Dr. Johan DE KEYSER, Member of the Jury

# Acknowledgements

I would like to thank all those who helped me during the four years of my thesis and made possible for me to achieve this objective. Firstly, I warmly thank my advisor Emmanuel Jehin who welcomed me in the TRAPPIST team and introduced me to the study of comets. Thank you four your availability during these four years and for your continued support. You gave me the freedom and the autonomy to pursue my own ideas and to learn a lot during these years. Thank you for transmitting me your passion for observing, and observing comets in particular; I am sure this will help me greatly in my new adventures. I am grateful to Damien Hutsemékers for his precious comments and perspectives on my work. Your advice have been essential to the achievement of this dissertation and to my work in general. Thank you Pierre Magain for your continuous support and guidance. I thank as well Jean Manfroid and Claude Arpigny for their help during these four years. Finally, I would like to thank the president and the members of my jury Denis Grodent, Colin Snodgrass, Matthew Knight, Benoît Hubert, Philippe Rousselot, and Johan De Keyser for taking the time to read this dissertation and for their useful comments on the first version of my manuscript.

Those years would not have been the same without all my colleagues from the institute. Laetitia, it has been a great pleasure to share an office with you. Not only you supported me during the bad times, but we also had a lot of good laughs over the years. Thanks to you too Gael for the coffee breaks, the chats, and the support (and good luck for your last year). I am grateful to the students, postdocs, and staffs working on the first floor for contributing to create such a nice environment to work in. Special thanks to Alice, Audrey, Judith, and Clementine for the nice talks, breaks, or advice. I would also want to thank warmly Sandrine and Angela, who were always available to help me with any computer-related or administrative problem and thus made everything much easier for me.

None of this would have been possible without my parents and the rest of my family, who allowed me to pursue my dreams, supported me during my studies and the four years of my thesis, put up with my mood swings and managed to instil confidence and motivation in me any time I needed it. A particular thank to Coraline for being always there for me in good times and bad, and for being the the best sister I could have wished for. Thank you Manon for your never failing friendship, for the climbing sessions who allowed me to release the pressure, for the good laughs and discussions. A big thank you to my "Coyotes". Over the years you have been a great team and even greater friends. Thank you Polo and Charlotte for the careful reading. Finally, thank you to all of those I could not mention here but are part of my life and make me who I am.

# Abstract

We present here the results of our narrow band photometry and imaging survey of comets with TRAPPIST. TRAPPIST is a 60-cm robotic telescope installed in 2010 at La Silla observatory. In six years of observations, we gathered more than 14,000 images of 30 bright comets from a variety of families and dynamical origins. The data have been reduced homogeneously and OH, NH, CN, $C_3$, and $C_2$ production rates have been derived using a Haser model, in addition to the $Af\rho$ parameter as a proxy for the dust production. The comets of our data set have been observed over a wide range of heliocentric distances, allowing us to study the evolution of the activity and coma composition of comets as a function of the distance from the Sun. Images enhancement techniques have been used to study the gas and dust morphology of the coma.

We study individually the evolution of the activity, composition, dust properties, and coma morphology of seven comets over a wide range of heliocentric distances, and on both sides of perihelion for four of these comets. For three comets, our dense monitoring allows us to derive the rotation period of the nucleus: comet C/2012 F6 (Lemmon), comet 103P/Hartley 2, and comet C/2014 Q2 (Lovejoy). Two comets, C/2013 A1 (Siding Spring) and C/2013 US10 (Catalina), were also observed with the FORS 2 spectrograph of the VLT. Both radial profiles of brightness and gas production rates derived from the spectroscopic observations are in good agreement with the TRAPPIST measurements. Finally, we develop a model to reproduce the shape of the radial profiles observed consecutively to the outburst of comet C/2013 A1 (Siding Spring). This model allows us to determine some of the characteristics of the outburst, such as the time at which it started, the expansion velocity of the gas ejected, and the amount of gas released.

We then perform a global analysis of the properties of the ensemble of comets of our data set. We find that the activity of dynamically new comets increases slower than the activity of other comets before perihelion, and decreases fast after the perihelion passage. This might be linked to the release of a halo of icy grains in the coma of these comets at large heliocentric distances pre-perihelion. From the observation of the composition of the coma of several comets in outburst, we infer that the nucleus of these comets might be homogeneous on large scales. Comparison of the comets of our sample shows that they have a remarkably uniform composition, with the exception of comets C/2011 L4 (PanSTARRS) and to a lesser extent C/2012 K5 (Linear), which have a high dust to gas ratios, and comet 168P/Hergenrother which is severely depleted in $C_2$ and $C_3$. As a consequence, we cannot define classes of comets based

on their composition. We observe an evolution of the coma composition of our ensemble of comets as a function of the heliocentric distance. The OH to CN ratio decreases with the heliocentric distance for distances large than 2 au, probably because the water outgassing becomes less efficient at those distances. The dust to gas ratio increases with the heliocentric distance and the origin of this trend is still unclear. At heliocentric distances larger than 1 au, the $C_2$ to CN ratio decreases with the heliocentric distance, by about a factor 2 between 1 and 2.5 au. We believe this trend is an artefact of the parameters used in the Haser model and their scaling with the heliocentric distance. Finally, we investigate the origin of species in the coma. We conclude that HCN and $C_2H_2$ are probably not the only/main parents of CN and $C_2$. CN and $C_2$ might be released from organic rich grains and the importance of this secondary source probably varies from one comet to another.

# Contents

# Introduction

Comets are among the most spectacular and unpredictable celestial bodies. For centuries, they inspired fear and amazement to mankind, and raised numerous questions about their origin and true nature. Over the last century, enormous progress has been made towards a better understanding of the nature, the evolution, and the origin of comets. However, numerous questions are still unanswered and the interest of the scientific community for these icy bodies remains strong, as illustrated by the ESA Rosetta mission in orbit around comet 67P/Churyumov-Gerasimenko. Comets are among the most pristine bodies of the solar system and are often considered as true fossils that can reveal information about the formation and early times of the solar system. They have been stored for most of their lifetime beyond the orbit of Pluto and have undergone very little alteration since their formation. Their nucleus should thus preserve invaluable clues about the evolution of the early solar nebula at the time of planets formation. When a comet is ejected from its reservoir and enters the inner solar system, the ices in the nucleus sublimate under the solar radiation and gas and dust are ejected to form the coma. Important information about the physical and chemical conditions of the early solar system can then be retrieved. Comets also contain complex organic molecules, in addition to large amounts of water, and were thought to have played a key role in the transfer of water and organics from the interstellar medium to the early Earth, contributing to the formation of the oceans and the atmosphere, and to pre-biotic chemistry.

When a comet approaches the Sun, the ices contained in the nucleus begin to sublimate and water and other complex molecules are released in the coma. These molecules, usually called parent species, are photodissociated by the solar UV light into daughter or even granddaughter species observed in the optical spectrum of comets. The observation of these daughter species from the ground provides a way to study the composition of comets remotely. Several of these radicals (OH, NH, CN, $C_3$, and $C_2$) can be observed with the 60-cm robotic TRAPPIST telescope, using narrow band filters. Four continuum windows also allow us to characterise the dust component of the coma. Over the last 6 years, we performed a regular monitoring of relatively bright comets visible from the Southern hemisphere. We gathered a sample of more than 14,000 images of 30 comets of various types and dynamical origins. This sample contains high quality data for a large number of comets over a large range of heliocentric distances on both sides of perihelion. It is also remarkable because of its homogeneity: all the data have been obtained with the same telescope and reduced in a consistent way. From

these observations, we study the morphology of the coma and we derive, using models of cometary atmospheres, the production rates and relative abundances of various species, the dust properties, as well as the dependence of these quantities with the heliocentric distance. The main goal of this work is the analysis of the sample of comets we observed with TRAPPIST to address with unprecedented details important and long debated questions like the "pristine" versus "evolutionary" scenarii for the origin of the comet compositional classes, the variation of molecular abundance ratios with the distance to the Sun and the link between chemical composition and dynamical origins, which is a fundamental step in understanding the formation of comets and the solar system. The dense monitoring also allows us to investigate topics like the heterogeneity of the nuclei composition and the determination of their rotation period through the monitoring of the flux variations and the analysis of coma features.

The first Chapter is a brief introduction to comets. We address the origin, formation mechanisms, and the main reservoirs of comets before describing the structure and properties of the nucleus, the coma, and the tail. This work focusses on the study of comets in the optical range. We thus feel it is important to describe a typical comet optical spectrum and the species we can detect at optical wavelengths. Even though cometary sciences made huge progresses in the past 20 years, with the advent of large telescopes, numerous questions remain unanswered. We give some background about important questions that will be addressed in this work, such as cometary outbursts, the composition of the coma of comets at various wavelengths, and the long-debated question of the species parentage in the coma.

The second part of the work focusses on the data collection and reduction. Most of the observations we used have been collected with the TRAPPIST telescope of the University of Liège. We describe the telescope and its instrumentation, as well as the set of narrow band filters we have used for the observation of comets. In addition to the TRAPPIST observations, three comets have been observed with the FORS 2 low resolution spectrograph of the Very Large Telescope. We apply a standardized reduction procedure to all our data and perform an absolute photometric calibration of our images. The fluxes are converted into production rates using the simple Haser model, while we use the $Af\rho$ parameter to estimate the dust production in the coma. Image enhancement techniques are also applied to the images to reveal morphological features in the coma.

Even though some comets have only been observed during a couple of days or weeks, several have been monitored during several months or years with TRAPPIST, before and after perihelion. In Chapter 3, we select seven particularly interesting comets, because of the large number of observations available, because simultaneous observations with the FORS 2 instrument were performed, or because they underwent an outburst. We perform a thorough analysis of the evolution of their activity, coma composition, and dust properties with the heliocentric distance. We also study the gas and dust morphology of their coma, searching for features such as jets, arcs, or spirals. For some comets, we analyse the rotational variability of their lightcurve and coma morphology in order to determine the rotation period of their nucleus.

Finally, we develop a new model to interpret the observations of comets just after an outburst and characterize the properties of the outburst.

The last Chapter is dedicated to the study of the properties of our ensemble of comets. We compare the evolution of their gas and dust activity as a function of the heliocentric distance and on both sides of perihelion, to detect differences between comets and asymmetries about perihelion. We also analyse several gas and dust production rates and production rate ratios, trying to define taxonomical classes of comets based on their coma composition. We then try to establish a link between these properties and the dynamical origin of the comets. We study the evolution of various production rate ratios with the heliocentric distance and the consequences of the variation of these ratios for the release mechanisms of the gas species and the dust in the coma. We discuss the importance of model parameters, especially the Haser model scalelengths, on the production rate and production rate ratios we derive and the consequences for our work. Finally, we investigate the origin of several daughter species in the coma in order to better understand species parentage.

# 1 General considerations about comets

Even though comets have been observed by humanity since Antiquity, their true nature remained mysterious until the last century. The earliest record of comet observations date from around 1,000 BC in China (Ho, 1962). The spectacular aspect of comets and their unpredictable apparitions both intrigued and frightened the population. They were often considered as bad omens of the death of kings or natural disasters. Over the centuries, the interpretation of comets evolved; they have been considered successively as wandering planets by the Pythagoreans, or as atmospheric phenomena by both Aristotle and Galileo, among others (Festou et al., 2004). However, from the sixteenth century, convincing clues about the nature of comets start to pile up. In 1531, Apian and Fracastor noticed that comet tails are oriented in the direction opposite to the Sun, underlining the link between comets and our star. In 1578, Tycho Brahe observed comet C/1577 V1 and determined its position with unprecedented precision. He measured its parallax to be smaller than $15'$, hence proving that the comet was farther away from the Earth than the moon. This lead some astronomers to think that comets could move on elongated elliptic or even parabolic orbits. In 1687, in *Philosophiae Naturalis Principia Mathematica*, Newton introduced his law of universal gravitation (Newton, 1687). Using the law of gravitation, Edmund Halley computed the orbit of a dozen comets. He realised that the bright comets observed in 1531, 1607, and 1682 were actually one single object observed on successive orbits and used Newton's law to predict its return in 1758. The successful recovery of comet 1P/Halley by Palitzsch in December 1758 definitely confirmed the astronomical nature of comets. Subsequent observations of comets showed that they occupy a wide range of orbits, some comets having short orbital periods of a few years to a few dozen years while others move on nearly parabolic orbits and have much longer orbital periods.

## 1.1 The dynamical origin and classification of comets

Comets have formed in the early solar nebula by agglomeration of dust grains and condensation of gas. Since comets are known to retain large quantities of volatile ices, they must have formed in the outer part of the protoplanetary disk, in the region of the giant planets (5-30 au).

However, the dynamical behaviour of the early solar system was unstable and a large part of the planetesimals formed in the region of the giant planets have been ejected from their place of formation (Gomes et al., 2005; Tsiganis et al., 2005). Comets have now two main reservoirs: the Kuiper Belt (KB) and the Oort Cloud (OC) (Fig. 1.1).

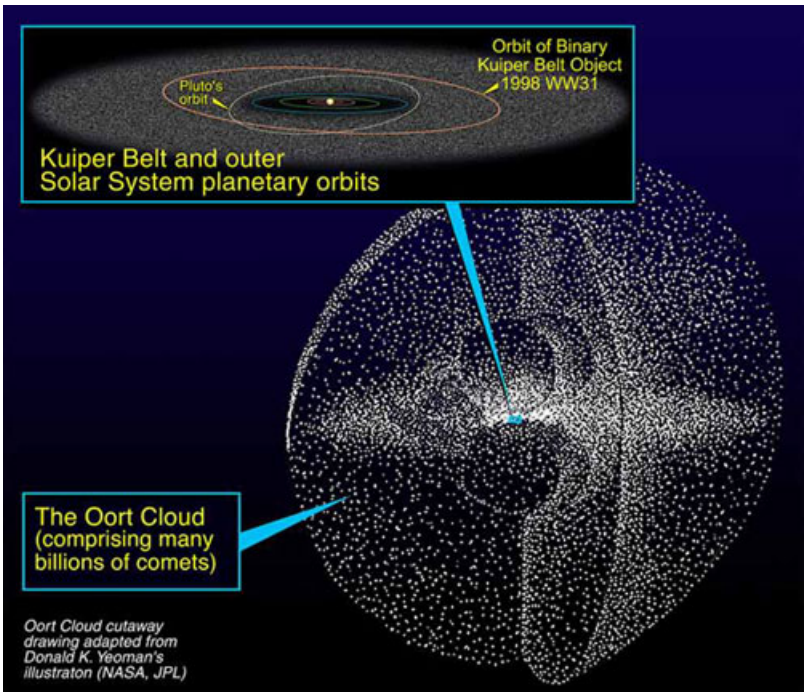


Figure 1.1: Artist view of the Oort Cloud and the Kuiper Belt. Credits: Oort Cloud cutaway drawing adapted from Donald K. Yeoman's illustration - NASA, JPL.

As the number of cometary orbits and periods known was rising, it soon became obvious that some comets are following short period elliptical orbits while others have much longer orbital periods and almost parabolic or even hyperbolic orbits. However, establishing a classification of comets using their orbital characteristics is not easy. The most widely used classification divides comets in two main families: ecliptic comets (ECs) and nearly isotropic comets (NICs) (Levison, 1996). The Tisserand parameter relative to Jupiter ($T_J$) is used to differentiate Jupiter Family Comets from NICs. It can be expressed as:

$$T_J = \frac{a}{a_J} + 2[\frac{a}{a_J}(1-e^2)]^{\frac{1}{2}} cos(i) \tag{1.1}$$

$a$ is the semi-major axis of the comet orbit, $e$ is its eccentricity, $i$ is its inclination with respect to the ecliptic plane, and $a_J$ is the semi-major axis of Jupiter orbit. NICs are defined as comets having $T_J < 2$ and ECs as those having $2 < T_J < 3$ (asteroids have a Tisserand parameter larger than 3). Within NICs one can also distinguish between long period comets (LPCs) with semi-major axes $a > 40$ au and Halley-type comets, named after the famous Halley comet, with semi-major axes $a < 40$ au. The family of ecliptic comets encompasses Jupiter family comets (JFCs), Encke-type comets (JFCs having their orbit entirely inside the orbit of Jupiter), and

centaurs.

Ecliptic comets are thought to originate from the Kuiper Belt. The existence of a disk of small bodies beyond the orbit of Neptune was already speculated by the Irish scientist Kenneth Edgeworth in the 1940s (Edgeworth, 1949), and the astronomer Gerard Kuiper in the 1950s (Kuiper, 1951). The first transneptunian object other than Pluto, 1992 QB1, was finally discovered in 1992 by Jewitt and Luu (Jewitt and Luu, 1993). Two decades after the first discovery, more than 1000 of these objects are known. However, the actual structure of the Kuiper Belt is far from the simple disk imagined by Edgeworth and Kuiper. The transneptunian objects population is usually divided into two main components: the Kuiper Belt itself and the Scattered Disk. The Kuiper Belt starts just beyond the orbit of Neptune at 30 au, extends until around 50 au, and is composed of transneptunian objects who do not cross the orbit of Neptune and are dynamically stable over long time scales (Levison et al., 2008). It can then be subdivided between objects in mean motion resonance with Neptune (like Pluto), a cold component containing objects having inclinations below 4°, and a hot component composed of larger inclination objects (Brown, 2001). The Scattered Disk contains objects on more eccentric orbits, with semi-major axis larger than 50 au and perihelion near Neptune. These objects are not stable over large time-scales and can migrate under the influence of Neptune (Morbidelli and Brown, 2004). The JFCs are thought to originate from the Scattered Disk and are characterised by aphelion distance close to Jupiter and small inclinations.

Nearly isotropic comets originate from the Oort Cloud. The Oort Cloud is a spherical reservoir of icy objects ranging from approximately 10,000 to 50,000 au. The idea of some comets originating from a large distant cloud was first introduced by the Estonian astronomer Ernst Öpik in 1932 (Öpik, 1932). Almost 20 years later, in 1950, Jan Oort also invoked a cloud of icy bodies on the borders of our solar system to explain the continuous supply of new comets in the inner solar system (Oort, 1950). By studying the orbits of several dozen comets, he showed that a peak of reciprocal semi-major axis occurs at very large heliocentric distances, hence reinforcing the hypothesis of a distant comet reservoir. Even though the Oort Cloud has never been observed directly, further studies of cometary orbits confirmed its existence (Królikowska et al., 2014). Recent studies estimated that the Oort Cloud could contain as much as $10^{11}$ comets (Dones et al., 2015). The orbits of potential comets in the Oort Cloud can be perturbed by galactic tides and passing stars, and these bodies are then re-injected in the inner solar system (Fouchard et al., 2011) (the very close passage of a star can trigger a comet shower). Comets entering the inner solar system for the first time since their placement in the Oort Cloud are called dynamically new comets. These comets are particularly interesting since they are some of the most pristine bodies available for a detailed study, and can reveal information about the conditions prevailing in the early solar nebula at the time they formed. Dynamically new comets are usually defined as long period comets having an original semi-major axis larger than $10^4$ au (Wiegert and Tremaine, 1999).

Various scenarios have been proposed over the years to explain the formation of the Oort Cloud and the Scattered Disk, inferring the place of formation of NICs and ECs. It was first

thought that NICs and ECs were formed at different distances from the Sun. The ECs would have formed in the Kuiper Belt region while NICs would have formed closer to the Sun, in the giant planet region. Given the gradient of temperature and physical conditions with the heliocentric distance in the protoplanetary disk, ECs and NICs should then have distinct compositions (Mumma et al., 1993). However, in the early 2000s, a new scenario, the Nice model, offered a different set of explanations to elucidate the formation of the Oort Cloud, the Kuiper Belt, and the Scattered Disk (Gomes et al., 2005; Tsiganis et al., 2005). This model states that the giant planets were in a much more compact configuration on circular orbits 3.8 billion years ago and were surrounded by a disk of planetesimals located between approximately 15 and 30 au. Gravitational interactions between the disk and the giant planets caused planets to start migrating. Jupiter migrated inward while Saturn was moving farther away from the Sun. When these two planets crossed the 2:1 mean-motion resonance, it created a large instability: the orbits of Uranus and Neptune were strongly perturbed and a large part of the planetesimals in the disk were ejected. Some of these planetesimals then entered the Oort Cloud and the Scattered Disk (Levison et al., 2008), the Oort Cloud being mainly populated by objects formed around 20-40 au scattered by the giant planets and the Scattered Disk by objects formed between 25 and 35 au mainly scattered by Neptune (Dones et al., 2004). A large number of planetesimals have also been ejected towards the inner solar system and impacted the terrestrial planets during the "Late Heavy Bombardment". According to this model, the Kuiper Belt should contain objects formed in-situ (Levison and Morbidelli, 2003). Even if a good picture of how the main comet reservoirs formed in relation with the dynamical history of the solar system is emerging, some inconsistencies between model predictions and observations remain. For this reason, it is extremely important to study large samples of both NICs and ECs, since composition differences may bring important constraints on their places of formation.

Finally, one more comet reservoir is worth mentioning: the Main Belt of Asteroids. The first member of this new class of comets was 133P/Elst-Pizarro. Previously known as an asteroid, it displayed a dust tail shortly after its perihelion passage in 1996. The dust tail was observed again in 2002 and 2007, confirming the probable cometary nature of its activity (Hsieh et al., 2004). Since then, several other objects in the main belt have been found to be active near their perihelion passage. Several explanations other than sublimation have been suggested to explain the activity of these bodies: impact with another asteroid or rotational bursting due to spin-up via the YORP effect (Rubincam, 2000). The bodies for which alternative explanations were discarded as probable cause of the activity have been considered as a new class of comets: the Main Belt Comets (MBCs). Simulations indicate that these bodies could have lost surface ice since the time of their formation at such short heliocentric distances. However, some ice could remain in subsurface pockets and the activity can then be triggered by impacts with small asteroids.

## 1.2 Nucleus

For a long time, little was known about cometary nuclei. The main reason for this is that cometary nuclei are small and dark objects almost impossible to resolve from Earth, even with the largest telescopes. Far away from the Sun, most nuclei are too faint to be directly detected and then studied. When they finally enter the inner solar system, the coma starts developing and completely outshines the nucleus. Except for some size estimates from radio or infrared observations, our knowledge of cometary nuclei mainly comes from comet flybys by space missions and of course from the Rosetta mission which orbited a comet for several months and landed on its nucleus.

Our current understanding of the structure of cometary nuclei is rather recent. Previously to 1950, Lyttleton described it as a cluster of gravitationally bound dust particles with adsorbed gas in orbit around the Sun (Lyttleton, 1948). However, some behaviours of comets such as non-gravitational motion could not be accounted for by the sandbank model. In the early 1950s, Whipple introduced in a trilogy of articles the concept of "icy conglomerate" to describe the cometary nucleus (Whipple, 1950, 1951, 1955). In these articles, Whipple compared the nucleus of a comet to a dirty snowball, a monolithic conglomerate of ices and rocks (meteoritic materials). The dirty snowball model allowed comet observers to account for many properties of comets such as the non-gravitational motion of comet Encke. Evidence was piling up in favour of this interpretation, but it was not confirmed until 1986 and the flyby of comet Halley (Keller et al., 1986). Even though the nature of cometary nuclei was unveiled, their internal structure remained poorly understood. Around the time of the Giotto flyby, several models were proposed to describe the underlying structure of the nucleus: the "fluffy aggregate" model (Donn et al., 1985), the "primordial rubble pile" (Weissman, 1986) and the "icy-glue" model (Gombosi and Houpis, 1986). The first two models consider cometary nuclei as weakly bound aggregates of smaller icy planetesimals. This would produce very porous, low-density, and easily fragmented nuclei. The "icy-glue" model describes the nucleus as refractory boulders similar in composition to main-belt asteroids held together by icy glue. In 2007, Belton et al. proposed a new model in which the nucleus is composed by a core surrounded by layers of ice and dust. Measurements of nucleus density, among others, seem to indicates that the fluffy aggregate and rubble pile models might be more likely (Weissman and Lowry, 2008). As a summary, cometary nuclei are small bodies made of volatile ices and refractory material, in approximately the same amount. Ices are composed of 80% of $H_2O$, 10 to 20% of $CO_2$ and CO, and tens of minor components, comprising complex organic molecules. $O_2$ was also recently found to be a abundant component of cometary ices (Bieler et al., 2015).

The measurement of the geometric albedo of comet P/Arend-Rigaux revealed a surprisingly dark nucleus for a body containing large amounts of ice, with a geometric albedo of less than 0.03 (Millis et al., 1985). This was further confirmed by the first flyby of comet Halley by the *Vega* spacecraft which provided a measurement of the geometric albedo of the nucleus of comet Halley of about 0.04(Sagdeev et al., 1986). Later ground-based visible and infrared observations of several comets provided albedos ranging from 0.02 to 0.06 (Keller and Jorda, 2002; Lamy

et al., 2004). Recent measurements with the VIRTIS and OSIRIS instruments onboard ROSETTA revealed an albedo of 0.06 for the nucleus of comet 67P/Churymov-Gerasimenko, in agreement with the range of values previously reported for other comets. The surface of the nucleus is then mainly dehydrated and composed of organic macromolecular material responsible for the low albedo of cometary nuclei.

The shape and size of cometary nuclei are extremely difficult to constrain, especially from ground-based observations. Analysis of the light reflected by the nucleus in the optical and of its thermal emission in the infrared can allow us to derive radius estimates in favourables cases where the contrast between the nucleus and the coma is high. However, these observations are challenging and only give an estimate of the effective radius of the nucleus without bringing any information about its shape. One way to better constrain the shape of a comet nucleus is to make a lightcurve of the comet at large heliocentric distances, when it is not active. Given the difficulty to observe cometary nuclei from the Earth, the most detailed information we have comes from flyby missions. So far, eight comets have been visited by space missions: 21P/Giacobini-Zinner, 1P/Halley, 26P/Grigg-Skjellerup, 19P/Borrely, 81P/Wild 2, 9P/Tempel 1, 103P/Hartley 2, and comet 67P/Churyumov-Gerasimenko. Fig. 1.2 shows images of some of these nuclei to scale. Nucleus sizes can vary from less than a kilometre for the smallest, like 45P/Honda-Mrkos-Pajdusakova (Lamy et al., 1996) (or even tens of meters for sungrazers comets, Knight et al. (2010)), to several tens of kilometres for the largest comets, like C/1995 O1 Hale-Bopp (Weaver et al., 1997). Nucleus shapes are usually more complex than simple spheroids and vary from comet to comet. As can be seen in Fig. 1.2, the nuclei of comet 103P/Hartley 2 and comet 19P/Borrelly are very elongated while those of comet 81P/Wild 2 and comet 9P/Tempel 1 are more symmetrical. Recent observations from the Rosetta mission revealed that the strange bi-lobed shape of comet 67P/Churyumov-Gerasimenko is likely the result of the gentle merger of two distinct bodies.

The density of cometary nuclei is difficult to estimate, since both the mass and volume have to be known. As mentioned earlier, the shape of a few nuclei has been constrained by mission flybys and effective radius estimates are possible from telescopic observations in some favourable cases. Estimating the mass of a cometary nucleus is even more difficult. Even in case of close flybys, the mass can not be estimated because of the low mass of the nucleus and the high relative speed of the spacecraft. The only exception is the Rosetta spacecraft which is in orbit around the nucleus of comet 67P/Churyumov-Gerasimenko. The Radio Science Investigation (RSI) instrument measured a mass of $1 \times 10^{13}$ kg (Sierks et al., 2015). This allowed for the first time the determination of the density of a nucleus with high precision, in this case $470 \pm 45$ kg/m$^3$. The only other way to determine the mass of a comet nucleus is to estimate the effect of non-gravitational forces (such as the effect of the sublimation of water ice from the nucleus) on a rotating nucleus. Typical masses and densities estimated that way lie respectively in the range $10^{10}$ to $10^{15}$ kg (Britt et al., 2006) and 200 to 1200 kg/m$^3$ (Weissman et al., 2004).

Cometary nuclei are usually rotating around one main axis. The determination of their

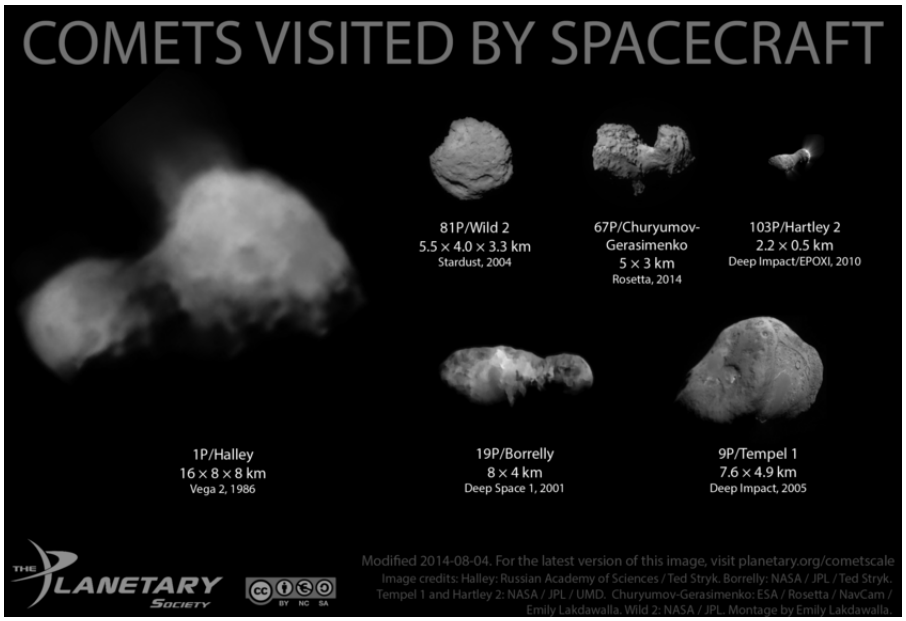


Figure 1.2: Comparison image of six comets visited by spacecrafts: 1P/Halley, 19P/Borrelly, 81P/Wild 2, 9P/Tempel 1, 103P/Hartley 2, and 67P/Churyumov-Gerasimenko. Credits: The planetary society, montage by Emily Lakdawalla - Images credits: Halley: Russian Academy of Sciences/Ted Stryk, Borrely: NASA/JPL/Ted Stryk, Tempel 1 and Hartley 2: NASA/JPL/UMD, Churyumov-Gerasimenko: ESA/Rosetta/NavCam/Emily Lakdawalla, Wild 2: NASA/JPL.

rotation period is difficult to achieve since the nucleus itself is hard to observe. However, several techniques allow the determination of reliable rotation periods. The first one is the observation of inactive comets at large heliocentric distances in order to build lightcurves. This technique requires large telescopes and a significant amount of observing time. Features such as jets, fans, or wings are often detected in the coma of comets. Depending on the viewing geometry, some of these features can move because of the nucleus rotation. The study of coma features and their periodic movement then provides a way to measure the rotation period. Finally, due to the change of the nucleus illumination with the rotation, gas production rates in the coma may vary. In favourable cases, one can see a periodic variation of gas production rates during the night, allowing us to constrain the rotation period. Some comets can have complex rotational states, in which case the nucleus has several rotation axes. This is for example the case of comet 103P/Hartley 2. Combining all techniques, nucleus rotation periods have only been determined for approximately two dozen comets. The measured values vary from a few hours for comets like Hyakutake (1996 B2) (Schleicher et al., 1998; Schleicher et al., 2003) or 10P/Tempel 2 (A'Hearn et al., 1989; Jewitt and Luu, 1989; Sekanina, 1991) to more than a day for comet 9P/Tempel 1 (Belton et al., 2005) or comet Halley (Belton et al., 1991), for example.

For some comets, the gas production rates measured in the coma are much lower than predicted if the whole surface were freely sublimating. This led to the idea that most cometary nuclei are not active on their whole surface, but that sublimation may take place on preferential

areas, usually called active regions. The first results from the Rosetta mission seem to confirm that the outgassing is heterogeneous and can be more important at certain locations. Several active pits have been detected on the nucleus of comet 67P/Churyumov-Gerasimenko and are believed to be signatures of the comet's activity (Vincent et al., 2015). Illumination changes on active zones are often invoked to explain changes of the activity evolution of comets, asymmetry of the activity about perihelion, or sudden rise of comet activity. Active zones are also believed to be the origin of jets and other features observed in the coma of most comets, even if the link between jets observed by the OSIRIS instrument onboard Rosetta and the much larger scale features visible in ground-based observations is still poorly understood.

## 1.3 Coma

When a comet is injected in the inner solar system and approaches the Sun, the ices in the nucleus sublimate. Gas is ejected from the nucleus, dragging along dust particles to form a huge atmosphere of gas and dust around the nucleus, called the coma. The exact size of the coma is somewhat difficult to estimate, since it strongly depends on the species under consideration and the distance from the comet to the Sun. It can reach hundreds of thousands of kilometres for comets at 1 au from the Sun, but the hydrogen envelope can be much larger than this. Nucleus ices do not have the same volatility, which means that the main drivers of cometary activity vary with the heliocentric distance of the comet. At large distances from the Sun, the activity is mainly controlled by CO and $CO_2$, while within 3 au from the Sun water sublimation is the main driver of comet activity (Crovisier and Encrenaz, 2000).

Gas molecules are ejected from the nucleus with typical outflow velocities of 0.8 km/s at 1 au (Bockelee-Morvan et al., 1990; Biver et al., 1999), which can be even lower near the nucleus (Lee et al., 2015). They first go through a dense region dominated by collisions usually called the inner coma. The size of the collision-dominated region depends on the activity level of the comet and its distance from the Sun and is of the order of one thousand kilometres. Chemical reactions between species may occur in this dense region of the coma but gas molecules only spend a short amount of time in the inner coma. The density of the coma then decreases as molecules move away from the nucleus and photochemical processes dominate in most of the coma.

Molecules ejected directly from the nucleus in the coma are called parent species. They mainly emit through fluorescence processes at ultraviolet, infrared, or radio wavelengths. The most abundant parent molecule is water. Even though its presence in the coma was known already in the 1970s from the observation of H and OH, the first detection of water bands only occurred a decade later (Mumma et al., 1986; Weaver et al., 1986) in the coma of comet 1P/Halley, almost simultaneously to its direct detection by mass spectrometry (Krankowsky et al., 1986). After water, the most abundant parent species are $CO_2$ and CO (which can also be the product of $CO_2$ photodissociation). A number of CHO-bearing molecules ($CH_3OH$, $H_2CO$, HCOOH, $HOCH_2CH_2OH$, ...), hydrocarbons ($CH_4$, $C_2H_2$, $C_2H_6$), sulphur- ($CS_2$, OCS, ...) and

nitrogen-bearing molecules ($NH_3$, HCN, ...) have also been detected in the coma of comets (see for example Cochran et al. (2015)). At a first approximation, the more complex the species are, the lower their abundances.

Parent molecules are photodissociated by the solar UV light to form smaller molecules, radicals or ions. Photolytic destruction of parent molecules can follow several paths depending on the energy of the incident photons, as it is the case for water (Feldman et al., 2004).

$$\begin{aligned} H_2O + h\nu &\rightarrow OH + H \\ &\rightarrow OH(A^2\Sigma^+) + H \\ &\rightarrow H_2 + O(^1D) \\ &\rightarrow H_2 + O(^1S) \\ &\rightarrow H + H + O(^3P) \\ &\rightarrow H_2O^+ + e \\ &\rightarrow H + OH^+ + e \\ &\rightarrow H_2 + O^+ + e \\ &\rightarrow OH + H^+ + e \end{aligned}$$

Fragments are themselves broken down by the solar UV light. In some cases, the photodissociation of the parent molecule leaves the radical in a short-lived excited state. The excess energy is then dissipated through the prompt emission of a photon. Among the most common fragment species observed in the optical, one can find OH, CN, $C_2$, $C_3$, CH, NH, $NH_2$, [OI], .... Several ions ($CO^+$, $CO_2^+$, $H_2O^+$, ...) are also detected in the optical spectrum of comets.

The second main component of the coma is the dust, which is ejected from the active nucleus by sublimating gas. Information about the dust composition and properties have been obtained so far in-situ during flybys, from the Stardust sample return mission, and from ground-based and space-borne spectroscopic and polarimetric studies. Grains found in the coma are composed of refractory materials such as silicates, organics, and amorphous carbon. The most abundant compounds are silicates (pyroxene, olivine, Mg-rich silicates, ...), which can be found in both amorphous and crystalline forms. Metals and sulphides are also found in the coma. Grains composed of carbon-hydrogen-oxygen-nitrogen compounds (commonly called "CHON" grains) have been found more recently. Dust grains usually have low albedo (similar to cometary nuclei) and low density, indicating that they are most probably fluffy and dark. It is thought that cometary dust could be composed of a mix of micron-sized fragile aggregates and more compact dust grains (Schulz et al., 2015). Absorption features detected at infrared wavelengths have been attributed to water ice, indicating the presence of icy aggregates composed of micron-sized icy grains. A halo of icy grains has indeed been detected in the coma of comet 103P/Hartley 2 during the flyby of the EPOXI mission (Kelley et al., 2013). The velocity of the dust grains is lower than the velocity of the gas. Measurements of dust shells expansion following outbursts are of the order of one to several hundred m/s (Hsieh et al., 2010; Lin et al., 2009; Lara et al., 2007).

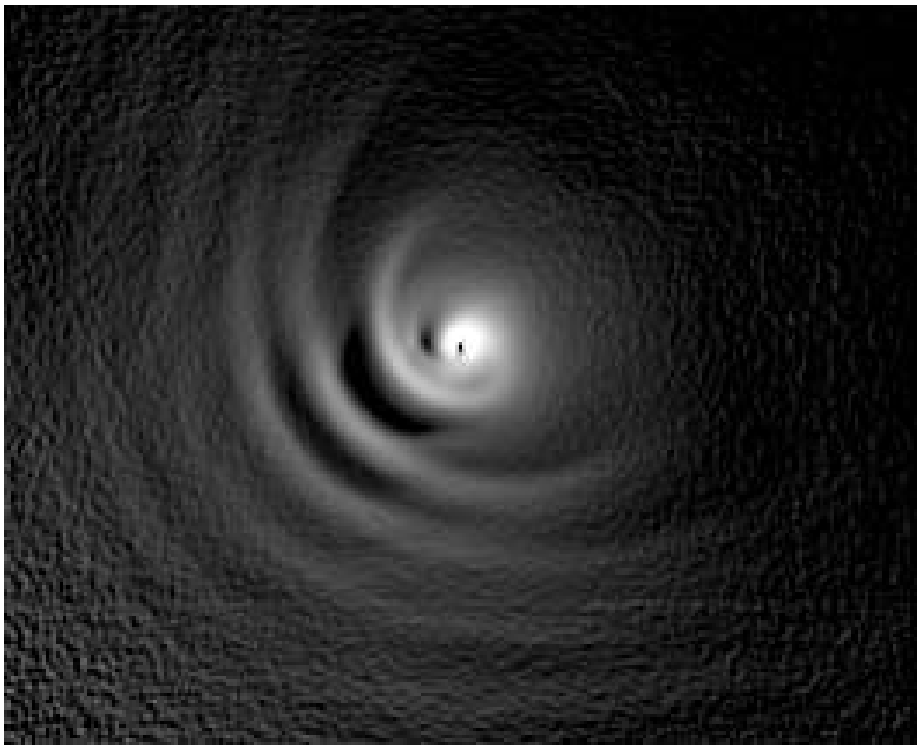

Figure 1.3: Bright arcs in the coma of comet C/1995 O1 (Hale-Bopp) (Picture obtained on 8 April 1997 at Pic du Midi observatory by J. Lecacheux and F. Colas).

Comets usually exhibit morphological features in the coma. These features can have various aspects: narrow jets, fans (similar to jets but broader), spirals, or arcs. Figure 1.3 shows an example of such arcs observed in the coma of comet C/1995 O1 (Hale-Bopp). Morphological features in the coma are thought to be the result of active areas on the nucleus. Depending on the position and number of active areas, the orientation of the nucleus, and its rotational state, different types of features can be observed. The study of morphological features in the coma is particularly important as it can provide information on the nucleus composition, topography, and rotational state. First, for some comets with favourable viewing geometry, periodic changes in the feature shape and position provide a way to measure the rotation period of the nucleus. Modelling of the coma to match the observed features also brings information about the location of the active areas on the nucleus, about the orientation of the rotation pole, or about the properties of the dust particles. Finally, the study of composition differences between jets and the ambient coma allows us to characterize the homogeneity of the nucleus itself. However, in most cases the contrast between the morphological features and the ambient coma is low. Image enhancement techniques are then used to increase the contrast and to reveal the morphology of the coma. Different types of techniques exist, some of them revealing mostly radial features while others enhance azimuthal variations of brightness (Schleicher and Farnham, 2004). Several of these techniques are used in this work and will be detailed later.

## 1.4 Tails

The most spectacular part of a bright comet is probably its tail, which can span over several tens of millions of kilometres. One can distinguish between two types of tails. The first one is the dust tail which arises from the dust particles of the coma pushed away from the Sun by the radiation pressure. The dust tail trails along the trajectory of the comet and the dust is pushed in the anti-solar direction by the solar radiation pressure. The scattering of the solar light by the dust grains gives a characteristic yellow-white colour. It is composed of sub-micron to micron-sized particles (recent measurements reported maximum grain sizes up to the millimetre, (Rotundi et al., 2015)) and often displays striae or other structures. Secondly, there is the ion tail, or plasma tail. It is straight and oriented in the direction opposite to the Sun. The plasma tail is composed of several types of ions dragged away by the solar wind. It is narrower than the dust tail and its colour depends on the dominating ions. The $CO^+$ is responsible for the blue colour often observed in comet tails. The aspect of the ion tail can change rapidly in conjunction with changes in the magnetic field of the solar wind, and can be completely severed during tail disconnection events. A neutral tail composed of sodium has also been discovered for the first time in observations of comet Hale-Bopp in 1997. However, the formation of this neutral tail and the origin of the sodium atoms are still poorly understood.

## 1.5 Observing comets in the optical

The first observations of comets have been made at optical wavelengths. Spectra of comets in the optical were already reported in the late nineteenth century (Huggins, 1882; Seabroke, 1881). In addition to a strong continuum, several emission bands, corresponding mostly to daughter species, are usually detected. The main species detected in optical spectra are the following: OH, CN, $C_2$, $C_3$, CH, NH, $NH_2$, [OI], and the ions $CO^+$, $CO_2^+$, $CH^+$, $OH^+$, and $H_2O^+$ (Feldman et al., 2004). A typical cometary optical spectrum in which several of these radicals can be identified is shown in Fig. 1.4.

Observing comets in the optical has several advantages. First, these observations have been carried out for a long time. Most of the emission lines observed have been identified and are well characterized. A large number of comets have been observed over more than a century, which provides a wide database to compare comets between each others and establish classifications based on their composition. Secondly, the high sensitivity of optical detectors allows us to observe faint comets. JFCs are usually fainter and thus more difficult to observe. In the optical, a larger number of JFCs can be observed compared to other wavelengths. As a consequence, optical data bases contain a significant number of comets of different origins and dynamical types. More sensitive detectors also means that we can observe comets at larger heliocentric distances. It is important to detect when the gas emissions first appear in the coma, in order to better understand the outgassing from the nucleus. This also allows us to follow the evolution of cometary activity over wide ranges of heliocentric distances and to better understand the link between species. Finally, given the efficiency of the detectors,

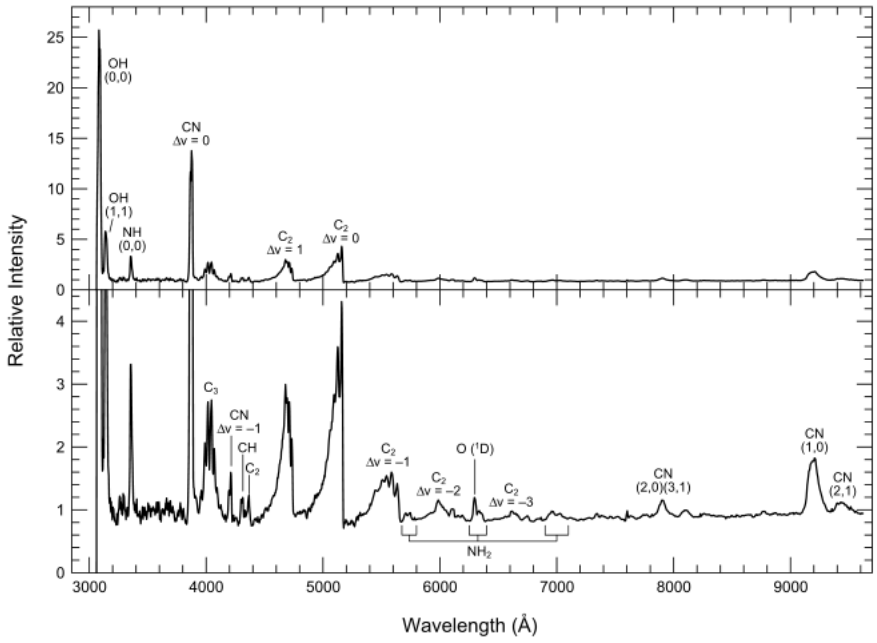


**Fig. 1.** Optical/near-IR CCD spectrum of Comet 109P/Swift-Tuttle obtained November 26, 1992. This spectrum is a composite of a UV/blue spectrum of Cochran (personal communication) and a red/near-IR spectrum of *Fink and Hicks* (1996). The cometary spectrum has been divided by a solar spectrum to show the cometary emissions. The two-pixel resolution was ~7 Å for the blue and ~14 Å for the red half. The upper panel shows the spectrum scaled by the strongest feature while the lower panel has an expanded ordinate to show the weaker features. The main features are labeled in one of the panels. This spectrum is typical of comets in the inner solar system.

Figure 1.4: Figure extracted from Feldman et al. (2004) showing the full optical spectrum of comet 109P/Swift-Tuttle.

smaller telescopes can be used to observe comets in the optical and provide larger fields of view. The high pressure on large telescopes makes it difficult to obtain large amounts of time to observe comets. Only smaller telescopes allow us to perform long-term monitoring. They are essential to follow the evolution of cometary composition over their orbit and to study the rotational variation of the coma brightness to determine nucleus rotation periods. Regular monitoring of comets also allows the detection of sudden changes of the activity soon after they happened.

Several techniques are used to observe comets in the optical. First, there is spectroscopy. Low-resolution spectroscopic observations allow us to observe simultaneously most of the radicals visible in optical spectra of comets and the dust continuum. Long slits sample a large part of the coma and allow the determination of the radial distribution of species. However, low-resolution spectroscopy only samples one direction of the coma. Information about its general morphology or about jets cannot be obtained with this technique. Several slit orientations can be used, allowing for example the detection of tail/anti-tail asymmetries, but the whole coma can never be sampled continuously, and the coma morphology may change between exposures because of the nucleus rotation. Spectroscopic observations allow us to

easily separate emission lines or bands from the underlying continuum. This is critical for weak emission features such as $NH_2$, CH, or [OI]. Optical fibres are also used but most of the time they do not provide spatial information about the distribution of the species in the coma. High-resolution spectroscopy up to R = $\frac{\lambda}{\Delta\lambda}$ = 100,000 allows us to resolve the rovibrational structure of the bands and provides a way to derive the isotopic ratio and the spin temperature of the observed species. Like for low-resolution spectroscopy, only one direction of the coma can be sampled and slits used are short, which means that we can only sample the coma close to the nucleus.

Another technique widely used to observe comets in the optical is narrow band photometry or imaging. Narrow band filters are used to isolate the emission of specific radicals or the dust continuum. As can be seen from Fig. 1.4, the strongest emissions in optical spectra of comets are usually those from OH, NH, CN, $C_3$, and $C_2$ along with the ions $CO^+$ and $H_2O^+$. Several attempts have been made to create individual filters isolating these radicals. The first set produced in large amounts and widely distributed was designed for the worldwide observing campaign of comet 1P/Halley and is known as the International Halley Watch (IHW) set of filters (Osborn et al., 1990). These filters have been commonly used for 10 years, especially for the optical study of a large number of comets performed by A'Hearn et al. (1995). It was further noticed that some of the IHW filters were contaminated by gas emissions and that these filters were degrading rapidly (Schleicher and Farnham, 2004). As a result, a new set of filters was designed for the international observing campaign of comet Hale-Bopp (Farnham et al., 2000). These filters have been used by most observers since then. They are described more thoroughly later in this work. Narrow band filters were first used in combination with photometers, which allowed the computation of the radicals production rates but did not provide any information about the distribution of species in the coma. Narrow band imaging was only made possible later with the advent of CCD detectors, allowing us to obtain maps of these radicals and the dust distribution in the coma. Some detectors have wide fields of view, making the mapping of the entire coma possible. Narrow band imaging is then useful to both compute gas production rates and study the coma morphology. However, only one radical can be sampled at a time and filters have to be cycled. This means that different species can not be sampled simultaneously. The dust removal is also more complicated than in spectroscopic observations, since dust observations have to be made regularly to decontaminate gas images from the dust contribution. The periodical variability of the comet lightcurve due to the rotation of the nucleus can then influence both the gas production rates and the production rate ratios obtained. However, the time necessary to cycle all filters is usually short compared to typical rotation periods of comet nuclei. Wide field of view integral field spectrographs recently developed should allow us to map the distribution of several radicals simultaneously and to avoid the drawbacks of both long slit spectroscopy and narrow band imaging. Nevertheless, these are usually only available on large telescopes.

In this work, we focus mainly on five radicals having bright emission bands or lines in the optical: OH, NH, CN, $C_3$, and $C_2$. As explained earlier, these radicals are not the only ones detected in optical spectra of comets. However, other radicals are difficult to observe with

narrow band filters due to the low contrast with the dust. Since most of the observations used for this work have been made with narrow band filters, we decided to focus only on these radicals.

The OH radical being the direct dissociation product of water, it is often used to estimate the water production rate in the coma of comets. The hydroxyl radical has a transition in the near-UV. It has been observed for the first time in 1941 in the spectrum of comet C/1940 R2 (Cunningham) (Swings et al., 1941). In the 307-310.5 nm region, several lines corresponding to OH have been identified. These strong lines are due to the $A^2\Sigma^+$-$X^2\Pi_i$ (0-0) transition and are usually produced by a fluorescence phenomenon, even though prompt emission also exists. Another weaker group of lines due to the (1-1) transition is visible between 313 and 316 nm. Finally, even weaker lines between 345 and 348 nm are due to the (0-1) transition (see e.g. Feldman et al. (2004)). Transitions of OH are also detected in the IR and radio domains (the 18-cm OH line has been observed in a large number of comets, Crovisier et al. (2002)).

The NH radical was also first detected in 1941 in the spectrum of C/1940 R2 (Cunningham) (Swings et al., 1941). The $A^3\Pi_i$-$X^3\Sigma^-$ (0-0) transition occurs between 335 and 337 nm (see e.g. Feldman et al. (2004)). This is usually the only NH band detected in cometary spectra.

The CN radical has two main band systems in the optical and near infrared (see e.g. Feldman et al. (2004)). The violet system is one of the most prominent features in spectra of comets and is due to the transition between the $B^2\Sigma^+$-$X^2\Sigma^+$ electronic states. This system has transitions between 359 and 422 nm. The (0-0) band at 388.3 nm is the brightest band of the system and the most commonly observed. It has been observed up to almost 10 au in comet Hale-Bopp (Rauer et al., 2003) and at 11.26 au in the centaur (2060) Chiron (Bus et al., 1991). The (0-1) band is also easily observed at 422 nm. The red system due to $A^2\Pi^+$-$X^2\Sigma^+$ transitions can be detected between 696 and 1494 nm. The strongest bands of this system in the optical are the (2-0) band at 791 nm, the (3-1) band at 807 nm, the (1-0) band at 917 nm, and the (2-1) band at 941 nm. Other bands from this system are also detected at longer wavelengths. The violet system is very sensitive to the Swings effect (see Sect. 2.3.3), especially for the (0-0) transition around perihelion.

The $C_3$ radical emission has long been identified as the 405 nm group, and spreads from approximately 375 to 410 nm (see e.g. Feldman et al. (2004)). It corresponds to a $\tilde{A}^1\Pi_u$-$\tilde{X}^1\Sigma_g^+$ electronic transition. However, the density of lines in that region of the spectrum almost results in a pseudo-continuum and makes difficult to identify every individual line.

Finally, the $C_2$ radical has two principal band systems in the optical, the Swan ($d^3\Pi_g$-$a^3\Pi_u$, $\Delta\nu = 2,1,0,-1,-2,-3$) and Phillips systems ($A^1\Pi_u$-$X^1\Sigma_g^+$, $\Delta\nu = 3,2,1,0$) (see e.g. Feldman et al. (2004)). The Swan system is largely spread over the optical spectrum of comets, from 434 to 676 nm, with two particularly bright bands corresponding to the $\Delta\nu = 1$ and $\Delta\nu = 0$ sequences, see Fig. 1.4. The Phillips system is spread across the near-IR, from 770 to 1210 nm. The Mulliken $D^1\Sigma_u^+$-$X^1\Sigma_g^+$ (0-0) band and the Ballik-Ramsay $b^3\Sigma_g^-$-$a^3\Pi_u$ systems are also observed respectively in the UV and the infrared.

## 1.6 Open questions about comets

### 1.6.1 Outbursts

Outbursts are sudden rises of the brightness of a comet over the course of a few hours or a few days. The magnitude of the brightness increase, the duration, and the frequency may vary strongly depending on the comet. In 2007, comet 17P/Holmes underwent a major outburst, its magnitude decreasing from 17 to 3 in less than two days (Buzzi et al., 2007). Such huge outbursts are rare but smaller ones occur more regularly. Several times a year, comet 29P/Schwassmann-Wachmann undergoes outbursts of 1 to 3 magnitudes (Trigo-Rodríguez et al., 2008). Frequent small and short duration outbursts of comet 9P/Tempel 1 were discovered prior to the collision with the Deep Impact impactor (A'Hearn et al., 2005). More recently, several outbursts have been detected by the Rosetta spacecraft in the coma of comet 67P/Churyumov-Gerasimenko, especially around the time of its perihelion passage (Steffl et al., 2015). It thus seems that outbursts are rather common among comets, and occur over a wide range of heliocentric distances, on different types of comets, in different conditions, and have various amplitudes and characteristic times. Even though a large number of outbursts have now been observed, their origin and the physical mechanisms at stake are still not well understood.

The first mechanism known to produce outbursts is a splitting of the nucleus. Such an event would expose a large amount a fresh ice that would explain the sudden rise of gas and dust production. The origin of the nucleus splitting is not always known, but among the possible causes one can distinguish the tidal splitting due to the proximity of a very massive body, like it was the case for comet Shoemaker-Levy 9, which was tidally disrupted following its close approach to Jupiter (Sekanina et al., 1994). A rotational splitting can occur if the centrifugal force overcomes the gravity and cohesive strength of the nucleus (Sekanina, 1997). In the case of sungrazing comets, the strong thermal stress at very low heliocentric distance can also cause the nucleus to disrupt. This is probably what happened to comet C/2012 S1 (Ison) which did not survive its perihelion passage at only 2.7 $R_{Sun}$ (Knight and Battams, 2014; Sekanina and Kracht, 2014). Outbursts and nuclei splitting can also be caused by a collision with another body, even though these collisions are extremely rare outside of the asteroid belt. Finally, the build-up of internal gas pressure could be invoked to explain nuclei splitting. In some cases, the nucleus only splits into a few large fragments that in turn behave like secondary nuclei, like comet 73P/Schwassmann-Wachmann 3 (Reach et al., 2009). Several fragments of comets 73P could be easily detected and studied individually. For some other comets, the nucleus only loses small fragments or boulders that can not be directly detected in the coma. However, it usually produces particular morphological features, like the so-called "coma wings" indicating that a fragmentation event occurred (Boehnhardt, 2000).

Cavities or pores under the surface of the nucleus have also been invoked to explain cometary outbursts. Ipatov and A'Hearn (2011) suggested that the outbursts triggered by the Deep Impact collision could be explained by subsurface cavities containing gas under high pressure.

Similarly, natural outbursts could be caused by build up of internal pressure in cavities or pores. At some point, the internal pressure is high enough to overcome the pressure and cohesive strength of the surface layers and new material is exposed. Gronkowski and Wesołowski (2015) proposed a model of outburst based on this idea. They argue that increasing gas pressure in subsurface cavities causes mechanical stresses leading to the apparition of cracks on the surface. The surface layer is eventually ejected into the coma and carbon monoxide is released through newly created crevices. Depending of the initial fraction of the nucleus active in the pre-outburst phase, the amplitude of the magnitude jumps varies. Other volatiles than CO, such as $CO_2$ or $CH_4$ could also be involved, explaining why outbursts are observed over a wide range of heliocentric distances and for a wide range of comet composition. Experimental work by Hartmann (1993) seems to confirm this explanation of cometary outbursts. Indeed, they concluded that gas pressure can build up in pore spaces inside the nucleus while a comet approaches the Sun until the pressure overcomes the top layer tensile strength, then leading to an eruption. They argue that this mechanism could explain the regular outbursts of comet 29P/Schwassmann-Wachmann 1. It thus seems that cavities or pores under the surface layers of the nucleus retaining gas under pressure could lead to eruptions and produce the outbursts observed for some comets.

Another hypothesis invoked to explain outbursts is the crystallization of amorphous water. Water ice, the main compound of nucleus ices, exits in two forms: amorphous and crystalline. Since comets are thought to have formed in very cold environments, they should mainly contain amorphous ice, the preferred form at these temperatures. When comets approach the Sun, the temperature rises and the transformation from amorphous to crystalline ice can occur more easily. This transformation is highly exothermic and provides a source of energy. At the same time, volatile gas (CO, $CO_2$) trapped in amorphous ice are released. The pressure of the released gas blows up the surface layers and fresh ice is exposed. Several outburst models based on the transformation from amorphous to crystalline ice have been proposed (Prialnik and Bar-Nun, 1987, 1992). More recent works have also invoked the transport of fluidized cometary material inside the nucleus (Belton and Melosh, 2009), or even liquid phases inside the nucleus as the origin of outbursts (Miles and Faillace, 2012).

As we can see, various scenarios have been proposed to explain cometary outbursts but this phenomenon still remains difficult to fully understand. It is probable that the mechanism producing the outburst varies depending on the comet composition, rotational state, or the heliocentric distance. It is thus important to observe and study as many of these events as possible, in order to get a better understanding of the processes involved in these rapid and dramatic changes of a comet brightness. Moreover, the observation and analysis of outbursts and nucleus splitting can provide information about the nucleus itself. It can inform us about the size, density, and structure of cometary nuclei, like it was the case for comet Shoemaker-Levy 9 that disrupted following its close approach from Jupiter (Asphaug and Benz, 1996). It can also help discriminate between models of the structure of the nucleus.

### 1.6.2 Comet composition

Spectroscopy has been used to study comets for more than a century. The very first observations revealed the two components of cometary spectra: the continuum and the emission bands. In the second part of the twentieth century, the number of comets observed at both low and high resolution in the optical and at other wavelengths quickly increased. At that point, it became possible to compare comets to each other and to try to define a comet taxonomy based on their specific characteristics. If one only takes a quick look, all comet spectra display the same two main components and are mostly very similar. However, a more thorough study reveals variations of composition among comets. Some comets have a very strong continuum while emission bands are barely visible. These comets are usually qualified as "dusty". Other comets have very weak continuum and strong emission bands. Additionally to variations of the dust-to-gas ratio from comet to comet, variations of the relative intensity of the emission bands are also detected. This is illustrated in Fig. 1.5. Comet 8P/Tuttle shows strong CN, $C_2$, and $C_3$ emission bands while comet 21P/Giacobini-Zinner has a strong CN emission but almost no $C_2$ and $C_3$.

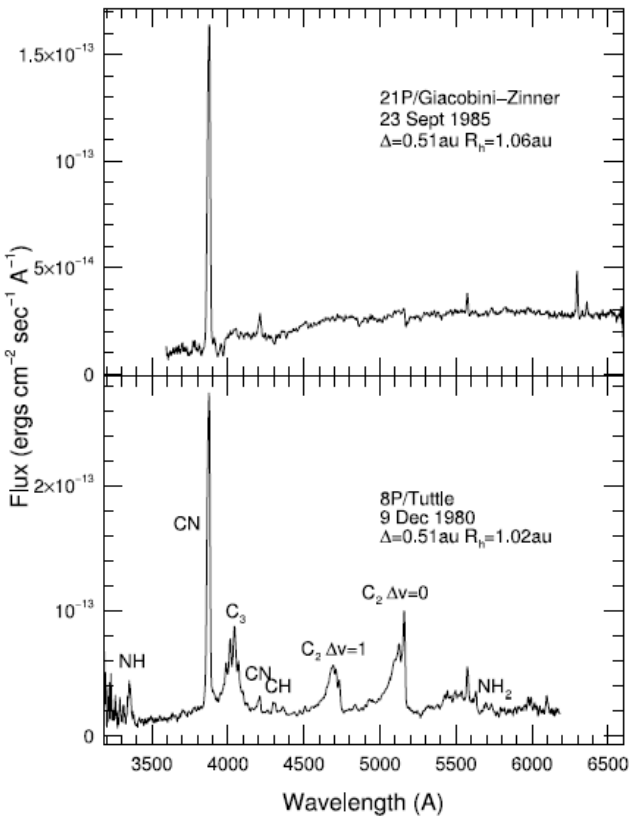


**Fig. 1** Spectra of 21P/Giacobini-Zinner and 8P/Tuttle obtained at McDonald Observatory are shown, scaled to the CN band at 3880 Å. The comets were observed at comparable heliocentric and geocentric distances. Inspection of the figure shows that the well-defined $C_2$ and $C_3$ bands seen in Tuttle are nearly absent in Giacobini-Zinner's spectrum. (Spectra courtesy of A. Cochran)

Figure 1.5: Figure extracted from Cochran et al. (2015) showing the comparison between spectra of comets 21P/Giacobini-Zinner and 8P/Tuttle.

### Abundance measurements at optical wavelengths

Optical studies of comets are the easiest to achieve from the ground and have been performed for more than 50 years. The largest databases available to perform compositional classification of comets mainly rest on optical observations. Current optical detectors are very sensitive and allow us to observe comets that are fainter and/or at larger heliocentric distances compared to other wavelengths. Low resolution spectroscopy has been used by several teams to analyse the composition of a large number of comets (Newburn and Spinrad, 1984; Cochran, 1987; Newburn and Spinrad, 1989; Cochran et al., 1992; Fink and Hicks, 1996; Fink, 2009; Langland-Shula and Smith, 2011; Cochran et al., 2012). Narrow band imaging or photometry is the second major technique used to characterize the composition of comets in the optical (A'Hearn et al., 1980; A'Hearn et al., 1995). Some of the largest published studies gather observations of more than 100 comets. They contain statistically significant samples of all dynamical types of comets (JFCs, HTCs, dynamically new and old NICs) and also periodic comets observed at several consecutive returns. These studies bring important clues to answer the long-debated question of pristine versus evolutionary origin of composition differences among comets. More and more comets are also observed over a wide range of heliocentric distances, allowing us to detect changes of the coma composition linked to the distance of the comet to the Sun. To directly compare comets from different studies is difficult since the observing techniques, the sizes of the field of view, the fluorescence efficiencies, and the parameters used in the Haser model (Haser (1957), this model will be discussed in more details later) differ. However, the main compositional classes derived from most studies are very similar and classification of common comets usually agrees once the difference in model parameters has been accounted for (Fink, 2009; Cochran et al., 2012).

A'Hearn et al. (1980) studied six comets observed with narrow band filters and compared their composition. They find it to be very similar from one comet to another but also as a function of the heliocentric distance, and they could not distinguish any particular composition classes. Spectroscopic observations of 17 comets by Cochran (1987) and Cochran et al. (1992) led to similar results. No strong variations of composition between comets or with the heliocentric distance could be detected. Newburn and Spinrad (1984, 1985), and Newburn and Spinrad (1989), however, gathered spectrophotometry of 25 comets and found that even though most of these comets have the same composition, two are severely depleted in both $C_2$ and $C_3$. Unlike previous studies, they noticed a variation of the $C_2$ to CN ratio with the heliocentric distance, indicating there might be different formation mechanisms for the two radicals. Fink and Hicks (1996) analysed spectra of 39 comets. They concluded that about 10% of comets have deviant composition but could not define specific taxonomical classes.

The first large study gathering a statistically significant number of comets was published by A'Hearn et al. (1995). They observed 85 comets with narrow band filters, among which 41 were sufficiently well studied to achieve a taxonomical classification. First, they found that for individual comets, there were no systematic trends of composition or dust-to-gas ratio with the heliocentric distance. However, the dust-to gas ratio can vary by two orders of

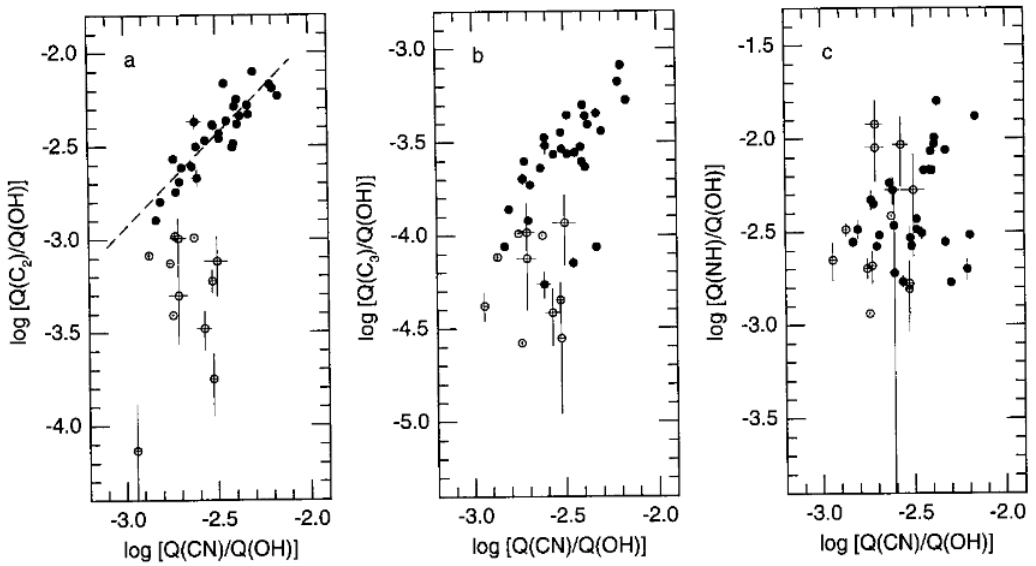


**FIG. 10.** Abundance ratios for taxonomic classification. These data, like those in Fig. 9, are for the 41 comets in the restricted dataset. Error bars are shown on all points but in most cases are smaller than the points. Filled symbols indicate comets in the typical taxonomic class. Our two primary taxonomic groups are identified based on the relative production rates of OH, CN, and $C_2$ (a). Within the typical group, CN and $C_2$ vary together with respect to OH (the dashed line has a slope of unity), and within the depleted group, CN is approximately constant with respect to OH while $C_2$ varies widely. The pattern for $C_3$ is similar to that for $C_2$ but with more scatter. NH exhibits no discernible pattern.

Figure 1.6: Figure extracted from A'Hearn et al. (1995) representing the logarithm of the $C_2$ to OH, $C_3$ to OH, and NH to OH ratios as a function of the logarithm of the CN to OH ratio. In the first two plots on the left, most comets lie on a diagonal band while carbon-chain depleted comets are located below this diagonal band.

magnitude from one comet to another and is correlated to their perihelion distance. Some comets display changes of trace species ratio relative to OH with the heliocentric distance but not relative to each other. The composition of the comets they studied do not vary with their dynamical age or after consecutive returns, which indicates that cometary nuclei are rather homogeneous in composition for those species. More importantly, they were able to distinguish a group of comets depleted in $C_2$ and $C_3$, see Fig. 1.6. This class of comets was called carbon-chain depleted comets. A'Hearn et al. (1995) noticed that almost all carbon-chain depleted comets were Jupiter Family comets, even though not all JFCs were carbon-chain-depleted. At that time, it was thought that JFCs formed at their current location in the Kuiper Belt. JFCs were then formed farther away from the Sun than NICs, formed in the giant planets region. The composition difference between JFCs and other comets was thus thought to reflect composition differences at their places of formation. Finally, this study showed that JFCs usually have steeper variations of gas and dust production rates with the heliocentric distance and larger asymmetries about perihelion compared to other comets, while dynamically new comets tend to show very shallow dependence of gas production rates with the heliocentric distance before their perihelion passage.

Since then, several other studies gathering observations of large numbers of comets have been published, bringing new insights to the taxonomical classification of comets. (Fink,

2009) presented a spectroscopic survey of 92 comets, out of which 50 had well detected emission bands. They found that about 70% of their comets have typical composition, 22% of comets have low $C_2$ but normal $NH_2$, and 6% have both low $C_2$ and $NH_2$ ($C_3$ emission was not observed for this study). In contradiction with the results obtained by A'Hearn et al. (1995), they noticed that one third of $C_2$ depleted comets were NICs and two third were JFCs. Similarly, Langland-Shula and Smith (2011) found both JFCs and long period comets among carbon-chain depleted comets. They also noticed that the $C_2$ to CN ratio of the comets in their sample is decreasing with the heliocentric distance while the $C_3$ to CN ratio is constant. From spectroscopic observations of 130 comets, Cochran et al. (2012) defined a restricted data set of comets observed at least 3 nights. They distinguished the two usual classes: typical and carbon-chain depleted comets, the proportion of comets in each class varying with the definition used. 9% of the comets in their restricted data set are depleted in both $C_2$ and $C_3$, while 25% are depleted only in $C_2$. In this study, 37% of JFCs are depleted and only 18.5% of LPCs. More recently, Schleicher and Bair (2014) applied principal component analysis on a sample of 101 comets and were able to define seven taxonomical classes: typical comets (about 70% of comets), comets strongly depleted in both $C_2$ and $C_3$, comets slightly depleted in both $C_2$ and $C_3$, comets depleted in $C_2$ but not $C_3$, comets depleted in $C_3$ but not $C_2$, comets depleted in NH but not depleted in carbon species, comets depleted in CN, $C_2$, and $C_3$ compared to OH.

In conclusion, it thus seems that the global picture of cometary taxonomy in the optical is more complex than first thought. Two main classes of comets seem to be distinguished in all studies: typical comets and carbon-chain depleted comets. However, the origin of this composition difference among comets is still unclear. It is probably not caused by evolutionary processes. Comets observed at several returns do not show variations of production rate ratios (A'Hearn et al., 1995). Moreover, the splitting of comet 73P/Schwassmann-Wachmann 3 probably exposed ices from deeper regions of the nucleus but no composition differences were observed among the fragments, nor after the outburst compared to previous passages of the comet (Villanueva et al., 2006; Dello Russo et al., 2007; Schleicher and Bair, 2011). The origin of carbon-chain depletion was first thought to be intrinsic, since early studies showed most depleted comets were JFCs. However, more recent studies revealed that some LPCs are also depleted. The origin of these main composition classes is thus more difficult to understand than previously thought and even larger data sets including comets observed over wide ranges of heliocentric distances are necessary to reach a clear understanding of the origin of taxonomical classes.

#### Abundance measurements at other wavelengths

Rotational transitions of some parent species (but also daughter species) can be detected at radio wavelengths. Contrarily to infrared observations, radio beams are usually large and allow us to measure a large part of the coma gas content, making possible to derive total gas production rates. High resolution is also easier to achieve than in the optical or in the

infrared. Line shapes and line-of-sight outflow velocities are then often measured from high resolution radio observations of comets. However, single-dish radio observations do not allow us to map the distribution of species in the coma. Recently, the rise of radio interferometry provided the first high spectral resolution maps at radio wavelengths. The new Atacama Large Millimeter/submillimeter Array (ALMA) is composed of 66 antennas working together, reaching a maximal angular precision of $0.005''$. ALMA was used to map the distribution of HCN, HNC, and $H_2CO$ in the coma of comets C/2012 F6 (Lemmon) and C/2012 S1 (Ison) with very promising results (Cordiner et al., 2014).

Parent species such as CO, $H_2CO$, $CH_3OH$, $CH_3CN$, HCN, $NH_3$, HCOOH, HNCO, and $H_2S$, and several daughter species (OH, CS, and HNC) have been observed in a dozen comets (Crovisier et al., 2009). Several other molecules have only been detected in the coma of comet C/1995 O1 (Hale-Bopp): $SO_2$, NS, $H_2CS$, $HC_3N$, $NH_2CHO$, $CH_3CHO$, $HCOOCH_3$, and $HO-CH_2CH_2-OH$ (the most complex molecule detected so far in a comet from ground-based observations) (Bockelée-Morvan et al., 2000; Crovisier et al., 2004). Water is not directly observed at radio wavelengths but its dissociation product OH has a transition around 18 cm and is used to derive water production rates from radio observations. The abundance of other species is thus usually measured relative to water.

The analysis of the composition of 35 comets by Crovisier et al. (2009) at radio wavelengths showed large differences from comet to comet. HCN only has a narrow range of abundances relative to water but the relative abundance of some other molecules such as $CH_3OH$, $CH_3CN$, or $H_2S$ can spread over a factor 10. At these wavelengths, the various molecules are not observed simultaneously to OH. The rotational variation of the gas production rates could then account for part of the scatter observed among comets but it is probably unlikely to produce such high differences. Even though a wide range of abundances was observed, no taxonomical classification could be made for this sample of comets. No composition difference could be detected between JFCs and NICs either (Crovisier et al., 2009).

Molecules lacking permanent dipoles can only be observed through their vibrational transitions at infrared wavelengths. The high opacity of the atmosphere in the infrared, mainly due to absorption by $H_2O$ and $CO_2$, makes observations at these wavelengths difficult. Some atmospheric windows still allow the observation of comets in the infrared, especially between 2.5 and 5 $\mu$m. Infrared detectors used to be much less sensitive than optical detectors and the sky background is usually high in infrared observations and extremely difficult to remove. Because of this, infrared observations of comets started late and faint comets, or comets at large heliocentric distances are still challenging to observe. We are missing large data bases of observations like those available in the optical. The slits used are also much shorter than in the optical, which means that the gas production rates derived are more sensitive to temporal variations or to the outflow velocity assumed in the model.

Water and prompt OH are both detected in the infrared, as well as several other parents ($CH_4$, $C_2H_2$, $C_2H_6$, $H_2CO$, $NH_3$, $CH_3OH$, HCN) and daughter species ($NH_2$, CN,..). Water can

be detected simultaneously to other species, allowing the computation of reliable relative abundances. About three dozen comets have been observed in the IR so far, including both JFCs and NICs. From these observations, Mumma and Charnley (2011) could define three main classes of comets: typical comets, organic enriched comets, and comets severely depleted in organics. Each class contains both NICs and JFCs. However, the picture is not as simple as it may sound. Comet 6P/d'Arrest, for example, is typical in $CH_3OH$ and $NH_3$ but depleted in $C_2H_6$, $C_2H_2$, and HCN (Dello Russo et al., 2009). In a more recent study gathering 30 comets observed in the infrared, Dello Russo et al. (2016b) found that JFCs are depleted in volatile species with respect to water compared to long-period Oort Cloud comets. They also defined a taxonomic classification system, separating their 30 comets in 4 groups and eleven subgroups. Figure 1.7 shows the range of abundances relative to water measured from IR and radio observations of comets. The crosses represent the bright comet C/1995 O1 (Hale-Bopp).

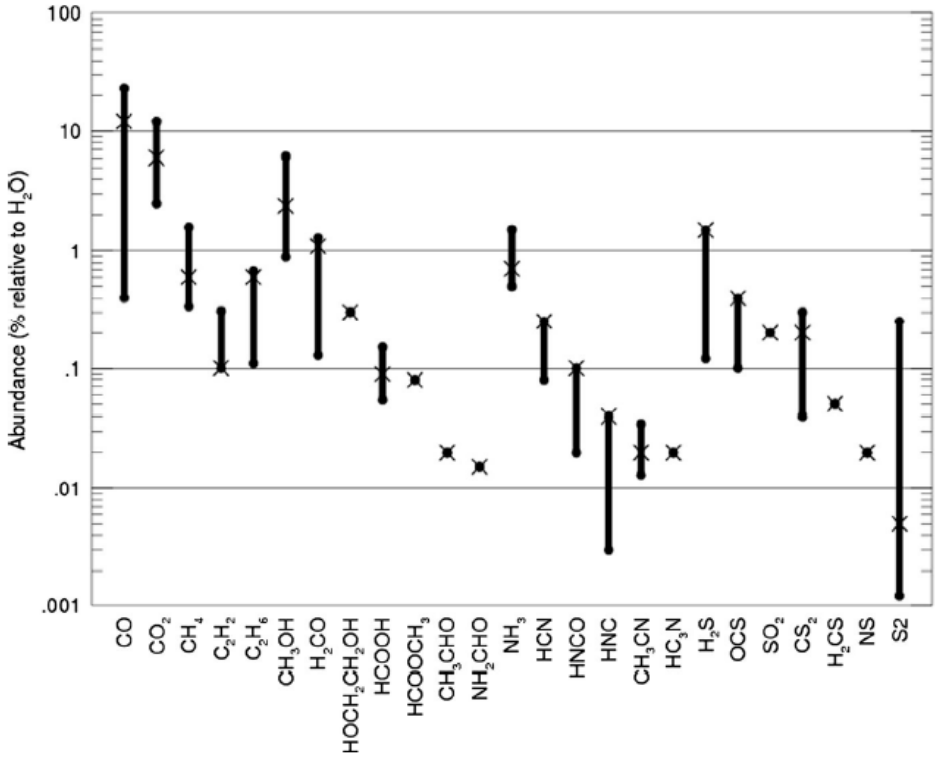


**Fig. 3** The abundances for many of the IR- and radio-observed species are shown as a percentage relative to water. The *bar* shows the range of values observed for each species. The "×" marks the value determined for comet C/1995 O1 (Hale-Bopp). CO, $CH_3OH$, $H_2CO$, HCN, $H_2S$ and $CS_2$ were all observed in at least 10 comets; all other species where observed in fewer. The species with a single value (an X-dot) were only observed in Hale-Bopp (based on Fig. 1 of Bockelée-Morvan 2011)

Figure 1.7: Figure extracted from Cochran et al. (2015) showing the range of composition relative to water of species detected at infrared and radio wavelengths.

After $H_2O$, CO and $CO_2$ are the most abundant volatiles in the coma of comets. CO can be both a parent species and the product of $CO_2$ or $H_2CO$ dissociation. CO can be observed at various wavelengths, in the radio, the IR, or the UV. UV observations of 12 comets revealed that

the CO abundance relative to water can vary over a huge range of values, from approximately 0.4% to about 30% (Bockelée-Morvan et al., 2004). CO emission has also been detected in 17 comets from IR ground-based surveys (Paganini et al., 2014b) and another dozen comets were observed with the Akari space telescope (Ootsubo et al., 2012). Similar ranges of abundances were found from IR observations and UV surveys. The CO abundance does not seem linked to the dynamical type of the comet, even though the comets with the higher CO abundances are LPCs (Cochran et al., 2015). $CO_2$ can not be detected directly from ground-based observations because of the strong absorption of atmospheric $CO_2$. $CO_2$ has been observed in-situ in a few comets but the first larger sample was gathered with the Akari space telescope (Ootsubo et al., 2012). They detected $CO_2$ in 17 comets and its abundance relative to water varies from a few to 30% within 2.5 au. Farther away from the Sun, the CO and $CO_2$ abundance relative to water increases, since these species are more volatile than water. Reach et al. (2013) observed 23 comets with the Spitzer space telescope. They did not find strong trends of $CO_2$ production with the heliocentric distance. They were able to define a class of $CO_2$-poor comets, most of which were also carbon-chain depleted.

Attempts have been made to reconcile taxonomical classifications made from observations of comets at different wavelengths. However, it does not seem that carbon-chained depleted comets are the same as comets depleted in organics. Comet 8P/Tuttle, for example, is typical in $C_2$ and CN (Schleicher, 2007) but depleted in $C_2H_2$ and HCN (Bonev et al., 2008). This emphasises the difficulty to understand the origin of composition differences among comets. Progress can only be made by increasing the number of comets observed in the optical and, more importantly, at radio and IR wavelengths. Simultaneous observations of comets at different wavelength ranges are also crucial to reach a better understanding of the origin of taxonomical classes.

### 1.6.3 The origin of species in the coma

Daughter species observed in the coma of comets, such as $C_2$, $C_3$, CN, or NH, are the products of the photodissociation of more complex species released directly from the nucleus. However, things are not as simple as they may seem. Indeed, the parent species of some radicals are sometimes difficult to identify unambiguously. Some daughter species probably have several parents while others are actually granddaughter species. It has also been suggested that gas could be released from organic-rich grains in the coma. The discrepancies between taxonomical classifications defined from optical and IR observations further emphasize that the relationship between parent, daughter and granddaughter volatiles is still not well understood. As it has already been mentioned earlier, optical observations allow us to observe comets over a wider range of heliocentric distances, to observe fainter comets, and to gather very large and homogeneous samples. The issue of species parentage in the coma of comets is then particularly important to correctly infer nucleus ice abundances from optical comet observations, and to retrieve information about the composition of the early solar system at the time comets formed.

The case of CN is a good illustration of the problems encountered while trying to link parent and daughter species. The most likely candidate for CN parentage was first thought to be HCN, which is detected in IR spectra of comets. However, comparisons of the abundance of CN from optical observations with the abundance of HCN derived from the IR showed that for some comets, there was not enough HCN produced to account for CN production rates measured. Comets C/1989 X1 (Austin), C/1983 H1 (IRAS-Aracki-Alcock), 21P/Giacobini-Zinner, C/1986 P1 (Wilson), 6P/d'Arrest, and C/2012 S1 (Ison) are examples of comets for which the CN abundances are higher than the measured HCN production rates (Fray et al., 2005; Dello Russo et al., 2009, 2016a). To the contrary, for some other comets like C/1995 O1 (Hale-Bopp), C/1990 K1 (Levy), C/1996 B2 (Hyakutake), or C/2013 R1 (Lovejoy), CN and HCN production rates are similar (Fray et al., 2005; Opitom et al., 2015b). This highlights the fact that, if HCN photodissociation is the principal source of CN for some comets, at least another CN production mechanism is necessary to account for the measured abundances. Bockelee-Morvan and Crovisier (1985) and Fray et al. (2005) also argued that the distribution of CN in the coma was inconsistent with the HCN lifetime, hence pointing to other sources of CN.

Several hypotheses about the origin of the CN in the coma of comets were explored. The first one is that other nitrogen-bearing species could be potential CN parents. The main candidates are $CH_3CN$, $HC_3N$, HNC, $C_2N_2$, and $C_4N_2$. Fray et al. (2005) compared CN parent lifetimes derived using the model of Combi and Delsemme (1980) to the lifetimes of possible parents. $CH_3CN$ and HNC lifetimes are too long to be the additional sources of CN. $HC_3N$ has a lifetime consistent with the one measured for the CN parent but its abundance in the coma is much lower than the HCN abundance, and it could not account for CN production rates measured for some comets. The photochemistry and lifetimes of $C_4N_2$ are poorly known, so it is difficult to estimate if it could be a possible CN parent. Finally, $C_2N_2$ has a lifetime consistent with the CN parent but it has never been detected in the coma of a comet. Its low vibrational band strength indicates that even if $C_2N_2$ was present in the coma with abundances similar to HCN, it would be extremely difficult to detect by remote sensing. No detection of $C_2N_2$ in the coma of 67P/Churyumov-Gerasimenko was reported yet by the Rosetta mission. The second hypothesis to account for the production of CN is the direct release of CN by the photochemical and/or thermal degradation of organic-rich grains (the so-called CHON grain) or other macro-molecules in the coma. A'Hearn et al. (1986) suggested for the first time that CN could come from grains to explain the CN jets seen in the coma of comet Halley. Lederer et al. (1997) observed similar CN jets in the coma of the bright comet Hale-Bopp. Since then, CN jets have been observed for a large number of comets. Klavetter and A'Hearn (1994) noticed that the CN radial profile in the jets of comet Halley was different than in the ambient coma, indicating that the CN jets are in part produced by an extended source. In addition, A'Hearn et al. (1995) showed that dust and CN production rates are correlated for several comets in their data set, reinforcing the idea that CN could be released from dust grains. Extended sources have also been invoked to explain the spatial distribution of $H_2CO$ and HNC (Cordiner et al., 2014). Finally, CN could also be produced by chemical reactions in the coma. This

mechanism was already invoked to explain the production of HNC (Irvine et al., 1998; Rodgers and Charnley, 1998), even if these reactions should not be very efficient for normally active comets. Chemical reactions producing CN in the coma have not been studied yet.

Parents of $C_3$ and $C_2$ are even more difficult to identify, even though these radicals have been among the first observed in cometary spectra. Jackson (1976) first suggested that $C_2H_2$ and $C_2H_6$ could be potential parents for $C_2$ but these species have only been detected for the first time in the coma of comets 20 years later (Crovisier, 1997). It has been noted that $C_2$ profiles in the inner coma of comets are usually flatter than would be expected if the $C_2$ was produced in a simple two-step process. O'dell et al. (1988) showed that the flat shape of $C_2$ radial profiles can be reproduced if it is a granddaughter species instead of a daughter species, as usually assumed. Helbert et al. (2005) developed a chemical network to explain the formation of $C_2$ and $C_3$ in the coma at large heliocentric distances and obtained results consistent with the observed profiles. Weiler (2012) complemented the chemical network and applied it to the observations of other comets at smaller heliocentric distances. The main path leading to the production of $C_2$ from $C_2H_6$ would be the following:

$$C_2H_6 \rightarrow C_2H_4 \rightarrow C_2$$

However, both Helbert et al. (2005) and Weiler (2012) noticed that the production of $C_2$ from $C_2H_6$ is not very efficient and that $C_2H_6$ alone could not account for the $C_2$ production rates observed. The main $C_2$ parent would then be $C_2H_2$, which is also dissociated in a two-step process.

$$C_2H_2 \rightarrow C_2H \rightarrow C_2$$

Helbert et al. (2005) were able to reproduced well the $C_2$ profiles observed in the coma of Hale-Bopp at large heliocentric distances.

The most likely parent of $C_3$ is thought to be $C_3H_4$, which produces $C_3$ through the following reaction (Weiler, 2012):

$$C_3H_4 \rightarrow C_3H_2 \rightarrow C_3 \rightarrow C_2$$

$C_3H_4$ can either be dissociated by photolysis or electron impact dissociation but the reaction rates for the electron impact photodissociation are poorly known, which makes it difficult to build a reliable model for the production of this radical. $C_3$ can also be further dissociated to form $C_2$ and contribute to its production. $C_3H_4$ has never been observed in the coma of a comet so far but its existence in comets could be confirmed by in-situ measurements from the Rosetta mission.

Combi and Fink (1997) discussed the possibility that the flat $C_2$ profile in the inner coma could be explained if the $C_2$ is released by a halo of CHON grains. They demonstrated that a three-generation model can only reproduce $C_2$ radial profiles if the additional ejection velocity communicated to the fragments after each dissociation is low, which seems rather unlikely.

They thus developed a model considering a halo of CHON grains releasing directly the $C_2$. They found that including a halo of CHON grains allows them to reproduce the observed profiles and they determined that the size of the halo should be around 88,000 km at 1 au. This is almost one order of magnitude larger than the extended source producing $H_2CO$ and CO but also larger than the extended source of CN in the jets of comet Halley (A'Hearn et al., 1986). This would imply there are two different populations of carbonaceous grains or that grains have a mantle/core structure.

NH and $NH_2$ are both thought to derive from $NH_3$. $NH_3$ is most likely the parent of $NH_2$, which in turns decays into NH. However, fluorescence efficiencies, reaction rates, and branching ratios for these species are poorly known, making any advanced modelling difficult. $NH_3$ is also difficult to observe and has only been detected for the first time in 1996 in the coma of C/1996 B2 (Hyakutake) (Palmer et al., 1996). Since this first discovery, several simultaneous measurements of $NH_3$ and its dissociation products $NH_2$ and NH have been made, confirming the probable parentage between these species (Dello Russo et al., 2009; Kawakita and Mumma, 2011; McKay et al., 2014; Dello Russo et al., 2014).

At the present time, reactions in the coma and the link between parent and daughter species remain difficult to understand. Several models have been developed, involving either complex chemical networks or halos of organic-rich grains, but some issues still remain and more information is needed to be able to provide a consistent picture of what is really happening in the coma of comets. Observations of comets over wide ranges of heliocentric distances are particularly important to study the changes in the way volatiles are released while comets are approaching the Sun. One way to better understand the species parentage in the coma from ground-based observations is to compare directly parent species measured from infrared observations with daughter species abundances, as it has already been done for several comets. However, these measurements are strongly dependent on model parameters for both IR and optical observations, some of which are poorly known. The different sizes of the fields of view and the difficulty to obtain actual simultaneous observations are also important issues. The study of the shape of the radial profile of radicals in the coma in order to derive parent and daughter lifetimes also provides a way to link daughter species to possible parents. However, these kinds of observations require high signal-to-noise ratios and large fields of view in order to sample the entire coma. The best way to address the problem would be to map directly the distribution of both parent and daughter species in the coma. The combined used of new facilities such as the radio-interferometer ALMA or new large field of view optical integral field spectrographs will bring clues to better understand species parentage in the coma of comets.

# 2 Observations and data reduction

This chapter focusses on the detailed description of the observations used for this work. We will first describe the instruments we used. Most of our observations are narrow band images and have been obtained using the TRAPPIST telescope at La Silla observatory. We also observed 3 comets with the FORS 2 low resolution spectrograph at the ESO/VLT. We will describe our data reduction and calibration procedures for both instruments. In order to derive gas production rates from our calibrated images, we adjusted a coma brightness model to our observations. For this work, we chose to use the Haser model (Haser 1957), which is described later in this section. We also estimated the dust production through the $Af\rho$ parameter. Finally, we used various image enhancement techniques to reveal morphological features in the coma. The main existing techniques as well as their advantages and drawbacks are described.

## 2.1 TRAPPIST

TRAPPIST (Transiting Planets and PlanetesImals Small Telescope, Fig. 2.1) has been installed in 2010 at the ESO La Silla observatory in Chile. This observatory, located on a 2400m-high mountain, offers ideal weather conditions for an astronomical observatory, with approximately 300 clear nights per year and low humidity. The TRAPPIST project is led by the ORCA (ORigins in Cosmology and Astrophysics) group from University of Liège in collaboration with the Geneva observatory (Jehin et al. 2011). It was funded by the Belgian Fund for Scientific Research (F.R.S.-FNRS) and the Swiss National Science Foundation (SNF). TRAPPIST is dedicated to two main projects: the detection and study of exoplanets in transit and the study of comets and small bodies of the solar system.

At this time, 3302 exoplanets have been discovered[1]. The most prolific method for exoplanet discovery is the transit method: when a planet passes in front of its host star, it eclipses the stellar disk, blocking part of the emitted light, and a diminution of the star apparent brightness can be detected. Important characteristics of the planet, such as its orbital inclination or

[1] Nasa Exoplanet Archive, consulted on July 14, 2016

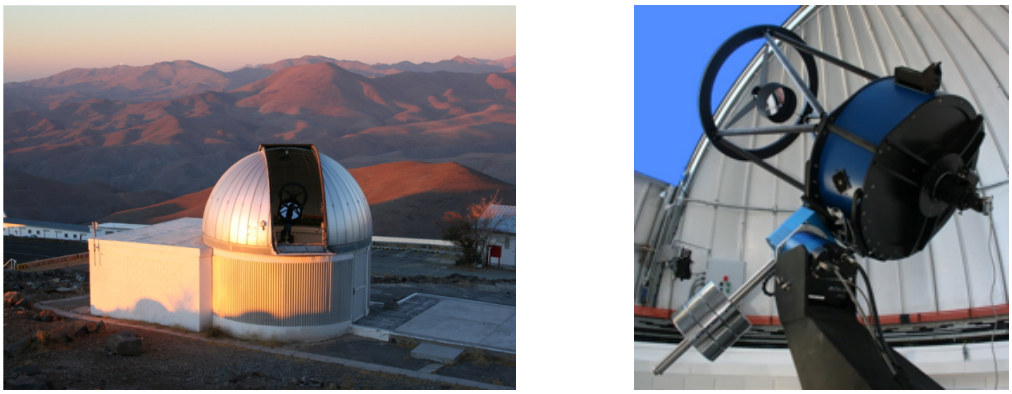

Figure 2.1: The 60-cm TRAPPIST telescope at La Silla Observatory.

the planet-to-star radius can be derived from the observation of its transit. If the planet is also detected with the radial velocity method, the mass and the radius of the planet can be determined, and then its density. Since TRAPPIST is a dedicated telescope, a large amount of time is available for the observation of exoplanets. This large amount of observing time combined with the high achievable photometric precision make it a good instrument for the study of exoplanets in transit. TRAPPIST is part of the SuperWASP transit survey[2]: it consists in two observatories (one in the Northern hemisphere and one in the Southern hemisphere), each composed of eight wide-angle cameras simultaneously monitoring the sky and searching for exoplanet transits. TRAPPIST observes exoplanet candidates visible from the Southern hemisphere in order to discriminate between planets and eclipsing binaries, for instance. Since 2010, 105 planets have been co-detected by TRAPPIST, among which 74 have already been published. Another aspect of the exoplanet project with TRAPPIST is the characterisation of known exoplanets in transit. Once an exoplanet is confirmed, high precision transit lightcurves allow us to constrain some parameters such as the size of the planet. In the case of highly irradiated hot Jupiters, the diminution of the near-infrared emission when the planet passes behind its star can be detected, providing valuable information about the temperature, the albedo, and the heat distribution in the atmosphere of the planet. TRAPPIST is also a part of the SPECULOOS project (Search for habitable Planets EClipsing ULtra-cOOl Stars), searching for terrestrial planets in the habitable zone around ultra cool dwarf stars. Around 500 stars have been selected and will be monitored regularly. This project consists in four 1m telescopes located at the ESO Paranal observatory, TRAPPIST at the ESO La Silla observatory and TRAPPIST-North at the Oukaimeden observatory in Morocco. The planets discovered by this project will make good targets to be observed with future large telescopes like the European Extremely Large Telescope (E-ELT) or the James Webb Space Telescope (JWST), searching for bio-signatures.

The second aspect of the TRAPPIST scientific project is the study of small bodies of the solar system, mainly comets. Bright comets ($V_{mag} \leq 12$ ) are observed about once or twice a week with narrow band filters in order to measure the production rates of several gas species (OH,

[2] SuperWASP Superwasp: http://www.superwasp.org

NH, CN, $C_3$, and $C_2$) and the dust. The large amount of observing time available allows us to follow the evolution of the activity of bright comets for several months around their orbit. With about 5 to 10 bright comets observed every year, we have rapidly gathered a statistical and homogeneous sample to study the evolution of the activity and composition of these comets, try to determine new taxonomic classes, and understand the origin of these classes. Our data are regularly used to assess the activity of a comet in order to prepare observations with larger telescopes. Image analysis is used to study the morphology of the coma (jets, fans, ...) and to measure the nucleus rotation period. The follow-up of outbursts (sudden rises of the comet activity) or split comets is also made possible by the rapid response time of the telescope. The study of the individual and ensemble properties of bright comets observed through narrow band filters with TRAPPIST is the main subject of this work and more details about these observations and the data reduction procedure will be given later.

In addition to the study of bright comets, a photometric monitoring of fainter comets is performed with broad band filters in order to measure the evolution of their dust production and detect outbursts. We will also observe periodic comets on consecutive returns and study the evolution of their secular lightcurve. Finally, TRAPPIST is part of an international collaboration aiming to observe stellar occultations by trans-Neptunian objects (TNOs). Observation of a stellar occultation is a powerful tool to determine the size of these distant icy bodies impossible to resolve from Earth. An occultation by Eris in 2011, for example, allowed the determination of its size with an accuracy of a few kilometres (Sicardy et al., 2011). More recently, an occultation by the centaur Chariklo revealed the first system of rings in the solar system except those around the giant planets (Braga-Ribas et al., 2014).

TRAPPIST is a 60-cm f/8 Ritchey-Chretien telescope built by the Astelco company. The telescope is placed under a 5m Ash-Dome dome. The open design and the use of aluminium and carbon fibre result in a very lightweight telescope (75 kg). It is mounted on a German equatorial mount NTM-500 built by the same company as the telescope. The direct drive technology allows us to avoid periodic errors and to achieve a pointing velocity up to 50 deg/s. The camera was built by Finger Lake Instrumentation and is equipped with a 2K×2K backside-illuminated Fairchild chip. The pixel size is 15 $\mu$m, providing a field of view of $22' \times 22'$ with a sampling of $0.65''$/pix. The chip is thermoelectrically cooled 55°C below the ambient temperature. The gain is 1.1 $e^-$/ADU. The camera has three different readout modes: a very fast readout mode (2s) with two quadrants (readout noise of 14 $e^-$), a fast readout mode (4s) with one quadrant (readout noise of 14 $e^-$) and a slow mode (6s) with low readout noise (9.5 $e^-$) for faint sources. The detector is very sensitive over the whole range of the optical spectrum; we still achieve a sensitivity of 60% at 300nm and of 40% at 950nm, see Fig. 2.2. The mirror and the window of the CCD are cleaned on a regular basis.

The camera is equipped with a double Apogee filter wheel, with 18 filters permanently mounted. We have a set of Johnson-Cousins broad band filters (B, V, Rc, and Ic - Bessel 1990), a Sloan $z'$ filter (Smith et al. 2002), a blue-blocking filter, and a special I+z filter for the observation of exoplanet transits, all from Astrodon. The broad band Johnson-Cousins filters

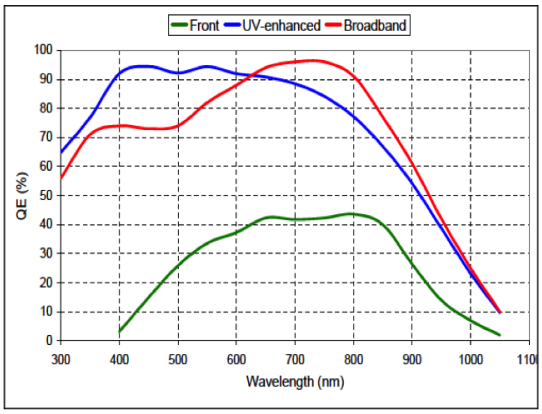


Figure 2.2: TRAPPIST detector quantum efficiency curve (broad band detector).

are mainly used for the observation of faint comets and their bandpasses are represented in Fig. 2.3.

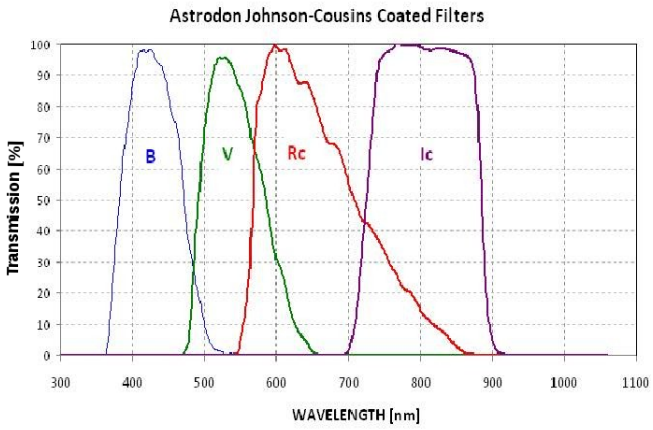


Figure 2.3: Transmission profiles of the Astrodon broad band B,V,Rc, and Ic filters.

The telescope is also equipped with a set of narrow band filters designed in 1997 for the observation of comet Hale-Bopp[3], see Figure 2.4 (Farnham et al. 2000). These filters isolate the emission of the main radicals visible in the optical spectrum of comets: OH (310nm), NH (336nm), CN (385nm), $C_3$ (405nm), and $C_2$ (515nm). The NH filter was only added to the filter wheel in 2012. Two filters isolate the ions $CO^+$ (427nm) and $H_2O^+$ (705nm), to study the ion tail of comets, and we also have a NaI filter. During the first two years of observations, the $H_2O^+$ (705nm) filter alone was mounted on the filter wheel. In 2012, we replaced the $H_2O^+$ filter with the $CO^+$ filter and added the sodium filter. The remaining narrow band filters isolate zones of the dust-reflected continuum free from gas emissions at four wavelengths: UC (345nm), BC (445nm), GC (525nm), and RC (712nm). Only BC and GC filters were used until

[3] We are grateful to David Schleicher and the Lowell Observatory for the loan of a set of NASA HB comet filters.

2012, at which time we added the UC and RC filters. Our narrow band filters are interference filters, whose design was carefully thought to maximize the fraction of the emission bands while minimizing the continuum contamination. The continuum filters are to be large enough to provide significant signal but avoid at the same time gas contamination. The final HB filter set was the result of these considerations. Detailed filter characteristics are presented in Table 2.1.

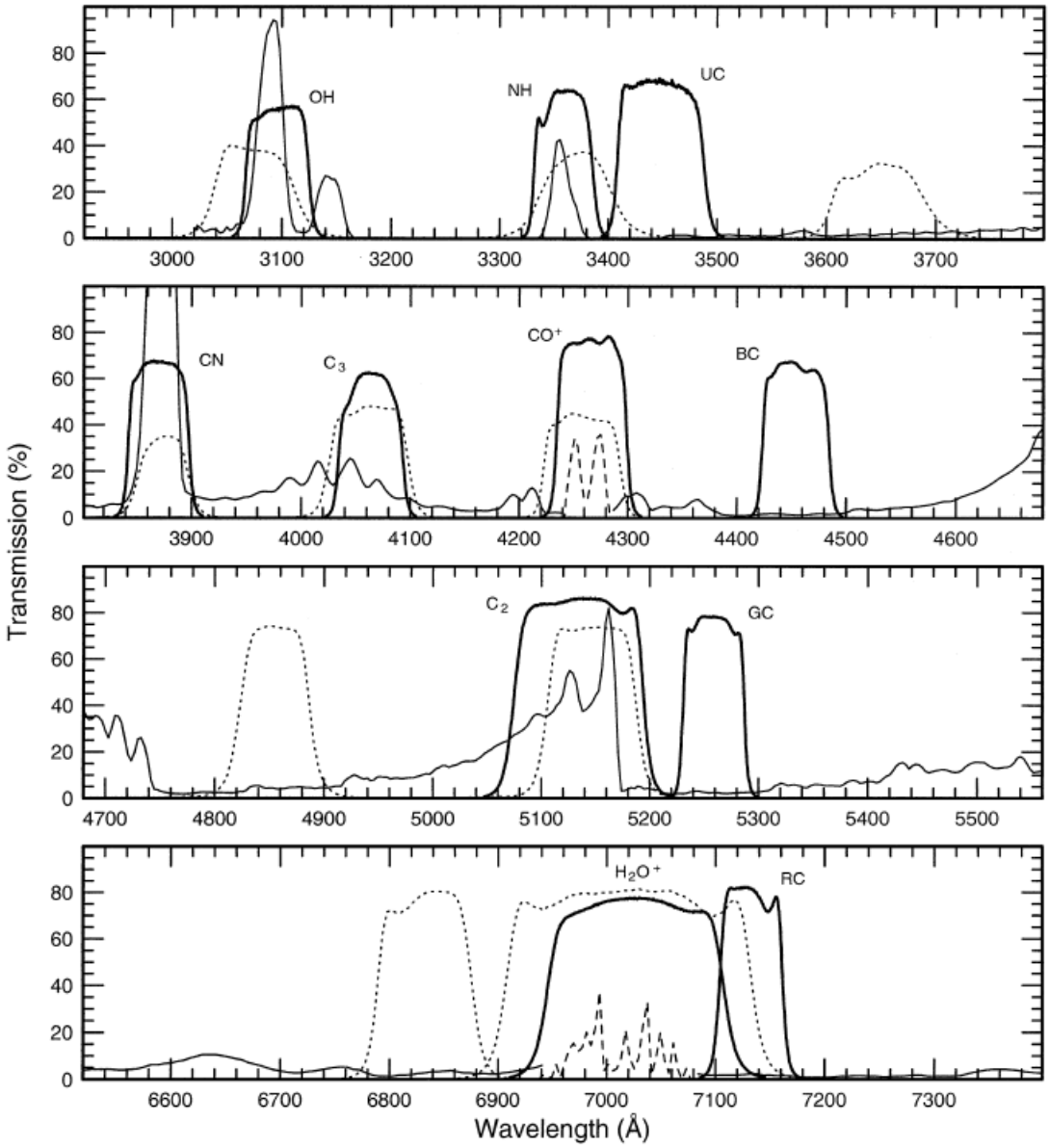


Figure 2.4: Transmission profiles of the narrow band comet filters, in bold, superimposed on a comet spectrum. The dashed line represents the bandpasses of the International Halley Watch filters that were previously used for comet narrow band imaging in the optical. This Figure is from Farnham et al. (2000).

Table 2.1: Narrow band HB filters characteristics.

| Species | ID | $\lambda_{central}(nm)$ | FWHM(nm) | Transmission(%) |
|---|---|---|---|---|
| OH(0-0) | OH | 309.5 | 5.65 | 58.4 |
| NH(0-0) | NH | 336.3 | 5.18 | 61.8 |
| Continuum UV | UC | 344.2 | 8.35 | 66.4 |
| CN($\Delta v = 0$) | CN | 387.1 | 5.84 | 66.3 |
| $C_3$ | C3 | 405.6 | 5.69 | 63.7 |
| $CO^+$(2-0) | CO | 426.2 | 5.70 | 73.6 |
| Blue Continuum | BC | 444.9 | 5.98 | 58.4 |
| $C_2(\Delta v = 0)$ | C2 | 513.5 | 11.7 | 85.0 |
| Green Continuum | GC | 525.7 | 5.65 | 78.7 |
| $H_2O^+$(0,6,0) | H2O | 701.6 | 15.7 | 75.0 |
| Red Continuum | RC | 713.0 | 6.30 | 80.5 |
| Sodium | NaI | 589.0 | 3.0 | 70.0 |

TRAPPIST is a robotic observatory. The observing plans are prepared during day time and a several softwares control all the steps of the observations: the dome opening, the cooling of the camera, the pointing of the targets, the focusing, and also the calibrations. We access to TRAPPIST main computer (Chimay) through a Virtual Private Network (VPN). A Boltwood II meteorological station installed on the roof of the control room stops the observations and closes the dome in case of bad weather (rain, high humidity, strong wind, clouds). An uninterruptable power supply (UPS) keeps the observatory running in case of power cuts and an IP power switch allows us to reboot almost all devices remotely. The telescope main computer can be accessed from any computer but also from tablets and smartphones through the VPN. The exoplanet observations are processed on site on two dedicated computers (Rochefort I and II) while the comet images are transferred to an archive computer in Liège (Orval) on a daily basis.

## 2.2 VLT/FORS 2

Three of the comets presented in this work have been observed with the Very Large Telescope (VLT) at the Paranal observatory. This observatory located in the Chilean desert is one of the best astronomical sites of the world, with very low humidity and 330 clear nights per year. The observatory is composed of four 8.2-m telescopes (UT) named Antu, Kueyen, Melipal, and Yepun and four movable 1.8-m auxiliary telescopes. The observations we used for this work were all made with the visual and near-UV FOcal Reducer and low dispersion Spectrograph (FORS 2, Fig. 2.5). This low resolution spectrograph is currently installed at the Cassegrain focus of the UT1 (Antu). In its default setting, FORS 2 is equipped with a detector optimised for the red part of the optical spectrum (mosaic of two 2kx4k MIT CCD, 15$\mu$m pixels) but a blue-optimised detector (mosaic of two 2kx4k E2V CCDs, 15$\mu$m pixels) can be requested. The instrument covers the wavelength range between 330 and 1100nm and provides images with

a plate scale of 0.25″/pix (or 0.125″/pix with the high resolution collimator) in the standard readout mode (2x2 binning). FORS 2 offers a large panel of observing modes for the imaging as well as for the spectroscopy (high time resolution, polarimetry, long slit spectroscopy, moveable slitlets, spectroscopic mask (MXU)).

Figure 2.5: FORS2 instrument at the Cassegrain focus of the VLT UT1 (Antu). Credit ESO.

Our observations were all made with the Long Slit Spectroscopy (LSS) mode and the red detector. The blue detector would have been more efficient to detect the CN emission at 385nm but this detector can only be used in visitor mode while our observations were mostly made in service mode. The FORS 2 slit is 6.8′ long. We used the 1.3″-wide slit for all our observations to maximise both the flux and the spectral resolution. We used the 150I Grism covering the wavelength range between 330 and 650nm with a dispersion of 3.45Å/pixel or the 300V Grism covering the same wavelength range with a dispersion of 1.68Å/pixel. The absorption in the blue part of the spectrum is less important for the 300V compared to the 150I Grism, which means they are more efficient to detect the CN emission. We did not use any sorting order filter.

## 2.3 Data Reduction

### 2.3.1 TRAPPIST

Calibration of the TRAPPIST data follows standard procedures that will be described in detail in this Section. TRAPPIST comet observations are usually made using a 2 by 2 binning providing a 1.3″/ pixel resolution and increasing the sensitivity. We use custom-made routines based on the IRAF (Image Reduction and Analysis Facility) software. Bias, dark, and sky flatfield frames are taken every day. We combine these calibration frames over 10 to 15 days (by taking the

median) to create master bias, flat, and dark frames. We combine calibration frames over a limited period of time to reduce the noise introduced by the data reduction, while avoiding changes in the flatfield frames aspect due to the apparition of new specks of dust.

After correcting the image from the master bias, dark, and flatfield, we subtract the sky contribution. The removal of the sky contribution may be problematic for extended objects. Indeed, in some cases comets extend over the whole field of view and it is then extremely difficult to determine the value of the sky background in the image. In theory, the best way to accurately determine the sky background in comet observations would be to take images with small offsets (but still large enough to avoid any comet contribution) in different directions around the comet and then interpolate the sky background under the comet from these images. However, this technique is very time-consuming and is then difficult to implement. Fortunately, the field of view of TRAPPIST is large ($22' \times 22'$) and, for the comets presented in this work, it was always possible to determine the sky contribution from parts of the image that did not contain any cometary contribution. We first determine the coma optocenter, using the IRAF task *imcntr* and then determine the closest distance from the coma optocenter where each image is free of cometary emission. We measure the median sky level at this nucleocentric distance and subtract it from the image. The standard deviation of the measured sky values is used to estimate the error on sky subtraction.

In a second time, we extract the radial brightness profile of the comet. We compute a median profile to eliminate the contribution of background stars. Even though narrow band filters have been carefully designed to isolate specific molecular emissions, images in these filters are contaminated by the underlying sunlight reflected by the dust. The dust subtraction is thus a very important step in the data reduction. We use images of the comet in the BC filter (or in the GC filter when we do not have BC images) to obtain the dust radial profile, we scale it depending on the contamination in the gas filter, and subtract it from the gas profile. The scaling factor of the dust continuum is different for each gas filter. The $C_3$ and $C_2$ filters are the most contaminated, while the dust contaminations in the OH, NH, and CN filters is much lower. The scaling factor also varies from comet to comet, depending on the colour of the dust. Continuum frames used for the dust subtraction are usually taken during the same hour as the associated frame to avoid changes in the observing conditions or in the rotational state of the comet.

Frequent observations of the narrow band photometric standard stars listed by Farnham et al. (2000) give the extinction coefficients and the zero points of the system. We usually use median values of these coefficients over a month, since we have noticed that zero points values were not changing over these timescales. Values of the zero points and extinction coefficients measured on the night of July 1, 2015 are given in Table 2.2, as an example. The long-term evolution of the zero points measured between November 2012 and April 2015 is also illustrated in Fig. 2.6. This shows that the zero points do not vary strongly on large time-scales. Farnham et al. (2000) provide the coefficients necessary to transform the count rates into spectral radiance and molecular band radiance (such as the solar spectrum colour

or the fraction of the emission band encompassed by the filter). These coefficients are given in Table 2.3. They are proper to the standard system, but the characteristics of our filters are sufficiently close to those used by Farnham et al. (2000) to allow their use without correction. In order to flux calibrate the radial profiles, we apply the following formula:

$$F_c = F_0 \times F \times 10^{(0.4(K \times am - 25 + ZP))}$$

in which $F$ is the flux of the comet in ADU/s, $F_0$ is the flux of a zero magnitude star in $erg\ cm^{-2}\ s^{-1}$ Å$^{-1}$ corresponding to $F_{x0}\ ADU/s$. $K$ is the extinction coefficient, $am$ the airmass of the comet, and $ZP$ the zero point of the filter. In order to obtain the total flux in the emission band, we still have to account for the fraction of the emission band encompassed in the filter, and its width and transmission characteristics, using the $\gamma$ coefficient from Table 2.3. The final result is then expressed in $erg\ cm^{-2}\ s^{-1}\ arcsec^{-1}$.

Table 2.2: Zero points and extinction coefficients measured on the night of July 1, 2015 for broad band and narrow band filters.

| Filter | K | ZP |
|---|---|---|
| OH | 1.616 | 6.467 |
| NH | 0.669 | 6.136 |
| UC | 0.623 | 5.516 |
| CN | 0.382 | 5.663 |
| $C_3$ | 0.309 | 5.612 |
| $CO^+$ | 0.253 | 5.573 |
| BC | 0.231 | 5.901 |
| $C_2$ | 0.142 | 4.970 |
| GC | 0.130 | 5.965 |
| RC | 0.057 | 6.400 |
| B | 0.228 | 2.399 |
| V | 0.118 | 2.513 |
| Rc | 0.093 | 2.299 |
| Ic | 0.045 | 2.960 |
| NaI | 0.136 | 6.556 |

The main uncertainties in the gas production rates and their dust equivalent (the so-called $Af\rho$) computed from TRAPPIST observations come from the absolute flux calibration and the sky background subtraction. A long-term analysis of our standard star observations showed that the scatter in extinction coefficients determined from different nights is around 5 %. This is almost negligible compared to the sky level uncertainty when the target is observed at low airmass, even though the effect of extinction coefficients uncertainty becomes significant at high airmasses. We estimate the 3-sigma level uncertainty on the sky background value and use it to compute the error on production rates due to the sky subtraction. As a result, errors given in the following sections are a quadratic combination of sky background and extinction coefficient uncertainties.

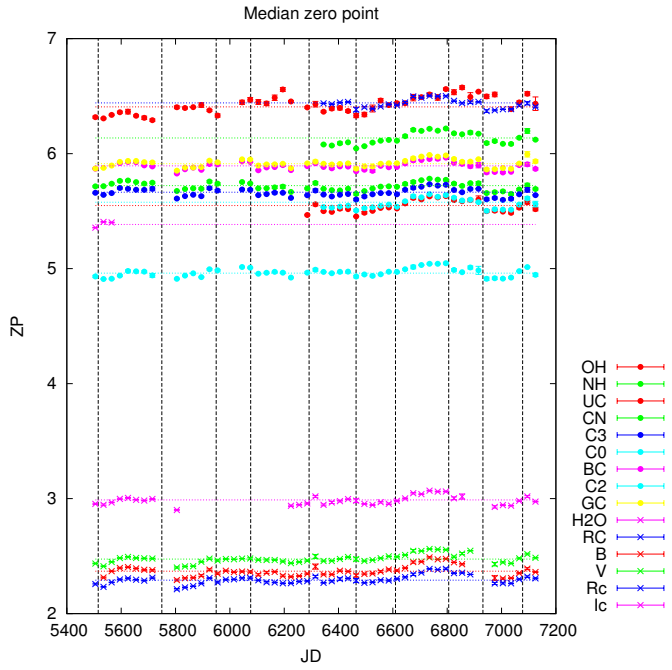


Figure 2.6: Evolution of the broad band and narrow band filters zero points between November 2010 and April 2015.

Table 2.3: Narrow band filters calibration coefficients from Farnham et al. (2000). Filter specifications are represented by the XX subscript. $F_{0XX}$ is the flux of a 0 magnitude star in $10^{-9}\ erg\ cm^{-2}\ s^{-1}$ Å$^{-1}$. $\gamma$' is the fraction of the emission band encompassed in the filter and $\gamma$ its normalisation by the filter width and transmission characteristics. $m_{\odot XX}$ is the colour of the solar spectrum.

| Species | $F_{0XX}$ | $m_{\odot XX}$ | $\gamma_{XX/XX}$ | $\gamma_{XX/XX}$' |
|---|---|---|---|---|
| OH | 10.560 | +1.791 | $1.698^{-2}$ | 0.98 |
| NH | 8.420 | +1.188 | $1.907^{-2}$ | 0.99 |
| CN | 8.6 | +1.031 | $1.812^{-2}$ | 0.99 |
| $C_3$ | 8.160 | +0.497 | $3.352^{-3}$ | 0.19 |
| $CO^+$ | 7.323 | +0.338 | $1.549^{-2}$ | 0.99 |
| $C_2$ | 3.887 | -0.423 | $5.433^{-3}$ | 0.66 |
| $H_2O^+$ | 1.380 | -1.249 | $5.424^{-3}$ | 1.00 |
| UC | 7.802 | +1.101 | - | - |
| BC | 6.210 | 0.000 | - | - |
| GC | 3.616 | -0.507 | - | - |
| RC | 1.316 | -1.276 | - | - |

All TRAPPIST images are reduced following the same procedure, providing highly homogeneous data sets for the study of the evolution of comet activity along their orbits as well as for the comparison of the coma composition among comets. Tests on the reproducibility of our

measurements in the case of comet C/2012 F6 (Lemmon) showed that the agreement between identical consecutive measurements is within a few percents.

### 2.3.2 FORS 2

The low resolution spectroscopic observations have been reduced using the ESO *Reflex* software and IRAF routines. Bias and flatfield frames are obtained the same night as the comet, as well as arc lamps and spectroscopic standard stars for the wavelength and flux calibration. We use the Reflex software to perform the spectrum calibration. Bias and flatfield frames are combined, the spectrum is wavelength calibrated, and then flux calibrated. For the first spectra we performed a parallel reduction using the IRAF software and obtained consistent results.

After obtaining two dimensional fully calibrated spectra, we subtract the background. Since the FORS 2 slit is only 6.8′ long, we are usually not able to use part of the spectrum free from comet emission to determine the sky background level. We then take observations with an offset to characterise the sky background. We measure the emission in the strongest sky lines from the background and comet images in order to properly scale the background and subtract it from the scientific images. This is done separately for each image and for each chip. The best way to account for the sky background would be to alternate comet and background expositions, but there is usually not enough observing time available to apply this strategy. After the background subtraction, we bin over 10 pixels in the spatial direction to increase the signal-to-noise ratio (S/N). Each bin is then extracted separately. Observations of solar analogues (made with the same grism and slit width as the comet observations) corrected from colour effects are used to subtract the continuum from each 1D spectrum across the spatial direction. In some cases we also use observations of Ceres to subtract the dust continuum. Spatial profiles of CN and $C_2$ are obtained by summing every 1D spectra over the 383-390.5 nm and 486-521 nm wavelength ranges. We discard the first point of each profile, containing the nucleus, to avoid PSF and seeing effects and also strong dust contamination difficult to remove close to the nucleus.

Simultaneous observations of a comet with TRAPPIST and VLT/FORS 2 proved to be very consistent. Examples of observed radial profiles will be shown later in this work. The consistency between TRAPPIST and VLT/FORS 2 observations means that these data can be combined and analysed together. This could allow us to observe comets over a wider range of heliocentric distances. Far away from the Sun, comets are usually fainter and larger telescopes are needed to detect the gas emission bands. Combining observations with large telescopes when comets are far away from the Sun and observations with smaller telescopes when they come closer would provide a way to study the composition of the coma and the behaviour of the outgassing over wide ranges of heliocentric distances.

### 2.3.3 Haser Model

A coma model is needed to convert radial profiles of brightness into gas production rates. Over the years, several models have been proposed to represent the coma of a comet, from the most simple models to more complicated physically realistic models. The first attempt to describe the distribution of molecules in the coma was the fountain model (Eddington, 1910). In this model, the comet was considered as a point source emitter of molecules in expansion, such as their density will fall off as the squared of the nucleocentric distance. However, it was soon realised that most species observed in the optical spectrum of comets (NH, CN, $C_2$, ...) were unstable and were then probably the product of the photodissociation of more complex molecules. Following this observation, Haser considered in 1957 the direct photodissociation of parent molecules into daughter molecules in a spherically symmetric coma (Haser, 1957). I this model, both parent and daughter species were assumed to flow radially. Even though not physically realistic, this model has been widely used by comet observers since 1957. In 1981, Festou introduced the so-called vectorial model, a more realistic model in which the excess velocity communicated to the daughter molecules after photodissociation was allowed to be in any direction. None of the previously mentioned models was able to reproduce some peculiarities of the observed radial profiles, among which the flattening of the $C_2$ radial profiles in the inner coma observed for comet Halley (O'dell et al. (1988), Fink et al. (1991)) and other comets. Three-generation Haser-like models (see O'dell et al. (1988)) were then proposed and these models were able to better reproduce the flat radial profiles observed in the case of comet Halley, for instance. However, the more complex the model used to derive production rates, the more free parameters. These free parameters are usually poorly determined and may be a major source of uncertainty in the determination of gas production rates.

We decided to use the Haser model (Haser, 1957) to compute gas production rates. Even though this model is not physically realistic, it has been used by many observers for the past 50 years and allows an easier comparison of data from different sources. Furthermore, this model has only three free parameters. The main hypotheses of the Haser model are the following:

- The nucleus is spherical and has a radius $r_0$.
- The molecules are ejected from the nucleus by the solar radiation with a constant radial velocity $v_0$. Daughter molecules flow in the radial direction with the same velocity after photodissociation.
- There is only one possible parent for each daughter species.
- Parent molecules are photodissociated in a one-step process to form daughter molecules.
- Daughter molecules are themselves dissociated into grand-daughter molecules.
- The molecules are photodissociated following the law:

$$n = n_0 e^{-t/\tau_0} \tag{2.1}$$

where $n_0$ is the number of molecules at a time zero and $\tau_0$ is the molecule lifetime (after a time $\tau_0$, the number of molecules decreased by a factor $1/e$).

Using these hypotheses, we can compute the distribution of the dissociation products in the coma. This development is from Haser (1957). $N(r_0)$ is the number of molecules ejected from the nucleus per second and per cm$^2$ and $N(X)$ is the number of molecules per second and per cm$^2$ at a distance $X$ from the nucleus. Taking into account the photodissociation of parent species into daughter species, the number of molecules crossing a sphere of radius $X$ is then:

$$4\pi X^2 N(X) = 4\pi r_0^2 N(r_0) exp\left[-\frac{1}{v_0\tau_0}(X - r_0)\right] \tag{2.2}$$

and the formation rate of daughter molecules (per second and cm$^2$) in a shell $dX$ at a distance $X$ from the nucleus is given by

$$-\frac{d}{dX}\left[4\pi X^2 N(X)\right] = 4\pi r_0^2 N(r_0)\frac{1}{v_0\tau_0} exp\left[-\frac{1}{v_0\tau_0}(X - r_0)\right] \tag{2.3}$$

The daughter molecules are then photodissociated by the UV solar radiation. The number of daughter molecules produced at a distance X from the nucleus has decreased by a factor $exp\left[-\frac{r-X}{v_1\tau_1}\right]$ when they reach the distance $r$. $v_1$ and $\tau_1$ are respectively the speed and the lifetime of daughter species. The number of daughter molecules (per second and cm$^2$) reaching a distance $r$ from the nucleus and originating from a layer $dX$ at a distance $X$ from the nucleus is:

$$4\pi r_0^2 N(r_0)\frac{1}{v_0\tau_0} exp\left[-\frac{1}{v_0\tau_0}(X - r_0)\right] exp\left[-\frac{r-X}{v_1\tau 1}\right] dX \tag{2.4}$$

The total number of daughter molecules (per second and cm$^2$) reaching a nucleocentric distance $r$ is then

$$N_1(r) = N(r_0)\left[\frac{r_0}{r}\right]^2 \frac{1}{v_0\tau_0} exp\left[\frac{r_0}{v_0\tau_0}\right]\int_{r_0}^{r} exp\left[-\frac{X}{v_0\tau 0} - \frac{r-X}{v_1\tau 1}\right] dX \tag{2.5}$$

$D(r)$ is the molecular density (number of molecules per $cm^3$). The molecular density is linked to the number of molecules per second and $cm^2$ by the relation $N(r_0) = v_0 D(r_0)$ (or $N_1(r) = v_1 D_1(r)$) for the daughter molecules. We also introduce the quantities $\beta_0$ and $\beta_1$ which are respectively the parent and daughter species scalelengths.

$$\beta_0 = \frac{1}{v_0 \tau 0} \qquad\qquad \beta_1 = \frac{1}{v_1 \tau 1}$$

The gas production rate Q can be expressed as:

$$Q = 4\pi v_0 r_0^2 D(r_0)$$

We finally obtain the expression for the density distribution of dissociation products in the coma of a comet:

$$D_1(r) = \frac{Q}{4\pi r^2 v_1} \frac{\beta_0}{\beta_1 - \beta 0} \left[ exp\left[-\beta_0 (r - r_0)\right] - exp\left[-\beta_1 (r - r_0)\right]\right] \tag{2.6}$$

The Haser model provides a rather simple mathematical expression to describe the density distribution of radicals in the coma. A significant advantage of this model is that it has only three free parameters: the parent and daughter scalelengths (their lifetime) and the outflow velocity of the gas. Nonetheless, as already stated earlier, this model is not physically realistic for several reasons. First, as shown in Section 1.2, the shape of a comet nucleus is usually far from spherical. Moreover, the nucleus is probably not uniformly active on its entire surface, some regions are more active than others. This produces large scale structures, such as fans, jets, or even spirals observed in the coma of a large number of comets (see for instance Schleicher and Farnham 2004). In most comets, the real morphology of both the nucleus and the coma is far from the spherical symmetry assumed in the Haser model. In addition, the reaction leading to the production of daughter species is probably more complex than the single-step photodissociation of parent molecules into daughter molecules. Three-step processes have for example been suggested to account for the shape of $C_2$ radial profiles (Feldman et al., 2004). The idea of gas released by dust grains was also raised to explain gas jets in the coma of some comets (A'Hearn et al., 1986). None of these complex processes are accounted for by the Haser model. Finally, as already discussed earlier, the excess energy released by the photodissociation of parents molecules provides an additional velocity component to the daughter species oriented randomly, which is not accounted for by the Haser model.

Despite these approximations, the Haser model is widely used among comet observers. However, in order for the model to be consistent with the data, we must replace the lifetime of parent and daughter species by effective scalelengths. These effective scalelengths have been adjusted on observed radial profiles in order to match the data as much as possible. Ideally,

Table 2.4: Haser model parent ($L_P$) and daughter ($L_D$) scalelengths at 1 au and their scaling with the heliocentric distance ($r$). The scalelengths used for computation of OH, NH, CN, $C_3$, and $C_2$ production rates in this work are marked in bold.

| Species | $L_P$ (km) | $L_D$ (km) | Reference |
|---|---|---|---|
| OH | $\mathbf{2.40 \times 10^4 r^2}$ | $\mathbf{1.60 \times 10^5 r^2}$ | **Cochran and Schleicher (1993)** |
| NH | $\mathbf{5.00 \times 10^4 r^2}$ | $\mathbf{1.50 \times 10^5 r^2}$ | **Randall et al. (1992)** |
| CN | $\mathbf{1.30 \times 10^4 r^2}$ | $\mathbf{2.10 \times 10^5 r^2}$ | **Randall et al. (1992)** |
| | $1.70 \times 10^4\ r^2$ | $3.0 \times 10^5\ r^2$ | Cochran (1985) |
| | $2.80 \times 10^4\ r^2$ | $3.2 \times 10^5\ r^2$ | Fink et al. (1991) |
| | $1.80 \times 10^4\ r^2$ | $4.2 \times 10^5\ r^2$ | Newburn and Spinrad (1989) |
| | $3.0 \times 10^4\ r^{1.3}$ | $1.99 \times 10^5\ r^{0.6}$ | Langland-Shula and Smith (2011) |
| | $5.4 \times 10^4\ r^{1.3}$ | - | Rauer et al. (2003) |
| $C_3$ | $\mathbf{2.80 \times 10^3 r^2}$ | $\mathbf{2.70 \times 10^4 r^2}$ | **Randall et al. (1992)** |
| | $3.10 \times 10^3\ r^2$ | $1.50 \times 10^5\ r^2$ | Cochran (1985) |
| | $3.00 \times 10^3\ r^2$ | $1.00 \times 10^5\ r^2$ | Newburn and Spinrad (1989) |
| | $6.0 \times 10^3\ r^{0.8}$ | $8.9 \times 10^4\ r^{2.8}$ | Langland-Shula and Smith (2011) |
| | $1.3 \times 10^3\ r^{2.6}$ | - | Rauer et al. (2003) |
| $C_2$ | $\mathbf{2.20 \times 10^4 r^2}$ | $\mathbf{6.60 \times 10^4 r^2}$ | **Randall et al. (1992)** |
| | $2.50 \times 10^4\ r^{2.5}$ | $1.20 \times 10^5\ r^2$ | Cochran (1985) |
| | $5.80 \times 10^4\ r^2$ | $5.8 \times 10^4\ r^2$ | Fink et al. (1991) |
| | $3.1 \times 10^4\ r^2$ | $1.3 \times 10^5\ r^2$ | Newburn and Spinrad (1989) |
| | $3.5 \times 10^4\ r^{1.4}$ | $4.2 \times 10^4\ r^{2.}$ | Langland-Shula and Smith (2011) |
| | $1.6 \times 10^4\ r^{2.8}$ | - | Rauer et al. (2003) |

effective scalelengths should be derived for each observation and then used to compute the production rates. This has been done for example by Rauer et al. (2003) in the case of comet Hale-Bopp. In practice, deriving effective scalelengths for each observation of each comet is impossible. In order to derive reliable effective scalelengths, a good sampling of the whole coma and a good signal-to-noise ratio are needed. An instrument with sufficient spatial resolution and field of view is absolutely necessary. For weak comets especially, it is challenging to get the edges of the radial profiles and then to derive daughter scalelengths. The variation of the scalelengths with the heliocentric distance is also difficult to determine. Since it is not feasible to derive scalelengths for every individual observation, several authors attempted to determine general Haser scalelengths and their evolution with the heliocentric distance. Successive studies have been made, whose results are presented in Table 2.4. Among these scalelengths, the most widely used are those summarised in A'Hearn et al. (1995). We thus chose to use these Haser scalelengths in our work to facilitate the comparison with the data presented in A'Hearn et al. (1995) and others works. The values of the scalelengths we used are given in bold in Table 2.4. The scalelengths are scaled as $r^2$, $r$ being the heliocentric distance. The heliocentric dependence has been determined from observations spanning a short range of heliocentric distances, which may induce larger uncertainties for comets

observed at large heliocentric distances. The scalelengths and their variations with the comet heliocentric distance remain the main source of uncertainty in the computation of production rates, especially for the NH. A re-determination of Haser scalelengths from a large sample of comets observed over a wide range of heliocentric distances would significantly improve the computation of gas production rates from optical observations but this represents a considerable amount of work. We use a constant outflow velocity of 1 km/s for both parent and daughter species. This velocity is different from the outflow velocity used to compute parent species production rates from infrared observations v = $0.8r^{-0.5}$ km/s (Mumma et al., 2001; Dello Russo et al., 2009; Paganini et al., 2014a). However, the scalelengths we use have been adjusted on observed profiles using a 1 km/s velocity. It is thus more consistent to use this velocity in our work.

Equation 2.6 gives the density profile of dissociation products in the coma $D_1(r)$. This quantity cannot be directly linked to the brightness profile we derive from our images. Indeed, from the ground , we can only derive radial profiles integrated along the line of sight. The integration along the line of sight is schematically represented on Fig. 2.7. Equation 2.6 must then be integrated along the line of sight to obtain the column density ($N(r)$) that can in turn be linked to the brightness profile. The integration of the density profile along the line of sight can be done in two different ways. The first one is by simply analytically integrating equation 2.6. This gives:

$$N(\rho) = \frac{Q}{4\pi \upsilon_1} \frac{\beta_0}{\beta_1 - \beta 0} [B_0 - B_1] \tag{2.7}$$

$$B_0 = \left[\frac{\pi}{2} - \int_0^{\rho\beta_0} K_0(y)\right] exp(r_0\beta 0) \qquad B_1 = \left[\frac{\pi}{2} - \int_0^{\rho\beta_1} K_0(y)\right] exp(r_0\beta 1)$$

$\rho$ is the projected nucleocentric distance and $K_0$ is the modified Bessel function of the second kind, which has to be computed numerically. A fully analytical solution is presented in Hubert et al. (2016) but since it was not available at the time we developed our pipeline, we chose to do a numerical integration along the line of sight. Since the number of images for which we have to compute production rates is significant, the amount of computational time may quickly become extremely important. For this reason, we use variable steps for the numerical integration.

The fluorescence efficiency of each molecule (also called g-factor) is used to convert between the flux and the column density. Fluorescence efficiencies are expressed as:

$$g_\lambda = (\frac{\pi e^2}{m_e c^2}) \lambda^2 f F_\lambda \frac{A_{ik}}{\sum_k A_{ik}} \tag{2.8}$$

$F_\lambda$ is the solar flux per unit of wavelength and $f$ is the oscillator strength. $A_{ik}$ are the Einstein

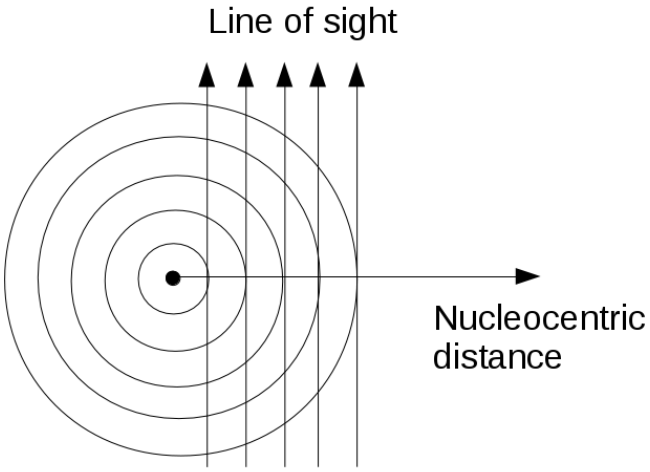


Figure 2.7: Illustration of the integration of the Haser model along the line of sight.

coefficients. Fluorescence efficiencies (also called g-factors) from David Schleicher's website[4] are used to convert fluxes into column densities. Since the ratio between $C_2$ in triplet and singlet state and its evolution with the heliocentric distance are not well understood, $C_2$ g-factors only consider the $C_2$ in triplet state (A'Hearn et al., 1985). $C_3$ g-factors are from A'Hearn (1982). CN and NH fluorescence efficiencies vary with both the heliocentric distance and velocity and are respectively taken from Schleicher (2010) and from Meier et al. (1998). For OH g-factors, which also vary with the heliocentric velocity, we consider unquenched values of the ground state (Schleicher and A'Hearn, 1988). All fluorescence efficiencies are scaled as $r^2$. These values account for the Swings effect (Swings, 1941). This effect was first discovered by Polydore Swings in 1941 and is caused by the Doppler shift of the solar spectrum because of the speed of the comet relatively to the Sun. For some values of the relative velocity, a cometary emission band can coincide with a solar absorption. Less photons are then available for the resonance-fluorescence mechanism. This effect has to be taken into account while computing the values of the fluorescence efficiencies.

We finally adjust the Haser model on the observations. Since the comets presented in this work have been observed over a wide range of heliocentric and geocentric distances, we decided to make the adjustment at a physical distance around 10,000km in the coma. In most cases, the signal-to-noise ratio is still high at this nucleocentric distance but the influence of the seeing effects (limited to first few pixels) and the dust contamination are lower. By adjusting directly the model on the radial profile instead of measuring the flux in a single aperture, we reduce aperture trends (variation of the production rates with the size of the aperture) often observed while computing production rates with the Haser model. In practice, we generate a brightness profile with the Haser model using a rough estimate of the real production rate. On this profile, we measure the mean of the flux between 4,000km and 12,500km from the nucleus.

[4] Link: http://asteroid.lowell.edu/comet/gfactor.html

We then measure the mean of the flux over the same nucleocentric distance on the observed profiles. The comparison of these two values allows us to determine the actual production rate. An illustration of the model adjustment in the case of comet C/2012 F6 (Lemmon) is given in Fig. 2.8. Except for NH, the agreement between the radial profiles and the Haser model is satisfactory. However, this is not always the case, depending on the comet or the heliocentric distance. This emphasises the need to re-determine more realistic effective Haser scalelengths.

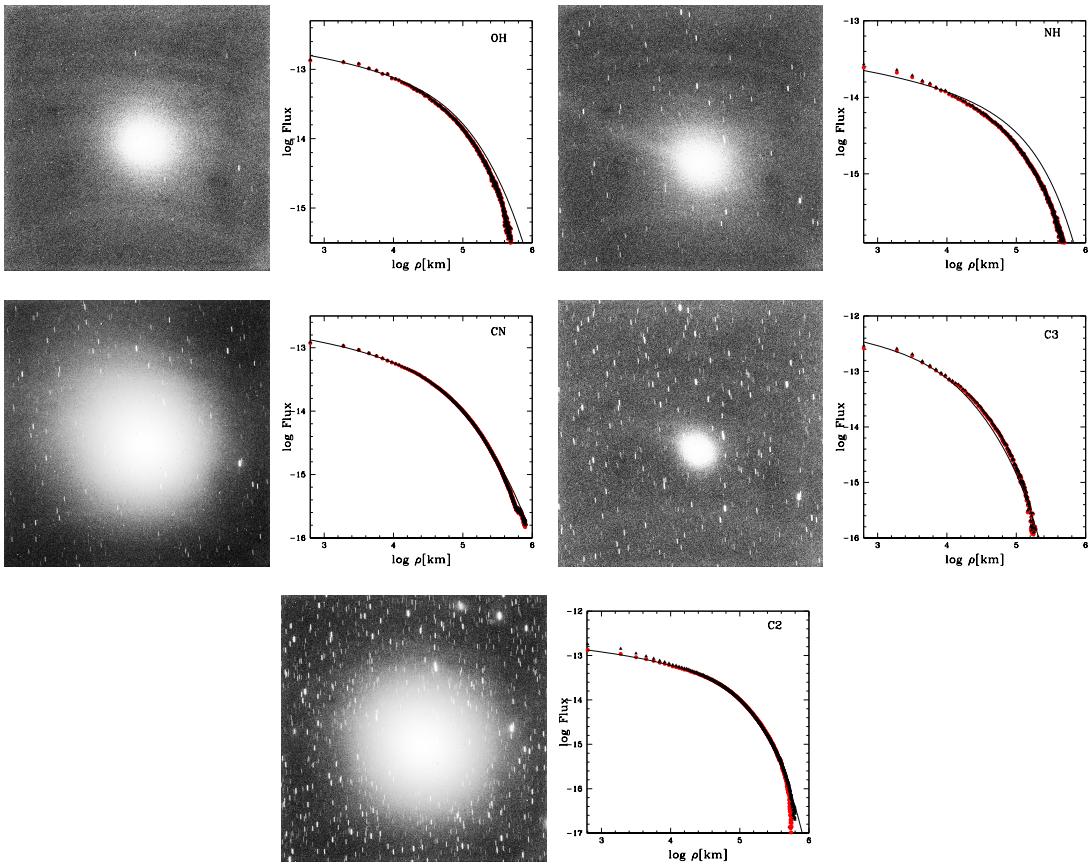


Figure 2.8: Original images of comet C/2012 F6 (Lemmon) and the corresponding radial profiles for OH, NH, CN, $C_3$, and $C_2$. These images have been taken on January 7, 2013 while the comet was 1.57 au from the Sun. We plotted the original radial profile (dark triangles), the radial profile obtained after dust subtraction (red circles) and the fitted Haser model (black line). As comet Lemmon is a relatively gaseous comet, the original radial profile and the dust-subtracted profile are mostly overlapping. The comet images are oriented north up and east left.

### 2.3.4 The $Af\rho$ parameter

In order to quantify the dust activity, we use the parameter $A(\theta)f\rho$. This parameter has first been introduced by A'Hearn et al. in 1984. This quantity is widely used to compare the dust

activity between comets observed with different instruments and techniques. The $A(\theta)f\rho$ is in theory independent of the field of view for simple radial outflow models (isotropic coma, grains with constant expansions speed, no grain fading). In this case, the radial brightness of the dust follows a $1/\rho$ decrease. As indicated by its name, the $A(\theta)f\rho$ is the product of three quantities. $A(\theta)$ is the Bond albedo at the phase angle of the observation ($\theta$). The Bond albedo of a body is a value between 0 (blackbody) and 1 (perfect reflector) that gives the ratio between the reflected flux in a direction and the incident solar flux. $f$ is the filling factor of the grains in the field of view (number of grains per unit of surface multiplied by their cross section and divided by the surface of the field of view, illustrated in Fig. 2.9). $\rho$ is the radius of the circular field of view. The $A(\theta)f\rho$ can also be expressed as :

$$A(\theta)f\rho = \frac{(2\Delta r)^2}{\rho}(\frac{F_{com}}{F_{\odot}}) \tag{2.9}$$

$r$ and $\Delta$ are respectively the heliocentric and geocentric distances (expressed respectively in au and cm). $F_{\odot}$ is the solar flux at 1 au in the bandpass of the filter used for the observation (expressed in $erg\ cm^{-2}\ s^{-1}\ \text{Å}^{-1}$). $F_{com}$ is the dust reflected flux in the bandpass of the filter inside an aperture $\rho$ (expressed in $erg\ cm^{-2}\ s^{-1}\ \text{Å}^{-1}$). The $A(\theta)f\rho$ is then expressed in cm. As for the gas production rates, we computed the $A(\theta)f\rho$ at approximately 10,000km from the nucleus. Since the $A(\theta)f\rho$ is independent from the nucleocentric distance (in ideal cases at least), the distance at which it is computed should not influence the results. However, our observations showed that for most comets, the dust brightness profile differs from the expected $1/\rho$ decrease.

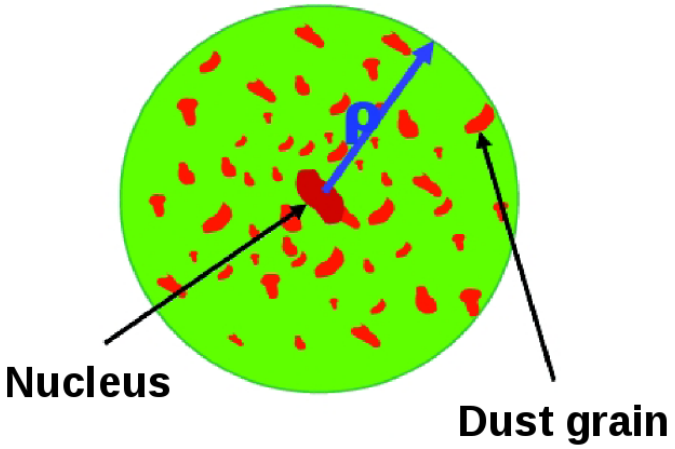


Figure 2.9: Illustration of the dust filling factor in the coma. This image has been modified from a presentation by Laurent Jorda (personnal communication).

We observed some comets in our data set during several months. For such extended data sets, the phase angle of the observations can change significantly over the orbit of the comet. As illustrated in Fig. 2.10, the effect of the phase angle can become important at low and high phase angles. In order to compare observations of a single comet made at different phase

angles, and observations of different comets, we thus need to correct the $A(\theta)f\rho$ values from the phase angle effect. Several phase functions have been successively proposed to correct the $A(\theta)f\rho$ for the phase angle effect (Divine 1981, Hanner and Newburn 1989, Schleicher et al. 1998 or Marcus 2007). We use the phase function described by David Schleicher[5], which is represented in Fig. 2.10. It is a composite of two different phase functions from Schleicher et al. (1998) and Marcus (2007). We normalize the $A(\theta)f\rho$ values at a 0° angle.

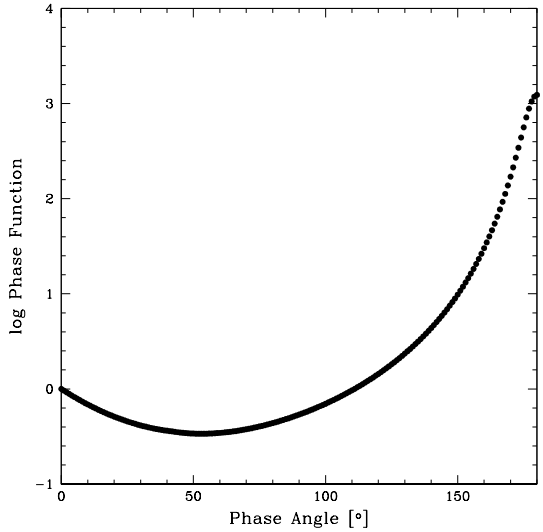


Figure 2.10: Phase function used to correct the $A(\theta)f\rho$ from the phase angle effect.

The measurement of the $A(\theta)f\rho$ at different wavelengths can be used to derive the dust normalized reflectivity gradient, also called dust colour (Jewitt and Meech, 1987). We should keep in mind that we do not actually measure the colour of the dust grains in the coma, but the colour of the light reflected by the dust. However, in the following discussion we will use the simpler term dust colour. The normalized gradient of $A(\theta)f\rho$ computed from two continuum filters is given by:

$$\text{colour}[\lambda_1,\lambda_2] = \frac{A(\theta)f\rho_1 - A(\theta)f\rho_2}{\lambda_1 - \lambda_2}\,\frac{2000}{A(\theta)f\rho_1 + A(\theta)f\rho_2}. \tag{2.10}$$

The normalized reflectivity gradient is expressed as the percentage of reddening per 1000 Å. We usually compute the dust colour using RC and BC filters. These two filters are the less contaminated by gas emissions (Farnham et al., 2000) and should therefore provide a good estimation of the dust colour. For very gaseous comets, the UC filter is strongly contaminated by gas emissions. Emission lines from OH (0-1), and from $CO_2^+$ to a lesser extent, are detected within the bandpass of the UC filter (Leach et al. 1978, Schleicher and A'Hearn 1988 and Valk et al. 1992). The main contamination in the UC filter is usually considered to be $C_3$ (Farnham et al. 2000). However, we examined VLT-UVES spectra of more than ten comets gathered by

[5] Link: http://asteroid.lowell.edu/comet/dustphase.html

our team and OH (0-1) is clearly the brightest emission in that wavelength range, while $C_3$ and $CO_2^+$ are very weak (Opitom et al., 2015a).

### 2.3.5 Image enhancement techniques

Morphological features are observed in the coma of a large number of comets. These features are caused by a non-uniformly active nucleus, with active areas. The study of coma morphology can bring clues about the size, number, and position of active areas, about the nucleus homogeneity, or about the nucleus rotation period. Among the features most commonly observed, there are jets, fans, arcs, spirals, or simple spatial asymmetries. However, morphological features are difficult to observe due to the brightness of the ambient coma and a number of techniques have been developed to increase the contrast between the features and the coma. Image enhancement techniques can introduce artefacts, and must then be used with caution. The comparison between the results from various techniques allows us to insure that the features observed are real and not artefacts.

Different kinds of techniques exist and usually reveal different kinds of features. Most techniques are very sensitive to the centring of the nucleus. Our centring method provides a centring accuracy better than 1 pixel, so that this should not be an issue for this work. Comprehensive reviews of image enhancement techniques are presented in Schleicher and Farnham (2004) and Samarasinha and Larson (2014), so we will only briefly present some of the main techniques in this Section. One of the most basic techniques is the removal of (or division by) a simple profile. For dust images, a $1/\rho$ profile is often considered as the best choice, as it represents the shape of a dust coma produced by steady state isotropic emission of dust. For gas images, azimuthally averaged or median profiles constructed from the original image are used. The removal of a simple profile is both very simple to implement and does not introduce strong artefacts, making the resulting images easy to interpret. Furthermore, it does not require manual optimization, making it very fast and easy to apply on large number of images. This technique reveals either deviations from the expected shape of the coma or deviations from the bulk brightness distribution. Edge Detection Techniques (EDT) cover a large family of techniques widely used. Among these, rotational shift differencing (rotational filter and Larson-Sekanina filter, Larson and Sekanina (1984)) subtracts a rotated version of the image. This technique reveals small features near the nucleus and larger features at greater distances. It only reveals azimuthal features (not radial features), and their size and position depend on the shift used, so one must be cautious when using these techniques. Spatial filters, such as Laplace filter or unsharp masking, are powerful tools but can introduce artefacts in the resulting images. More complex techniques like azimuthal re-normalisation or techniques specifically enhancing time changes also exist but are more complicated to implement and more time-consuming.

We tested several techniques to find the most appropriate ones for our data: subtraction and division of an azimuthal median profile, rotational filter, and Larson-Sekanina filter (Schleicher

and Farnham, 2004; Larson and Sekanina, 1984). We show here an example of these techniques applied on a CN image of comet C/2012 F6 (Lemmon). As it can be seen in Fig. 2.11, the Larson- Sekanina (bottom right) and rotational filters (bottom left) reveal essentially the same features even though their orientation is slightly different. These two techniques use rotations of the original image around its center by a certain angle combined in different ways. Several rotation angles were tested, always revealing the same features and we finally chose to use a 30° angle, which provides the higher contrast images. The removal of an azimuthal median profile is illustrated in the upper right panel of Fig. 2.11. Features close to the nucleus are not as contrasted and sharp as when using rotational and Larson-Sekanina filters but this technique reveals fainter large-scale features. Given that the subtraction of an azimuthal median profile generally does not introduce artefacts and that we observe essentially the same features using the three different techniques we are confident that the structures described in this work are real. We thus decided to mainly use subtraction or division by an azimuthal median profile to process our images. Gas images are first decontaminated from the dust contribution before being processed.

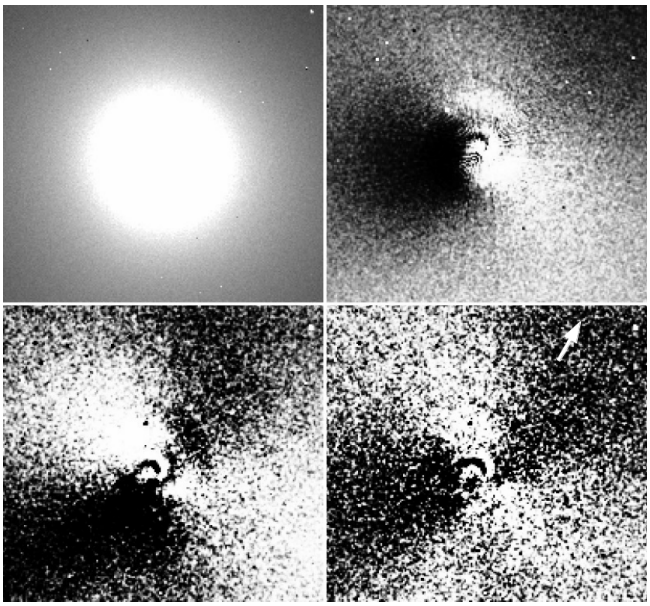

Figure 2.11: Representative CN image of comet C/2012 F6 (Lemmon) from February 12, 2013, and three different enhancement techniques. The original image of the comet is shown at the upper left of the panel. At the upper right, the removal of an azimuthal median profile is shown. The results of the rotational and Larson-Sekanina filters are shown respectively at the bottom left and right of the figure. The images are oriented north up and east left. The field of view is 4.3' × 4.3'. The arrow indicates the direction of the Sun.

# 3 Observation of individual comets

In this Chapter, we present a thorough analysis of several comets from our sample. Since the installation of the telescope in 2010, we observed 30 bright comets with narrow band filters. All these comets have been observed with the same instrument, the observations have been reduced using the same pipeline, and gas production rates have been computed using the same model. This provides an homogeneous sample to compare comets coma composition from optical observations. Before analysing and comparing our whole sample in Chapter 4, we present a thorough study of several comets. Some comets of our sample were particularly bright and remained observable for a long time from the Southern hemisphere. Given the large number of observations gathered and the peculiarities of these comets, we believe they deserve to be studied individually. It will also allow us to demonstrate the high quality and internal consistency of our data, as well as the possibilities to study the rotation and the long-term evolution of the activity, composition, and coma morphology of individual comets with a dedicated 60-cm telescope. We chose to study seven comets in this Chapter: 103P/Hartley 2 (Section 3.1), C/2009 P1 (Garradd) (Section 3.2), C/2012 F6 (Lemmon) (Section 3.3), C/2013 A1 (Siding Spring) (Section 3.4), C/2013 R1 (Lovejoy) (Section 3.5), C/2013 US10 (Catalina) (Section 3.6), and C/2014 Q2 (Lovejoy) (Section 3.7). Comets C/2012 F6 (Lemmon), C/2009 P1 (Garradd), C/2013 R1 (Lovejoy), and C/2014 Q2 (Lovejoy) were selected because of the large number of observations performed over wide ranges of heliocentric distances, and on both sides of perihelion for comets C/2012 F6 (Lemmon) and C/2013 R1 (Lovejoy). Comets C/2013 A1 (Siding Spring) and C/2013 US10 (Catalina) were observed in parallel with the FORS 2 instrument at the VLT, and comet Siding Spring also underwent an outburst shortly after its perihelion passage. Finally, comet 103P/Hartley 2 is particularly interesting because it was the target of the EPOXI mission. From the images of these seven comets, we derived OH, NH, CN, $C_2$, and $C_3$ production rates, as well as the $Af\rho$ parameter and followed their evolution over wide ranges of heliocentric distances. We also computed various production rate ratios to study their coma composition and applied image enhancement techniques to reveal features in the coma. Contrary to what was done in Opitom et al. (2015a,b, 2016), we decided to compute production rates ratios relatively to CN instead of OH to follow the evolution of the coma composition of these comets. OH is often used to normalise gas production rates and

make comparison from comet to comet since it is an indicator of the water production rate, which is the most abundant species in comets. However, we usually can not detect OH at large heliocentric distances, or for weak comets. In general, the first species we are able to detect is CN. We are able to measure CN production rates for all the comets of our sample, and we detect it at larger heliocentric distances than OH. We then decided to compute production rates ratios relatively to CN. In this Chapter, we analyse those data to study the evolution of these comets activity, the composition of their coma, and their morphology. In some cases, we were also able to determine or at least constrain the comet rotation period.

## 3.1 103P/Hartley 2

Comet 103P/Hartley 2 was discovered in 1986 by Malcolm Hartley at Siding Spring observatory in Australia. Hartley 2 is a short-period (P=6.48 years) Jupiter Family Comet. This comet has been observed by a large number of astronomers with both ground-based and space-borne observatories, because it was the target of the EPOXI mission (Extrasolar Planet Observation and Deep Impact Extended Investigation, Meech et al. (2011); A'Hearn et al. (2011)). EPOXI was an extension of the Deep Impact mission, which dropped an impactor on the nucleus of 9P/Tempel 1 in July 2005. The spacecraft was then redirected in order to fly by comet Hartley 2 on November 4, 2010, shortly after its perihelion passage on October 28 ($r$ = 1.06 au). The 2010 passage of the comet was particularly interesting because the comet passed at only 0.12 au from the Earth. A worldwide observing campaign involving dozens of telescopes allowed astronomers to obtain observations of the comet at various wavelengths simultaneously to the EPOXI flyby.

The EPOXI mission provided images and spectra of the nucleus of comet Hartley 2. Images revealed a bi-lobe-shaped nucleus with a maximum length of 2.333 km, as illustrated in Fig. 3.1. It was found that $CO_2$ is the main driver of comet Hartley 2 activity, dragging in the coma icy grains responsible for the large amount of water released by the comet. This also explains the significant activity of the comet despite the small size of its nucleus. Large inhomogeneities of the gas released from different parts of the nucleus were also observed, the main source of $CO_2$ being different from the main source of water vapour (Fig. 3.1). The rotation period of the comet has been measured both from ground-based and EPOXI observations (Jehin et al., 2010b; Meech et al., 2011; A'Hearn et al., 2011; Samarasinha et al., 2011; Knight et al., 2015). It is increasing with time, from $16.4 \pm 0.1$ h in April-May, 2009 (Meech et al., 2009) to 19 h in early December 2010 (Jehin et al., 2010b). The slow down of the comet rotation was attributed to the effect of jets and outgassing. Lightcurves analyses revealed that the nucleus of comet Hartley 2 is actually in an excited rotation state. The period of the non principal axis rotation is probably about three times the above-cited rotation period (Knight and Schleicher, 2011; Belton et al., 2013; Knight et al., 2015).

The deuterium to hydrogen isotopic ratio of this comet has been measured from observations with the Herschel Space Telescope (Hartogh et al., 2011). The D/H isotopic ratio had already

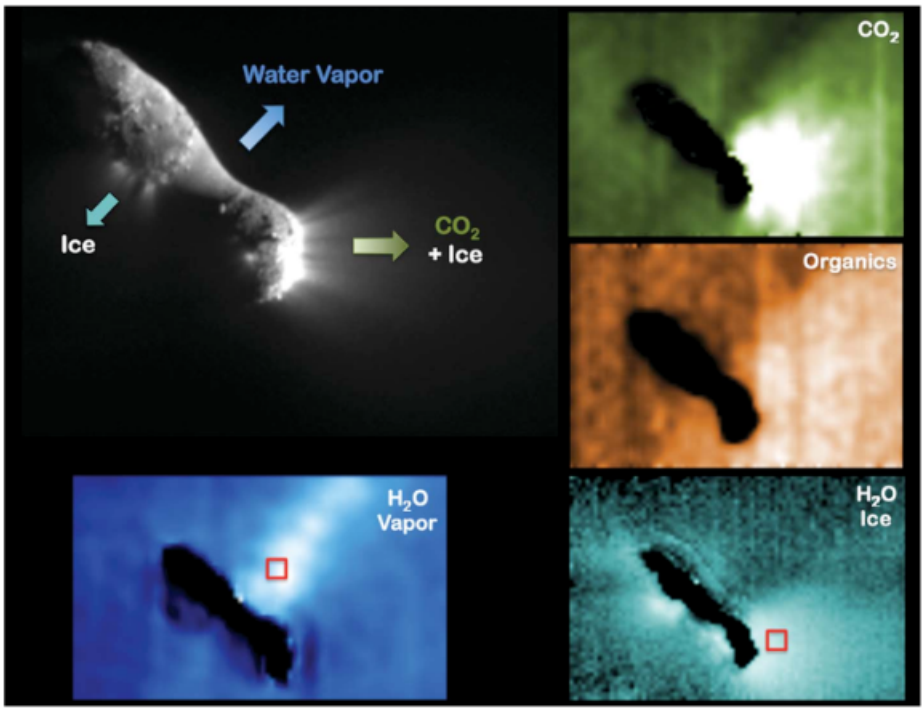


**Fig. 5.** Relative spatial distribution in the coma of Hartley 2. The red boxes (5 by 5 pixels; 52 m pixel$^{-1}$) indicate regions sampled to produce the spectra in Fig. 6. Panels labeled $CO_2$, Organics, and $H_2O$ Vapor are maps of the total flux in the relevant emission bands. The panel labeled $H_2O$ Ice is a map of the depth of the ice absorption feature at 3 μm. Each panel has been individually linearly stretched. All spectral images are from a scan at E+7 min, hi5006000. Sun is to the right.

Figure 3.1: Nucleus of comet 103P/Hartley 2 and spatial distribution of water, carbon dioxide, and organics from the EPOXI mission. This image is from A'Hearn et al. (2011)

been measured in other comets before, but only in Oort Cloud comets. It was thus the first measurement of the D/H ratio in the coma of a Jupiter Family Comet. The ratio found is lower than previous measurements, and consistent with the value measured in terrestrial water. This was the very first proof of a link between cometary and terrestrial water. Other measurements in the coma of JFCs have been made since then, especially by the ROSETTA mission in the coma of comet 67P/CHuryumov-Gerasimenko, but a D/H ratio five times higher than the terrestrial value was measured (Altwegg et al., 2015).

### 3.1.1 Activity

We observed comet Hartley 2 with TRAPPIST from October 30, 2010 ($r$ = 1.06 au), two days after the perihelion passage, until February 21, 2011 ($r$ = 1.80 au). This comet was the first and the most intensively observed with TRAPPIST. We monitored the comet 3 to 6 times a week during this period. For most of the nights, we were able to observe several hours in a row, collecting an extremely dense data set for the study of comet Hartley 2 rotation. At the time of

comet Hartley 2 observations, fewer filters were mounted on the filter wheel, so we observed only with the OH, CN, $C_3$, $C_2$, and GC filters.

We first discuss the evolution of comet Hartley 2 activity as the comet moves away from the Sun and compare the gas species and the dust. The evolution of the gas production rates and the $Af\rho$ values after the comet perihelion passage is shown in Fig. 3.2 for the gas species all together and in Fig. 3.3. for both the gas species and the dust. We fitted power-law slopes to represent the evolution of the production rates and the $Af\rho$ with the heliocentric distance, and these are overplotted to the data in Fig. 3.3. As already mentioned, comet Hartley 2 is a very active comet given the small size of its nucleus, OH production rates reach $7 \times 10^{27}$ mol/s at the peak. The evolution of all gas production rates with the heliocentric distance looks very similar. OH, CN, $C_3$, and $C_2$ production rates first increase slowly and peak between 7 and 15 days after the comet perihelion passage. The exact date of the peak is difficult to determine because of the dispersion of the data within each night. After the peak, the gas production rates decrease regularly until the end of our observations. Table 3.1 summarises the slopes we derived to represent the evolution of the gas production rates and $Af\rho$ values with the heliocentric distance post-perihelion. These slopes are similar for all the gas species, even though the OH and $C_2$ slopes are slightly steeper than the CN and $C_3$ slopes. From Fig. 3.2 and 3.3, we observe a dispersion of gas production rates measured at different times during the same night, which is larger than the errors. This dispersion is interpreted as due to the rotation of comet Hartley 2 nucleus, producing variations of the gas production rates. The amplitude of the rotational variation reaches about 20 % for gas species.

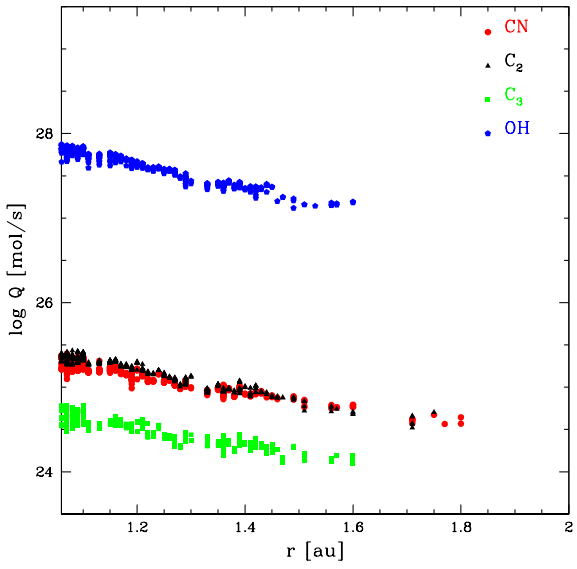


Figure 3.2: The logarithm of comet 103P/Hartley 2 OH, CN, $C_3$, and $C_2$ production rates as a function of the heliocentric distance $r$ (au) post-perihelion. The origin of the $r$-axis is perihelion (1.06 au).

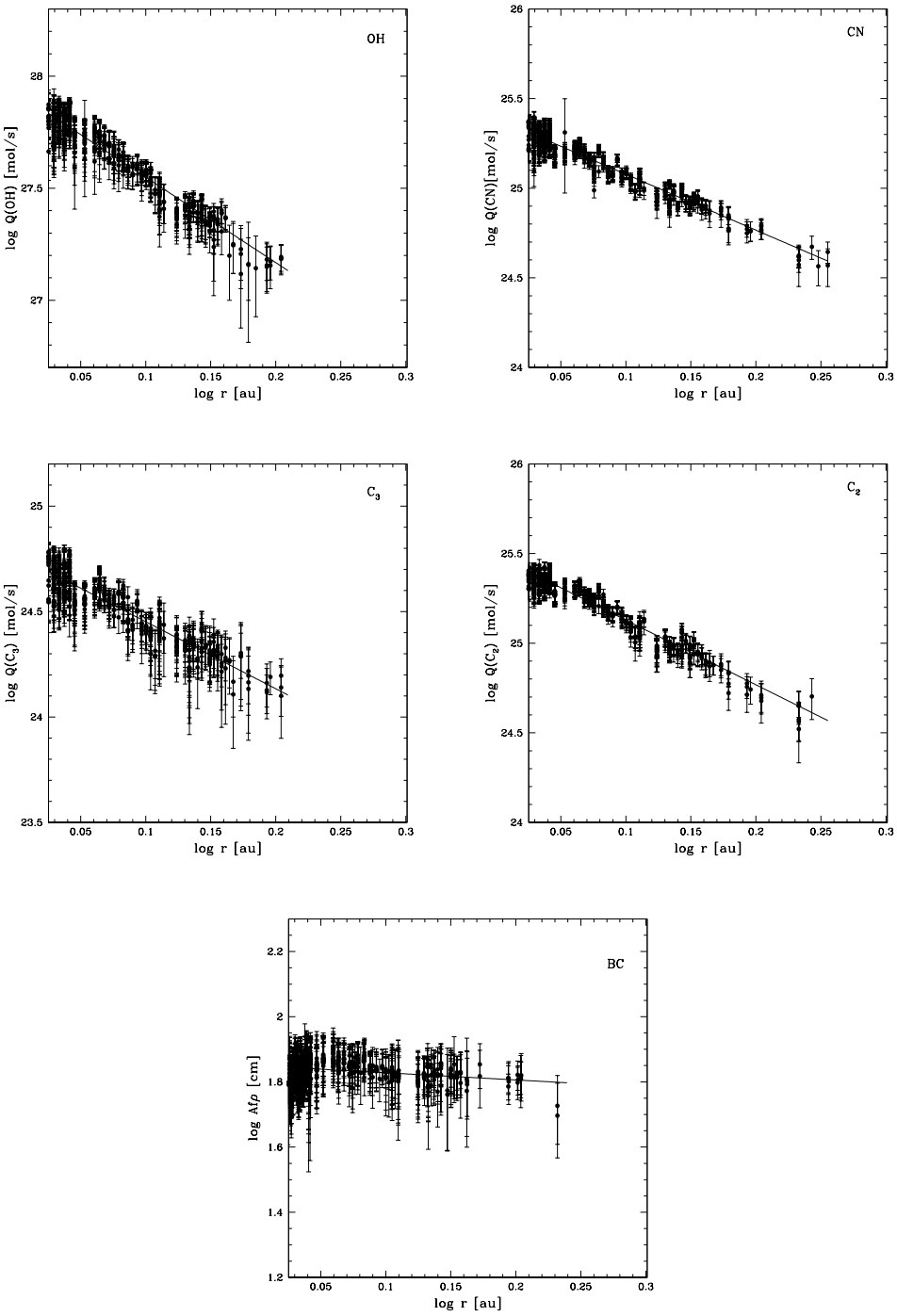


Figure 3.3: Comet 103P/Hartley 2 OH, CN, $C_3$, and $C_2$ production rates and $A(0)f\rho$ as a function of the heliocentric distance ($r$). Full lines represent power-law fits of the production rates and $A(0)f\rho$ variation with the heliocentric distance.

The dust lightcurve (last plot of Fig. 3.3) looks different from the one of the gas. The $Af\rho$ values keep increasing after the comet reaches perihelion, similarly to the gas, but they peak several days later. For the dust too, the date of the peak is difficult to determine because of the nightly dispersion. After the peak, the $Af\rho$ decreases but only very slowly. This is confirmed by the value of the slope in Table 3.1, which is much shallower than those derived for gas species. We also observe rotational variability for the dust but the amplitude is lower than for the gas. This is not surprising, given that dust grains have lower velocities than the gas molecules and will then stay longer within the aperture, which smooths the rotational variation.

Table 3.1: Fitted power-law slopes for comet 103P/Hartley 2 OH, CN, $C_3$, and $C_2$ production rates and $A(0)f\rho$ heliocentric dependences post-perihelion.

| Species | r-dependence |
|---|---|
| OH | -3.81±0.10 |
| CN | -3.12±0.11 |
| $C_3$ | -3.18±0.15 |
| $C_2$ | -3.61±0.11 |
| $A(0)f\rho$ | -0.22±0.06 |

Comet Hartley 2 has been intensively observed with numerous telescopes both from space and from the ground during this apparition. These observations were performed with various instruments and at different wavelengths. A large number of data sets are thus available for comparison with our measurements. In order to keep this section brief, we will not compare our results with every available data set. The easiest comparison to make is with Knight and Schleicher (2013), since they use the same filters and the same model parameters as we do. On November 16 ($r$ = 1.09 au) they measure production rates ranging from: Q(OH)=7.08 - $7.41\times10^{27}$ mol/s, Q(CN)=1.86 - $1.95\times10^{25}$, Q($C_3$)=4.57 - $5.0\times10^{24}$ mol/s, Q($C_2$)=2.34 - $2.51\times10^{25}$ mol/s, and $A(0)f\rho$=59 - 68 cm. During the same night, we measure: Q(OH)=$(5.73\pm0.94)$ - $(6.71\pm0.90)\times10^{27}$ mol/s, Q(CN)=$(1.70\pm0.16)$ - $(1.93\pm0.15)\times10^{25}$, Q($C_3$)=$(4.27\pm0.99)$ - $(5.22\pm0.42)\times10^{24}$ mol/s, Q($C_2$)=$(2.08\pm0.19)$ - $(2.37\pm0.18)\times10^{25}$ mol/s, and $A(0)f\rho$=$(68\pm13)$ - $(79\pm16)$ cm. Within the error bars and considering the rotational variation of the comet, our measurements are in excellent agreement with those reported by Knight and Schleicher (2013). Comparison of measurements made on other dates shows the same agreement. Knight and Schleicher (2013) also derive power-law slopes to represent the heliocentric dependence of production rates. They report slopes equal to $-3.99\pm0.05$ for OH, $-3.20\pm0.10$ for CN, $-3.20\pm0.13$ for $C_3$, $-3.45\pm0.09$ for $C_2$, and $-1.68\pm0.19$ for the $A(0)f\rho$. Slopes for gas species are mostly consistent with those we derive, while the $A(0)f\rho$ is much steeper. This difference in the $A(0)f\rho$ slope is probably produced by the variable aperture size used by Knight and Schleicher (2013). They noticed that larger apertures result in smaller $A(0)f\rho$ values, since the dust brightness radial profile is steeper than $1/\rho$. Since they used larger aperture at larger heliocentric distance, this might explain why they derive a steeper $A(0)f\rho$ slope. Finally, Knight and Schleicher (2013) find that the production rates peak about 10 days after perihelion.

This shows the very good agreement between our measurement and those made by Knight and Schleicher (2013), using the same filters, model, and parameters. Combi et al. (2011a) report water production rates derived from observations with the SWAN camera on SOHO. As an example, on October 31 they measure a water production rate of $(6.38 \pm 0.12) \times 10^{27}$ mol/s. One day earlier, we measure an OH production rate equal to $(6.26 \pm 1.50) \times 10^{27}$ mol/s, equivalent to a water production rate[1] of $(8.77 \pm 2.10) \times 10^{27}$ mol/s. Generally speaking, values measured by Combi et al. (2011a) are slightly lower than our measurements and those from Knight and Schleicher (2013) but their field of view is much larger. Lara et al. (2011) derive CN, $C_3$, and $C_2$ production rates with the ACAM instrument mounted on the William Herschel Telescope (WHT) at La Palma Observatory. These values are lower than ours and those from Knight and Schleicher (2013) but some of the parameters used in the Haser model differ, which may explain the difference. Crovisier et al. (2013) compared water production rates derived by various authors around the time of the EPOXI flyby and found that these span over at least a factor 3. This emphasizes again the difficulty to compare production rates derived from observations at different wavelengths, from the submillimeter to the near-UV, and using different model parameters.

### 3.1.2 Composition

We computed production rate ratios to examine the comet composition and its evolution with the heliocentric distance. The results are shown in Fig. 3.4 along with fitted power-law slopes. The examination of the $C_2$ to CN ratio confirms that comet Hartley 2 is a typical comet in terms of carbon-chain species (A'Hearn et al., 1995). The $C_2$ to CN ratio decreases while the comet moves away from the Sun, as illustrated by the value negative value of the slope in Table 3.2. However, the comet always remains typical in terms of carbon-chain species. The OH to CN ratio also decreases as the comet moves away from the Sun, while we do not see strong changes of the $C_3$ to CN ratio. Finally, the dust to gas ratio strongly increases with the heliocentric distance, as the comet becomes dustier while moving away from the Sun. Since we only have observations with one narrow band dust filter, we are not able to derive the dust colour for this comet and to study its evolution with the heliocentric distance.

Table 3.2: Fitted power-law slopes for the heliocentric dependence of comet 103P/Hartley 2 OH, $C_3$, $C_2$, and $A(0)f\rho$ to CN ratios post-perihelion.

| Species | r-dependence |
|---|---|
| log[Q(OH)/Q(CN)] | -0.73±0.11 |
| log[Q($C_3$)/Q(CN)] | -0.04±0.06 |
| log[Q($C_2$)/Q(CN)] | -0.47±0.10 |
| log[Q($A(0)f\rho$)/Q(CN)] | +2.87±0.10 |

Several parent species have been observed at infrared wavelengths as part of the worldwide

[1] Using $Q(H_2O) = 1.361 r^{-0.5} Q(OH)$, Cochran and Schleicher (1993)

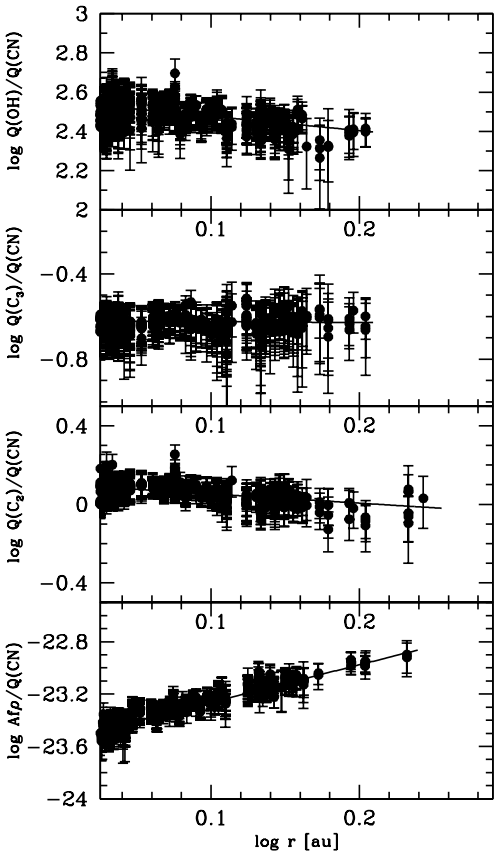


Figure 3.4: Comet 103P/Hartley 2 OH, $C_3$, $C_2$, and $A(0)f\rho$ to CN production rate ratios as a function of the heliocentric distance. Full lines represent power-law fits of the ratio variations with the heliocentric distance.

campaign in support of the EPOXI mission. Dello Russo et al. (2011) observed comet Hartley 2 with NIRSPEC on Keck II on November 4, 2010. They derive gas production rates ranging from: Q(HCN) = $(3.06 \pm 0.37)$ - $(3.10 \pm 0.39) \times 10^{25}$ mol/s, Q($C_2H_2$) = $(1.37 \pm 0.23)$ - $(2.21 \pm 0.70) \times 10^{25}$ mol/s, and Q($C_2H_6$) = $(5.55 \pm 0.69)$ - $(12.7 \pm 1.5) \times 10^{25}$ mol/s. On the same date, Drahus et al. (2012) measure HCN production rates of Q(HCN) = $(0.73 \pm 0.16)$ - $(1.71 \pm 0.34) \times 10^{25}$ mol/s with the IRAM 30-m telescope. On Novermber 5, we measure production rates of daughter species with TRAPPIST: Q(CN) = $(1.25 \pm 0.22)$ - $(1.67 \pm 0.25) \times 10^{25}$ mol/s, Q($C_2$) = $(1.83 \pm 0.26)$ - $(2.54 \pm 0.28) \times 10^{25}$ mol/s. Despite the large dispersion of HCN production rates, they are consistent with HCN being the principal parent of CN, and $C_2H_2$ production rates are consistent with it being the parent of $C_2$. Mumma et al. (2011) also observed comet Hartley 2 with CRIRES at ESO/VLT on November 16, 2010. They report: Q(HCN) = $(1.76 \pm 0.61) \times 10^{25}$ mol/s, Q($C_2H_2$) = $(0.69 \pm 0.23) \times 10^{25}$ mol/s, and Q($C_2H_6$) = $(5.29 \pm 0.92) \times 10^{25}$ mol/s. Almost simultaneous TRAPPIST observations give: Q(CN) = $(1.70 \pm 0.16)$ - $(1.93 \pm 0.15) \times 10^{25}$ mol/s, Q($C_2$) = $(2.08 \pm 0.19)$ - $(2.37 \pm 0.18) \times 10^{25}$ mol/s. In conclusion, from the comparison between

potential parent and daughter species production rates, it seems that HCN may be the main CN parent. The conclusion is less obvious for the $C_2$. Some data sets suggest that $C_2H_2$ could be the main $C_2$ parent (Dello Russo et al., 2011) but other observations indicate that another source of $C_2$ is required (Mumma et al., 2011; Drahus et al., 2012). $C_2H_6$ is abundant in the coma but not very efficient to produce $C_2$ (Weiler, 2012). Part of the $C_2$ in the coma of Hartley 2 could then be released by CHON grains, as suggested by McKay et al. (2014).

### 3.1.3 Morphology

We processed images of comet Hartley 2 by dividing by an azimuthal median profile to enhance features in the coma. The result is shown in Fig. 3.5 for observations made on November 7, 2010. We observe a strong dust jet in the direction opposite to the Sun, caused by the dust grains pushed away from the Sun by the radiation pressure. The morphology of the gas species is different from the dust. The OH, $C_3$, and $C_2$ processed images are enhanced in the anti-sunward hemisphere. The CN has a typical hourglass shape, with two large jets in opposite directions. The difference between the OH, $C_3$, $C_2$ and the CN morphology could indicate that these species are released from different active areas but we have to be cautious since the S/N in the gas filters other than CN is low.

The coma morphology observed on November 07 and illustrated in Fig. 3.5 is mostly representative of the general morphology of the coma during our observing period. We show an example of the evolution of the CN morphology during November and the first half of December in Fig. 3.6. The position and the aspect of the jets vary smoothly with the changing viewing geometry but the hourglass shape is visible during the whole period. The relative intensity of the two jets is varying too. This is probably due to the rotation of the comet nucleus. However, these changes are weak and we are then not able to determine the rotation period from periodic changes of the observed coma morphology. After mid-December, no gas features are visible in our processed images because of the low S/N. The only visible feature at that time is the dust tail.

### 3.1.4 Rotation

In Section 3.1.1, we report a dispersion of gas and dust production rates derived at different times during the same night. We attribute this dispersion to rotational variation. Indeed, as indicated by the morphology of the coma and as confirmed by the images of the nucleus from the EPOXI spacecraft, the gas is probably emitted preferentially from some active areas. Because of the nucleus rotation, the illumination of active areas varies, and the production rates vary too. In this section, we study the variation of the gas production rates with the rotation in order to derive the nucleus rotation period.

Several authors used variations of production rates, lightcurves, or morphological variations of features in the coma to derive the rotation period of comet Hartley 2 (Knight and Schleicher,

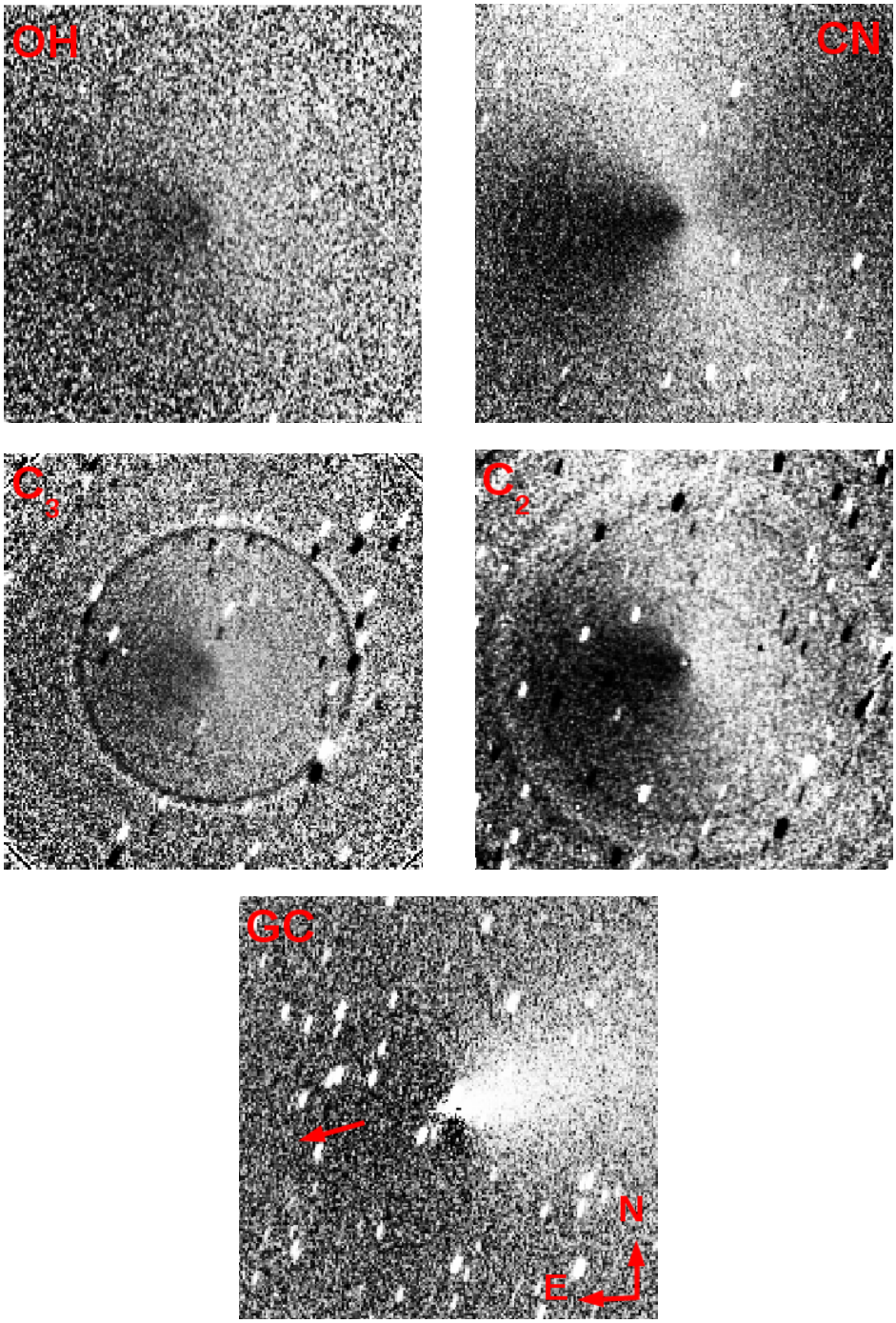


Figure 3.5: Comet 103P/Hartley 2 OH, CN, $C_3$, $C_2$, and dust from GC filter images from November 7, 2010 processed by dividing by an azimuthal median profile. All images are oriented with north up and east left. The field of view is $4.3' \times 4.3'$. The arrow indicates the direction of the Sun. The circles in the images are artefacts due to a bright star in the field of view.

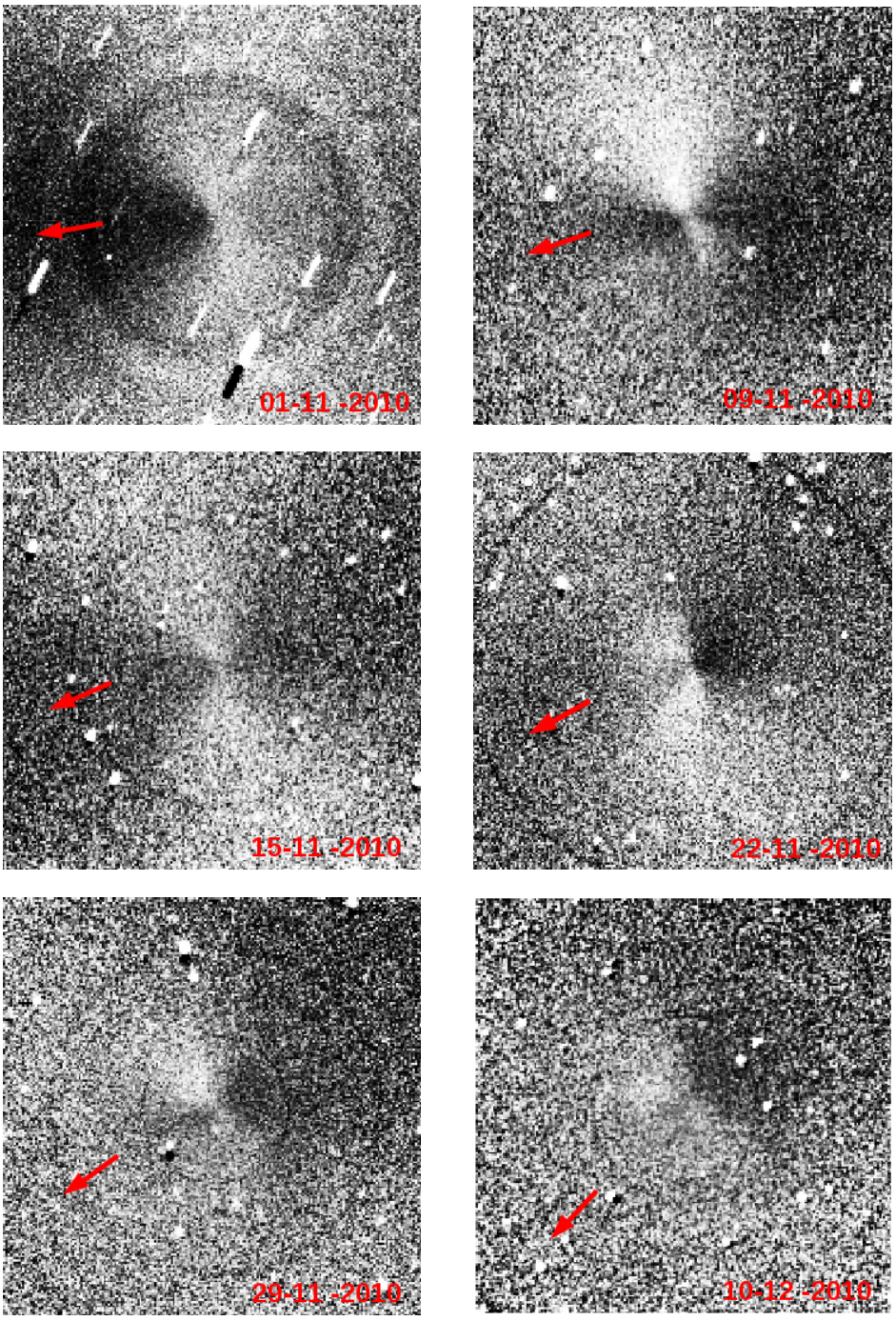


Figure 3.6: Comet 103P/Hartley 2 CN images from November 1, November 9, November 15, November 22, November 29, and December 10, 2010 processed by dividing by an azimuthal median profile. All images are oriented with north up and east left. The field of view is $4.3' \times 4.3'$. The arrow indicates the direction of the Sun. The circles in the images are artefacts due to a bright star in the field of view.

2011; Samarasinha et al., 2011; Waniak et al., 2012; Belton et al., 2013; Knight et al., 2015). Samarasinha et al. (2011) find a period of 16.7 hr in August, increasing to 18.7 hr in early November. Jehin et al. (2010a) also report an increase of the apparent rotation period from 18.2 to 19 hr from October 29 to December 7. These values of the rotation period are consistent with those derived by other authors. Even though the main rotation period seems to be between 16 hr and 19 hr depending on the epoch, thorough studies have revealed that the comet is in Non Principal Axis rotation (A'Hearn et al., 2011). The morphology is better reproduced after a period of about three times the main period, and this longer period also produces better lightcurves. A re-analysis of several data sets by Knight et al. (2015) combining morphology of the coma and lightcurves confirms that the rotation period of the comet is increasing with time up to mid-November, with a possible flattening in late-November and December. Phasing using triple-peaked period near 54-55 hr (i.e. the lightcurve has three maxima and three minima per rotation) also produces better lightcurves. They observe changes of the aspect of the triple-peaked lightcurve from one cycle to the next, the phase and amplitude of the peaks varying over time-scales of a few rotation periods. This might explain the dispersion of the rotation periods derived by other authors and the difficulty to derive a reliable rotation period for this comet. Despite numerous observations by various telescopes and data from the EPOXI flyby, the rotation state of comet Hartley 2 is not yet well constrained. Large studies including lightcurves and morphological feature analysis from several data sets are still ongoing with the objective to reach a better understanding of the rotational state of comet 103P/Hartley 2.

Here, we analyse our gas and dust production rates lightcurves to derive the rotation period of the comet and study its evolution with time. Since we expect the rotation period of the comet to vary with time, we do not perform an analysis of our entire data set simultaneously. We divided it in 15-day epochs, from October 30, 2010 until January 15, 2011. After that, the temporal coverage of our observations is not sufficient to study the rotation period of the comet and the S/N is lower. We subtract the long-term trend from the data by fitting a first order cubic spline for each species. The periodicity analysis is performed using a Lomb-Scargle algorithm (Scargle, 1982). We are only able to perform the period analysis on CN, $C_3$, and $C_2$ production rates. The S/N is not sufficient in the OH filter and variations of the $Af\rho$ with the rotation period are difficult to analyse, since dust grains are heavy and move slowly in the coma compared to gas particles. Variations of the dust production due to the illumination of active areas are then averaged in the coma.

Rotation periods we derive are summarized in Table 3.3. By testing various rotation period determination methods, we determined that the uncertainty of the rotation periods given in Table 3.3 is about 0.12 hours. For some epochs, the period in Table 3.3 does not correspond to the highest peak in the periodogram but in these cases we selected the period with the best looking phase curve. Periods measured from CN, $C_3$, and $C_2$ are consistent with each other within the uncertainty for each period. We can not measure the rotation period from $C_3$ and $C_2$ lightcurves in early January due to the combination of lower S/N in these filters at that time and lower time coverage of the observations. Periods measured in the first and second half of November are similar for all species. This is consistent with the flattening of the rotation

period increase observed in late November by Knight et al. (2015). After that, the rotation period of the comet increases again to reach 19 hr in January. This increase is observed for all species.

Table 3.3: Measured rotation period of comet 103P/Hartley 2 nucleus for different epochs measured from CN, $C_3$, and $C_2$ lightcurves.

| Epoch | Period (Hours) | | |
|---|---|---|---|
| | CN | $C_3$ | $C_2$ |
| 30/10/2010 - 14/11/2010 | 18.36 | 18.43 | 18.26 |
| 15/11/2010 - 30/11/2010 | 18.34 | 18.36 | 18.24 |
| 01/12/2010 - 15/12/2010 | 18.41 | 18.43 | 18.48 |
| 16/12/2010 - 31/12/2010 | 18.50 | 18.38 | 18.55 |
| 01/01/2011 - 15/01/2010 | 19.10 | - | - |

Figure 3.7 shows CN, $C_3$, and $C_2$ phase curves for the first epoch (first half of November). We considered October 30 0h00 UT as the zero phase. At first glance, the three phase curves have very similar sine-like shapes and their aspect confirms the values of the rotation periods in Tab. 3.3. However, further examination of the CN lightcurve, for example, shows that the amplitude and the phase of peaks from different rotations vary. Such variations have already been noticed by other authors for this comet (Knight et al., 2015). Peaks and minima of CN and $C_3$ production rate occur at the same phase, while the $C_2$ curve is shifted. The $C_2$ phase shift is of approximately 1 hour.

Phase curves from Fig. 3.7 are satisfying but it has been reported in previous works that comet Hartley 2 is in a complex rotation state and that triple-peaked phase curves work better than single-peaked lightcurves. Figure 3.8 shows the phase curve we obtain using the triple of the rotation period given in Tab 3.3 for CN, $C_3$, and $C_2$ for the first half of November. As expected, the dispersion is lower than in Fig. 3.7, confirming that comet 103P/Hartley 2 is in Non Principal Axis rotation. For all species, the three peaks do not have the same amplitude, which explains the dispersion observed when we use the rotation period we derived to build the phase curve. From Fig. 3.7 too, we notice that CN and $C_3$ are in phase while $C_2$ is shifted.

Figure 3.9 illustrates the evolution of the CN phase curve for the five epochs we used to perform the period analysis. As for the first epoch, other CN phase curves look satisfying, even though there is some dispersion. Figure 3.10 shows the CN triple-peaked phase curve for all epochs. For all epochs, the triple-peaked light curve gives better results. The same conclusions can be drawn for $C_3$ and $C_2$.

Finally, we study the variation of various production rate ratios with the nucleus rotation. Figure 3.11 shows phase curves of the $C_2$, $C_3$, OH, and $Af\rho$ to CN ratios for the period 30/10/2010 - 14/11/2010. The $C_2$ to CN ratio varies with the rotational phase. This is caused by the phase shift between $C_2$ and CN lightcurves. McKay et al. (2014) suggested that $C_2$ might be released

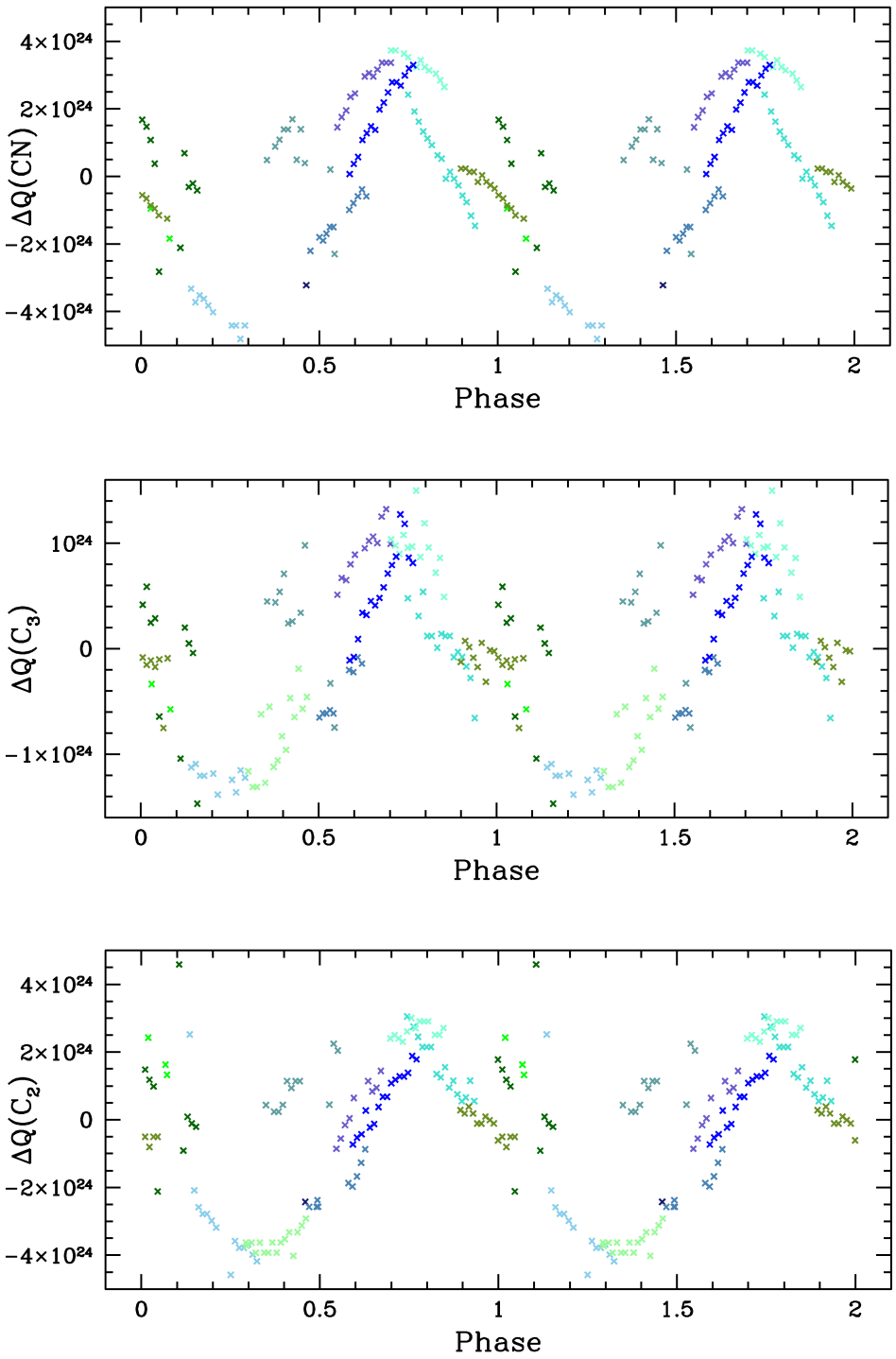


Figure 3.7: 103P/Hartley 2 CN, $C_3$, and $C_2$ phase curves for the epoch: 30/10/2010 - 14/11/2010. Each night is represented with a different colour.

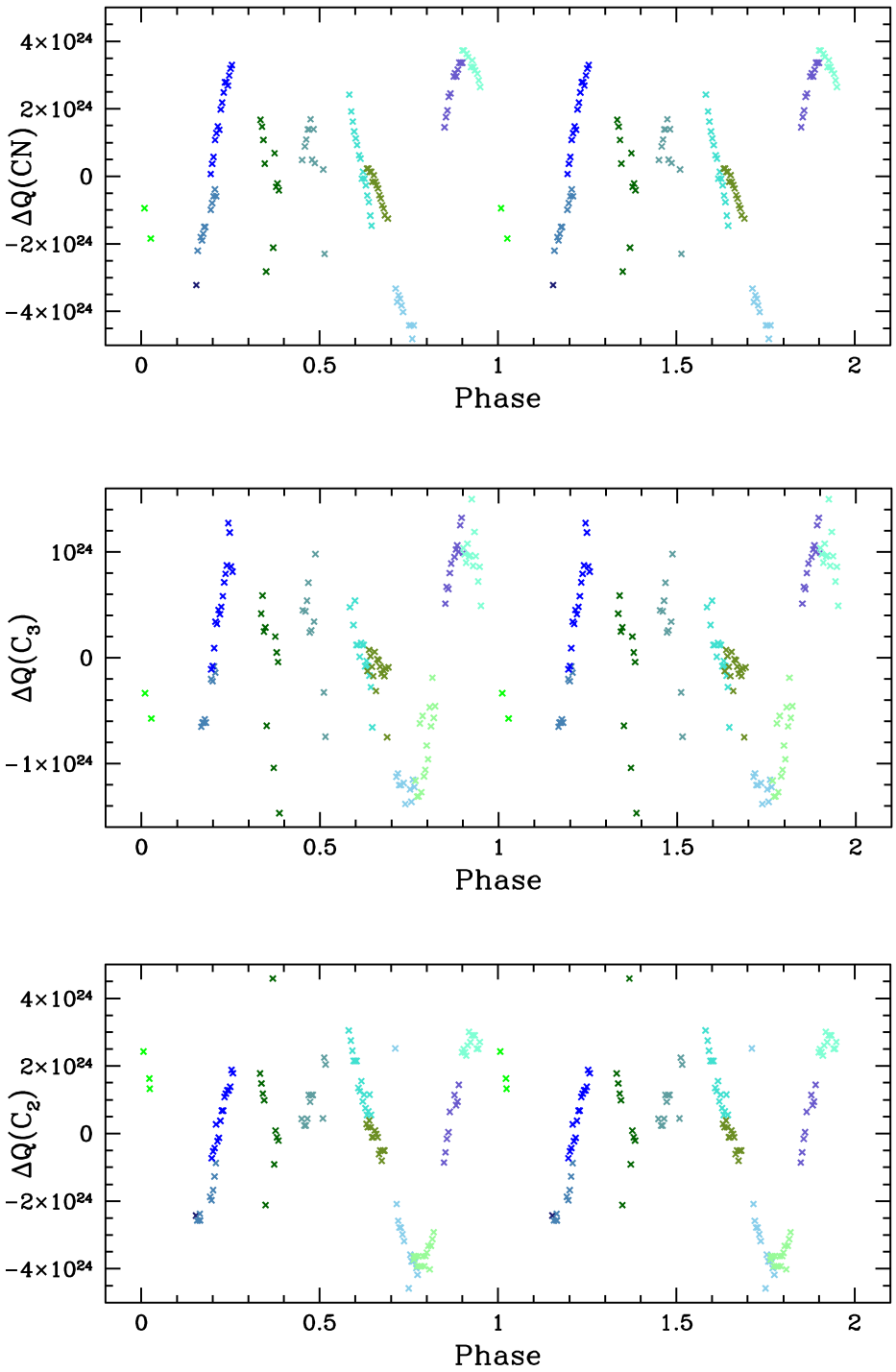


Figure 3.8: 103P/Hartley 2 CN, $C_3$, and $C_2$ triple-peaked phase curves for the epoch: 30/10/2010 - 14/11/2010. We used a period equal to three times the period in Table 3.3. Each night is represented with a different colour.

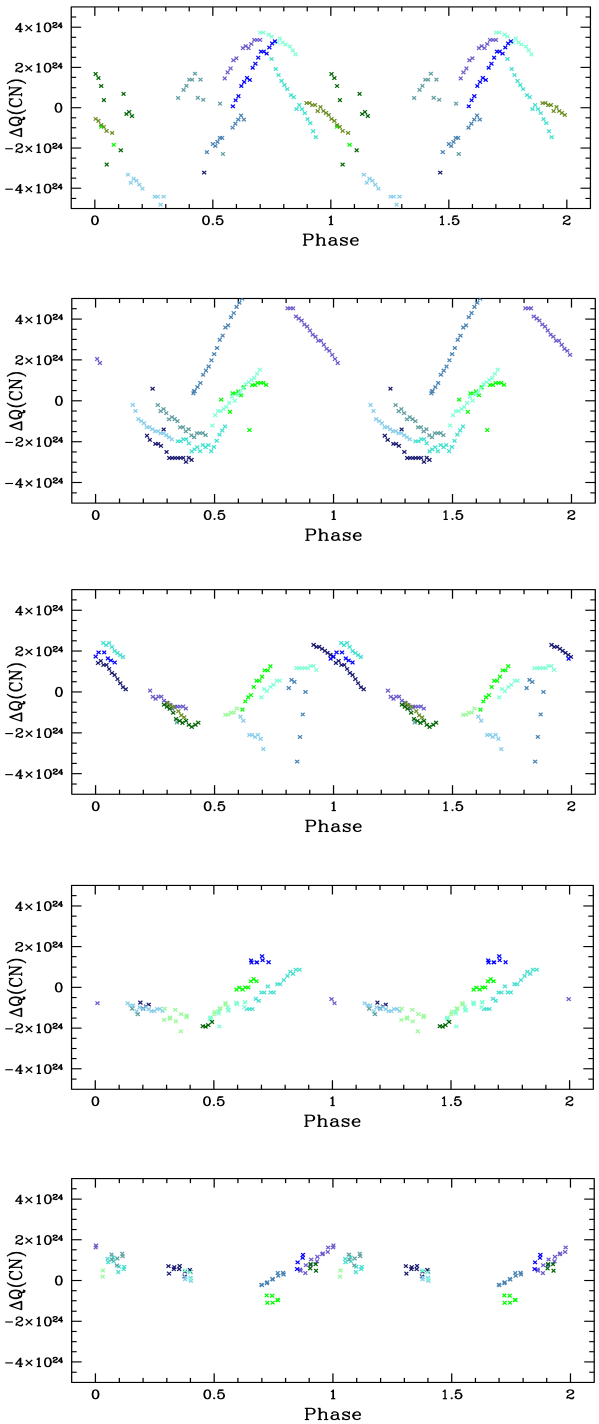


Figure 3.9: 103P/Hartley 2 CN phase curves for the epochs: 30/10/2010 - 14/11/2010, 15/11/2010 - 30/11/2010, 01/12/2010 - 15/12/2010, 16/12/2010 - 31/12/2010, 01/01/2011 - 15/01/2011 (from top to bottom). Each night is represented with a different colour.

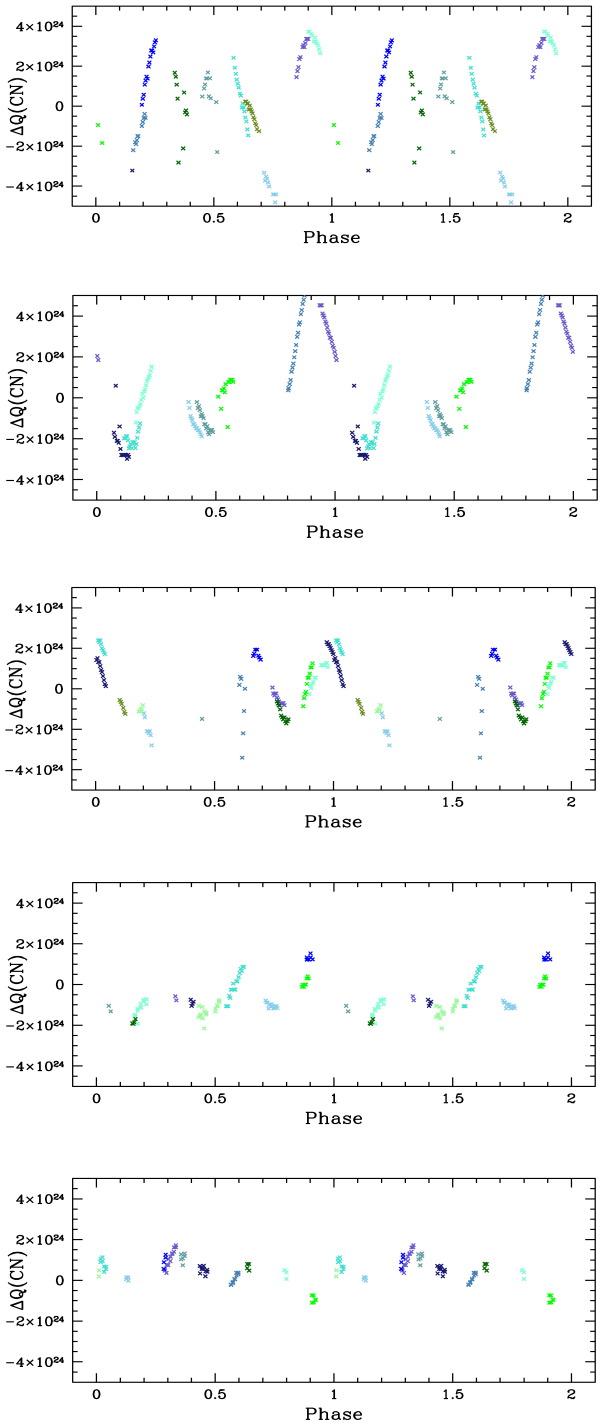


Figure 3.10: 103P/Hartley 2 CN triple-peaked phase curves for the epochs: 30/10/2010 - 14/11/2010, 15/11/2010 - 30/11/2010, 01/12/2010 - 15/12/2010, 16/12/2010 - 31/12/2010, 01/01/2011 - 15/01/2011 (from top to bottom). We used a period equal to three times the period in Table 3.3. Each night is represented with a different colour.

from CHON grains in the coma of Hartley 2. If this is the case, it could probably explain the phase difference between $C_2$ on one side and $C_3$ and CN on the other side. This is consistent with the comparison between $C_2$ and $C_2H_2$ production rate which indicates that $C_2H_2$ might not be the only parent of $C_2$. $C_3$ and OH to CN ratios do no strongly vary. Finally, the dust to gas ratio also varies with the rotational phase. The variation of the dust to gas ratio is mainly due to the variation of the CN production rates, since the $Af\rho$ do not vary much.

### 3.1.5 Summary

We monitored intensively comet 103P/Hartley 2 during the months following its perihelion passage and followed the decrease of the activity of the comet as it was moving away from the Sun. We first demonstrated that the production rates we measure from TRAPPIST observations are in very good agreements with those measured by other authors using similar filters, model, and model parameters. We then noticed that the rate of the production rates decrease is similar for the OH, CN, $C_3$, and $C_2$ while we do not see a strong decrease of the $Af\rho$ with the heliocentric distance. The dust to gas ratio of the comet is then changing with the heliocentric distance, the comet becoming more dusty as it moves away from the Sun. We observed the comet regularly for several hours during a night and we see variations of the gas production rates of the order of 20 % over the course of a few hours, induced by the rotation of the nucleus. We performed a period analysis of the CN, $C_3$, and $C_2$ lightcurves and derived the rotation period of the nucleus, which is increasing from 18.36 hours in early November to 19.10 hours in early January from the analysis of the CN lightcurve. We provided the only measurement of the rotation period of comet Hartley 2 in January 2011. We noticed that the phase curve is cleaner if we use the triple of the measured rotation period, indicating that the nucleus of comet Hartley 2 is in a complex rotational state. Finally, we observed a phase lag between the $C_2$ phase curve on one side and the $C_3$ and CN phase curves on the other side. This could be explained if the $C_2$ is not actually a daughter species but is released from CHON grains in the coma and is confirmed by the comparison of the $C_2$ and $C_2H_2$ production rates.

## 3.2 C/2009 P1 (Garradd)

Comet C/2009 P1 (Garradd) was discovered on August 13, 2009 by Gordon J. Garradd at the Siding Spring Observatory in Australia while at 8.7 au from the Sun. Garradd is a dynamically young Oort-Cloud comet (this is not its first passage in the inner solar system) on a highly inclined hyperbolic orbit. The comet reached perihelion on December 23, 2011 at an heliocentric distance of 1.55 au. Comet Garradd has been observed by a large number of telescopes, both ground-based (e.g. Gicquel et al. (2015); DiSanti et al. (2014); Paganini et al. (2012); Villanueva et al. (2012); Boissier et al. (2013); McKay et al. (2015)) and space-borne (e.g. Farnham et al. (2012); Bockelée-Morvan et al. (2012); Combi et al. (2013); Bodewits et al. (2014); Feaga et al. (2014)).

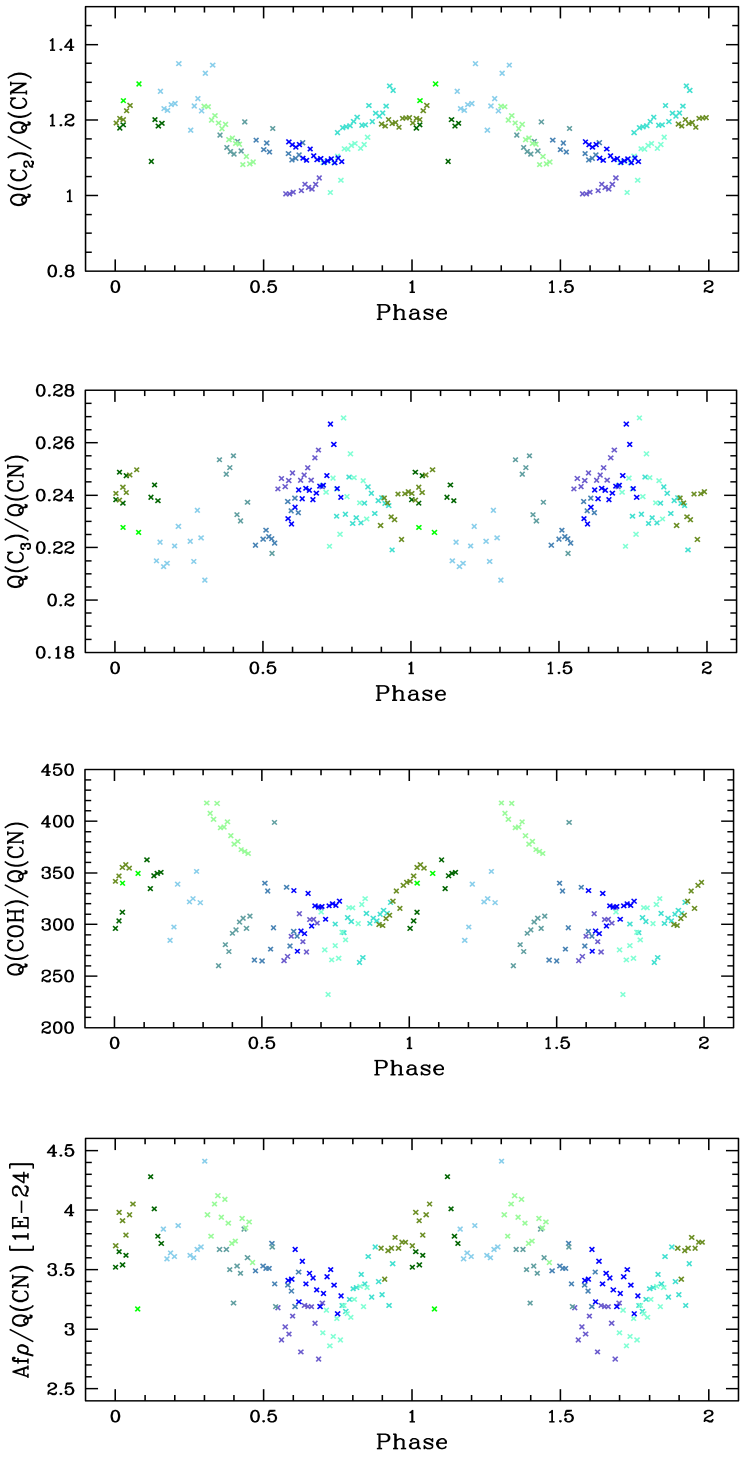


Figure 3.11: 103P/Hartley 2 production rate ratios phase curves for the epochs: 30/10/2010 - 14/11/2010. Each night is represented with a different colour.

### 3.2.1 Activity

We started to observe the comet with TRAPPIST on May 5, 2011 while at 3.33 au from the Sun. At that time, we were already able to detect CN, $C_3$, and $C_2$ in the coma. We observed the comet continuously with those filters as well as the BC and GC continuum filters until October 22, 2011. From late July, we were also able to detect the OH emission. At that time, the NH filter was not mounted on the filter wheel, neither were the UC and RC continuum filters. We do not have post-perihelion observations of comet Garradd. In late August and September we were able to observe the comet several hours in a row, trying to study rotational variations and to determine its rotation period.

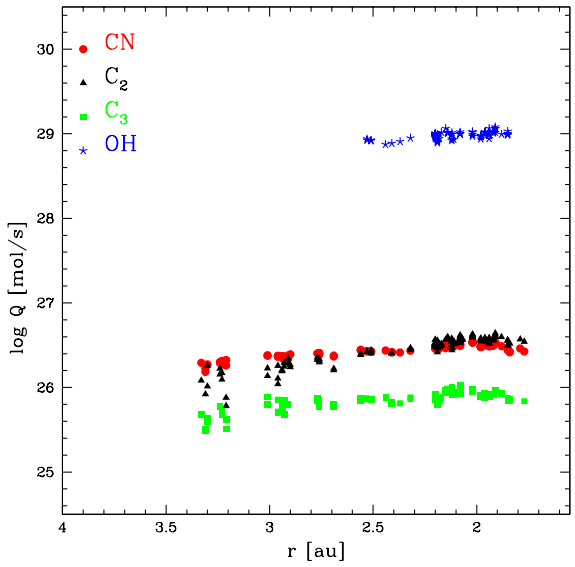


Figure 3.12: The logarithm of comet C/2009 P1 (Garradd) OH, CN, $C_3$, and $C_2$ production rates as a function of the heliocentric distance r (au). The *r*-axis is interrupted at perihelion (1.55 au).

We derived gas production rates and $Af\rho$ values corrected from the phase angle effect from the narrow band images of comet Garradd. The evolution of these production rates with the heliocentric distance is shown in Fig. 3.12 for the gas species all together and in Fig.3.13 for the gas and the dust. We also fitted power-law slopes to represent the evolution of production rates as a function of the heliocentric distance, allowing an easier comparison of the evolution of the activity between species. The results of these fits are given in Table 3.4 and overplotted on the gas production rates in Fig. 3.13. We observed comet Garradd over a wide range of heliocentric distances pre-perihelion, from 3.3 to 1.8 au, and at unusually large heliocentric distance for a relatively small telescope. This data set provides an opportunity to study how radicals are released in the coma far from the Sun, and how this may change when the comets approaches the Sun.

Overall, the evolution of CN, $C_3$, and $C_2$ production rates with the heliocentric distance looks

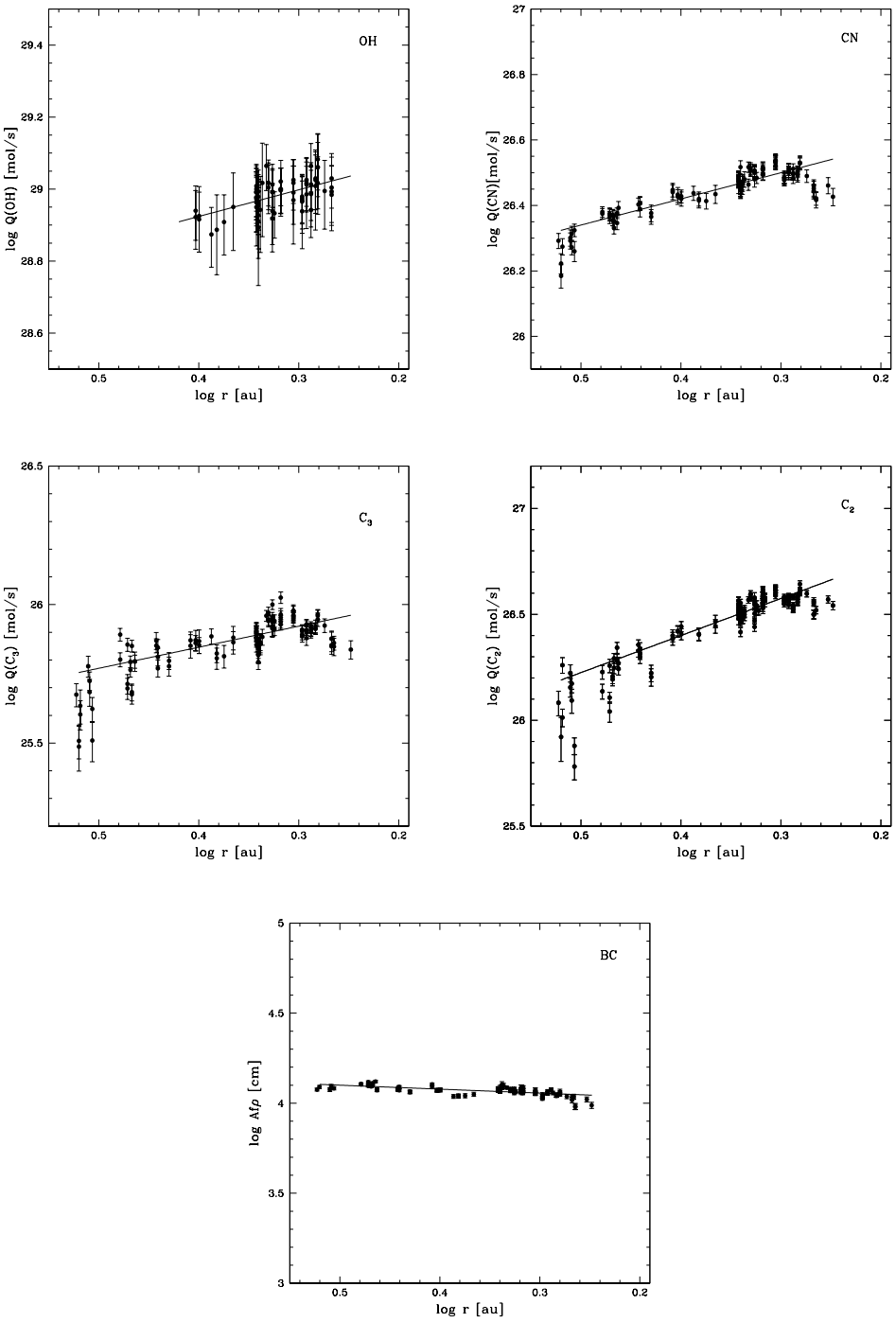


Figure 3.13: Comet C/2009 P1 (Garradd) OH, CN, $C_3$, and $C_2$ production rates and $A(0)f\rho$ as a function of the heliocentric distance ($r$). Full lines represent power-law fits of the production rates and $A(0)f\rho$ variation with the heliocentric distance.

similar. They increase from 3.3 au until approximately 2 au, reach a peak, and then start to decrease. Since we have less observations with the OH filter, we do not see the peak around 2 au, but we rather observe a plateau starting around 2 au. The comparison of the slopes given in Table 3.4 shows that they are similar for OH, CN, and $C_3$. The slope measured for the $C_2$, however, is steeper, indicating that the $C_2$ production rates increase faster than the production rates of other radicals while the comet approaches the Sun. The behaviour of the dust is different from the gas. The $A(0)f\rho$ slowly decreases from 3.3 au until the end of our observations at 1.8 au, and we do not see the peak of activity observed for the gas. This slow increase of gas production rates and decrease of the $A(0)f\rho$ as the comet approaches the Sun is usually characteristic of dynamically new comets. Even though Garradd is not a dynamically new comet, it is dynamically young, which means the comet has not entered the inner solar system a large number of times. This probably explains the similarity between the comet activity evolution and the behaviour of dynamically new comets.

Table 3.4: Comet C/2009 P1 (Garradd) fitted power-law slopes for OH, CN, $C_3$, and $C_2$ production rates and $A(0)f\rho$ heliocentric dependences.

| Species | r-dependence |
|---|---|
| OH | -0.74±0.12 |
| CN | -0.80±0.04 |
| $C_3$ | -0.76±0.08 |
| $C_2$ | -1.75±0.09 |
| $A(0)f\rho$ | +0.22±0.02 |

As mentioned previously, in late August and in September, we observed the comet for several hours during the same night. For these nights, we see variations of both gas and dust production rates of the order of a few to ten percents over the course of a few hours, caused by the rotation of the nucleus. We tried to analyse the CN and $C_2$ production rates lightcurves in order to determine the rotation period of comet Garradd nucleus. However, the temporal coverage of our observations is not sufficient to determine the rotation period of the comet. The rotation period of comet Garradd nucleus was measured by Farnham et al. (2012) from observations with the Deep Impact spacecraft made between February 20 and April 8, 2012. They observed variations of 4% of the CN production rate, of similar amplitude to those observed with TRAPPIST, and were able to determine a rotation period of $10.40 \pm 0.05$ hours.

Combi et al. (2013) observed comet Garradd with the SWAN instrument onboard SOHO from August 15, 2011 to April 6, 2012. They observe a peak of the comet water production rate around November 3 ($Q(H_2O) = 4 \times 10^{29}$ mol/s, $r = 1.70$ au) and report that the comet is less active after the perihelion passage. They observe the same plateau between 2 and 1.7 au pre-perihelion as we observed in the TRAPPIST OH production rates. Combi et al. (2013) report an increase of water production rates from $(1.13 \pm 0.08) \times 10^{29}$ mol/s to $(2.70 \pm 0.03) \times 10^{29}$ mol/s between 2.32 and 1.8 au. Bodewits et al. (2014) observe a similar increase from $(8.5 \pm 0.6) \times 10^{28}$ mol/s to (1.9±

0.03) × $10^{29}$ mol/s between approximately the same heliocentric distances from observations with UVOT onboard Swift. The OH production rates measured with TRAPPIST can be used to estimate the vectorial-equivalent water production rate (Cochran and Schleicher, 1993). Our values range from $(8.54 \pm 0.6) \times 10^{28}$ mol/s to $(1.00 \pm 0.19) \times 10^{29}$ mol/s. The increase we measure is lower than reported by Combi et al. (2013) and Bodewits et al. (2014) but the distance at which we adjust the Haser model is much lower than the SWAN and UVOT fields of view. Villanueva et al. (2012) and McKay et al. (2015) also report measurements of water production rates made with NIRSPEC at Keck II and CSHELL at IRTF at 2.1, 2, and 1.85 au pre-perihelion: $(8.62 \pm 0.65) \times 10^{28}$, $(1.41 \pm 0.38) \times 10^{29}$, and $(1.64 \pm 0.99) \times 10^{29}$ mol/s respectively. These values are consistent with our measurements. Large discrepancies between water production rates computed from instruments with different aperture sizes, especially between 2 and 3 au pre-perihelion, are reported by several authors (Combi et al., 2013; Paganini et al., 2012; Bodewits et al., 2014). This implies that between 2 and 3 au pre-perihelion, part of the water should be released by an extended source, probably icy grains. They report that it does not seem to be the case anymore after the perihelion passage.

### 3.2.2 Composition

We computed production rate ratios to follow the evolution of the coma composition with the heliocentric distance. These production rate ratios are represented in Fig 3.14. We also fitted power-law slopes to represent the heliocentric dependence of the ratios (Table 3.5) and to detect more easily changes of the coma composition. We do not see large variations of the OH to CN and $C_3$ to CN ratios while the comet approaches the Sun. The $C_2$ to CN ratio increases regularly with decreasing heliocentric distances. This is similar to what we observed for comet 103P/ Hartley 2 post-perihelion. Because of this variation of the $C_2$ to CN ratio with the heliocentric distance, comet Garradd can be classified as carbon-chain depleted comet according to A'Hearn et al. (1995) ($log(Q(C_2)/Q(CN)) < -0.18$) at large heliocentric distances ($r > 3$ au). At smaller heliocentric distances, it is a typical comet. We also follow the evolution of the dust to gas ratio. It is decreasing with decreasing heliocentric distances, which means that the comet becomes less dusty as it approaches the Sun. Bodewits et al. (2014) noticed a similar trend in their pre-perihelion data.

Table 3.5: Fitted power-law slopes for the heliocentric dependence of comet C/2009 P1 (Garradd) OH, $C_3$, $C_2$, and $A(0)f\rho$ to CN ratios pre-perihelion.

| Species | r-dependence |
|---|---|
| log[Q(OH)/Q(CN)] | -0.20±0.12 |
| log[Q($C_3$)/Q(CN)] | -0.03±0.05 |
| log[Q($C_2$)/Q(CN)] | -1.16±0.07 |
| log[Q($A(0)f\rho$)/Q(CN)] | +1.01±0.04 |

We computed the dust colour from the $A(0)f\rho$ values measured in the BC and GC filters. The

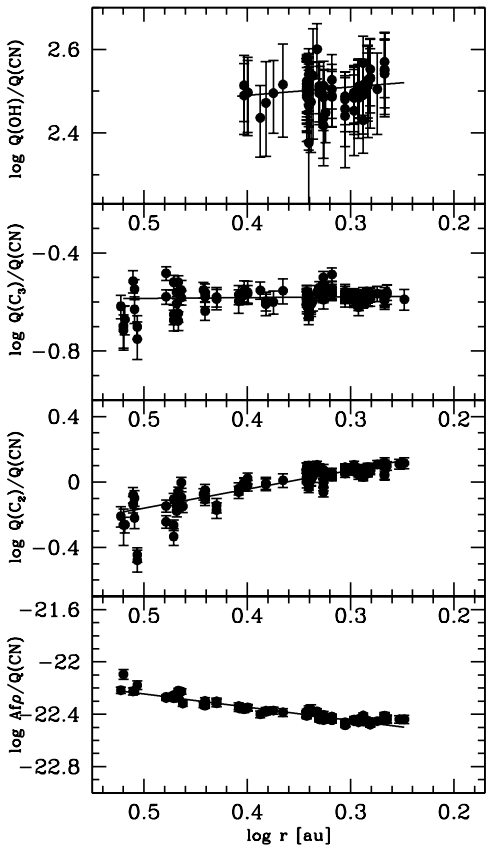


Figure 3.14: Comet C/2009 P1 (Garradd) OH, $C_3$, $C_2$, and $A(0)f\rho$ to CN production rate ratios as a function of the heliocentric distance. Full lines represent power-law fits of the ratio variations with the heliocentric distance.

evolution of the dust colour with the heliocentric distance is represented in Fig. 3.15. The wavelengths of the two filters are close to each other (BC at 445 nm and GC at 526 nm) and the accuracy of the colour measurements is low. This might explain the dispersion of the colour values in Fig. 3.15. We measure a mean value of 4.85 %/1000 Å for our observations. We do not see any variation of the colour with the heliocentric distance within our data.

Candidate parent species for CN and $C_2$ have also been observed in the infrared. Paganini et al. (2012) and Villanueva et al. (2012) measure upper limits for the $C_2H_2$ production rates of $1.1 \times 10^{26}$ mol/s and $0.85 \times 10^{26}$ mol/s at 2 and 2.1 au pre-perihelion, respectively. At these distances, the $C_2$ production rates we measure with TRAPPIST are of $(4.09 \pm 0.13) \times 10^{26}$ and $(3.30 \pm 0.16) \times 10^{26}$ mol/s. The $C_2H_2$ abundance is thus not sufficient to account for the $C_2$ production rates we measure. This means that part of the $C_2$ is probably released by another parent or by organic-rich grains in the coma. $C_2H_6$ is detected in the coma of comet Garradd in much larger abundances than $C_2H_2$ (Paganini et al., 2012; Villanueva et al., 2012), but

$C_2H_6$ is not efficient to release $C_2$. The same authors also measure HCN production rates of $(3.1 \pm 0.3) \times 10^{26}$ and $(2.44 \pm 0.15) \times 10^{26}$ mol/s at 2.1 and 2.0 au, almost consistent within the error bars with the CN production rates we measure at the same time. So, no additional parent or extended source is needed to explain CN abundances, and HCN is probably the main CN precursor in the coma of comet Garradd.

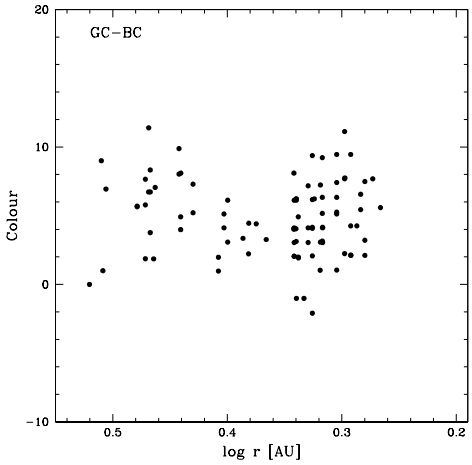


Figure 3.15: Evolution of comet C/2009 P1 (Garradd) dust colour as a function of the heliocentric distance.

### 3.2.3 Morphology

After removing an azimuthal median profile from every image, we studied the morphology of comet Garradd coma. We show a representative result from September 19, 2011 on Fig. 3.16. We do not see any morphological features in the OH, $C_3$, or $C_2$ filters in Fig. 3.16 nor in any other observation made with those filters. The CN image has an hourglass shape, with two jets in opposite directions around PA 10° and 190°. These two jets are visible from late August and their position slightly varies with the changing geometry of the system. We can not detect any variation of the jets shape or strength with the rotation of the nucleus for the nights we were able to observe the comet for several hours in a row. We also observe a strong dust jet in the sunward direction along with a dust enhancement in the direction of the tail. This type of dust morphology is observed since July 2011. Before that, we can only detect one strong jet whose direction is difficult to determine because of its wideness and small spatial extent. The strong sunward dust jet might coincide with the strong excess of water in the direction of the Sun observed by Paganini et al. (2014a).

### 3.2.4 Summary

We observed comet Garradd between 3.3 and 1.8 au before it reached perihelion. The gas production rates of the comet, except for the $C_2$, are increasing very slowly as it approaches

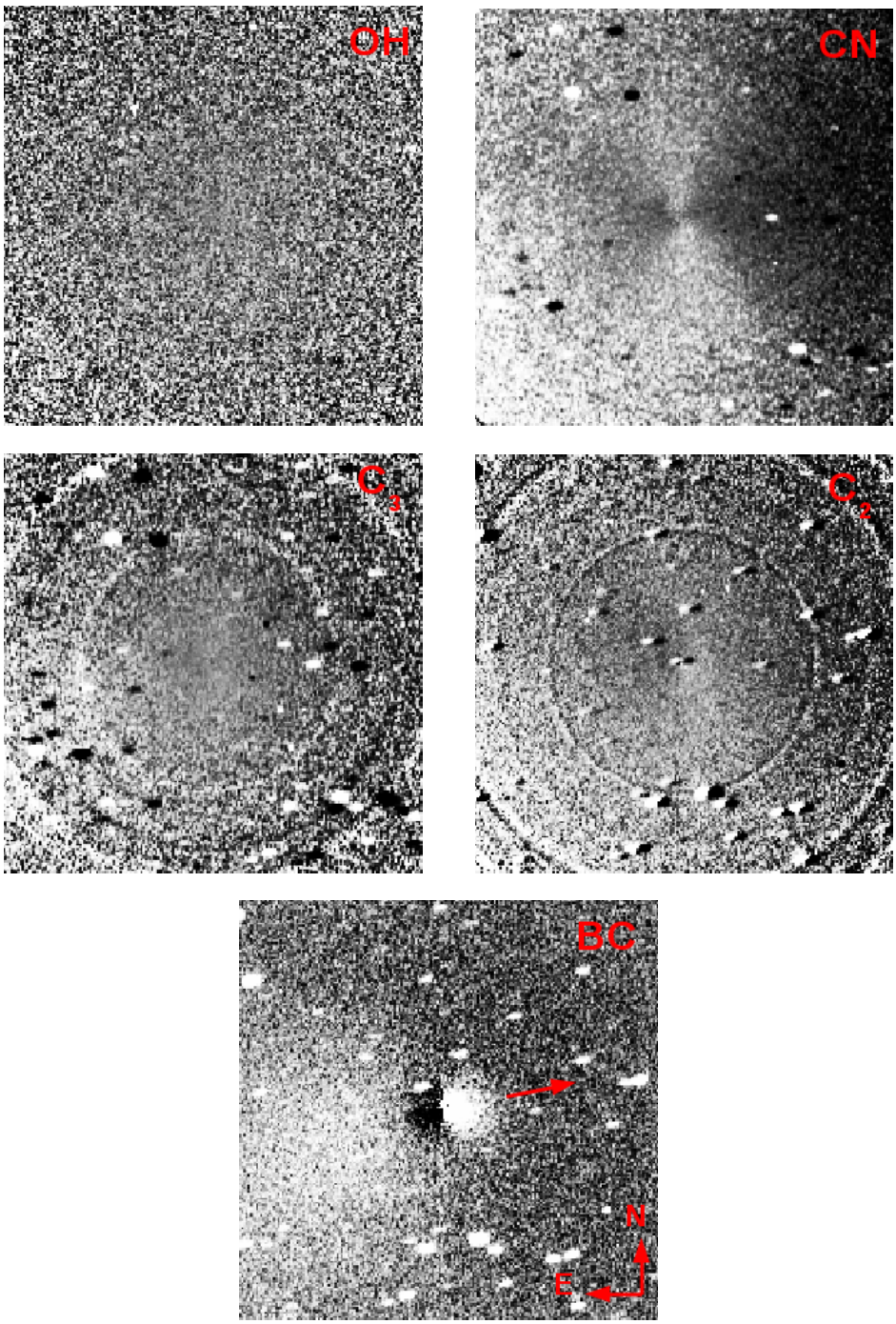


Figure 3.16: C/2009 P1 (Garradd) OH, CN, $C_3$, $C_2$, and dust from BC filter images from September 19, 2011 processed by dividing by an azimuthal median profile. All images are oriented with north up and east left. The field of view is $4.3' \times 4.3'$. The arrow indicates the direction of the Sun. The circles in the images are artefacts due to a bright star in the field of view.

the Sun while the $A(0)f\rho$ is decreasing with decreasing heliocentric distances. This behaviour is typical of dynamically new comets (or dynamically young in the case of comet Garradd) and will be further analysed and discussed in Chapter 4. We observed an increase of the $C_2$ to CN ratio and a decrease of the dust to gas ratio as the comet is approaching the Sun. We measured a mean dust colour of 4.85 %/1000 Å and we could not see any strong trend of the colour with the heliocentric distance.

## 3.3 C/2012 F6 (Lemmon)

The results presented in this Section are based on Opitom et al. (2015a). Differences between the production rates presented here and those from Opitom et al. (2015a) might exist, since we updated our calibration and dust subtraction procedure. However, it does not impact any of the results we present.

Comet C/2012 F6 (Lemmon) (hereafter comet Lemmon) was discovered by A. R. Gibbs on March 23, 2012 at the Mount Lemmon observatory, when it was at approximately 5 au from the Sun. It remained weak until it was lost because of Sun conjunction in June 2012. When the comet was recovered in October it had brightened by -4 magnitude, reaching mag 15. In January and February 2013, the comet was observable several hours per night from the southern hemisphere. Comet Lemmon follows a highly eccentric and inclined orbit with a perihelion distance of 0.73 au (March 24, 2013). It is a long-period comet (around 10000 years) originating from the Oort Cloud that has already entered the inner solar system many times. In December 2012, the comet was unexpectedly bright, allowing us to start an intensive monitoring of its activity through narrow band filters.

### 3.3.1 Activity

One thousand three hundred and fifty-eight images of comet Lemmon were collected on 52 nights spanning over 6 months both pre- and post-perihelion. We started the observations as soon as the comet was bright enough on December 11, 2012, at about 2 au from the Sun, and we observed two to three times a week until January 13, 2013. A technical problem suspended the observations between January 13 and February 7. We were able to follow the comet pre-perihelion until it was too close to the Sun on March 4. We then recovered it on April 29 and observed it until June 11 at a heliocentric distance of 1.6 au, after which the comet was too far north to be observed from La Silla. Exposure times ranged from 15 to 90 seconds for broad band filters and from 60 to 480 seconds for narrow band filters. Most observing nights were photometric and cloudy nights were discarded from the final data set. Observational circumstances and number of exposures per filter are given in Table 3.6.

Table 3.6: Observational circumstances of comet C/2012 F6 (Lemmon).

| UT Date | r | Δ | ṙ | Phase | Sun | Number of observations | | | | | | | | | | | | |
|---|---|---|---|---|---|---|---|---|---|---|---|---|---|---|---|---|---|---|
| | (au) | (au) | (km s$^{-1}$) | Angle (°) | PA (°) | OH | NH | CN | $C_3$ | $C_2$ | UC | BC | GC | RC | B | V | R | I |
| 2012 Dec 11.30-11.35 | -1.95 | 1.97 | -23.8 | 29.1 | 289.0 | 1 | | 1 | 1 | 1 | | 1 | 1 | 1 | | | | |
| 2012 Dec 15.26-15.34 | -1.89 | 1.87 | -24.0 | 30.3 | 289.7 | 1 | | 1 | 1 | 1 | | 1 | 1 | 1 | | | | |
| 2012 Dec 19.28-19.33 | -1.84 | 1.76 | -24.1 | 31.6 | 290.5 | 1 | | 1 | 1 | 1 | | | 1 | | | | | |
| 2012 Dec 20.24-20.34 | -1.82 | 1.74 | -24.1 | 31.9 | 290.7 | | 2 | 1 | 2 | 2 | | 2 | 3 | 2 | | | | |
| 2012 Dec 22.31-22.35 | -1.80 | 1.69 | -24.2 | 32.6 | 291.2 | 1 | 1 | 1 | 1 | | | | 2 | 1 | | | | |
| 2012 Dec 28.22-28.35 | -1.71 | 1.54 | -24.3 | 34.7 | 292.8 | 2 | 2 | 2 | 2 | 2 | | 2 | 2 | 2 | 1 | 1 | 1 | 1 |
| 2012 Dec 31.30-28.35 | -1.67 | 1.47 | -24.4 | 35.8 | 293.7 | 1 | 1 | 1 | 1 | 1 | 1 | 1 | 1 | 1 | | | | |
| 2013 Jan 5.27-5.34 | -1.60 | 1.47 | -24.5 | 37.8 | 295.4 | 1 | 1 | 1 | 1 | 1 | 1 | 1 | 1 | 1 | | | | |
| 2013 Jan 7.17-7.34 | -1.57 | 1.31 | -24.5 | 38.6 | 296.1 | 2 | 1 | 12 | 2 | 2 | 1 | 2 | 2 | 1 | | | | |
| 2013 Jan 13.18-13.35 | -1.49 | 1.20 | -24.6 | 41.3 | 298.3 | 3 | 3 | 12 | 2 | 12 | | 1 | | | 2 | 2 | 2 | 2 |
| 2013 Feb 7.16-7.38 | -1.13 | 0.99 | -23.6 | 54.9 | 178.1 | 7 | 7 | 13 | 7 | 6 | 5 | 6 | 3 | 6 | | | | |
| 2013 Feb 9.21-9.28 | -1.11 | 0.99 | -23.3 | 55.8 | 160.5 | 2 | 1 | 3 | 2 | 2 | | 2 | 2 | | 3 | 3 | 3 | 3 |
| 2013 Feb 12.03-12.33 | -1.07 | 1.00 | -22.9 | 56.8 | 152.6 | 11 | 11 | 22 | 11 | 11 | 11 | 11 | 11 | 11 | 13 | 13 | 10 | 10 |
| 2013 Feb 13.02-13.05 | -1.06 | 1.01 | -22.7 | 57.1 | 151.6 | 1 | 1 | 1 | 1 | 1 | 1 | 1 | 1 | 1 | 1 | 1 | 1 | 1 |
| 2013 Feb 14.02-14.31 | -1.04 | 1.01 | -22.5 | 57.4 | 150.7 | 12 | 13 | 25 | 13 | 12 | 12 | 12 | 12 | 12 | 14 | 14 | 14 | 14 |
| 2013 Feb 17.05-17.15 | -1.01 | 1.04 | -21.9 | 57.9 | 149.6 | 6 | 6 | 12 | 6 | 6 | 6 | 6 | 6 | 6 | | | | |
| 2013 Feb 19.02-19.06 | -0.98 | 1.05 | -21.4 | 58.0 | 149.7 | 2 | 2 | 4 | 2 | 2 | 2 | 2 | 2 | 2 | | | | |
| 2013 Feb 21.03-21.05 | -0.96 | 1.07 | -20.9 | 58.0 | 150.0 | 1 | 1 | 2 | 1 | 1 | 1 | 1 | 1 | 1 | | | | |
| 2013 Feb 23.03-23.05 | -0.93 | 1.10 | -20.3 | 57.8 | 150.5 | 1 | | 2 | 1 | 1 | | 1 | 1 | 1 | | | | |
| 2013 Feb 25.02-25.03 | -0.91 | 1.12 | -19.5 | 57.4 | 151.3 | 1 | 1 | 2 | 1 | 1 | 1 | 1 | 1 | 1 | | | | |
| 2013 Feb 26.02-26.05 | -0.90 | 1.13 | -19.2 | 57.1 | 151.7 | 1 | 1 | 2 | 1 | 1 | 1 | 1 | 1 | 1 | 3 | 3 | 3 | 3 |
| 2013 Feb 27.01-27.03 | -0.89 | 1.14 | -18.8 | 56.8 | 152.2 | 1 | 1 | 2 | 1 | 1 | 1 | 1 | 1 | 1 | 3 | 3 | 3 | 3 |
| 2013 Feb 28.01-28.04 | -0.88 | 1.15 | -18.3 | 56.4 | 152.7 | 1 | 2 | 3 | 1 | 1 | 1 | 1 | 1 | 1 | 3 | 3 | 3 | 3 |
| 2013 Mar 2.01-2.03 | -0.86 | 1.18 | -17.4 | 55.6 | 153.9 | 1 | 1 | 2 | 1 | 1 | 1 | 1 | 1 | 1 | 3 | 3 | 3 | 3 |
| 2013 Mar 3.01-3.03 | -0.85 | 1.19 | -16.9 | 55.1 | 154.5 | 2 | 1 | 3 | 1 | 1 | 1 | 1 | 1 | 1 | 3 | 3 | 3 | 3 |
| 2013 Mar 4.01-4.03 | -0.84 | 1.21 | -16.3 | 54.5 | 155.3 | | 1 | 2 | 1 | 1 | 1 | 1 | 1 | | 3 | 3 | 3 | 3 |
| 2013 Apr 29.42-29.43 | 1.01 | 1.70 | 22.0 | 32.7 | 254.3 | 1 | | 1 | 1 | 1 | | 1 | 1 | | | | | |
| 2013 May 3.42-3.43 | 1.06 | 1.71 | 22.8 | 33.5 | 257.7 | 1 | 1 | 1 | | 1 | | 1 | | | 1 | 1 | 1 | 1 |
| 2013 May 5.42-5.43 | 1.09 | 1.71 | 23.1 | 33.9 | 259.0 | 1 | | | | | 1 | | 1 | 1 | 1 | 1 | 1 | 1 |
| 2013 May 6.42-6.43 | 1.10 | 1.71 | 23.3 | 34.0 | 259.6 | 1 | 1 | 1 | 1 | 1 | 1 | 1 | 1 | 1 | 1 | 1 | 1 | 1 |
| 2013 May 7.42-7.43 | 1.12 | 1.71 | 23.4 | 34.2 | 260.2 | | | | | | | | | | 3 | 3 | 4 | 3 |
| 2013 May 8.42-8.43 | 1.13 | 1.72 | 23.5 | 34.4 | 260.7 | | | | | | | | | | 2 | 2 | 2 | 2 |
| 2013 May 9.42-9.43 | 1.14 | 1.72 | 23.6 | 34.5 | 261.2 | | | | | | | | | | 2 | 2 | 2 | 1 |
| 2013 May 10.42-10.43 | 1.16 | 1.72 | 23.7 | 34.6 | 261.6 | | 1 | 1 | 1 | 1 | | | | | | | | |
| 2013 May 11.42-11.43 | 1.17 | 1.72 | 23.8 | 34.8 | 262.0 | 1 | 1 | 1 | 1 | 1 | 1 | 1 | 1 | 1 | | | | |
| 2013 May 14.42-14.43 | 1.21 | 1.72 | 24.1 | 35.1 | 263.1 | 1 | 1 | 1 | 1 | 1 | 1 | 1 | 1 | 1 | 1 | 1 | 1 | 1 |
| 2013 May 16.41-16.43 | 1.24 | 1.73 | 24.2 | 35.3 | 263.6 | 1 | 1 | 1 | 1 | 1 | 1 | 1 | 1 | 1 | 1 | 1 | 1 | 1 |
| 2013 May 20.42-20.44 | 1.30 | 1.73 | 20.4 | 35.5 | 264.3 | 1 | 1 | 1 | 1 | 1 | | 1 | 1 | 1 | 1 | 1 | 1 | 1 |
| 2013 May 22.42-20.43 | 1.33 | 1.73 | 24.5 | 35.6 | 264.5 | 1 | 1 | 1 | 1 | 1 | 1 | 1 | 1 | 1 | 1 | 1 | 1 | 1 |
| 2013 May 23.42-23.43 | 1.34 | 1.74 | 24.5 | 35.6 | 264.5 | 1 | 1 | 1 | 1 | 1 | 1 | 1 | 1 | 1 | 1 | 1 | 1 | 1 |
| 2013 May 24.43-24.44 | 1.35 | 1.74 | 24.5 | 35.6 | 264.6 | | | | | 1 | | | | 1 | 1 | 1 | 1 | 1 |
| 2013 May 25.42-25.43 | 1.37 | 1.74 | 24.5 | 35.6 | 264.6 | 1 | 1 | 1 | 1 | 1 | 1 | 1 | 1 | 1 | 1 | 1 | 1 | 1 |
| 2013 May 26.42-26.43 | 1.38 | 1.74 | 24.6 | 35.6 | 264.6 | 1 | 1 | 1 | 1 | 1 | | 1 | 1 | 1 | 1 | 1 | 1 | 1 |
| 2013 May 29.41-29.43 | 1.42 | 1.74 | 24.6 | 35.6 | 264.4 | 1 | | 1 | 1 | 1 | 1 | | 1 | 1 | | 1 | | |
| 2013 May 30.41-30.42 | 1.44 | 1.74 | 24.6 | 35.5 | 264.2 | 1 | 1 | 2 | 2 | 2 | 1 | 1 | 2 | | 1 | 1 | 1 | 1 |
| 2013 Jun 2.41-2.44 | 1.48 | 1.75 | 24.6 | 35.4 | 263.8 | 1 | 1 | 3 | 2 | 3 | 1 | 1 | 3 | 3 | 2 | 2 | 2 | 2 |
| 2013 Jun 4.41-4.44 | 1.51 | 1.75 | 24.6 | 35.3 | 263.3 | 2 | 1 | 2 | 1 | 3 | 1 | 1 | 3 | 3 | 2 | 2 | 2 | 2 |
| 2013 Jun 5.42-5.44 | 1.52 | 1.75 | 24.6 | 35.2 | 263.1 | 1 | 1 | 1 | 1 | 1 | 1 | 1 | 1 | 1 | 1 | 1 | 1 | 1 |
| 2013 Jun 6.41-6.44 | 1.54 | 1.76 | 24.6 | 35.1 | 262.8 | | 1 | 2 | 1 | 3 | 1 | 1 | 2 | 3 | 3 | 2 | 2 | 2 |
| 2013 Jun 11.42-11.44 | 1.61 | 1.77 | 24.5 | 34.6 | 261.1 | 1 | | 1 | 1 | 1 | | 1 | 1 | 1 | | | | |

r and ṙ are the heliocentric distance and velocity. Δ is the geocentric distance. Phase and position angles are given for the midtime of each observing run. Number of observations in every filter are given in the last columns.

### Gas

The gas production rates have been computed from each frame taken in the gas filters and nightly means are given in Table 3.7. The evolution of comet Lemmon gas activity vs heliocentric distance is summarized in Fig. 3.17. The comet activity rises as it approaches perihelion and then decreases after perihelion. As shown in Fig. 3.18, there is some dispersion in the production rates computed during the same night (at the same heliocentric distance). These variations larger than the error bars are observed for all the species and are attributed to the nucleus rotation (see Section 3.3.4). The detection in the images of jets whose position and orientation vary with the nucleus rotation further confirmed that the nightly variation was due to the nucleus rotation (see Section 3.3.4).

Each species' evolution as a function of the heliocentric distance is represented on a log-log scale in Fig. 3.18. Pre-perihelion data are represented with filled symbols and post-

Table 3.7: Nightly averages of gas production rates for comet C/2012 F6 (Lemmon).

| UT Date | | Q (mol $s^{-1}$) | | | | | |
|---|---|---|---|---|---|---|---|
| | r | OH | $H_2O$ | NH | CN | $C_3$ | $C_2$ |
| 2012 Dec 11 | -1.95 | $3.45 \pm 0.39\ 10^{28}$ | $3.45 \pm 0.39\ 10^{28}$ | | $9.62 \pm 0.26\ 10^{25}$ | $2.42 \pm 0.08\ 10^{25}$ | $9.88 \pm 0.33\ 10^{25}$ |
| 2012 Dec 15 | -1.89 | $3.42 \pm 0.40\ 10^{28}$ | $3.42 \pm 0.40\ 10^{28}$ | | $9.90 \pm 0.28\ 10^{25}$ | $2.53 \pm 0.09\ 10^{25}$ | $1.07 \pm 0.03\ 10^{26}$ |
| 2012 Dec 19 | -1.84 | $4.21 \pm 0.44\ 10^{28}$ | $4.22 \pm 0.44\ 10^{28}$ | | $1.13 \pm 0.03\ 10^{26}$ | $2.82 \pm 0.10\ 10^{25}$ | $1.25 \pm 0.03\ 10^{26}$ |
| 2012 Dec 20 | -1.82 | | | $2.69 \pm 0.25\ 10^{26}$ | $1.17 \pm 0.03\ 10^{26}$ | $2.91 \pm 0.10\ 10^{25}$ | $1.30 \pm 0.03\ 10^{26}$ |
| 2012 Dec 22 | -1.80 | $4.50 \pm 0.47\ 10^{28}$ | $4.56 \pm 0.48\ 10^{28}$ | $2.66 \pm 0.22\ 10^{26}$ | $1.27 \pm 0.03\ 10^{26}$ | $3.02 \pm 0.07\ 10^{25}$ | |
| 2012 Dec 28 | -1.71 | $5.27 \pm 0.57\ 10^{28}$ | $5.48 \pm 0.59\ 10^{28}$ | $3.82 \pm 0.33\ 10^{26}$ | $1.39 \pm 0.04\ 10^{26}$ | $3.97 \pm 0.14\ 10^{25}$ | $1.72 \pm 0.04\ 10^{26}$ |
| 2012 Dec 31 | -1.67 | $5.47 \pm 0.49\ 10^{28}$ | $5.76 \pm 0.52\ 10^{28}$ | $3.99 \pm 0.36\ 10^{26}$ | $1.51 \pm 0.04\ 10^{26}$ | $4.21 \pm 0.11\ 10^{25}$ | $1.95 \pm 0.04\ 10^{26}$ |
| 2013 Jan 5 | -1.60 | $5.88 \pm 0.52\ 10^{28}$ | $6.33 \pm 0.56\ 10^{28}$ | $4.40 \pm 0.26\ 10^{26}$ | $1.56 \pm 0.03\ 10^{26}$ | $4.34 \pm 0.11\ 10^{25}$ | $2.06 \pm 0.03\ 10^{26}$ |
| 2013 Jan 7 | -1.57 | $6.38 \pm 0.69\ 10^{28}$ | $6.93 \pm 0.75\ 10^{28}$ | $5.17 \pm 0.36\ 10^{26}$ | $1.67 \pm 0.05\ 10^{26}$ | $4.90 \pm 0.13\ 10^{25}$ | $2.34 \pm 0.04\ 10^{26}$ |
| 2013 Jan 13 | -1.49 | $7.48 \pm 0.80\ 10^{28}$ | $8.34 \pm 0.89\ 10^{28}$ | $6.23 \pm 0.41\ 10^{26}$ | $1.89 \pm 0.05\ 10^{26}$ | $5.78 \pm 0.15\ 10^{25}$ | $2.95 \pm 0.05\ 10^{26}$ |
| 2013 Feb 7 | -1.13 | $1.16 \pm 0.22\ 10^{29}$ | $1.49 \pm 0.28\ 10^{29}$ | $9.58 \pm 0.78\ 10^{26}$ | $3.17 \pm 0.14\ 10^{26}$ | $1.06 \pm 0.04\ 10^{26}$ | $6.06 \pm 0.14\ 10^{26}$ |
| 2013 Feb 9 | -1.11 | $1.39 \pm 0.31\ 10^{29}$ | $1.80 \pm 0.40\ 10^{29}$ | $1.25 \pm 0.12\ 10^{27}$ | $3.71 \pm 0.19\ 10^{26}$ | $1.15 \pm 0.05\ 10^{26}$ | $6.68 \pm 0.14\ 10^{26}$ |
| 2013 Feb 12 | -1.07 | $1.65 \pm 0.41\ 10^{29}$ | $2.17 \pm 0.54\ 10^{29}$ | $1.39 \pm 0.15\ 10^{27}$ | $4.19 \pm 0.23\ 10^{26}$ | $1.29 \pm 0.06\ 10^{26}$ | $7.63 \pm 0.18\ 10^{26}$ |
| 2013 Feb 13 | -1.06 | $1.68 \pm 0.12\ 10^{29}$ | $2.35 \pm 0.16\ 10^{29}$ | $1.51 \pm 0.12\ 10^{27}$ | $4.40 \pm 0.20\ 10^{26}$ | $1.39 \pm 0.05\ 10^{26}$ | $7.95 \pm 0.14\ 10^{26}$ |
| 2013 Feb 14 | -1.04 | $1.78 \pm 0.50\ 10^{29}$ | $2.38 \pm 0.68\ 10^{29}$ | $1.56 \pm 0.19\ 10^{27}$ | $4.58 \pm 0.28\ 10^{26}$ | $1.36 \pm 0.08\ 10^{26}$ | $8.29 \pm 0.22\ 10^{26}$ |
| 2013 Feb 17 | -1.01 | $2.25 \pm 0.63\ 10^{29}$ | $3.05 \pm 0.85\ 10^{29}$ | $1.88 \pm 0.23\ 10^{27}$ | $5.41 \pm 0.32\ 10^{26}$ | $1.67 \pm 0.09\ 10^{26}$ | $9.80 \pm 0.25\ 10^{26}$ |
| 2013 Feb 19 | -0.98 | $2.11 \pm 0.38\ 10^{29}$ | $2.90 \pm 0.52\ 10^{29}$ | $1.77 \pm 0.15\ 10^{27}$ | $5.54 \pm 0.26\ 10^{26}$ | $1.70 \pm 0.07\ 10^{26}$ | $9.73 \pm 0.19\ 10^{26}$ |
| 2013 Feb 21 | -0.96 | $2.27 \pm 0.45\ 10^{29}$ | $3.15 \pm 0.63\ 10^{29}$ | $1.94 \pm 0.17\ 10^{27}$ | $6.29 \pm 0.30\ 10^{26}$ | $2.00 \pm 0.08\ 10^{26}$ | $1.10 \pm 0.02\ 10^{27}$ |
| 2013 Feb 23 | -0.93 | $2.07 \pm 0.43\ 10^{29}$ | $2.92 \pm 0.61\ 10^{29}$ | | $6.16 \pm 0.31\ 10^{26}$ | $1.91 \pm 0.09\ 10^{26}$ | $1.08 \pm 0.02\ 10^{27}$ |
| 2013 Feb 25 | -0.91 | $2.50 \pm 0.53\ 10^{29}$ | $3.57 \pm 0.76\ 10^{29}$ | $2.21 \pm 0.21\ 10^{27}$ | $7.47 \pm 0.36\ 10^{26}$ | $2.36 \pm 0.10\ 10^{26}$ | $1.30 \pm 0.03\ 10^{27}$ |
| 2013 Feb 26 | -0.90 | $2.45 \pm 0.54\ 10^{29}$ | $3.51 \pm 0.77\ 10^{29}$ | $2.12 \pm 0.21\ 10^{27}$ | $7.46 \pm 0.37\ 10^{26}$ | $2.34 \pm 0.11\ 10^{26}$ | $1.32 \pm 0.03\ 10^{27}$ |
| 2013 Feb 27 | -0.89 | $2.40 \pm 0.52\ 10^{29}$ | $3.46 \pm 0.75\ 10^{29}$ | $2.15 \pm 0.20\ 10^{27}$ | $7.55 \pm 0.36\ 10^{26}$ | $2.28 \pm 0.10\ 10^{26}$ | $1.32 \pm 0.03\ 10^{27}$ |
| 2013 Feb 28 | -0.88 | $2.53 \pm 0.57\ 10^{29}$ | $3.67 \pm 0.83\ 10^{29}$ | $2.20 \pm 0.24\ 10^{27}$ | $8.13 \pm 0.43\ 10^{26}$ | $2.34 \pm 0.11\ 10^{26}$ | $1.39 \pm 0.03\ 10^{27}$ |
| 2013 Mar 2 | -0.86 | $2.20 \pm 0.53\ 10^{29}$ | $3.23 \pm 0.78\ 10^{29}$ | $1.93 \pm 0.20\ 10^{27}$ | $8.15 \pm 0.43\ 10^{26}$ | $2.42 \pm 0.13\ 10^{26}$ | $1.38 \pm 0.03\ 10^{27}$ |
| 2013 Mar 3 | -0.85 | $2.70 \pm 0.84\ 10^{29}$ | $3.99 \pm 1.24\ 10^{29}$ | $2.23 \pm 0.24\ 10^{27}$ | $9.16 \pm 0.55\ 10^{26}$ | $2.59 \pm 0.14\ 10^{26}$ | $1.52 \pm 0.04\ 10^{27}$ |
| 2013 Mar 4 | -0.84 | | | $2.03 \pm 0.23\ 10^{27}$ | $8.91 \pm 0.53\ 10^{26}$ | $2.55 \pm 0.15\ 10^{26}$ | $1.51 \pm 0.04\ 10^{27}$ |
| 2013 Apr 29 | 1.01 | $1.07 \pm 0.28\ 10^{29}$ | $1.45 \pm 0.38\ 10^{29}$ | | $4.49 \pm 0.25\ 10^{26}$ | $1.47 \pm 0.08\ 10^{26}$ | $7.89 \pm 0.23\ 10^{26}$ |
| 2013 May 3 | 1.06 | $1.05 \pm 0.25\ 10^{29}$ | $1.39 \pm 0.33\ 10^{29}$ | $1.32 \pm 0.14\ 10^{27}$ | $4.33 \pm 0.22\ 10^{26}$ | | $7.49 \pm 0.19\ 10^{26}$ |
| 2013 May 5 | 1.09 | $1.12 \pm 0.26\ 10^{29}$ | $1.46 \pm 0.34\ 10^{29}$ | | | | |
| 2013 May 6 | 1.10 | $1.01 \pm 0.23\ 10^{29}$ | $1.31 \pm 0.30\ 10^{29}$ | $1.32 \pm 0.13\ 10^{27}$ | $4.03 \pm 0.20\ 10^{26}$ | $1.22 \pm 0.06\ 10^{26}$ | $7.10 \pm 0.18\ 10^{26}$ |
| 2013 May 10 | 1.16 | | | $1.09 \pm 0.11\ 10^{27}$ | $3.35 \pm 0.17\ 10^{26}$ | $9.92 \pm 0.51\ 10^{25}$ | $5.88 \pm 0.15\ 10^{26}$ |
| 2013 May 11 | 1.17 | $9.06 \pm 0.20\ 10^{28}$ | $1.14 \pm 0.25\ 10^{29}$ | $1.27 \pm 0.13\ 10^{27}$ | $3.95 \pm 0.20\ 10^{26}$ | $1.19 \pm 0.06\ 10^{26}$ | $6.74 \pm 0.17\ 10^{26}$ |
| 2013 May 14 | 1.21 | $1.08 \pm 0.22\ 10^{29}$ | $1.34 \pm 0.27\ 10^{29}$ | $1.23 \pm 0.12\ 10^{27}$ | $3.78 \pm 0.18\ 10^{26}$ | $1.13 \pm 0.05\ 10^{26}$ | $6.25 \pm 0.15\ 10^{26}$ |
| 2013 May 16 | 1.24 | $9.45 \pm 0.21\ 10^{28}$ | $1.15 \pm 0.26\ 10^{29}$ | $1.04 \pm 0.11\ 10^{27}$ | $3.19 \pm 0.16\ 10^{26}$ | $1.03 \pm 0.05\ 10^{26}$ | $5.26 \pm 0.14\ 10^{26}$ |
| 2013 May 20 | 1.30 | $9.99 \pm 2.00\ 10^{28}$ | $1.19 \pm 0.24\ 10^{29}$ | $1.09 \pm 0.11\ 10^{27}$ | $3.21 \pm 0.15\ 10^{26}$ | $9.79 \pm 0.45\ 10^{25}$ | $5.20 \pm 0.13\ 10^{26}$ |
| 2013 May 22 | 1.33 | $8.99 \pm 1.87\ 10^{28}$ | $1.06 \pm 0.22\ 10^{29}$ | $9.33 \pm 0.96\ 10^{26}$ | $2.99 \pm 0.14\ 10^{26}$ | $9.13 \pm 0.43\ 10^{25}$ | $4.83 \pm 0.12\ 10^{26}$ |
| 2013 May 23 | 1.34 | $9.30 \pm 1.98\ 10^{28}$ | $1.09 \pm 0.23\ 10^{29}$ | $9.26 \pm 0.95\ 10^{26}$ | $3.04 \pm 0.14\ 10^{26}$ | $9.02 \pm 0.44\ 10^{26}$ | $4.66 \pm 0.12\ 10^{26}$ |
| 2013 May 25 | 1.37 | $8.29 \pm 1.85\ 10^{28}$ | $9.64 \pm 2.15\ 10^{28}$ | $8.43 \pm 0.99\ 10^{26}$ | $2.87 \pm 0.14\ 10^{26}$ | $8.32 \pm 0.50\ 10^{25}$ | $4.43 \pm 0.13\ 10^{26}$ |
| 2013 May 26 | 1.38 | $7.04 \pm 1.59\ 10^{28}$ | $8.16 \pm 1.84\ 10^{28}$ | $6.31 \pm 0.88\ 10^{26}$ | $2.40 \pm 0.12\ 10^{26}$ | $7.03 \pm 0.39\ 10^{25}$ | $3.65 \pm 0.11\ 10^{26}$ |
| 2013 May 29 | 1.42 | $6.25 \pm 1.52\ 10^{28}$ | $7.14 \pm 1.74\ 10^{28}$ | | $2.71 \pm 0.13\ 10^{26}$ | $8.94 \pm 0.41\ 10^{25}$ | $3.99 \pm 0.10\ 10^{26}$ |
| 2013 May 30 | 1.44 | $8.37 \pm 2.01\ 10^{28}$ | $9.49 \pm 2.28\ 10^{28}$ | $8.48 \pm 1.06\ 10^{26}$ | $2.69 \pm 0.14\ 10^{26}$ | $8.01 \pm 0.44\ 10^{25}$ | $3.99 \pm 0.12\ 10^{26}$ |
| 2013 Jun 2 | 1.48 | $6.75 \pm 1.71\ 10^{28}$ | $7.55 \pm 1.91\ 10^{28}$ | $7.44 \pm 0.99\ 10^{26}$ | $2.36 \pm 0.13\ 10^{26}$ | $6.59 \pm 0.42\ 10^{25}$ | $3.30 \pm 0.10\ 10^{26}$ |
| 2013 Jun 4 | 1.51 | $7.13 \pm 1.82\ 10^{28}$ | $7.90 \pm 2.03\ 10^{28}$ | $7.14 \pm 1.05\ 10^{26}$ | $2.40 \pm 0.13\ 10^{26}$ | $6.92 \pm 0.43\ 10^{25}$ | $3.45 \pm 0.11\ 10^{26}$ |
| 2013 Jun 5 | 1.52 | $7.20 \pm 1.74\ 10^{28}$ | $7.95 \pm 2.11\ 10^{28}$ | $6.81 \pm 0.81\ 10^{26}$ | $2.34 \pm 0.13\ 10^{26}$ | $6.52 \pm 0.37\ 10^{25}$ | $3.22 \pm 0.11\ 10^{26}$ |
| 2013 Jun 6 | 1.54 | | | $7.10 \pm 1.04\ 10^{26}$ | $2.29 \pm 0.14\ 10^{26}$ | $6.28 \pm 0.44\ 10^{25}$ | $3.14 \pm 0.11\ 10^{26}$ |
| 2013 Jun 11 | 1.61 | | | $5.66 \pm 0.95\ 10^{26}$ | $2.01 \pm 0.13\ 10^{26}$ | $5.77 \pm 0.43\ 10^{25}$ | $2.74 \pm 0.10\ 10^{26}$ |

The $H_2O$ production rate in this table is the vectorial-equivalent water production rate given by the relation: $Q(H_2O) = 1.361 r^{-0.5} Q(OH)$ (Cochran and Schleicher 1993).

perihelion data with open symbols. A least square power-law fit has been performed for each radical to study the evolution of the production rates with the heliocentric distance. We made two separate fits for pre- (solid lines) and post-perihelion (dotted lines) data to point out asymmetries around perihelion. Even though the heliocentric range covered post-perihelion is shorter than pre-perihelion, it is sufficient to derive a slope for the heliocentric dependence of the post-perihelion production rates. The best pre- and post-perihelion slopes are overplotted on the data in Fig. 3.18.

Examination of the power-law slopes given in Table 3.8 shows that the heliocentric dependence of the gas production rates is similar for all the species. There is an asymmetry about perihelion, the slope being steeper before than after perihelion and the production rates being in general higher after perihelion over the same distance, except for OH. A'Hearn et al. (1995) showed that the heliocentric dependence of the gas production rates strongly varies from comet to

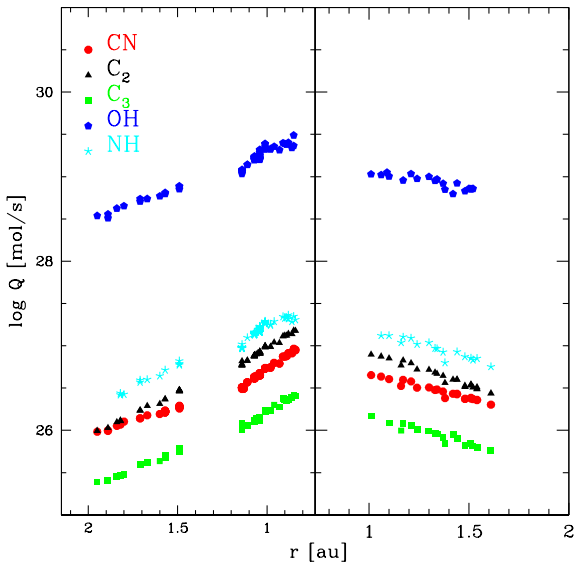


Figure 3.17: Logarithm of comet C/2012 F6 (Lemmon) OH, NH, CN, $C_3$, and $C_2$ production rates as a function of the heliocentric distance r (au). The x-axis is interrupted at perihelion (0.73 au).

comet. The average trend for their comet sample is $Q(\text{gas}) \propto r^{-2.7}$. Pre-perihelion slope values for comet Lemmon from Table 3.8 are in good agreement with this average trend.

Table 3.8: Comet C/2012 F6 (Lemmon) pre- and post-perihelion fitted power-law slopes for the heliocentric dependences of the OH, NH, CN, $C_3$, and $C_2$ production rates.

| Species | r-dependence | |
|---|---|---|
| | pre-perihelion | post-perihelion |
| OH | -2.48±0.05 | -1.20±0.20 |
| NH | -2.70±0.09 | -1.97±0.20 |
| CN | -2.59±0.04 | -1.70±0.11 |
| $C_3$ | -2.82±0.04 | -1.90±0.16 |
| $C_2$ | -3.17±0.04 | -2.32±0.13 |

### Dust

The use of narrow band continuum filters at four wavelengths allows us to make a study of the evolution of both dust production and properties along the orbit of the comet. In addition to what was done in Opitom et al. (2015a), we corrected the $Af\rho$ values from the phase angle effect. This will facilitate the direct comparison of the comet dust activity with the activity of other comets presented in this work. Since we corrected the $Af\rho$ from the phase angle effect, the values presented in Table 3.9 and the slopes given in Table 3.10 are different from Opitom

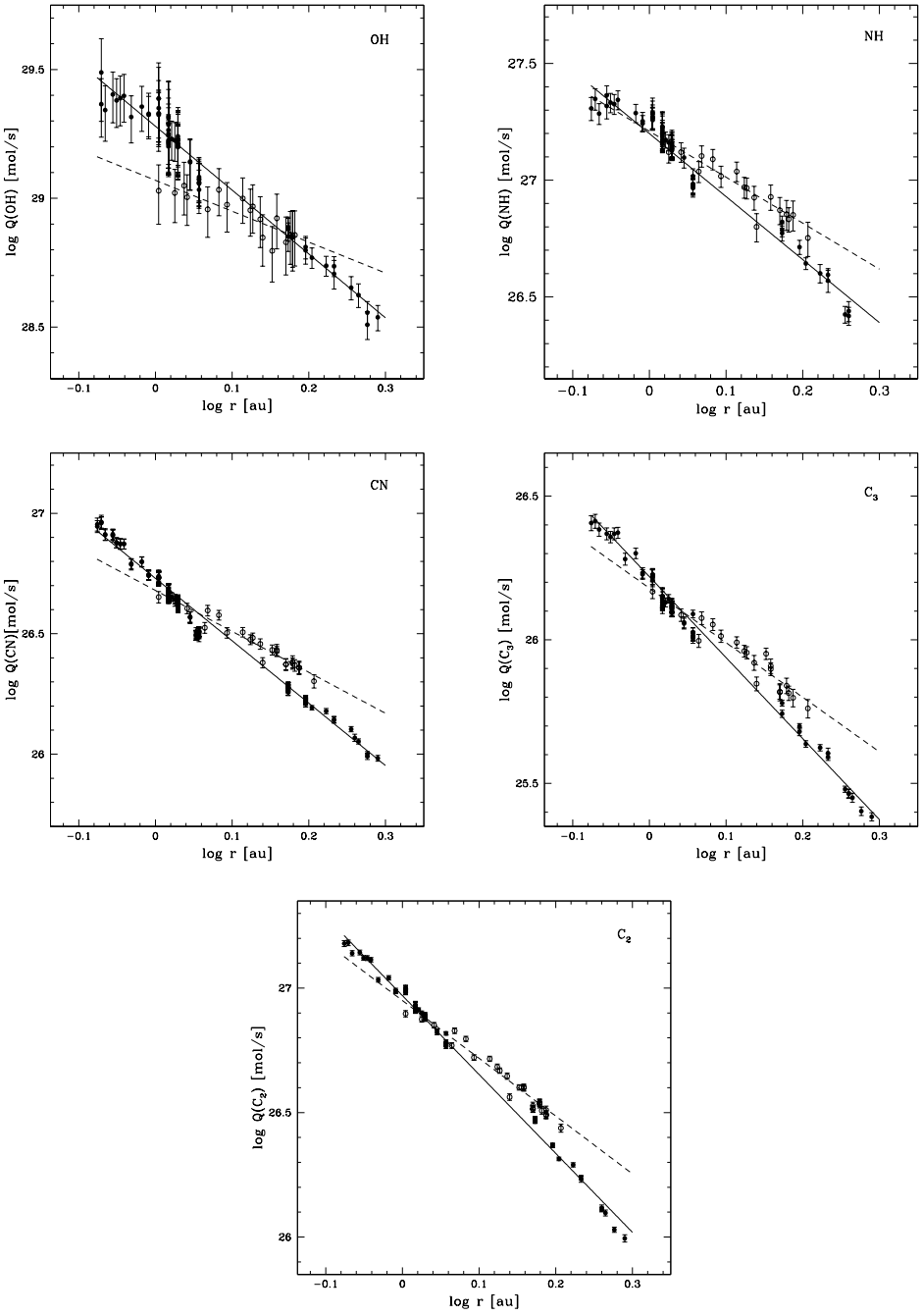


Figure 3.18: Logarithm of OH, NH, CN, $C_3$, and $C_2$ production rates of C/2012 F6 (Lemmon) as a function of the logarithm of the heliocentric distance (r). Pre-perihelion data points are represented with filled symbols and post-perihelion data points are represented with open symbols. The origin of the x-axis is perihelion. Solid lines are power-law fits of the production rates variation with the pre-perihelion heliocentric distance. Dotted lines are the same for post-perihelion values.

et al. (2015a).

Table 3.9: $Af\rho$ nightly averages of comet C/2012 F6 (Lemmon).

| UT Date | r | $Af\rho$ (cm) | | | |
|---|---|---|---|---|---|
| | (au) | UC | BC | GC | RC |
| 2012 Dec 11 | -1.95 | | 1.63±0.05 $10^3$ | 1.75±0.03 $10^3$ | 2.05±0.03 $10^3$ |
| 2012 Dec 15 | -1.89 | | 1.75±0.04 $10^3$ | 1.80±0.02 $10^3$ | 2.22±0.03 $10^3$ |
| 2012 Dec 19 | -1.84 | | | 1.97±0.03 $10^3$ | |
| 2012 Dec 20 | -1.82 | | 1.96±0.06 $10^3$ | 1.91±0.03 $10^3$ | 2.35±0.02 $10^3$ |
| 2012 Dec 22 | -1.80 | | | 2.01±0.03 $10^2$ | 2.46±0.02 $10^3$ |
| 2012 Dec 28 | -1.71 | | 2.17±0.08 $10^3$ | 2.17±0.06 $10^3$ | 2.70±0.03 $10^3$ |
| 2012 Dec 31 | -1.67 | 2.00±0.10 $10^3$ | 2.27±0.05 $10^3$ | 2.34±0.03 $10^2$ | 2.92±0.03 $10^3$ |
| 2013 Jan 5 | -1.60 | 2.20±0.10 $10^3$ | 2.42±0.06 $10^3$ | 2.50±0.03 $10^3$ | 3.04±0.03 $10^3$ |
| 2013 Jan 7 | -1.57 | 2.41±0.10 $10^3$ | 2.55±0.05 $10^3$ | 3.65±0.05 $10^3$ | 3.26±0.03 $10^3$ |
| 2013 Jan 13 | -1.49 | | 2.69±0.10 $10^3$ | | |
| 2013 Feb 7 | -1.13 | 5.57±0.39 $10^3$ | 5.38±0.16 $10^3$ | 5.45±0.10 $10^3$ | 6.43±0.05 $10^3$ |
| 2013 Feb 9 | -1.11 | | 6.07±0.20 $10^3$ | 6.27±0.13 $10^3$ | |
| 2013 Feb 12 | -1.07 | 7.21±0.65 $10^3$ | 6.94±0.26 $10^3$ | 7.04±0.15 $10^3$ | 8.14±0.07 $10^3$ |
| 2013 Feb 13 | -1.06 | 7.58±0.48 $10^3$ | 6.99±0.18 $10^3$ | 7.19±0.11 $10^3$ | 8.37±0.06 $10^3$ |
| 2013 Feb 14 | -1.04 | 8.42±0.85 $10^3$ | 7.75±0.31 $10^3$ | 7.81±0.18 $10^3$ | 8.96±0.09 $10^3$ |
| 2013 Feb 17 | -1.01 | 9.86±1.00 $10^3$ | 8.91±0.36 $10^3$ | 8.93±0.21 $10^3$ | 1.01±0.01 $10^4$ |
| 2013 Feb 19 | -0.98 | 1.07±0.07 $10^4$ | 9.36±0.30 $10^3$ | 9.71±0.18 $10^3$ | 1.11±0.01 $10^4$ |
| 2013 Feb 21 | -0.96 | 1.13±0.08 $10^4$ | 1.06±0.03 $10^4$ | 1.07±0.02 $10^4$ | 1.22±0.01 $10^4$ |
| 2013 Feb 23 | -0.93 | | 1.09±0.04 $10^4$ | 1.14±0.03 $10^4$ | 1.26±0.01 $10^4$ |
| 2013 Feb 25 | -0.91 | 1.29±0.11 $10^4$ | 1.25±0.04 $10^4$ | 1.30±0.03 $10^4$ | 1.47±0.01 $10^4$ |
| 2013 Feb 26 | -0.90 | 1.42±0.11 $10^4$ | 1.35±0.05 $10^4$ | 1.37±0.03 $10^4$ | 1.54±0.01 $10^4$ |
| 2013 Feb 27 | -0.89 | 1.41±0.11 $10^4$ | 1.34±0.05 $10^4$ | 1.42±0.03 $10^4$ | 1.59±0.01 $10^4$ |
| 2013 Feb 28 | -0.88 | 1.58±0.13 $10^4$ | 1.48±0.05 $10^4$ | 1.55±0.03 $10^3$ | 1.77±0.01 $10^4$ |
| 2013 Mar 2 | -0.86 | 1.74±0.15 $10^4$ | 1.69±0.06 $10^4$ | 1.74±0.04 $10^4$ | 1.98±0.02 $10^4$ |
| 2013 Mar 3 | -0.85 | 1.88±0.17 $10^4$ | 1.82±0.07 $10^4$ | 1.86±0.04 $10^4$ | 2.09±0.02 $10^4$ |
| 2013 Mar 4 | -0.84 | 1.86±0.18 $10^4$ | 1.93±0.08 $10^4$ | 1.93±0.04 $10^4$ | |
| 2013 Apr 29 | 1.01 | | 1.02±0.04 $10^4$ | 1.04±0.02 $10^4$ | |
| 2013 May 3 | 1.06 | | 9.56±0.34 $10^3$ | | |
| 2013 May 5 | 1.09 | 1.01±0.09 $10^4$ | | 9.72±0.20 $10^3$ | 1.09±0.01 $10^4$ |
| 2013 May 6 | 1.10 | 9.72±0.79 $10^3$ | 8.84±0.32 $10^3$ | 9.25±0.18 $10^3$ | 1.09±0.01 $10^4$ |
| 2013 May 11 | 1.17 | 9.27±0.79 $10^3$ | 8.25±0.29 $10^3$ | 8.62±0.17 $10^3$ | 9.99±0.01 $10^3$ |
| 2013 May 14 | 1.21 | 8.73±0.72 $10^3$ | 7.61±0.27 $10^3$ | 8.40±0.16 $10^3$ | 9.62±0.01 $10^4$ |
| 2013 May 16 | 1.24 | 7.87±0.62 $10^3$ | 7.08±0.24 $10^3$ | 7.47±0.15 $10^3$ | 9.04±0.01 $10^3$ |
| 2013 May 20 | 1.30 | | 6.89±0.24 $10^3$ | 7.31±0.14 $10^3$ | 8.47±0.01 $10^3$ |
| 2013 May 22 | 1.33 | 7.14±0.61 $10^3$ | 6.74±0.24 $10^3$ | 7.03±0.15 $10^3$ | 8.34±0.01 $10^3$ |
| 2013 May 23 | 1.34 | 7.14±0.61 $10^3$ | 6.82±0.23 $10^3$ | 7.08±0.15 $10^3$ | 8.19±0.01 $10^4$ |
| 2013 May 25 | 1.37 | 6.67±0.60 $10^3$ | 6.56±0.24 $10^3$ | 6.80±0.15 $10^3$ | 7.95±0.01 $10^3$ |
| 2013 May 26 | 1.38 | | 5.88±0.24 $10^3$ | 6.25±0.14 $10^3$ | 7.19±0.01 $10^3$ |
| 2013 May 29 | 1.42 | 6.11±0.75 $10^3$ | | 6.22±0.14 $10^3$ | 7.26±0.01 $10^3$ |
| 2013 May 30 | 1.44 | 6.61±0.67 $10^3$ | 6.29±0.25 $10^3$ | 6.41±0.15 $10^3$ | 7.81±0.01 $10^3$ |
| 2013 Jun 2 | 1.48 | 5.99±0.62 $10^3$ | 6.23±0.27 $10^3$ | 6.17±0.14 $10^3$ | 7.26±0.01 $10^3$ |
| 2013 Jun 4 | 1.51 | 5.51±0.59 $10^3$ | 6.04±0.35 $10^3$ | 5.98±0.14 $10^3$ | 7.11±0.01 $10^3$ |
| 2013 Jun 5 | 1.52 | 5.64±0.55 $10^3$ | 6.06±0.25 $10^3$ | 6.00±0.13 $10^3$ | 7.28±0.01 $10^3$ |
| 2013 Jun 6 | 1.54 | 5.09±0.58 $10^3$ | 5.82±0.25 $10^3$ | 5.80±0.14 $10^3$ | 6.83±0.01 $10^3$ |
| 2013 Jun 11 | 1.61 | | 5.52±0.27 $10^3$ | 5.49±0.15 $10^3$ | 6.53±0.01 $10^3$ |

Nightly averaged $Af\rho$ values are given in Table 3.9 for each filter. The complete data set with the corresponding error bars is represented in Fig. 3.19 in a logarithmic scale. Few data are available in the near-UV (UC) filter at heliocentric distances larger than 1.5 au because the comet was too faint.

In the same way as for the gas production rates, we studied the slope of the $Af\rho$ heliocentric

dependence. We separated pre- and post-perihelion data and fitted a slope. Post-perihelion data fitting was satisfactory but we were unable to represent the pre-perihelion $Af\rho$ heliocentric dependence with a single slope. We then split the pre-perihelion data into two data sets. The first set (pre-perihelion-1) contains $Af\rho$ values obtained while the comet was beyond 1.4, au and the second set contains the pre-perihelion data below 1.4 au (pre-perihelion-2). This results in a much better representation of the $Af\rho$ trend with the heliocentric distance as shown in Fig. 3.19. The best-fit slope values for the split data set are given in Table 3.10. Since only four images of the comet were taken during the first period with the UC filter, no slope of the $Af\rho$ heliocentric dependence is given for the first data set. The same asymmetry about perihelion as for most gas species is observed, with $Af\rho$ values being higher after perihelion.

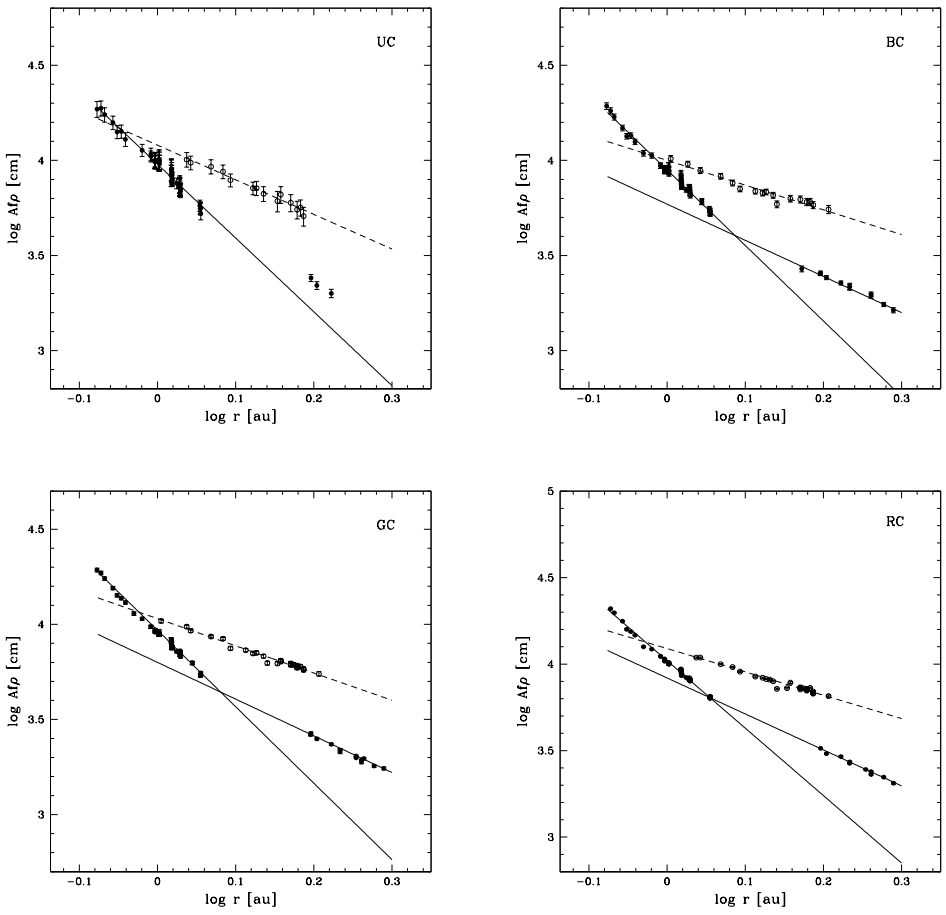


Figure 3.19: Logarithm of comet C/2012 F6 (Lemmon) $A(0)f\rho$ computed from UC, BC, GC, and RC narrow band continuum filters as a function of the logarithm of the heliocentric distance r (au). Pre-perihelion data are represented with filled symbols and post-perihelion data with open symbols. The origin of the x-axis is perihelion. Solid lines represent power-law fits of the $A(0)f\rho$ variation with the pre-perihelion heliocentric distance. Dotted lines are the same for post-perihelion values.

These results do not show a wavelength dependence of the slope derived for any of our data sets. The slopes are consistent with those measured by A'Hearn et al. (1995) for their large sample of comets even though there are strong changes of dust behaviour with time and heliocentric distance. The slope of the $Af\rho$ heliocentric dependence rises significantly between January 13 and February 7, 2013. The gap in the data makes it difficult to determine precisely when the change took place. Trends in visual magnitude lightcurves from Seiichi Yoshida website[2] also show a change of slope taking place around February 2, 2013: $m_v = 4.5+5\log(\Delta) + 18.0\log(r)$ before February 2, $m_v = 5.2+5\log(\Delta) + 10.0\log(r)$ between February 2 and March 4, and $m_v = 5.2+5\log(\Delta) + 9.5\log(r)$ after that. The agreement between dust production and the comet visual magnitude is not surprising as most of the light we observe visually is the solar light reflected by the coma dust continuum. The change in $Af\rho$ evolution can not be caused by a phase angle effect as we know that the maximum amplitude of this effect (around 25% in this case) is smaller than the observed changes.

Table 3.10: C/2012 F6 (Lemmon) pre- and post-perihelion fitted power-law slopes for $Af\rho$ computed from the UC, BC, GC, and RC filters. The pre-perihelion data have been separated into two data sets: beyond 1.4 au (pre-perihelion-1), and below 1.4 au (pre-perihelion-2).

| Filter | r-dependence | | |
|---|---|---|---|
| | pre-perihelion-1 | pre-perihelion-2 | post-perihelion |
| UC | | -3.88±0.10 | -1.82±0.08 |
| BC | -1.90±0.09 | -3.97±0.09 | -1.30±0.08 |
| GC | -1.93±0.08 | -4.02±0.07 | -1.43±0.05 |
| RC | -2.08±0.08 | -3.90±0.10 | -1.35±0.06 |

As mentioned above, we observe significant aperture effects in $Af\rho$ which can be easily understood by looking at the dust radial brightness profiles in Fig. 3.20. The logarithm of the measured flux is plotted against the logarithm of the nucleocentric distance ($\rho$) expressed in kilometres. We performed profile extraction for a 20° wide wedge in three directions: the sunward direction (dark blue triangles), the anti-sunward direction (the tail, black crosses), and the ambient coma at 90° of the tail (light blue points). The profile inner cutoff is 3.3″to avoid PSF and seeing effects. For a coma with constant dust production in steady state and no radiation pressure effects or grain fading, the radial brightness profile follows a canonical $1/\rho$ decay (Jewitt et al. 1982). The canonical $1/\rho$ law (corresponding to a -1 slope in a log-log representation) is overlaid on the radial profiles presented in Fig. 3.20.

At all epochs we find that the profile aspect and slope strongly depend on the azimuthal direction. For the first two profiles we observe a significant deviation from $1/\rho$ whatever the direction. The deviation is clearly seen even at small nucleocentric distances. The fitted slope in the anti-sunward direction for observations between December 11 and January 13 is about $-1.25$ and even steeper in the sunward and perpendicular directions. The slopes become

[2] Link:http://aerith.net/comet/catalog/2012F6/2012F6.html

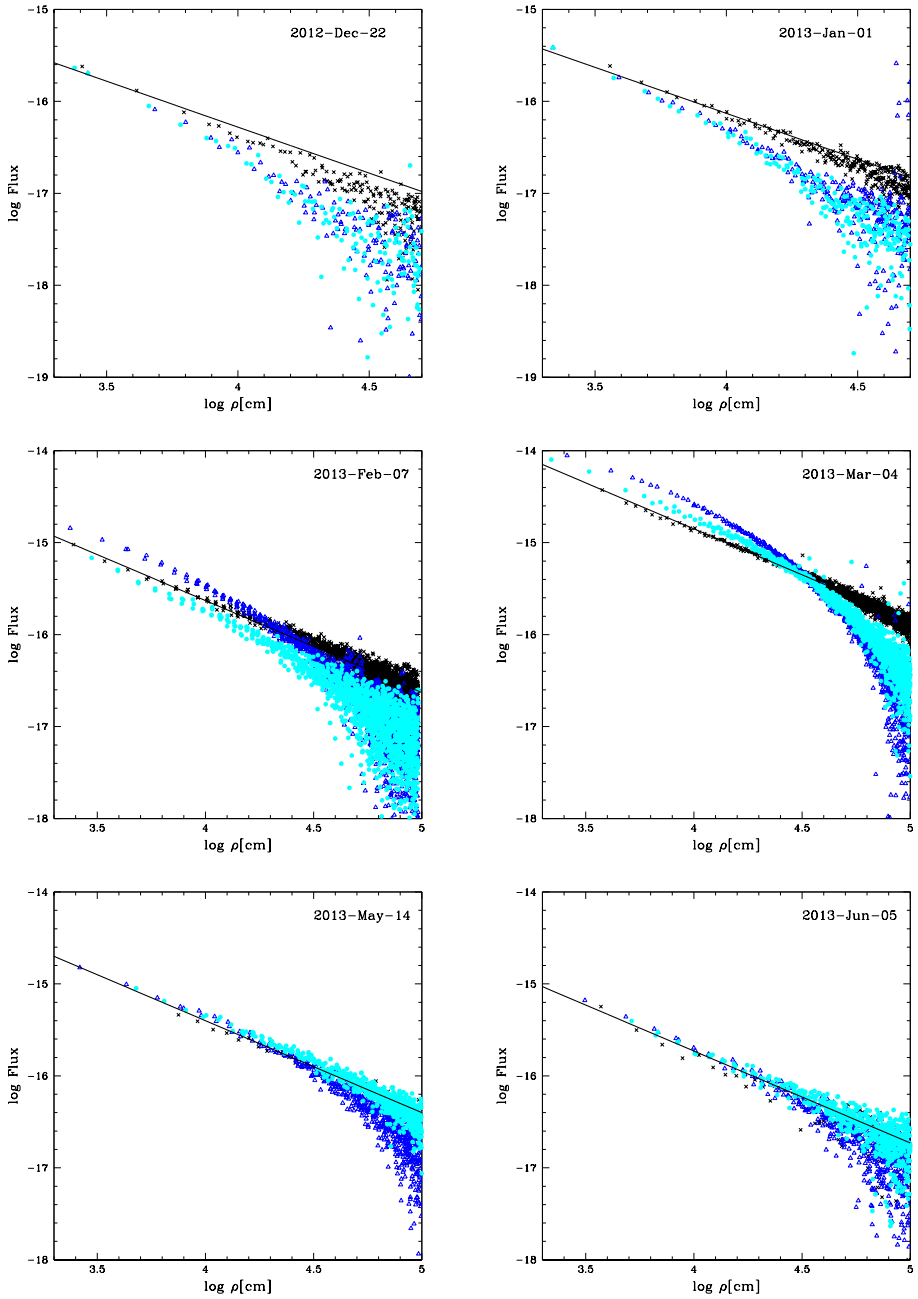


Figure 3.20: Dust brightness radial profiles of comet C/2012 F6 (Lemmon) at 6 epochs are represented: 2012-Dec-22 ($10^4$km = 22.5″), 2013-Jan-07 ($10^4$km = 17.5″), 2013-Feb-07 ($10^4$km = 13.2″), 2013-Mar-04 ($10^4$km = 16.1″), 2013-May-14 ($10^4$km = 22.9″), 2013-Jun-05 ($10^4$km = 23.3″). The profile extraction was made for 20° wide wedges in the tail direction, i.e., the anti-sunward direction (black crosses), the sunward direction (dark blue triangles), and the ambient coma perpendicular to the sunward direction. A $1/\rho$ profile is overlaid on each plot.

progressively closer to −1 as the comet approaches the Sun. For observations after February 6, the slope in the tail direction is always very close to −1. In the other two directions the radial profile close to the nucleus follows a $1/\rho$ law and then progressively deviates from it at larger nucleocentric distances.

In February and March 2013, we observe that the dust radial profile in the sunward direction is significantly brighter close to the nucleus than in the perpendicular direction. If we examine the original images and we apply a Larson-Sekanina filter we see a strong jet almost coinciding with the sunward direction (see Section 3.3.4). As the jet is brighter than the ambient coma, this explains the excessive brightness in the sunward direction compared to the perpendicular direction. In May and June 2013, no strong jets are seen in our images, in agreement with the radial profile aspect. In December and January, we detect a small jet in the direction perpendicular to the Sun-comet line. Since this jet is weaker than the one observed in February and its extension is only a few pixels from the nucleus, it has almost no influence on the radial profiles.

We use $A(\theta)f\rho$ computed at four wavelengths to derive the dust normalized reflectivity gradients, also called colour of the dust, and study their evolution with the comet heliocentric distance (Jewitt and Meech 1987). In Fig. 3.21 we show the dust colours computed from the gradient between RC (713 nm) and UC (334 nm), BC (445 nm), and GC (526 nm). The dust colour is also computed at 10,000 km from the nucleus, in the same way as the $Af\rho$.

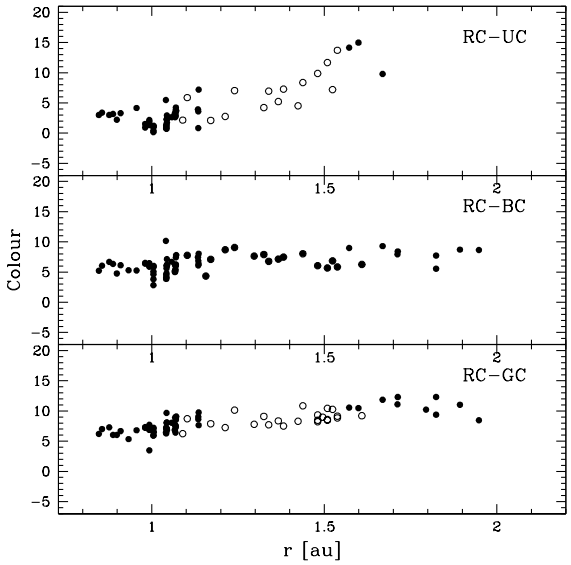


Figure 3.21: Evolution of the dust normalized reflectivity gradient of comet C/2012 F6 (Lemmon) computed from $Af\rho$ values as a function of the heliocentric distance. The origin of the x-axis is the perihelion. Pre-perihelion values are represented with filled symbols and post-perihelion values with open symbols. The dust colour is computed from RC and UC filters (top), RC and BC filters (middle), and RC and GC filters (bottom).

For RC-BC and RC-GC continuum pairs, the dust is clearly reddened by approximately the same amount with a mean value of $6.49 \pm 1.42$ %/1000 Å for the RC-BC pair and $8.08 \pm 1.63$ %/1000 Å for the RC-GC pair. These values are close to those observed for other comets. A reddening between 5 and 12 %/1000 Å was found by Lin et al. (2013) for comet Hartley 2. Lin et al. (2012) found that comet 81P/Wild 2 was reddened by approximately 8.2-8.6 %/1000 Å. Dust reddening for comet C/2000 WM1 was also around the same value (Lara et al. 2004). There is no strong trend in dust colour with heliocentric distance. This is not surprising, as a study performed by Solontoi et al. (2012) on 35 comets did not show any correlation between the colours of active comets and the heliocentric distance.

For the RC-UC continuum pair, the reddening is significantly lower than for the other two pairs and even sometimes negative. However, we do not think that the comet is really bluer in the near-UV. As comet Lemmon is quite gaseous, this is probably due to the contamination of the UC filter by some molecular emission artificially raising the $A(\theta) f\rho$, as explained in Section 2.3.4. We see that the reddening from these filters is higher at larger heliocentric distances. Around 1.6 au it comes close to the reddening computed from the RC-BC and the RC-GC pairs. Indeed, at this distance, the comet was less active and the contamination of the UC filter by molecular emissions was lower. Knowing this effect we discarded the UC-BC and the UC-GC continuum pairs.

In Fig. 3.22 we analyse the effect of aperture size on the dust colour. For December and January observations, the reddening rises with the nucleocentric distance, while for observations made after February the percentage of reddening by 1000 Å slowly decreases with the aperture size. This confirms that dust grains properties change around February 2, as already seen for the radial profiles. Aperture effects are quite small though, i.e., on the order of 5%, but they could explain the dispersion in dust colour observed in Fig. 3.21.

### 3.3.2 Composition

We can compare the production rates measured in this paper with those derived from other observations of the comet. Paganini et al. (2014a) obtained near-infrared spectra of comet Lemmon pre- and post-perihelion at three heliocentric distances: 1.2 au (February 2 and 4), 0.75 au (March 31 and April 1), and 1.74 au (June 20). February and June observations are sufficiently close to TRAPPIST observations to allow comparison between production rates of mother species detected in the infrared domain and production rates of daughter species observed by TRAPPIST in the optical domain. Combi et al. (2014a) also derived water production rates for comet Lemmon from observations of the hydrogen Ly$\alpha$ emission with the SWAN camera onboard the SOHO spacecraft. Their observations cover the period from November 29, 2012, to June 31, 2013. Paganini et al. derived a water production rate of $Q(H_2O) = (1.9 \pm 0.1) \times 10^{29}$ mol/s for both February 2 and 4 and $Q(H_2O) = (1.1 \pm 0.1) \times 10^{29}$ mol/s for June 20. On February 6 and June 5 Combi et al. respectively measured $Q(H_2O) = (2.07 \pm 0.01) \times 10^{29}$ mol/s and $Q(H_2O) = (2.03 \pm 0.02) \times 10^{29}$ mol/s. We measured a mean value

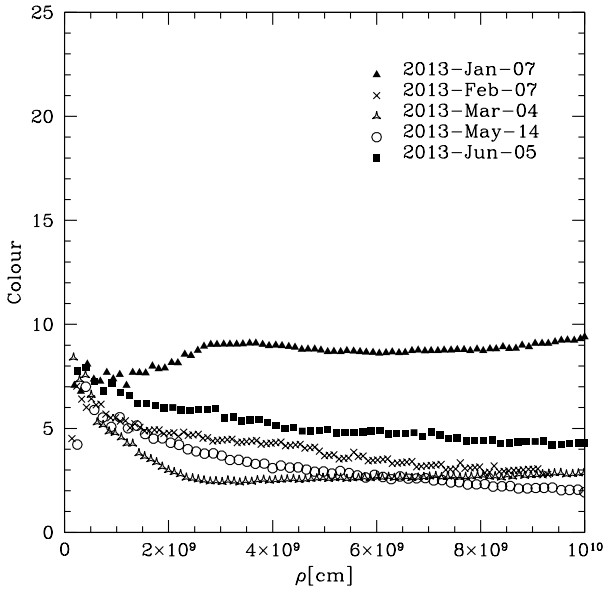


Figure 3.22: Dust normalized reflectivity gradient as a function of nucleocentric distance ($\rho$) for the RG-GC continuum pair. The evolution of dust colour with nucleocentric distance is plotted for five dates sampling our observing run.

of $Q(\mathrm{OH}) = (1.16 \pm 0.22) \times 10^{29}$ mol/s on February 7 and $Q(\mathrm{OH}) = (0.72 \pm 0.17) \times 10^{29}$ mol/s on June 5 with TRAPPIST. From OH production rates we can compute vectorial-equivalent water production rates using the relation given in Cochran and Schleicher (1993) which takes into account the heliocentric dependence of the water velocity and the branching ratio for photodissociation of water into OH: $Q(\mathrm{H_2O}) = 1.361 r^{-0.5} Q(\mathrm{OH})$. This gives $Q(\mathrm{H_2O}) = (1.48 \pm 0.28) \times 10^{29}$ mol/s for February 7 and $Q(\mathrm{H_2O}) = (0.79 \pm 0.19) \times 10^{29}$ mol/s for June 5. Our production rates are lower than those obtained by Paganini et al. (2014a) and Combi et al. (2014a). When comparing the water production rates in comets computed from different sources there is usually a discrepancy between the values computed from observations of H, OH, or $H_2O$ directly at different wavelengths. The scatter can be as large as a factor of two. This could be explained by the differences in the aperture sizes (as small as 30 or 40" in the infrared vs 22' in the optical), the type of model, and the value of parameters used to compute production rates and the effect of the nucleus rotation.

Paganini et al. (2014a) detected HCN emission in the near-infrared on February 2 and June 20. The origin of the CN radical in cometary coma has not been yet firmly determined. HCN photodissociation seems to be the process responsible for most of the CN production but other mother molecules or other processes are necessary to explain the discrepancies observed between HCN and CN production rates in some comets (Fray et al. 2005). A'Hearn et al. (1986) first proposed that CN radical could also be produced from grains to explain the existence of CN jets in comet Halley. Evidences for extended sources in jets and correlation between CN and dust production (Newburn and Spinrad 1989 and A'Hearn et al. 1995) further

reinforced the hypothesis of CN production from grains. In this context, comparison between infrared and optical data is of great importance to study the origin of the CN radical in the coma. Paganini et al. (2014a) obtained $Q$(HCN) = $(2.1 \pm 0.08) \times 10^{26}$ mol/s on February 2 and $Q$(HCN) = $(2.3 \pm 0.2) \times 10^{26}$ mol/s on June 20. We can compare it to TRAPPIST measurements: $Q$(CN) = $(3.17 \pm 0.14) \times 10^{26}$ mol/s on February 7 and $Q$(CN) = $(2.01 \pm 0.13) \times 10^{26}$ mol/s on June 11. If we take into account the rapid rise of production rates from one day to another in February and the rotational variability, there is no strong discrepancy between our values and those from Paganini et al. (2014a). Biver et al. (2014) also derived comet Lemmon HCN production rate on April 06.4 to 08.6, 2013 from observations with the 30 m telescope of the Institut de radioastronomie millimétrique (IRAM). They measured $Q$(HCN) = $(1.27 \pm 0.09) \times 10^{27}$ mol/s. We only have measurements of the CN production rate a month before on March 4: $Q$(CN) = $(0.89 \pm 0.31) \times 10^{27}$ mol/s. Within the error bars and taking into account the rapid evolution of the comet activity and the nucleus rotation, the HCN and CN productions rates are consistent with each other, indicating that HCN could be the main source of CN radicals in the coma of comet Lemmon and that only a small fraction of CN could be released from grains.

A'Hearn et al. (1995) distinguished two main compositional classes among comets: typical and carbon-chain depleted comets. These classes are defined by the ratio of the CN production rate to the carbon-chain species $C_2$ and $C_3$. They obtained a mean $Q(C_2)/Q(CN)$ value of 1.15 for typical comets with limits around 0.7 and 2 while depleted comets are defined as those having $log(Q(C_2)/Q(CN)) < -0.18$. About half of the Jupiter family comets are carbon-chain depleted and almost no long-period comets are depleted. From the production rate ratios of $C_2$, $C_3$, and CN shown in Fig. 3.23, we conclude that comet Lemmon is a typical comet, as expected for a long-period comet. The $C_2$ to CN ratio varies between 1.2 and 2, well within the range defined by A'Hearn et al. (1995) for typical comets. We also computed ratios of the other production rates relative to the CN production rates and the results are shown in Fig. 3.24. We fitted power-law slopes to represent the evolution of these ratios with the heliocentric distance pre- and post-perihelion. The resulting slopes are given in Table 3.11.

In Fig. 3.23 we observe a variation of the $C_2$ to CN ratio with the heliocentric distance. The ratio does not vary significantly near the perihelion, but $Q(C_2)/Q(CN)$ starts decreasing when the heliocentric distance is larger than 1.4 au (both pre- and post-perihelion), showing that the apparent chemical composition of the coma can evolve with the heliocentric distance. Since the amplitude of the variation remains small, with a maximum variation smaller than a factor of 2 between the most extreme values, the chemical classification of comet Lemmon as a typical comet does not change. The $C_3$ to CN ratio remains constant within the error bars during the whole observing run (for all distances).

In the upper part of Fig. 3.25, the ratio of $C_2$ to OH production rates is plotted against the ratio of CN to OH. We can distinguish two groups of points: a diagonal band across the graph and a group of points below the diagonal. The group of points below the diagonal is due to the lower $C_2$ to CN ratio at large heliocentric distances. The full line indicates temporal evolution

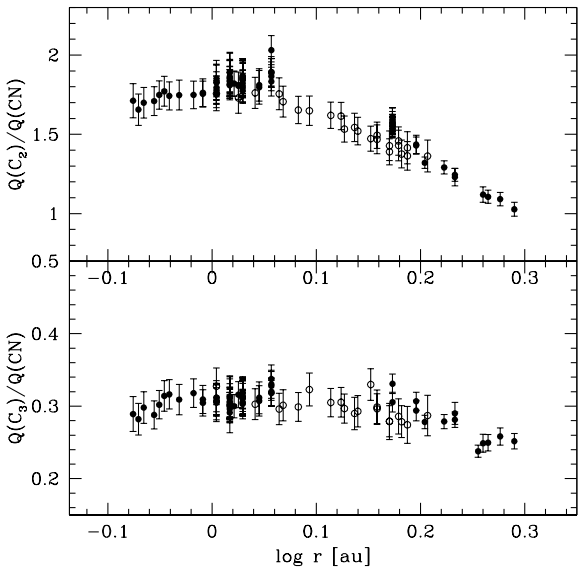


Figure 3.23: Ratio of $C_2$ to CN (top) and $C_3$ to CN (bottom) production rates as a function of the heliocentric distance. The x-axis origin is the perihelion. Pre-perihelion values are represented with filled symbols and post-perihelion values with open symbols.

Table 3.11: Fitted power-law slopes for the heliocentric dependence of comet C/2012 F6 (Lemmon) OH, NH, $C_3$, $C_2$, and $A(0)f\rho$ to CN ratios pre- and post-perihelion.

| Species | r-dependence | |
|---|---|---|
| | pre-perihelion | post-perihelion |
| log[Q(OH)/Q(CN)] | +0.09±0.05 | +0.57±0.20 |
| log[Q(NH)/Q(CN)] | -0.09±0.10 | -0.24±0.11 |
| log[Q($C_3$)/Q(CN)] | -0.23±0.05 | -0.22±0.09 |
| log[Q($C_2$)/Q(CN)] | -0.59±0.06 | -0.64±0.05 |
| log[Q($A(0)f\rho$)/Q(CN)] | -0.14±0.06 | +0.47±0.11 |

of the comet between December 11 and January 13. The comet moves upwards in the diagram during this period of time, indicating an increase of the $C_2$ to CN production rates ratio when the comet is beyond 1.4 au. This effect has already been pointed out in Fig. 3.23. Between February 7 and March 4, the data points move on a diagonal band from the lower left towards the upper right. This indicates a decrease in the OH production rate compared to the CN and $C_2$ production rates for heliocentric distances smaller than 1.4 au. If we plot the $C_2$ to OH and CN to OH ratios as a function of the heliocentric distance we clearly see they rise while the comet approaches the Sun for heliocentric distances smaller than 1.4 au. A'Hearn et al. (1995) also found a peak of $Q(OH)/Q(CN)$ between 1 and 2 au for their global analysis of a large sample of comets. The variation observed in $Q(OH)/Q(CN)$ and $Q(OH)/Q(C_2)$ is less than a factor of 2. The number of post-perihelion observations is not sufficient to detect any

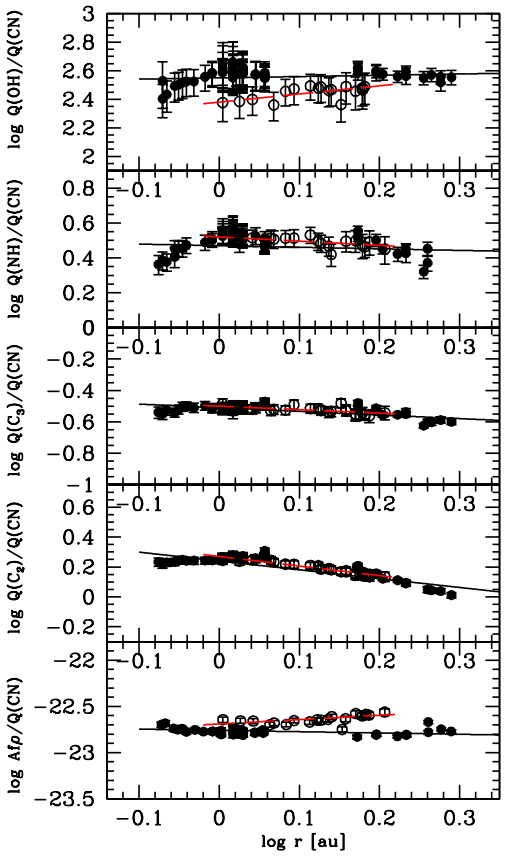


Figure 3.24: Comet C/2012 F6 (Lemmon) OH, NH, $C_3$, $C_2$, and $A(0)f\rho$ to CN production rate ratios as a function of the heliocentric distance. Pre-perihelion values are represented with filled symbols and post-perihelion values with open symbols. Full lines represent power-law fits of the ratio variations with the heliocentric distance pre-perihelion. Dotted red lines are the same for post-perihelion values.

significant trend.

The lower part of Fig. 3.25 shows the $C_3$ to OH ratio against the CN to OH ratio. Both pre- and post-perihelion data points lie on a diagonal band indicating that there is no strong variation of $Q(C_3)/Q(CN)$ with the heliocentric distance. This is in complete agreement with what we deduced from Fig. 3.23. No clear trend within the diagonal band could be found because of the large dispersion of the data points. However the study of the $C_3$ to OH ratio shows the same trend as for $C_2$ and CN.

The dust to gas ratio is usually defined as the ratio of $Af\rho$ to the OH production rate or the ratio of $Af\rho$ to the CN production rate. We derive both ratios and we show their evolution with the heliocentric distance in Fig. 3.26. The logarithm of $Af\rho/Q(OH)$ is between -25.5 and

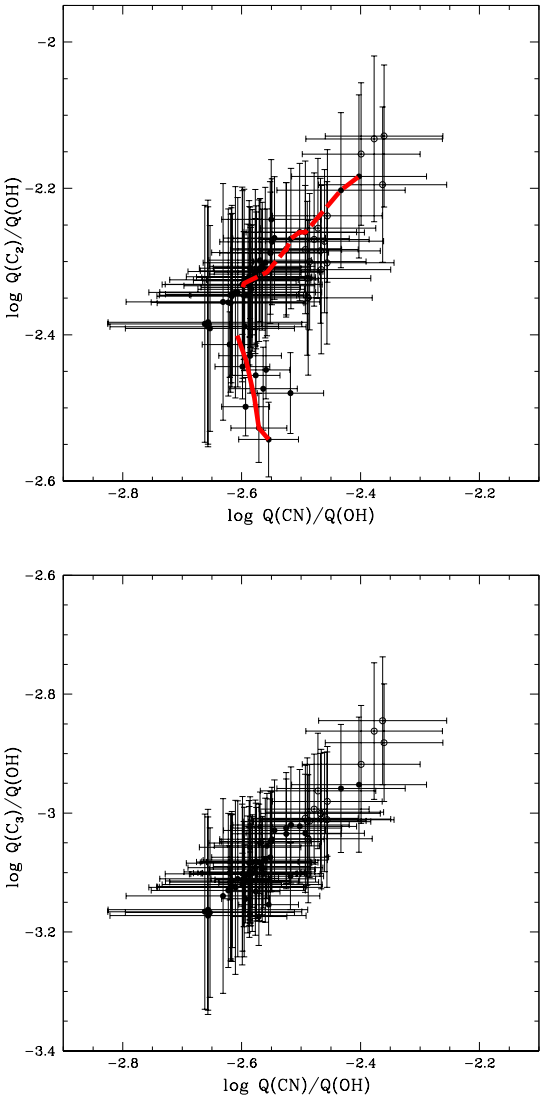


Figure 3.25: The logarithm of the ratio of $C_2$ (top) and $C_3$ to OH production against the logarithm of the ratio of CN to OH and their error bars. Pre-perihelion values are represented with filled symbols and post-perihelion values with open symbols. The solid red line indicates the evolution of comet Lemmon between December 11 and January 13 and the dashed line between February 7 and March 4.

-25.0. There is an asymmetry about perihelion. The dust to gas ratio is higher after perihelion. In Section 3.3.1 we found higher gas production rates and $Af\rho$ values post-perihelion. The asymmetry is stronger for the dust than for gas species, explaining the lower value of dust to gas ratio before perihelion.

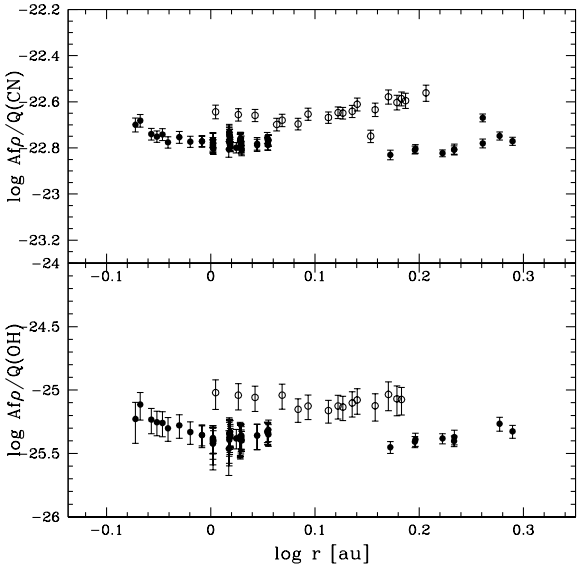


Figure 3.26: Ratio of $Af\rho$ to CN (top) and OH (bottom) production rates as a function of the heliocentric distance. The x-axis origin is the perihelion. Pre-perihelion values are represented with filled symbols and post-perihelion values with open symbols.

### 3.3.3 Morphology

Images from December 2012 and January 2013 and post-perihelion images (after April 2013) have a lower signal-to-noise ratio. For these images we used preferentially Larson-Sekanina filtering to enhance faint features. We only used the azimuthal median removal on CN images from February and March 2013.

Features are detected mainly in the CN, $C_3$, $C_2$, and in the dust filters, suggesting the existence of at least one active zone on the nucleus. As expected, the feature aspect is strongly dependent on the viewing geometry of the comet at the time of the observations. If the Earth is oriented inside the cone described by the rotation of the active region around the spin axis, features appear as spirals or arcs. When the Earth is outside the cone, we mainly see radial features. Three main configurations are seen during the whole period. We chose one representative night from each of these configurations; the result of the Larson-Sekanina filtering on OH, NH, CN, $C_3$, $C_2$, and RC images is shown in Fig. 3.27. We only show the enhanced result for the RC filter as the features are similar in all dust filters.

In December and January the features are difficult to detect because of the low signal-to-noise of the images (Fig. 3.27, top panel). No clear structures are found in OH and NH filters. Both Larson-Sekanina filtering and azimuthal median profile removal revealed a roughly hourglass shaped morphology in the CN filter. The features are oriented respectively to the sunward and anti-sunward directions. Both $C_3$ and $C_2$ display the same morphology even if very weak and less extended in $C_3$ because of the poor signal-to-noise ratio and shorter $C_3$ lifetime. The dust

morphology is quite different from the hourglass shape observed for the gas coma. We clearly see the dust tail in the anti-sunward-direction. A second feature is detected perpendicular to the anti-sunward direction, towards the northeast. Both gas and dust morphologies are almost identical from night to night. The two long series of observations from January 7 and 13 do not show variations in gas and dust morphologies due to the nucleus rotation.

When we recovered the comet in early February, we observed significant changes in the coma morphology. As in December and January, no feature is detected in the OH filter because of the rather poor signal-to-noise ratio, but other gas filters display a more complex morphology. The broad structure in the anti-sunward direction in the NH filter clearly reveals the contamination by the ionic tail ($CO_2^+$ ion). Corkscrew-like shaped features are identified in the CN, $C_3$, and $C_2$ filters. Close to the nucleus, two sharp features are observed. The remnants of these features after one nucleus rotation period are detected as a broad structure at larger nucleocentric distances, see Figs. 3.27 and 3.28. The gas coma is enhanced in the anti-sunward direction in CN, $C_3$, and $C_2$. Given that contamination by the dust in the CN filter is very weak, we do not think that the gas coma enhancement in the anti-sunward direction is only due to contamination by the dust tail. A strong dust tail is detected in the RC filter in the anti-sunward direction. However, no corkscrew-like shaped structures similar to the gas are observed in the RC filter. Instead, we see a strong jet in the sunward direction and a weaker one oriented to the west. In February, comet Lemmon has been observed during several almost entire nights. We observe variations of the gas morphology during these nights caused by the nucleus rotation. No morphological change is observed for the dust. The detailed description of the morphology evolution with the nucleus rotation as well as the determination of the rotation period are given below. The features described here remained observable as the comet was approaching the Sun until March 4, when the observations were interrupted.

We observed comet Lemmon again after perihelion, from April 28 to June 11, 2013. The comet was weaker, making structures in the coma very difficult to identify. A feature in the anti-sunward direction is detected in all filters except OH. No other feature could be identified in the NH and $C_3$ filters. Only weak CN and $C_2$ features could be distinguished close to the nucleus. In the dust processed images we observe a second feature oriented to the south.

Structures observed in the coma suggest that the nucleus of comet Lemmon has at least one discrete active zone. The similarity of the CN, $C_3$, and $C_2$ features strongly suggests that these species originate from the same areas. No conclusion can be drawn about OH and NH. Dust morphology is different from that of the gas, in agreement with the differences observed between gas and dust production evolution in the previous sections.

### 3.3.4 Rotation

We mentioned earlier that the gas morphology, especially in the CN filter, was evolving during the long observing runs performed in February. In Fig. 3.28, examples of CN images processed with Larson-Sekanina filtering (left) and azimuthal median profile subtraction (right) are

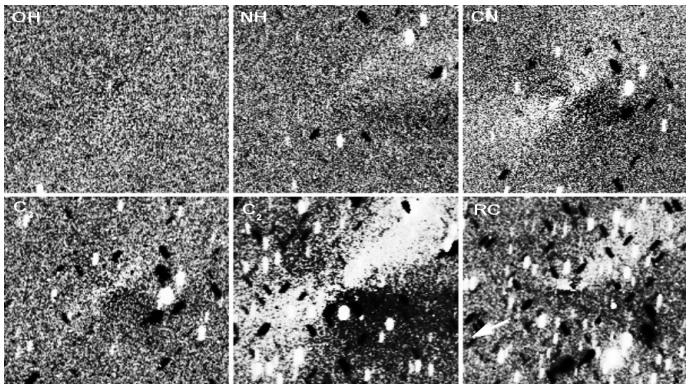


(a) OH, NH, CN, $C_3$, $C_2$, and RC images from January 13 after application of Larson-Sekanina filtering

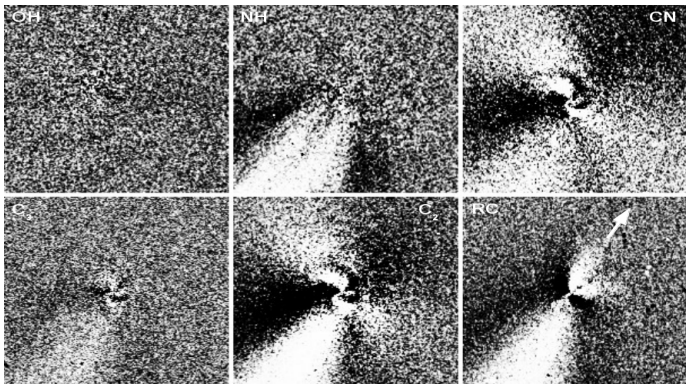


(b) OH, NH, CN, $C_3$, $C_2$, and RC images from February 25 after application of Larson-Sekanina filtering

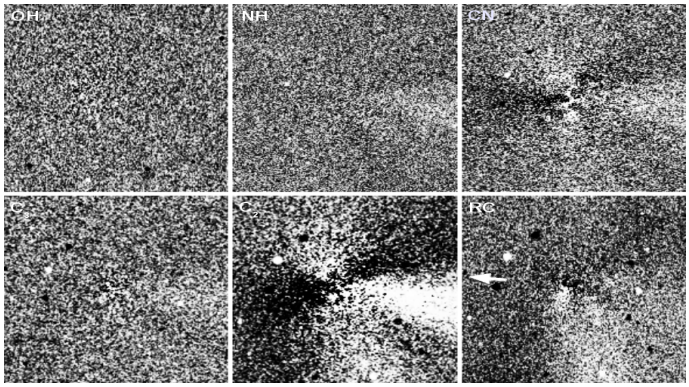


(c) OH, NH, CN, $C_3$, $C_2$, and RC images from May 14 after application of Larson-Sekanina filtering

Figure 3.27: C/2012 F6 (Lemmon) enhanced OH, NH, CN, $C_3$, $C_2$, and RC images from January 13 (top panel), February 25 (middle panel), and May 14 (bottom panel). Each image is enhanced by Larson-Sekanina filtering. The field of view is 4.3' × 4.3' and images are oriented with north up and east left. The arrow indicates the direction of the Sun.

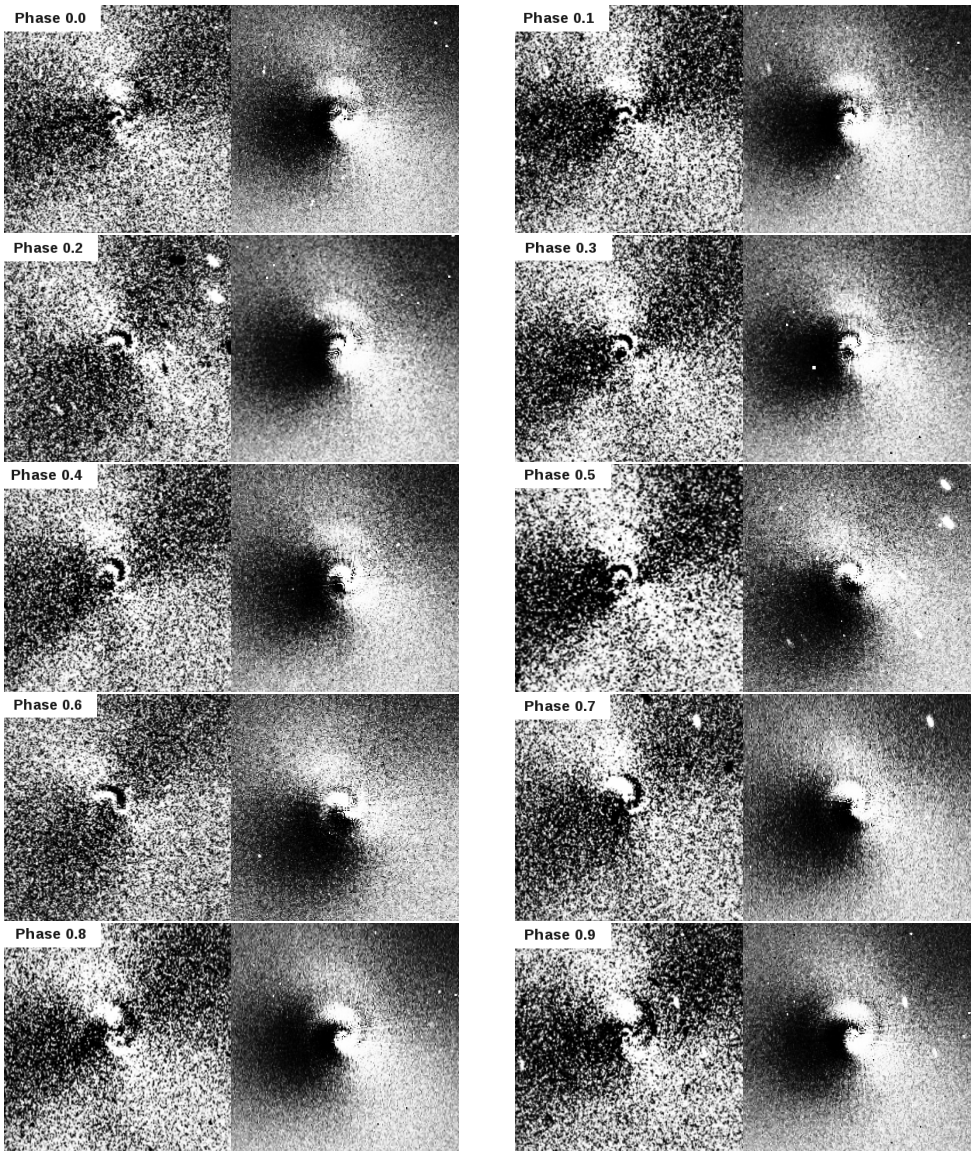


Figure 3.28: C/2012 F6 (Lemmon) CN images processed with Larson-Sekanina filtering (left) and azimuthal median profile subtraction (right) acquired between February 7 and February 12, 2013. The images have been sorted out by rotational phase assuming a rotation period of 9.52 h and a zero point on February 7.16. All images are oriented with north up and east left. The field of view is 4.3' × 4.3'.

shown. We selected images taken between February 7 and February 12. We assumed a rotation period of 9.52 hours and sorted the images according to their rotational phase. Two small spiral-like features appear close to the nucleus. Then they progressively extend and rotate clockwise as the gas expands. At the end of the rotation cycle, structures are broad and extend farther away from the nucleus. As a new rotational cycle begins, new spiral-like shaped features appear. Features from the previous rotation cycles can be distinguished at larger nucleocentric distances.

The periodic repetition of similar coma morphology in CN and $C_2$ filters allowed us to determine the nucleus rotation period. Images taken between February 9 and 25 were selected, as this epoch has the best temporal coverage. We first searched for pairs of matching images and recorded the time interval between matching pairs. Tens of pairs were found and the only possible rotation period was around 9 hours. We then refined the period determination. We decided to work on CN images as these were the ones with the highest signal-to-noise ratio and were less contaminated by the dust. All the original CN images from February 9 to February 25 were normalized and divided between each other. We computed the RMS of the images resulting from each division. The division of two images displaying the same morphology gives a minimum RMS, so that minima in the RMS should repeat with the nucleus rotation period. We studied the value of the RMS as a function of the time interval between the images and the result is shown in Fig. 3.29. We eliminated all possible aliases and determined the rotation period by dividing the time interval between matching pairs by the number of cycles between them. We measured a period of $9.52 \pm 0.05$ hours from 13 matching pairs between February 9 and February 25. The uncertainty in the rotation period is given by the standard deviation of the period measurements. We do not detect any increase or decrease of the comet rotation period during this time. We performed a similar study on $C_2$ images. The average rotation period derived from $C_2$ images is $9.50 \pm 0.18$ hours. This is in agreement within the error bars with the measurement made from CN images even though the uncertainty is bigger, probably as a result of the contamination by the dust in the $C_2$ filter. The signal-to-noise ratio in the other filters is not sufficient to perform this kind of analysis. The morphological evolution of CN during a complete rotation cycle is shown in Fig. 3.28. Nucleus rotation periods have only been determined for approximately two dozen comets. The measured values vary from a few hours for comets like Hyakutake (1996 B2) (Schleicher et al. 1998, Schleicher and Woodney 2003) or 10P/Tempel 2 (A'Hearn et al. 1989, Jewitt and Luu 1989, Sekanina 1991) to more than a day for comet 9P/Tempel 1 (Belton et al. 2005) or comet Halley (Belton et al. 1991), for example. The rotation period measured for comet Lemmon lies within the range of values usually observed for comets.

### 3.3.5 Discussion

We have presented the analysis of comet Lemmon long-term photometry and imaging monitoring with the robotic telescope TRAPPIST. We observed the comet during several months both pre- and post-perihelion. We have studied the evolution of the activity and the coma chemical composition along a part of the orbit from 1.95 au pre-perihelion to 1.61 au post-perihelion. We also performed an analysis of the variation of the coma structures that allowed us to determine the nucleus rotation period.

The heliocentric dependence of OH, NH, CN, $C_3$, and $C_2$ production rates displays similar slopes. Morphological study of the coma also showed that identical features are observed for CN, $C_3$, and $C_2$, ranging from a roughly hourglass shape in December and January to a corkscrew-like shape in February and March. The agreement between evolution and mor-

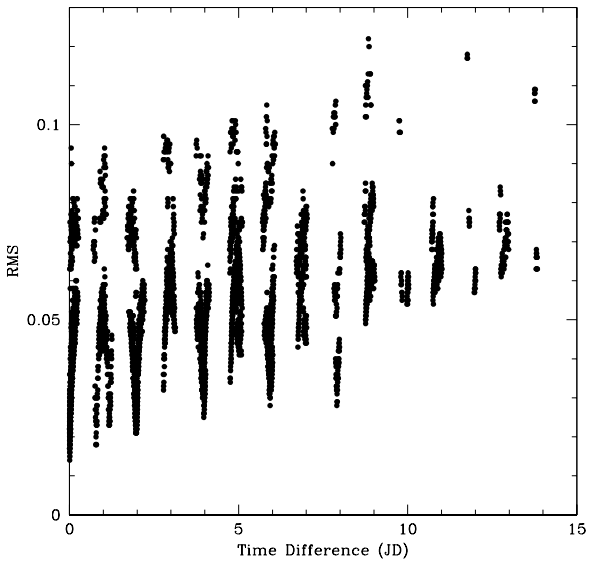


Figure 3.29: Result of C/2012 F6 (Lemmon) rotation analysis. CN images from February 9 to February 25 have been normalized and divided between each other. We plot the RMS resulting from each division as a function of the time difference between the images. Minima in the RMS repeat with the nucleus rotation period. We measured a period of 9.52 ± 0.05 hours from 13 matching pairs between February 9 and February 25.

phology for all gas species suggests that they have the same origin. All five gas species exhibit an asymmetry about perihelion, the rate of brightening being steeper than the rate of fading and the production rates of all radicals except OH being higher after perihelion. Such asymmetries are not unusual for comets (see, e.g., A'Hearn et al. 1995, Knight and Schleicher 2013, Schleicher et al. 1998) but their origin is still difficult to understand because of the lack of comets observed over a sufficient range of heliocentric distances both pre- and post-perihelion. However, in some cases, such as comet Halley, the increased brightness after perihelion was probably linked to seasonal effects (Weissman 1987). For comets on highly eccentric orbits with one or several active zones on their nuclei, rapid changes of insolation and active zone illumination can occur near perihelion. Since the orientation of the rotation axis is assumed to be random, different kinds of asymmetries should be observed among comets: higher activity pre-perihelion, post-perihelion, or almost no asymmetry. The monitoring of a large number of comets both pre- and post-perihelion is then critical in order to study the impact of seasonal effects on comet activity. In the case of comet Lemmon, we observed features in the coma indicating one or several active region(s) on the nucleus and a possible seasonal effect that could explain the asymmetry about perihelion. In order to confirm this hypothesis, modelling of the nucleus and determination of the comet pole orientation would be needed.

Even though all gas species display similar behaviour, small variations of the production rate ratios are observed. The $C_2$ to CN ratio is almost constant for heliocentric distances smaller

than 1.4 au and decreases at larger distances. Both pre- and post-perihelion data exhibit the same trend. This seems thus only linked to the comet heliocentric distance. However, the $C_3$ to CN ratio does not vary with the heliocentric distance. We also found that for heliocentric distances smaller than 1.4 au, the OH production rate rises at a slower pace than carbonaceous species. The coma chemical composition then evolves with the comet heliocentric distance confirming the importance of studying the composition of comets along their orbits and not only at a specific moment. Evolution of the production rate ratios has already been found for other comets, such as for comet Halley which displayed temporal variation of the carbon species relative to OH (Schleicher et al. 1998). A'Hearn et al. (1995) also noticed a slight but systematic decrease of $Q(C_2)/Q(CN)$ with increasing heliocentric distance for several comets in their data set.

In Section 2.3.3 we explain that in some cases there are discrepancies between the observed gas radial profiles and the fitted Haser model. This indicates that the Haser scalelengths used for modelling did not perfectly correspond to the observed profiles. Scalelengths determinations are usually performed only on small ranges of heliocentric distances and from profiles with poor spatial resolution. We scaled scalelengths as $r^2$ for all gas species, as is usually done. However, Rauer et al. (2003) showed in the case of comet Hale-Bopp at large heliocentric distances, that the scalelength variation with heliocentric distance could be more complex than assumed here, and could also depend on the radical under study. Even though the use of radial profiles allows us to sample the entire coma, the effect of model parameters that do not exactly match the spatial distribution of the species has to be considered. This could of course affect the $C_2$ and CN production rates computed with these scalelengths and their ratio with the heliocentric distance for example. The $C_2$ abundance is particularly affected since its profile is often less steep in the inner coma than can be reproduced with the Haser model (Schulz et al. 1994). A re-determination of Haser scalelengths for comet Lemmon and other comets and a study of their dependence on the heliocentric distance would be necessary. We plan to address Haser scalelengths determination in a forthcoming paper. However, some tests performed for comet Lemmon showed that the effect of the Haser scalelengths on the CN and $C_2$ production rates becomes really significant only when the comet is close to the Sun and then should not strongly affect the trend in the $C_2$ to CN ratio we observed here.

The study of the dust radial profiles showed some peculiarities. For a simple steady-state coma, the radial brightness profile should decrease as $1/\rho$ with the nucleocentric distance $\rho$ (i.e. follow a -1 slope in a log-log representation). However, significant deviations of the dust radial brightness profile from the expected canonical distribution were noted. In most cases, the slope of the profile was steeper than expected for a steady-state dust coma and variations of the slope with the azimuthal direction were observed. In February, early March, and after perihelion, the slope was close to -1 in the tail direction. In the other directions, it was close to -1 at small nucleocentric distances and then progressively deviated at larger nucleocentric distances. However, in December and January, the dust profile slope was about -1.25 in the tailward direction and even steeper in the sunward and perpendicular directions. Radial profiles steeper than $1/\rho$ have already been observed for a number of comets see, e.g.,

Baum and Kreidl (1986), Jewitt and Luu (1989), Baum et al. (1992) and Schleicher et al. (2003). This behaviour is partially explained by the radiation pressure effect. Radiation pressure accelerates grains in the anti-sunward direction. Baum et al. (1992) modeled the effect of radiation pressure on a dust coma. In the tailward direction, their modeled profile follows a $1/\rho$ law. In the sunward direction, the modeled profile follows a $1/\rho$ law at small nucleocentric distances and is steeper farther away from the nucleus. This is exactly what we observe for the dust radial profiles in February, early March, and after perihelion. The effect is particularly strong for March 4 when the comet was only at 0.73 au from the Sun. This was the observation where the comet was the closest to the Sun and was thus undergoing the strongest radiation pressure effects. The dust behaviour is quite different in December and January. At that time, the dust brightness profile is steeper than $1/\rho$ even at small nucleocentric distances and, more importantly, even in the tailward direction. This indicates that another phenomenon is taking place in the dust coma. Baum et al. (1992) proposed different possible explanations for this departure of the $1/\rho$ law. The first one is grain fading, already invoked by Jewitt and Luu (1989) to explain profiles observed for comet Tempel 2. They also considered the issue of large old grains that could have a brightness profile different than $1/\rho$. A halo of large old grains could have dominated the dust coma brightness profile at large heliocentric distances pre-perihelion. When the comet comes closer to the Sun new dust ejecta would then account for most of the dust coma brightness and produce a nearly canonical profile in the tail direction. This could also explain the change in the profile aspect observed before and after February; the large old grains being progressively outnumbered by smaller grains more sensitive to radiation pressure.

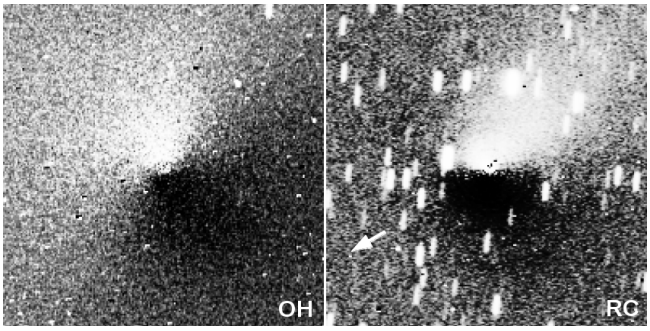


Figure 3.30: Representative OH (left) and RC (right) images from January 12, 2013, processed by removing the azimuthal median profile. Since the signal-to-noise ratio in the OH images is low and since we could not see any variation between images from the same night, we added three processed OH images from January 13 to obtain the result presented here. The images are oriented north up and east left. The field of view is 4.3' × 4.3'. The arrow indicates the direction of the Sun.

We found significant differences between dust and gas behaviour. First, the heliocentric dependence of $Af\rho$ values differs from that of the gas production rates. In December and January, the slope of the $Af\rho$ heliocentric dependence was shallower than that of the gas. Between January 14 and February 7, the slope became much steeper, and steeper than that of

the gas. After perihelion, the slope was similar to that observed in December and January. The evolution of the dust activity thus does not seem to be correlated to the evolution of the gas activity. A second piece of evidence of the decoupling between dust and gas is given by the study of the coma morphology. The features observed in the RC filter do not correspond to the structures observed in the CN, $C_3$, and $C_2$ filters. Changes due to the nucleus rotation were observed in the CN, $C_3$, and $C_2$ morphology during the night but no morphological changes were observed for the dust jet. This is quite surprising given that according to almost all models, the dust is lifted by the gas. Hence, the absence of morphological changes for the dust seems to indicate that the structures that control the dust lifting could be much larger than those involved in the radicals outgassing. Such large-scale structures could remain undetected using our image enhancement techniques. Alternatively, if the dust jet is located around the pole of the nucleus rotation axis, little or no changes in morphology are expected over one rotation. Other volatiles could also drive the dust activity and lift dust grains from the surface; CO and $CO_2$ are good candidates, as we detected a relatively strong $CO_2^+$ ion tail contaminating the NH filter in the dust tail direction. These species have already been found by A'Hearn et al. (2011) to drive comet Hartley 2 dust ejection, for example. In the case of Hartley 2, most of the water comes from icy grains lifted by $CO_2$. If this is also the case for comet Lemmon, we would expect to see an enhancement of OH in the anti-sunward direction, the icy grains being pushed away in the direction opposite to the Sun by the radiation pressure before releasing water. We do not see such enhancement at any time in the images presented in Fig. 3.27. These images were obtained by applying a Larson-Sekanina filtering to the original OH images. However, as presented in Section 2.3.5, this technique better enhances sharp small-scale features while the subtraction of the azimuthal median profile detects fainter large-scale features more efficiently. We then reprocessed the OH and dust images by subtracting an azimuthal median profile and the result is shown in Fig. 3.30. With this technique we could see a slight enhancement in OH in a given direction. Since this feature did not vary between images taken on the same night, we added three OH images to increase the signal-to-noise ratio. In the resulting image we clearly see that OH is enhanced in a region around PA 20°. In the dust image we see the dust tail around PA 300° and the dust jet. From this image we can see that the OH feature is not centred in the tail direction, but is 80° from the anti-sunward direction and then we do not have any observational evidence of the effect of radiation pressure on the icy grains. Another interesting point is that in the case of Hartley 2 an onset of the CO and $CO_2$ activity around 1.4 au pre-perihelion is required to model the lightcurve (Meech et al. 2011). If we assume that the dust grains are lifted by $CO_2$ in comet Lemmon, the change in slope of the dust production around 1.4 au could be explained by the $CO_2$ activity turning on at that time (maybe caused by the illumination of new active areas). However, we could also expect a change in slope of the water production due to the lifting of icy grains by $CO_2$. No such change in the slope of the OH production with the heliocentric distance is detected, but the dispersion of the OH production rates is much higher than for the dust and this prevents us from drawing a clear conclusion.

Evidence suggest that the dust properties changed in February. The slope of the heliocentric dependence and the slope of the dust radial brightness profile both change in early February,

and are correlated with a change in visual magnitudes lightcurves. Moreover, the trend of the dust normalized reflectivity gradient with the nucleocentric distance is completely reversed at the same time: it increased with nucleocentric distance in December and January whereas decreased with nucleocentric distance after February. It is then clear that the properties of the grains changed at that time. However, no trend or sudden variation of the dust colour with the heliocentric distance could be detected. Seasonal effects could be invoked to explain the sudden change in the dust behaviour: different dominant source regions having different grain properties. However, with only optical observations it is difficult to determine if the change occurred in the physical properties of the grains or in their size distribution, and what caused it.

### 3.3.6 Summary

The monitoring of comet Lemmon during several months with TRAPPIST permitted us to obtain several interesting results. The coma morphology indicates the existence of one or several active region(s) on the nucleus. The active region(s) are probably the cause of the seasonal effect observed for the gas species. Indeed, the evolution of the OH, NH, CN, $C_3$, and $C_2$ production rates with heliocentric distance is similar and shows an asymmetry about perihelion, the rate of brightening being steeper than the rate of fading. The abundance ratios in the coma vary: the $C_2$ to CN ratio increases with the heliocentric distance (r) below -1.4 au and decreases with r beyond 1.4 au while the $C_3$ to CN ratio does not vary. Both the morphology and the activity evolution indicate that the dust and the gas are not coupled. Several pieces of evidence also point to a sudden change in the dust properties in early February. Last but not least, thanks to several large sets of continuous data acquired during several hours on a few nights, we could follow gas coma features of CN and $C_2$ and determine a nucleus rotation period of $9.52 \pm 0.05$ hours.

## 3.4 C/2013 A1 (Siding Spring)

These results have been published in Opitom et al. (2016). Minor differences between the production rates presented here and those from Opitom et al. (2016) might exist, since we updated our calibration and dust subtraction procedure. However, it does not impact any of the results we presented.

Comet C/2013 A1 (Siding Spring) (hereafter Siding Spring) is a new NIC, discovered in January 2013 (McNaught et al., 2013) while at 7.2 au from the Sun. Early orbit determinations suggested a very close encounter with the planet Mars on October 19, 2014. This close encounter occurred at 134,000 km from the centre of Mars, at a relative speed of 56 km/s (Kelley et al., 2014). This close approach represented both a threat for orbiters around Mars and a tremendous opportunity to observe this comet from both ground- and Mars-based facilities. In particular, it allowed the study of the deposition of cometary dust into Mars atmosphere, with potential studying the dust composition. The SHARAD radar aboard Mars Reconnaissance Orbiter

(MRO) recorded high values of its Total Electron Content on the nightside (Restano et al., 2015), while the MARSIS radar aboard Mars Express (MEX) detected a strong ionospheric layer just below 100km of altitude, consistent with a meteor shower produced by cometary dust particles (Gurnett et al., 2015). These observations were complemented by the MAVEN data, in which metallic ions, Na, Mg, Al, K, Ti, Cr, Mn, Fe, Co, Ni, Cu, and Zn, and possibly Si and Ca, were identified from ion mass and ultraviolet spectrometry (Benna et al., 2015; Schneider et al., 2015).

We present the analysis of the observations of comet Siding Spring obtained over more than a year with TRAPPIST, along with low-resolution spectra obtained by the ESO/VLT at 6 epochs between July 27 and September 28, 2014. These observations allow us to study the evolution of this comet activity from ~5 au pre-perihelion to ~1.4 au post-perihelion, and to detect an outburst shortly after perihelion, which we try to characterize by modelling the comet thermal evolution.

### 3.4.1 Activity

We started to observe the comet with TRAPPIST on September 20, 2013, when at 4.95 au from the Sun. At this time, it was too faint for gases to be detected with TRAPPIST, so we mainly observed with broad band B, V, Rc, and Ic filters. We also got a few observations with the narrow band continuum filters. Observations were performed once or twice a week, until the comet was lost due to the solar conjunction on April 7, 2014. We recovered the comet on May 21, 2014 and started to observe with both broad band and narrow band filters. We followed the comet until November 15, 2014, a few weeks after its perihelion passage. Exposure times range from 60 s to 240 s for the broad band filters, and from 300 s to 900 s for the narrow band filters. The observational circumstances and production rates for each night are given in Table 3.12.

Low-resolution spectra were acquired with the FORS 2 instrument on six dates between July and September 2014, see Table 3.13. All observations were made using the grism 150I covering the 330-600 nm range. For each observation, 2 or 3 short exposures (from 30 to 180 s depending on the comet brightness and geocentric distance) ensured non-saturated observations of the nucleus and one long exposure (1500 s) allowed us to get good signal-to-noise (S/N) ratio for the gas at larger nucleocentric distances. Except for the first observations, the slit was oriented perpendicular to the tail of the comet. Since the coma was filling the whole slit, we took exposures with a large offset every night to account for the sky background. We noticed a strong contamination from unknown origin in all September 28 spectra. This contamination was mostly located in the blue part of the spectra and prevented us from deriving reliable production rates.We thus discarded these observations from the dataset presented here. Gas production rates derived from spectroscopic observations are presented in Table 3.13. The values in this table are the mean values for each night, and the error bars are computed from the dispersion of the production rates from a single night.

Table 3.12: OH, NH, CN, $C_3$, and $C_2$ production rates and $Af\rho$ of comet C/2013 A1 (Siding Spring) from TRAPPIST observations.

| UT Date | r | Δ | Sun PA | Production rates | | | | | $A(0)f\rho$ |
|---|---|---|---|---|---|---|---|---|---|
| | (au) | (au) | (deg) | | | ($10^{25}$ mol/s) | | | ($10^3$ cm) |
| | | | | Q(OH) | Q(NH) | Q(CN) | Q($C_3$) | Q($C_2$) | (445.3 nm) |
| 2013 Nov 16.52 | 4.42 | 3.82 | 336 | | | | | | 1.54 ± 0.13 |
| 2014 Jan 25.09 | 3.73 | 3.70 | 70 | | | | | | 1.46 ± 0.10 |
| 2014 Jan 29.09 | 3.69 | 3.71 | 74 | | | | | | 1.48 ± 0.08 |
| 2014 Feb 04.06 | 3.63 | 3.73 | 79 | | | | | | 1.46 ± 0.08 |
| 2014 Feb 12.05 | 3.55 | 3.76 | 86 | | | | | | 1.50 ± 0.13 |
| 2014 Mar 26.01 | 3.13 | 3.76 | 127 | | | | | | 1.06 ± 0.08 |
| 2014 Jun 02.42 | 2.43 | 2.93 | 230 | | | | | | 1.03 ± 0.05 |
| 2014 Jun 03.42 | 2.42 | 2.91 | 209 | | | 1.10 ± 0.11 | | | |
| 2014 Jun 17.40 | 2.27 | 2.60 | 220 | | | 1.20 ± 0.11 | | | 1.14 ± 0.08 |
| 2014 Jun 20.44 | 2.24 | 2.53 | 222 | | | | | | 1.19 ± 0.06 |
| 2014 Jun 21.43 | 2.23 | 2.51 | 223 | | | 1.27 ± 0.13 | | | 1.16 ± 0.04 |
| 2014 Jun 22.43 | 2.22 | 2.49 | 223 | | | 1.27 ± 0.14 | | | |
| 2014 Jun 24.42 | 2.20 | 2.44 | 225 | | | 1.26 ± 0.09 | | 1.67 ± 0.11 | 1.15 ± 0.03 |
| 2014 Jun 25.43 | 2.19 | 2.41 | 225 | | | 1.13 ± 0.12 | | 1.51 ± 0.14 | 1.11 ± 0.03 |
| 2014 Jun 26.43 | 2.18 | 2.39 | 226 | | | | | | |
| 2014 Jun 30.42 | 2.15 | 2.29 | 228 | | | 1.42 ± 0.15 | | | 1.11 ± 0.03 |
| 2014 Jul 01.42 | 2.14 | 2.26 | 229 | | | 1.32 ± 0.08 | | | |
| 2014 Jul 06.38 | 2.09 | 2.14 | 232 | | | 1.11 ± 0.07 | 0.58 ± 0.03 | 1.48 ± 0.11 | 1.11 ± 0.06 |
| 2014 Jul 10.42 | 2.05 | 2.03 | 235 | 833 ± 130 | | 1.52 ± 0.09 | | 1.78 ± 0.09 | 1.18 ± 0.03 |
| 2014 Jul 13.41 | 2.02 | 1.95 | 236 | | | | 0.33 ± 0.05 | | 1.12 ± 0.06 |
| 2014 Jul 18.42 | 1.97 | 1.82 | 240 | | | 1.50 ± 0.13 | | 1.38 ± 0.11 | 1.19 ± 0.05 |
| 2014 Jul 21.42 | 1.94 | 1.74 | 242 | 735 ± 100 | | | | | |
| 2014 Jul 24.39 | 1.92 | 1.66 | 244 | | | 1.38 ± 0.07 | 0.38 ± 0.03 | 1.70 ± 0.10 | 1.15 ± 0.02 |
| 2014 Jul 25.40 | 1.91 | 1.63 | 245 | | | | 0.35 ± 0.03 | 1.68 ± 0.07 | |
| 2014 Aug 07.27 | 1.79 | 1.31 | 257 | | | 1.57 ± 0.10 | | 2.00 ± 0.21 | 1.10 ± 0.04 |
| 2014 Aug 10.34 | 1.77 | 1.24 | 261 | 863 ± 106 | 2.04 ± 0.87 | 1.51 ± 0.09 | 0.36 ± 0.05 | 1.77 ± 0.15 | 1.08 ± 0.04 |
| 2014 Aug 17.39 | 1.71 | 1.09 | 274 | 830 ± 132 | 2.45 ± 1.03 | 1.57 ± 0.11 | 0.49 ± 0.05 | 1.91 ± 0.12 | 1.07 ± 0.08 |
| 2014 Aug 20.35 | 1.69 | 1.04 | 281 | 808 ± 143 | | 1.37 ± 0.14 | 0.35 ± 0.05 | 1.51 ± 0.16 | 1.11 ± 0.05 |
| 2014 Sep 04.22 | 1.58 | 0.89 | 13 | 757 ± 117 | 3.49 ± 0.65 | 1.45 ± 0.07 | | 2.04 ± 0.13 | 1.05 ± 0.04 |
| 2014 Sep 06.98 | 1.56 | 0.89 | 37 | 712 ± 129 | 2.89 ± 0.98 | 1.59 ± 0.10 | 0.43 ± 0.04 | 1.87 ± 0.13 | 0.97 ± 0.05 |
| 2014 Sep 07.31 | 1.56 | 0.89 | 39 | 780 ± 154 | | 1.65 ± 0.10 | | 2.04 ± 0.13 | |
| 2014 Sep 19.08 | 1.49 | 1.00 | 84 | 785 ± 109 | | 1.36 ± 0.06 | 0.37 ± 0.02 | 1.56 ± 0.11 | 0.88 ± 0.02 |
| 2014 Sep 24.08 | 1.47 | 1.08 | 90 | 824 ± 111 | 3.79 ± 0.53 | 1.47 ± 0.08 | 0.38 ± 0.03 | 1.83 ± 0.19 | 0.91 ± 0.06 |
| 2014 Oct 06.05 | 1.43 | 1.33 | 95 | 879 ± 112 | 3.40 ± 0.62 | 1.56 ± 0.07 | 0.39 ± 0.05 | 1.63 ± 0.17 | 0.99 ± 0.04 |
| 2014 Oct 13.05 | 1.41 | 1.48 | 95 | 1040 ± 139 | 4.19 ± 0.48 | 1.51 ± 0.06 | 0.40 ± 0.03 | 2.72 ± 0.09 | 0.99 ± 0.03 |
| 2014 Oct 17.03 | 1.40 | 1.57 | 94 | | | | | 2.14 ± 0.07 | |
| 2014 Oct 19.04 | 1.40 | 1.61 | 93 | | 3.74 ± 0.52 | 1.45 ± 0.06 | | | 1.02 ± 0.03 |
| 2014 Oct 20.03 | 1.40 | 1.63 | 93 | 832 ± 137 | 4.08 ± 0.67 | 1.59 ± 0.07 | 0.41 ± 0.04 | 1.82 ± 0.14 | 1.06 ± 0.03 |
| 2014 Oct 29.02 | 1.40 | 1.82 | 89 | 1040 ± 210 | | 2.83 ± 0.13 | | 2.67 ± 0.15 | 1.18 ± 0.05 |
| 2014 Nov 07.02 | 1.41 | 2.00 | 84 | | | 5.60 ± 0.33 | | 4.81 ± 0.45 | 3.07 ± 0.13 |
| 2014 Nov 11.02 | 1.42 | 2.07 | 80 | | | 22.1 ± 1.4 | | 28.9 ± 1.5 | 9.21 ± 0.42 |
| 2014 Nov 12.01 | 1.42 | 2.09 | 79 | 9010 ± 3370 | | 14.7 ± 1.2 | 3.69 ± 0.47 | 25.5 ± 1.7 | 10.10 ± 0.60 |
| 2014 Nov 13.02 | 1.43 | 2.10 | 78 | | | 10.1 ± 0.9 | 1.80 ± 0.38 | 14.0 ± 1.4 | 9.08 ± 0.55 |
| 2014 Nov 14.02 | 1.43 | 2.12 | 77 | | | 7.84 ± 0.92 | 1.31 ± 0.40 | 12.2 ± 1.4 | 8.52 ± 0.65 |
| 2014 Nov 15.01 | 1.43 | 2.13 | 76 | | | 6.77 ± 0.79 | 1.58 ± 0.38 | 9.90 ± 1.39 | 6.50 ± 0.54 |

$r$ and Δ are respectively the heliocentric and geocentric distances (at 2 au one pixel represents about 2000 km). The date given in the first column is the mid-time of the observations.

### Comparative analysis of TRAPPIST and FORS 2 data

We start our analysis by comparing the radial profiles and production rates obtained from TRAPPIST and FORS 2 data to ensure that they are consistent with each other. It is usually difficult to compare data obtained with different instruments, and even more difficult to compare data obtained with different techniques. We only have almost simultaneous observations with

Table 3.13: CN and $C_2$ production rates of C/2013 A1 (Siding Spring) from VLT/-FORS 2 observations

| UT Date | r | Δ | Sun PA | Slit PA | Production rates ($10^{25}$ mol/s) | |
|---|---|---|---|---|---|---|
| | (au) | (au) | (deg) | (deg) | Q(CN) | Q($C_2$) |
| 2014 Jul 25.38 | 1.91 | 1.65 | 245 | 206 | 1.33±0.34 | 1.29±0.18 |
| 2014 Aug 1.38 | 1.85 | 1.46 | 251 | 195 | 1.35±0.26 | 1.29±0.16 |
| 2014 Aug 29.17 | 1.62 | 0.92 | 320 | 256 | 1.42±0.26 | 1.41±0.04 |
| 2014 Aug 31.05 | 1.61 | 0.91 | 334 | 256 | 1.25±0.16 | 1.43±0.14 |
| 2014 Sep 19.01 | 1.49 | 1.00 | 84 | 180 | 1.22±0.10 | 1.65±0.10 |

$r$ and Δ are respectively the heliocentric and geocentric distances (at 2 au one pixel represents about 400 km). The date given in the first column is the mid-time of the observations.

FORS 2 and TRAPPIST for two dates, so we use these observations to assess the agreement between the two data sets. Figure 3.31 shows CN and $C_2$ radial brightness profiles for FORS 2 and the closest TRAPPIST observations. We first notice that the data dispersion is usually smaller in TRAPPIST profiles, especially at large nucleocentric distances, even though we binned the FORS 2 data by 10 pixels in the spatial direction to increase the S/N. The reason is that TRAPPIST profiles result from a median of the flux over the whole coma while FORS 2 profiles are only extracted over a narrow 1.3″-wide slit.

In the case of CN, TRAPPIST radial brightness profiles are in good agreement with the FORS 2 profiles (Fig. 3.31). The two FORS 2 profiles extracted in opposite directions match each other, indicating that the coma is symmetric along the slit axis. The comparison of production rates derived from both telescopes (see Tables 3.12 and 3.13) shows that, within the error bars, production rates derived from FORS 2 observations fit within the trend of TRAPPIST production rates. Comparison of $C_2$ fluxes between narrow band images and low-resolution spectroscopy is more difficult than for the CN fluxes because of the extent of the band and the higher dust contamination. Nevertheless, our measurements of $C_2$ radial profiles and production rates are also in good agreement with each other. Given that the TRAPPIST and FORS 2 radial profiles are a good match for two dates two months apart and that production rates seem consistent with each other, we conclude that these observations can be merged into a single data set. We then analysed this entire data set while studying the evolution of the comet activity and coma composition. The results presented in the next sections thus rely on both FORS 2 and TRAPPIST observations.

**Dust**

We observed comet Siding Spring almost uninterruptedly over more than a year. Figure 3.32 shows the evolution of the $A(0)f\rho$ corrected from phase angle effects, from almost 5 au pre-

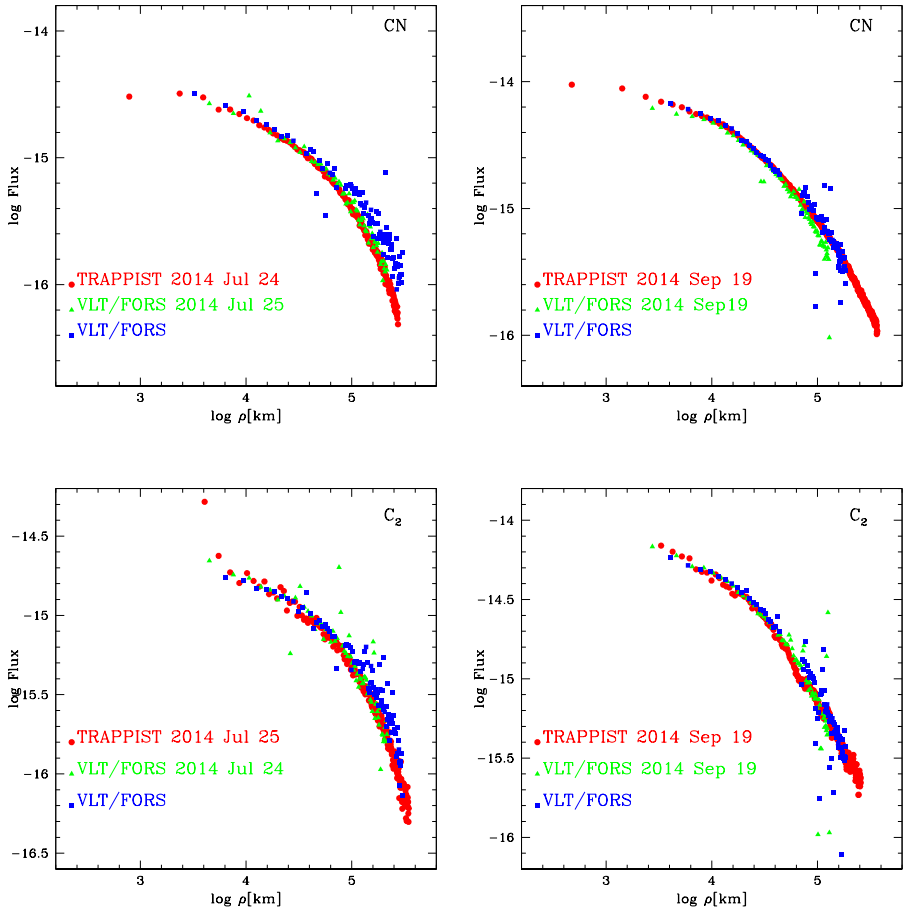


Figure 3.31: C/2013 A1 (Siding Spring) CN (top) and $C_2$ (bottom) brightness profiles from Jul 25 and Sep 19, 2014. TRAPPIST data are represented with red circles and the closest VLT data is overplotted. Data extracted from both sides of the nucleus in the spectra are represented respectively with green triangles and blue squares.

perihelion to more than two weeks after perihelion passage. The long-term trend observed is the same for all continuum filters. The major features are the following:

- The comet activity slowly rises as it approaches the Sun.
- At approximately 4.3 au, the activity starts to decrease at a regular pace until the comet reaches 3 au. Because of the solar conjunction that prevented us from observing between Apr 7 and May 21, 2014, it is difficult to determine when the activity decrease stopped.
- From late May 2013 ($r = 2.5$ au) to mid July ($r = 2.0$ au) the dust activity rises again, then goes through a standstill or a slow decrease period until the comet reaches perihelion.
- After the perihelion passage on October 25 ($r = 1.4$ au), the comet activity rises regularly.

- Between November 7 and November 11 ($r$ = 1.4 au), the data show a sudden rise in activity, consistent with an outburst: both gas and dust production rates increase by a factor of 5 within a few days. Dust production peaks on Nov 12, then decreases regularly. This outburst was also observed from total visual magnitudes measurements by amateur astronomers (see e.g. Seiichi Yoshida's web page[3]).

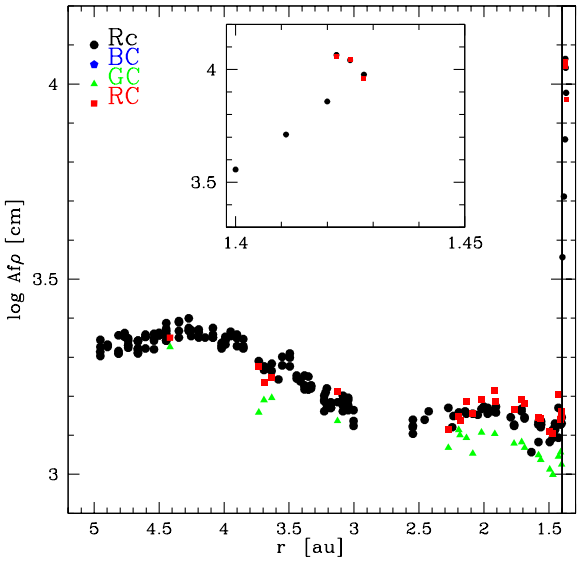


Figure 3.32: Logarithm of comet C/2013 A1 (Siding Spring) $A(0)f\rho$ corrected from phase angle effect as a function of the heliocentric distance $r$. The $A(0)f\rho$ was measured from Rc broad band filter and from narrow band BC, GC, and RC filters when the comet was bright. The vertical line indicates perihelion. The inset shows zoomed image of post-perihelion data.

Li et al. (2014) reported measurements of comet Siding Spring $Af\rho$ from observations performed with the Hubble Space Telescope. They measured a value of 2520 cm, 2120 cm, and 1720 cm at heliocentric distances of 5.58, 3.77, and 3.28 au respectively. These measurements are corrected from the phase angle effect using the same function that we used in this paper. From the closest TRAPPIST observations in the broad band Rc filter, we measured $Af\rho$ values of $2230 \pm 30$, $1870 \pm 24$, and $1540 \pm 22$ cm at respectively 4.61, 3.73, and 3.33 au from the Sun. Our measurements are lower than those reported by Li et al. (2014); however, the $Af\rho$ values we report here are measured at a cometocentric distance of 10,000 km instead of 5,000 km for the Li et al. (2014) values. We observed a decrease in $Af\rho$ with cometocentric distance, and measured values around 5,000 km of $2360 \pm 32$, $2060 \pm 26$, and $1720 \pm 25$ cm at respectively 4.61, 3.73, and 3.33 au from the Sun, consistent with Li et al. (2014). Other $Af\rho$ values have been published by Stevenson et al. (2015) from NEOWISE infrared observation, but any comparison between infrared and visible measurements is made difficult by colour effects and the different size of the field of view.

[3] http://www.aerith.net/comet/catalog/2013A1/2013A1.html

Taking advantage of our regular observations of the dust continuum through RC and BC narrow band filters during the same night, we are able to study the dust colour and its evolution with heliocentric distance. The dust colour is usually computed as the normalized gradient of $A(\theta)f\rho$ from two continuum filters:

$$\text{colour}[\lambda_1, \lambda_2] = \frac{Af\rho_1 - Af\rho_2}{\lambda_1 - \lambda_2} \frac{2000}{Af\rho_1 + Af\rho_2} \tag{3.1}$$

The normalized reflectivity gradient is expressed as the percentage of reddening per 1,000 Å. Fig. 3.33 shows the evolution of the dust colour as a function of heliocentric distance. Because of the large dispersion, it is impossible to draw a clear trend with the heliocentric distance. Our values are higher than those published by Li et al. (2014) at about the same heliocentric distance (6%/1,000 Å at 3.8 au), but consistent if we consider the large dispersion in the data. Li et al. reported a reddening of the dust between 4.6 and 3.3 au, which they attributed to icy grains sublimating in the coma. We only have a few colour measurements after perihelion, so it is difficult to assess the effect of the outburst on the dust colour, even though we may be seeing a bluer dust colour at that time.

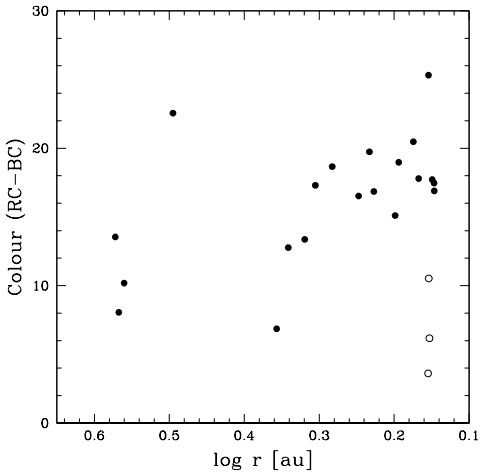


Figure 3.33: Evolution of comet C/2013 A1 (Siding Spring) dust colour as a function of the heliocentric distance. Pre-perihelion values are represented with filled circles and post-perihelion values with open circles.

### Gas

Figures 3.34 and 3.35 show the evolution of the gas production rates and $A(0)f\rho$ with the heliocentric distance from 2.43 au pre-perihelion until after perihelion. Fig. 3.35 and Table 3.12 reveal there is no clear increase in most gas production rates while the comet approaches the Sun. They vary only slightly between 2.43 au and perihelion, which may seem surprising. The NH production rates are the only values that increase significantly while the comet approaches the Sun. However, the uncertainties of the NH production rates are larger given the low S/N.

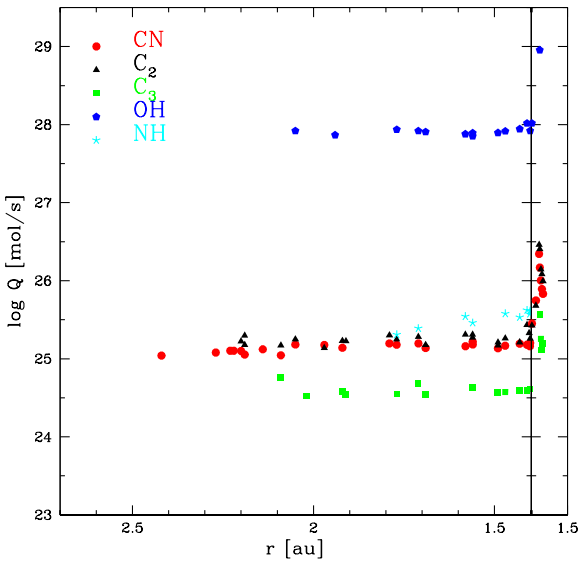


Figure 3.34: Logarithm of comet C/2013 A1 (Siding Spring) OH, NH, CN, $C_3$, and $C_2$ production rates as a function of the heliocentric distance $r$ (au). The $r$-axis is interrupted at perihelion (1.4 au).

The rise of the activity after perihelion followed by the outburst is also clearly visible in Fig. 3.35. Gas production rates are multiplied by a factor of approximately 5 between November 7 and November 11, 2014. They peak on November 11 and decrease during the following days. This outburst is further analysed later. We fitted power-law slopes on pre-perihelion data in order to study the activity evolution of the comet. We did not fit slopes for post-perihelion data because of the outburst we detect in the data. These slopes are given in Table 3.14. OH, CN, and $C_2$ slopes are low, which confirms that these production rates only slightly increase as the comet approaches the Sun. As already mentioned, the NH production rates increase faster than other species. The $C_3$ slope is positive, which should mean that $C_3$ production rates decrease with decreasing heliocentric distance. However, this is probably artificially induced by the first point, which seems higher than the general trend. The general dust slope is also slightly positive. This confirms the observations we reported in the previous section.

Water production rates were reported by Bodewits et al. (2015) from observations with the UltraViolet-Optical Telescope on board Swift between November 2013 and October 2014. They measured $H_2O$ production rates of $(11.1 \pm 1.0) \times 10^{27}$, $(12.1 \pm 0.27) \times 10^{27}$, $(13.0 \pm 0.45) \times 10^{27}$, $(12.5 \pm 0.62) \times 10^{27}$, and $(17.2 \pm 0.5) \times 10^{27}$ mol/s on July 09, August 19, September 18, October 13, and October 23, 2014, respectively. They could not detect water until the comet reached 2.46 au pre-perihelion. Then they observed an increase in water production rates and active area between 2.46 and 2.0 au, followed by a plateau of water production rate along with a decrease in active area between 2 au and perihelion. The closest TRAPPIST observations allowed us to derive equivalent water production rates ($Q(H_2O) = 1.361 r^{-0.5} Q(OH)$, Cochran and Schleicher

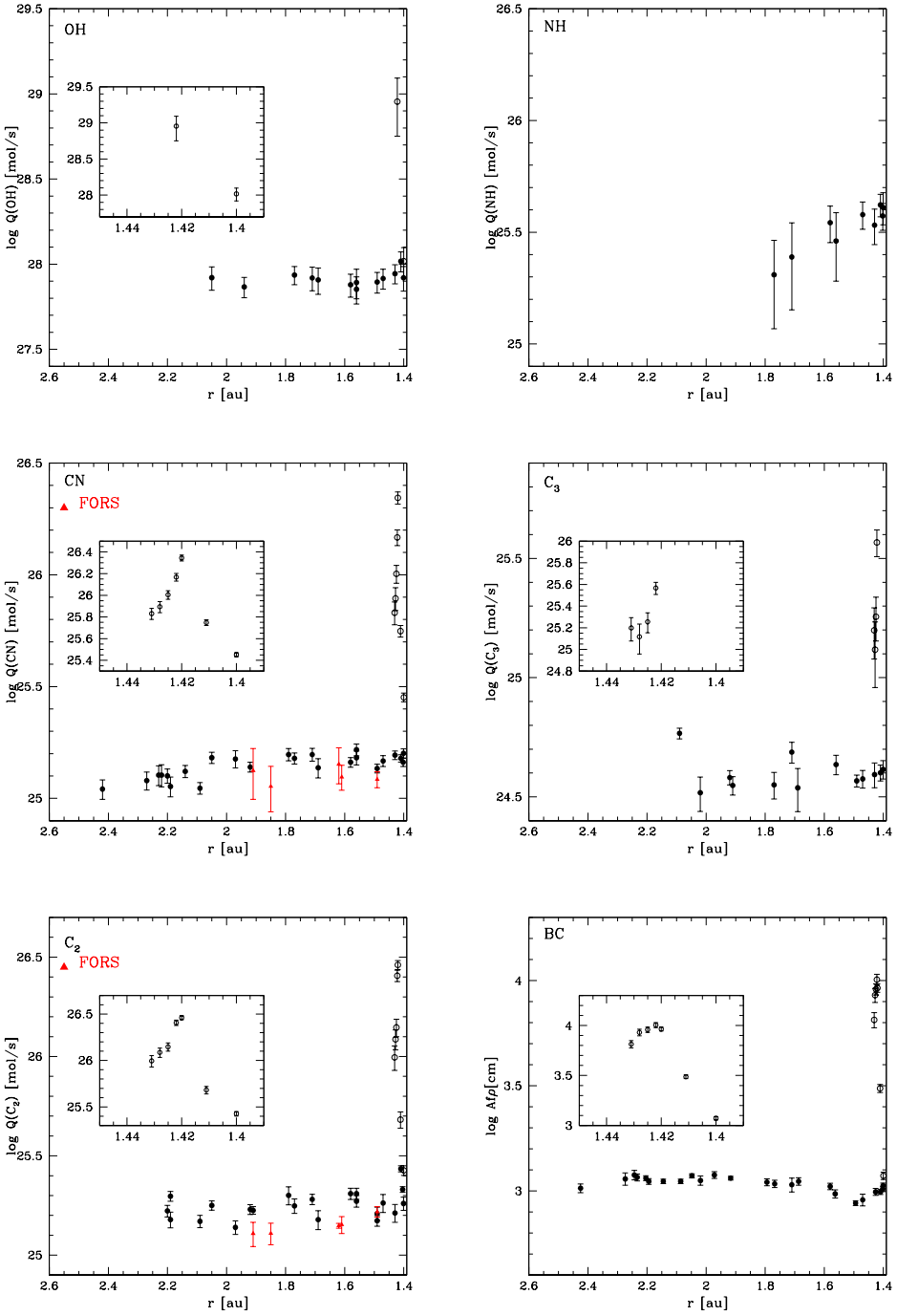


Figure 3.35: Comet C/2013 A1 (Siding Spring) OH, NH, CN, $C_3$, and $C_2$ production rates and $A(0)f\rho$ as a function of the heliocentric distance ($r$). Pre-perihelion data are represented with filled symbols and post-perihelion data with open symbols. The inset shows zoomed image of post-perihelion data. For CN and $C_2$, spectroscopic determinations from FORS 2 have been added.

Table 3.14: Fitted power-law slopes for comet C/2013 A1 (Siding Spring) OH, CN, $C_3$, and $C_2$ production rates and $A(0)f\rho$ heliocentric dependences pre-perihelion.

| Species | r-dependence |
|---|---|
| OH | -0.31±0.22 |
| NH | -2.10±0.55 |
| CN | -0.38±0.09 |
| $C_3$ | +0.65±0.30 |
| $C_2$ | -0.79±0.20 |
| $A(0)f\rho$ | +0.21±0.04 |

1993) of $(8.3\pm1.3)\times10^{27}$, $(8.5\pm1.5)\times10^{27}$, $(8.75\pm1.2)\times10^{27}$, $(11.9\pm1.6)\times10^{27}$, and $(9.6\pm1.6)\times10^{27}$ mol/s for observations made respectively on July 10, August 20, September 19, October 13, and October 20, 2014. Most of these observations are consistent within the error bars with values reported by Bodewits et al. (2015). The only large discrepancy is between the $H_2O$ production rates measured by Bodewits et al. (2015) on October 23 and our observations performed on October 20. The origin of this discrepancy is not clear, even though the production rate we report for October 20 is lower than the contemporary observation in Table 3.12. Measurements of OH production rates have also been reported by Crovisier et al. (2014) from observations with the Nancay radio telescope. They measured production rates of $(1.3\pm0.3)\times10^{28}$ mol/s between October 5 and 8, 2014, and of $(3.3\pm0.4)\times10^{28}$ mol/s between October 11 and 13, 2014. The first measurement is in agreement within the error bars with the value we report for October 6 (Table 3.12). The second is larger than the OH production we measured on October 13, but Crovisier et al. (2014) mention that their value might be overestimated owing to uncertain Galactic background. Finally, OH, CN, and $C_2$ production rates have also been reported by Schleicher et al. (2014) from observations at the Lowell Observatory on October 12 and 20, 2014, and are mostly in good agreement with the values we report in Table 3.12.

### 3.4.2 Composition

We computed several production rate ratios in order to characterize the coma composition. Comet Siding Spring is a typical comet in terms of $C_2$/CN and $C_3$/CN ratios, as defined by A'Hearn et al. (1995). The evolution of NH, CN, $C_3$, $C_2$ production rates, and the $A(0)f\rho$ relative to OH, are represented in Fig. 3.36. A power-law fit is adopted for each ratio in order to assess the evolution of the coma composition more easily. The $C_2$/OH, $C_3$/OH and CN/OH ratios do not significantly vary with heliocentric distance. On the contrary, the NH/OH ratio increases with decreasing heliocentric distance. However, NH scalelengths and their dependence with heliocentric distance are poorly known, which makes it difficult to interpret the trend in the evolution of the NH/OH ratio. The bottom part of Fig. 3.36 shows the evolution of the dust to gas ratio. The slope of the fit is significantly larger than zero, meaning that the coma becomes less dusty as it approaches the Sun. Although we only have a few measurements of these ratios

during the outburst, no significant variation of the coma composition at that particular time can be pointed out.

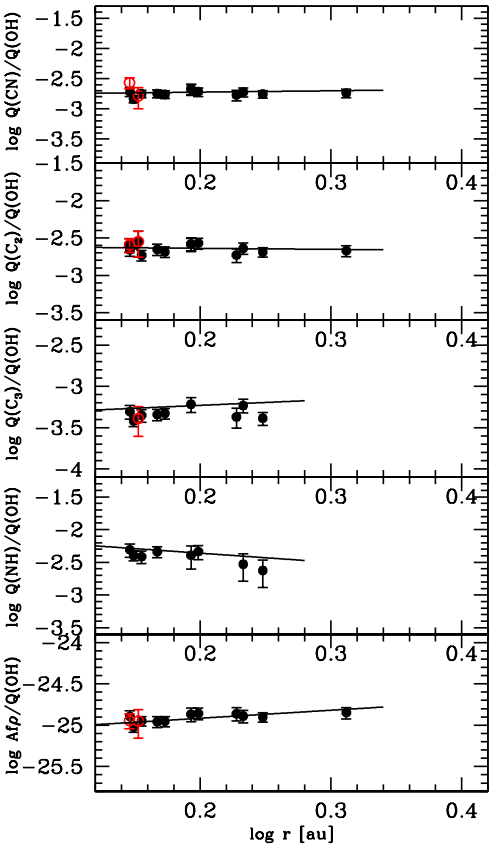


Figure 3.36: Comet C/2013 A1 (Siding Spring) NH, CN, $C_3$, $C_2$, and $A(0)f\rho$ to OH production rate ratios as a function of the heliocentric distance. Pre-perihelion values are represented with filled symbols and post-perihelion values with open red symbols. Full lines represent power-law fits of the ratio variations with the heliocentric distance pre-perihelion.

We also computed ratios of the production rates relative to the CN production rates, since this species is the easiest, and then usually the first one, we detect. The results are shown in Fig. 3.37. We fitted power-law slopes to represent the evolution of these ratios with the heliocentric distance pre-perihelion. The resulting slopes are given in Table 3.15. As previously stated, most ratios do not vary strongly with the heliocentric distance, except for the NH to CN ratio. The higher positive slope for the $C_3$ is caused by the first point, which is out of the trend.

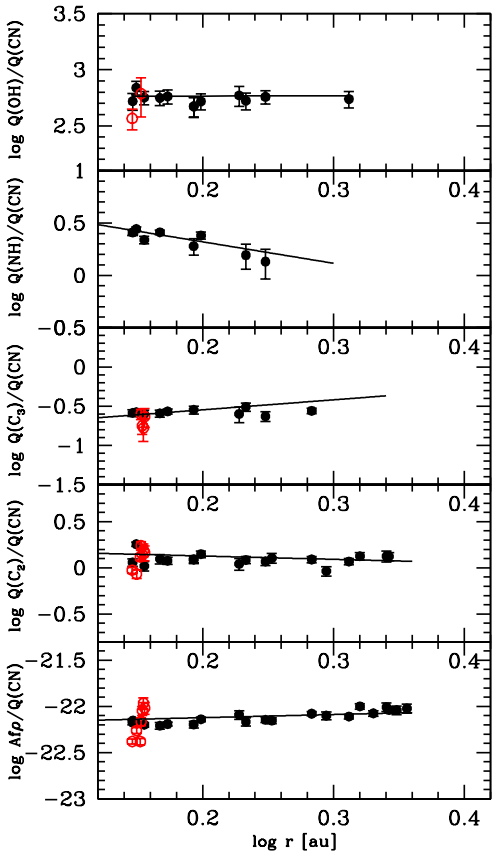


Figure 3.37: Comet C/2013 A1 (Siding Spring) OH, NH, $C_3$, $C_2$, and $A(0)f\rho$ to CN production rate ratios as a function of the heliocentric distance. Pre-perihelion values are represented with filled symbols and post-perihelion values with open red symbols. Full lines represent power-law fits of the ratio variations with the heliocentric distance pre-perihelion.

Table 3.15: Fitted power-law slopes for the heliocentric dependence of comet C/2013 A1 (Siding Spring) OH, $C_3$, $C_2$, and $A(0)f\rho$ to CN ratios pre-perihelion.

| Species | r-dependence |
|---|---|
| log[Q(OH)/Q(CN)] | -0.20±0.25 |
| log[Q(NH)/Q(CN)] | -2.05±0.65 |
| log[Q($C_3$)/Q(CN)] | +1.27±0.37 |
| log[Q($C_2$)/Q(CN)] | -0.36±0.27 |
| log[Q($A(0)f\rho$)/Q(CN)] | +0.34±0.07 |

### 3.4.3 Morphology

In this section, we discuss the morphology of the coma and its evolution during our observations. We subtracted an azimuthal median profile from every image in order to enhance

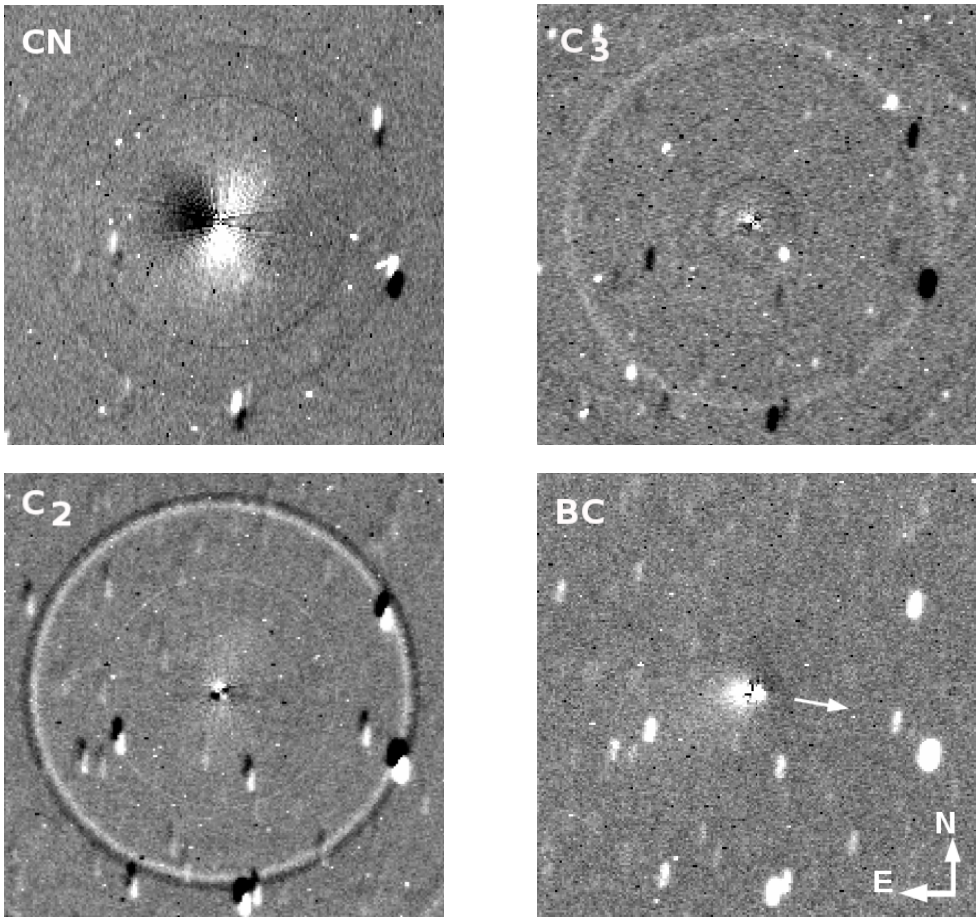


Figure 3.38: C/2013 A1 (Siding Spring) CN, $C_3$, $C_2$, and dust from BC filter images from November 11 and 12 processed by subtracting an azimuthal median profile. All images are oriented with north up and east left. The field of view is $4.3' \times 4.3'$. The arrow indicates the direction of the Sun. The circles in the images are artefacts due to a bright star in the field of view.

the contrast between the average coma and the morphological features. Except for CN, we only detect weak or no features. We show an example of CN, $C_3$, $C_2$, and dust from BC filter images in Fig.3.38. These images were taken one day after the outburst on November 11, 2014 (but on November 12 for $C_3$). The features visible in Fig. 3.38 were already there in the August and September images, but they were not as bright and contrasted. We do not observe any particular change of the coma morphology during the observations, or at the time of the outburst, except for a change in the position of the features caused by a variation of the viewing geometry.

The BC enhanced image shows two small jets in opposite directions, different from the tail direction. Some of the BC images (not shown here) also display an enhancement of the coma in the tail direction, which is barely visible in Fig. 3.38. The position of the dust jets is difficult

to determine precisely, given their small spatial extension. The $C_3$ and $C_2$ enhanced images are very similar to each other. They both display two short jets in opposite directions. Even though it is difficult to determine their precise position, they appear close to the dust jets we identified before. However, they are weaker than the dust jets, and are not detected in every image before the outburst. Finally, the CN morphology is completely different: two broader and more extended fans can be observed around PA 185° and PA 330°.

### 3.4.4 Outburst

#### Observational characterization

In section 3.4.1, we inferred that Siding Spring underwent an outburst approximately two weeks after its perihelion passage. From our data set, we can indeed observe an increase in both gas and dust productions consistent with an outburst occurring between November 7.02 and November 11.02, 2014. The CN and $C_2$ radial profiles observed on November 11 diverge from stationary profiles. Fig. 3.39 shows CN and $C_2$ radial profiles from November 11 (i.e. our first observation after the outburst), November 12, and November 13. The most prominent feature visible on the November 11 CN profile is a bump with a rather well-defined shoulder at around 60,000 km from the nucleus, in addition to the usual stationary radial profile which is still visible at large nucleocentric distance (after 125,000 km). In the following two profiles, this feature is moving away from the nucleus as it propagates into the coma. The same feature is also visible in the $C_2$ profiles. We believe that this is the signature of the outburst. A large amount of gas is released at the time of the outburst, and then expands through the coma. Measuring the position of this shell of material from day to day could in theory allow us to derive the expansion speed of the gas in the coma. However, as can be seen in Fig. 3.39, its edge is not sharp enough to unambiguously determine the position of the gas shell in each profile. On November 14 and 15, the shape of the CN profile gradually comes back to its pre-outburst shape.

We attempted to reproduce the shape of the radial profiles observed in Fig. 3.39 in order to constrain the expansion velocity of the gas during the outburst, and the time at which it occurred. For each profile in Fig. 3.39, the dashed line represents the Haser model adjusted on the data. As expected, the Haser model fails to reproduce the shape of these radial profiles observed shortly after the outburst. This also means that the production rates we derived in Sect. 3.4.1 are not representative of the real gas production at the time of the outburst. From the profile shape, we estimate that a two-components model could reproduce the observations. We thus considered a constant underlying gas emission $Q_b$ in stationary state and described by the Haser model, to which we added the brief emission of a large amount of gas that expands at a given velocity $v_o$ into the coma.

The true physical meaning of this velocity $v_o$ is somewhat difficult to interpret. As has already been mentioned, the Haser model is not physically realistic (Combi et al., 2004). It assumes that both parent and daughter species follow purely radial motion. However, as a result of

the photodissociation of the parent species, the daughter species have an additional velocity component distributed isotropically in the reference frame of the parent species, which is not accounted for in the Haser model. This problem has been addressed using more complicated models, such as the Vectorial Model (Festou, 1981), or using Monte Carlo techniques (Combi and Delsemme, 1980). In this paper, we use the velocity $v_o$ to describe the expansion of a shell of material (in our case CN or $C_2$) observed in the coma of comet Siding Spring following its outburst. We thus refer to this as the gas expansion velocity, but it is important to keep in mind that it probably does not represent the velocity of the gas directly ejected from the nucleus at the time of the outburst.

We used two exponentials to describe the gas release during the outburst: an increasing exponential with a characteristic timescale $\tau_1$ of typically a few hours to describe the onset of outburst activity, and a decreasing exponential with a characteristic timescale $\tau_2$ of typically a few days to describe the slow decrease in the gas emission following the outburst. We consider the start of the outburst $t_o$ as the time at which the peak gas emission $Q_o$ occurs. As for the Haser model, we assumed spherical symmetry for the gas emission, a constant radial velocity $v_o$, and a single-step photodissociation of parent molecules into daughter molecules. We used the same scalelengths as for the rest of our analysis. In our model, the radial density distribution of daughter molecules $n(r)$ is thus described by:

$$n(r) = \frac{Q}{4\pi r^2}\left[\frac{\beta_0}{\beta_1-\beta_0}\right]\left[\exp(-\beta_0 r)-\exp(-\beta_1 r)\right] \tag{3.2}$$

with

$$Q = \frac{Q_b}{v} + \frac{Q_o}{v_o}\exp(-\frac{t_o-t}{\tau_1}) \qquad \text{if} \quad t < t_o \tag{3.3}$$

$$Q = \frac{Q_b}{v} + \frac{Q_o}{v_o}\exp(-\frac{t-t_o}{\tau_2}) \qquad \text{if} \quad t > t_o \tag{3.4}$$

In these equations $r$ is the radial distance in the coma, $v$ is the velocity of the gas in stationary equilibrium fixed to 1 km/s as in Sect. 3.4.1, and $\beta_0$ and $\beta_1$ are respectively the parent and daughter scalelengths. First, we tried to model the outburst using only one exponential to simulate the decrease in the gas emission directly following the outburst. However, the transition between stationary equilibrium and the outburst was too sharp compared to the profiles shown in Fig. 3.39, and so we added a second exponential to simulate the onset of the activity. We also tried to use simpler functions as slopes, but they could not reproduce the shape of the profiles observed at the time of the outburst as did exponentials.

For CN we determined the constant gas emission $Q_b$ by adjusting the Haser model on the November 11 observations. We made the adjustment between cometocentric distances of 100,000 km and 160,000 km, since the gas released during the outburst could not have had the time to reach this part of the coma yet. We obtained $Q_b(\mathrm{CN}) = 4.2 \times 10^{25}$ mol/s. This

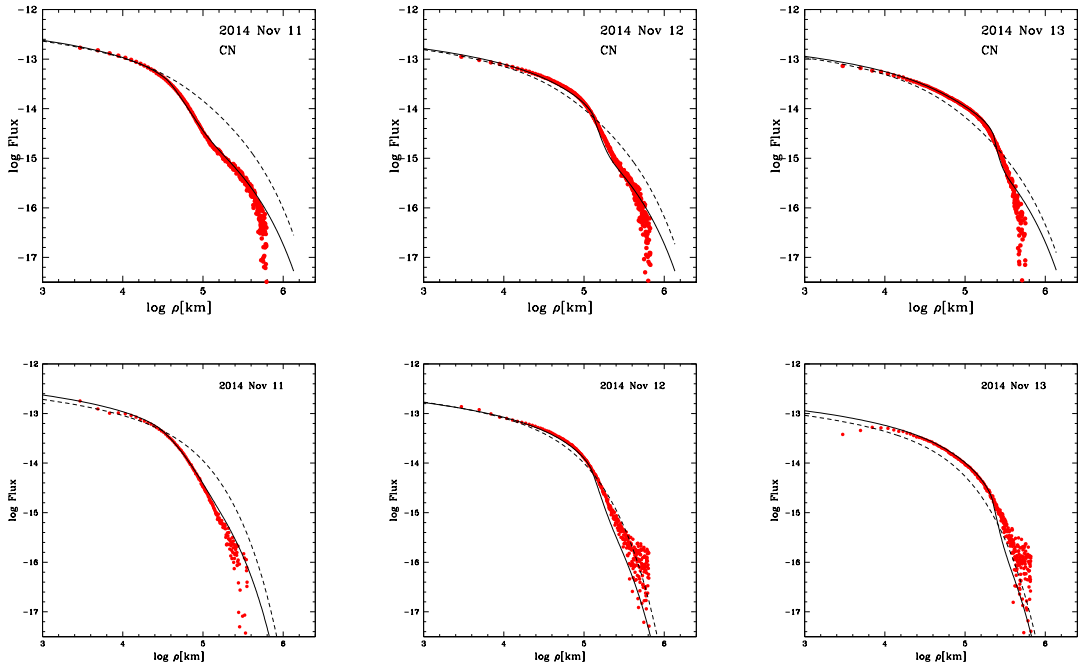


Figure 3.39: Comet C/2013 A1 (Siding Spring) CN (top) and $C_2$ (bottom) brightness profiles from November 11, 12, and 13, 2014 ($r$ = 1.4 au). The observed profiles are represented with red dots, the Haser model is represented by the dashed line and the outburst model is represented by the black line.

production rate is close to the one measured four days earlier, on November 7 (see Table 3.12). As explained before, we used a constant value of $Q_b$ for all outburst profiles. Even if the gas production rates vary from day to day, as can be seen from Table 3.12, this variation is small compared to the amount of gas released at the time of the outburst. Furthermore, in the November 12 and 13 profiles, the influence of the gas released during the outburst extends so far into the coma that it is impossible to independently adjust the value of $Q_b$ as was done for the November 11 profile. We then tried to constrain the values of $Q_o$, $v_o$, $t_o$, $\tau_1$, and $\tau_2$ that match simultaneously the observed profiles on Nov 11, 12, and 13. From the CN profiles, we obtained $Q_o(CN) = (2.7 \pm 0.5) \times 10^{26}$ mol/s, $v_o = 1.1 \pm 0.2$ km/s, $\tau_1 = 0.3 \pm 0.1$ d, $\tau_2 = 1.6 \pm 0.2$ d, and $t_o$ = Nov 10.6±0.2. This set of models is overplotted on the observed CN profiles in the upper part of Fig. 3.39 using a black line. For the three dates, the observed CN profile is much better represented by our model (black curve) than by the Haser model (black dashed line). This model is able to reproduce the bump observed in the radial profile, and its propagation through the coma during the days following the outburst. Larger discrepancies between the observed and modelled profiles only appear at large nucleocentric distances, however. This is mainly caused by the uncertainties in the measurements due to the high airmass of these observations and the faint signal at these distances.

We repeated the same process for the $C_2$ profiles. We measured $Q_b(C_2) = 6.55 \times 10^{25}$ mol/s.

Once again, this value is close to the one measured on November 7. We then attempted to find the best set of parameters to simultaneously reproduce the three $C_2$ profiles. We obtained $Q_o(C_2) = (3.9 \pm 0.5) \times 10^{26}$ mol/s, $v_o = 1.1 \pm 0.2$ km/s, $\tau_1 = 0.4 \pm 0.1$ d, $\tau_2 = 1.8 \pm 0.2$ d and $t_o =$ Nov 10.7±0.2. This set of models is overplotted on the observed $C_2$ profiles in the lower part of Fig. 3.39. For the November 11 profile, our model is a much better representation of the data than the Haser model. For the other two profiles, the agreement is not as good as for CN, especially at large nucleocentric distances, but still better than with the Haser model. We were not able to apply our model on the OH data because the S/N of these profiles was too poor. We do not have any NH observations at the time of the outburst, nor do we have $C_3$ observations the day after the outburst to perform the same analysis. We note that it is usual for a cometary outburst's typical time to reach the peak emission to be shorter than the recovery time, even though the characteristic times for an outburst vary from one comet to another (see Schleicher and Osip 2002, Li et al. 2011, Manfroid et al. 2007). The $C_2$/CN ratio produced during the outburst is 1.46. Within the error bars, this is consistent with the ratios measured before the outburst, indicating that no obvious change of the coma gas composition occurred during the outburst.

Our model provides a satisfactory representation of the shape of the radial brightness profile of the coma of comet Siding Spring for the three days following the outburst using one single set of parameters for each species. Parameters derived from the $C_2$ profiles and from the CN profiles agree with each other within the error bars. We can determine that the outburst most probably occurred on November 10 around 15:30 UT (± 5h). The expansion velocity of the gas after the outburst was $v_o = 1.1 \pm 0.2$ km/s. This velocity is consistent with the gas outflow velocity of 1 km/s that we assumed in the Haser model. Only a few measurements of gas velocity during an outburst have been made, but our value is close to the CN radial expansion velocity of $0.85 \pm 0.04$ km/s measured by Schulz et al. (2000) during the activity outburst of comet C/1995 O1 (Hale-Bopp). Manfroid et al. (2007) measured gas velocities of $0.4 - 0.6$ km/s in the coma of comet 9P/Tempel 1 after the Deep Impact event. This is lower than the velocity we measured here, but the outburst of comet Tempel 1 was caused by the impact of a 362 kg mass on the nucleus and the outburst mechanism is thus different from the one observed here. Finally, the velocity we measure here is also in agreement with OH expansion velocities in the coma of quiescent comets at the same heliocentric distance (e.g. Bockelee-Morvan et al. 1990, Tseng et al. 2007).

Unfortunately, we were only able to determine an upper limit for the velocity of the dust ejected during the outburst. We attempted to measure the position of the dust shell ejected during the outburst in successive BC images taken on the days after the outburst. However, the S/N in the images is low, making the determination of the dust shell position difficult. The S/N was higher in RC filter but we do not have regular observations in this filter around the time of the outburst. We could only determine an upper limit of 100 m/s. This seems low compared to the dust velocities usually measured during cometary outbursts. Indeed, Hsieh et al. (2010) and Lin et al. (2009) measured velocities around 550 m/s for the outburst of comet 17P/Holmes, while Schulz et al. (2000) measured a velocity of 200 m/s for the outburst of

comet C/1995 O1 (Hale-Bopp). Lara et al. (2007) measured velocities ranging from 150 to 230 m/s in the coma of comet 9P/Tempel 1 after the Deep Impact event. Such a low dust velocity could indicate that the outburst mostly released large grains.

**Modelling the outburst and activity pattern**

Based on the gas production rates determined in the previous sections, our goal is to estimate the thickness of dust that would be required at the surface to reproduce the pre-perihelion production rates and the outburst observed in our dataset, using a technique similar to the one described in Guilbert-Lepoutre et al. (2014). We based our calculation on the measurement of the CN production rates. CN is the daughter molecule of HCN, which if present in the nucleus under a dusty crust, may not sublimate freely. If buried under a dusty crust, it would follow a diffusion regime, with a mass loss rate written as (assuming an ideal gas law, Fanale and Salvail (1984); Schorghofer (2008); Gundlach et al. (2011); Guilbert-Lepoutre et al. (2014))

$$J \sim \frac{\varphi}{\Delta r} \sqrt{\frac{2m}{\pi k_B T}}\, P_S(T), \tag{3.5}$$

where $J$ is the ice loss rate from a subsurface layer buried under the crust, $\varphi$ the permeability of the crust, $\Delta r$ [m] its thickness, $m$ [kg] the molecular weight, $k_B$ [JK$^{-1}$] the Boltzmann constant, $T$ [K] the temperature, and $P_S(T)$ [Pa] the saturation vapour pressure given by the Clausius-Clapeyron equation

$$P_S(T) = \alpha\, e^{-E_a/k_B T} \tag{3.6}$$

with $\alpha = 3.86 \times 10^{10}$ Pa and $-E_a/k_B = 4023.66$ K for HCN. In our calculations, the temperature distribution at the surface and in the nucleus of the comet is determined using a numerical model of three-dimensional heat transport (Guilbert-Lepoutre et al., 2011). The model solves the heat equation taking into account conduction via contacts between grains, radiation within pores, insolation, and thermal emission at the surface. This distribution is computed as a function of time and orbital position of the comet. Since Siding Spring is a dynamically new comet with no previously known perihelion passage, we start our simulation at 100 au with a temperature of 20 K. We assume that the upper layer is made of porous dust, with 85% porosity and thermal inertia of 15 $Jm^{-2}K^{-1}s^{-1/2}$, which is consistent with the measurements of low thermal inertias for comets in general and 67P/Churyumov-Gerasimenko, which is being thoroughly studied by the ESA/Rosetta mission (Lowry et al., 2012; Gulkis et al., 2015). We then estimate the thickness $\Delta r$ of the dusty crust by inverting Eq.3.5 for each orbital position of the comet where we have a measurement of CN production rate.

Given that our study of the coma morphology has shown that Siding Spring presents jets, it is unlikely that the entire surface of its nucleus is active: we expect that this would lead to local variations in the crust thickness. We must therefore keep in mind that our modelling is aimed at providing order of magnitude results, in order to understand the general behaviour of Siding Spring's activity. Before the outburst, our calculations show that CN production

rates can be reproduced if we assume that the thickness of the dusty crust at the surface of Siding Spring (assuming that the overall surface is active) is steadily increasing, from 3.5 cm on June 03, when at 2.42 au, to ~8 cm on October 29, when at 1.4 au. This is consistent with the expected progressive formation of a dust mantle at the surface of an active comet, and also consistent with our inference of a coma becoming less dusty when the comet approaches the Sun. Eventually, the porosity of the dust mantle may become too small to allow any particle to be released, thus forming a stable crust, with a cohesive strength greater than the vapour pressure building up below it. However, with insolation becoming more efficient in sublimating subsurface ice when the comet reaches perihelion, the gas pressure below the crust would increase, and the dust mantle could be totally or partially blown off. This process can be invoked to explain the outburst of comet Siding Spring. From November 7, our calculations show that the crust thickness required to reproduce the CN production rates decreases with a minimal thickness of 4.5 cm achieved on November 11. Afterwards, the crust thickness increases again. It is unclear from the available data whether the whole dust mantle was blown off, or only part of it. Although many parameters involved in these calculations are unknown or poorly constrained, we can estimate that 50 to 120 $\times$ $10^6$ kg of dust were released during the outburst. These numbers are in fact consistent with the dust production we measured, and the low velocity of dust particles at the time of the outburst, which indicates that large grains were emitted. A very rough estimation of the total mass of the gas ejected during the outburst can be made by using the CN production rates and characteristic times we derived, and the CN to OH ratio we measured. We then obtain that about 9 $\times$ $10^3$ kg of water were ejected during the outburst. This implies that the dust to gas ratio of the material ejected during the outburst is about 10000, which is very high compared to what was measured in the coma of 67P for example ((Rotundi et al., 2015)) and reinforces our hypothesis of a dust crust blown away as the origin of the outburst. It is however important to keep in mind that this is only an order of magnitude result. Comparing this value to pre-outburst values would require to make numerous hypotheses on the grain properties to estimate the dust mass production rate from the $Af\rho$ measurements and is out of the scope of this work. The dust particles forming a dust mantle are expected to be the heaviest relative to their cross section to be entrained by the outgassing. Therefore, by basing our calculations on the CN production rates measured before and during the outburst, we can reproduce the activity pattern and dust properties observed for comet Siding Spring in a self-consistent way. This may indicate that the mechanism at the origin of Siding Spring's outburst is related to dust mantle formation and destruction.

### 3.4.5 Summary and Conclusion

We present a unique data set consisting of more than a year of regular observations of comet C/2013 A1 (Siding Spring) with TRAPPIST in Chile, along with low-resolution spectra obtained with the ESO/VLT FORS 2 instrument. We first demonstrated that simultaneous measurements of gas radial profiles and production rates from narrow band photometry with TRAPPIST and low-resolution spectroscopy with FORS 2 are in good agreement and could be used to

complement each other in the future. We then studied the evolution of the comet activity, along with its gas and dust composition, using various ratios such as CN/OH, $C_2$/OH, or $C_3$/OH, which showed little or no variation with heliocentric distance. Only the NH/OH ratio increased while the comet approached the Sun, but this could just be the effect of poorly known NH scalelengths. Enhancement techniques applied to all images allowed us to detect morphological features in the coma. Except for the dust and CN, these features were weak and could not be detected in all images. The orientation of $C_3$ and $C_2$ features is difficult to determine owing to their small spatial extension. CN and dust features both have an hourglass shape, but are not oriented in the same direction. This indicates that they probably do not originate from the same source region(s). This monitoring allowed us to detect an outburst of activity, which we have characterized and modelled. The CN and $C_2$ production rates were measured at the peak of the outburst. The $C_2$/CN ratio measured at that time is consistent within the error bars with the ratios measured before the outburst, while the production rates were multiplied by about a factor of 5. Overall, we could not detect any significant change in the coma composition or dust to gas ratio after perihelion, nor at the time of the outburst, which may indicate a certain level of homogeneity of the nucleus composition.

The gas radial profiles observed shortly after the outburst were different from those usually observed for this comet. We provided a simple model for representing them. This model considers the outburst as a sudden emission of a large quantity of gas that expands in the coma at a given velocity. The outburst is added to the equilibrium gas emission described by the Haser model. We considered an exponential rise in the gas emission with a characteristic timescale $\tau_1$ to reach a maximum production rate, then an exponential decrease with a characteristic timescale $\tau_2$. For consistency, we used the same hypothesis as in the Haser model, as well as the same scalelengths. We found a set of modelling parameters that simultaneously provided a good representation of the radial profiles for the three days following the outburst. In addition, the parameters determined from CN and $C_2$ profiles agree within the error bars. We used a thermal evolution model to reproduce the activity pattern and outburst, by constraining the thickness of a dusty crust present at the surface of the comet. Our results are consistent with the progressive formation of a dust mantle, which may be partially blown off during the outburst. Overall, our observations and modelling results, i.e. the shallow dependence of pre-perihelion gas production rates, consistent with the progressive formation of a dust mantle, are in fact quite typical for dynamically new comets as concluded by A'Hearn et al. (1995). Comet Siding Spring is therefore behaving like a typical dynamically new comet.

For example, the evolution of Siding Spring's activity between 2.5 au and perihelion is relatively similar to that of comet C/2009 P1 (Garradd) (Combi et al. 2013 and Bodewits et al. 2014) at around the same pre-perihelion heliocentric distance. The behaviour of comet Garradd's activity was attributed to the presence of an extended source of water. According to Bodewits et al. (2015), $CO_2$ sublimation from a constant area on the nucleus may have dominated the activity of comet Siding Spring at heliocentric distances larger than 2.5 au. At this distance, the sublimation of icy grains, in addition to ice sublimating from the nucleus itself, may explain the increase in the water production, as was the case for comet Garradd. Icy grains in the

coma of this comet have also been invoked by Li et al. (2014) to explain the dust colour trend in the coma and its temporal evolution.The scenario suggested by Bodewits et al. (2015) thus seems consistent with our results.

Even though outbursts may seem to be a rather common phenomenon among comets, their origin is still not well understood. The amplitude of the brightness increases and the frequency varies from comet to comet. Some comet nuclei may be splitting: such an event would expose a large amount a fresh ice that would explain the sudden increase in gas and dust production. We carefully searched the enhanced images of the comet for five days after the outburst and could not detect any sign of nucleus fragmentation such as a blob of material in the coma, or the so-called coma wings (Boehnhardt, 2000). A nucleus splitting being the origin of the outburst thus seems unlikely. Outbursts can also be caused by a collision with another body. However, these collisions are extremely rare and no evidence in our observations points to an external source as the origin of this outburst. Cavities under the surface of the nucleus containing gas under high pressure have already been invoked to explain cometary outbursts (Ipatov and A'Hearn, 2011). This process is similar to the one we have inferred in our model, where a dusty crust may be totally or partially blown away by an increase of the gas pressure underneath. Although this scenario may adequately reproduce both gas and dust production evolution before and during the outburst, we can not exclude other mechanisms. In particular, by studying the coma morphology, Li et al. (2014) determined two pole solutions for comet Siding Spring resulting in different seasonal effect on the nucleus. For their second solution (rotational pole: Right Ascension = $190 \pm 10°$ and Declination = $50 \pm 5°$), they predicted that the Sun would illuminate a new area just after perihelion. The onset of sublimation on this fresh newly active area of the nucleus just after perihelion may thus also explain the outburst we observed on November 10. However, we do not observe changes of the coma morphology after the outburst, which could have been expected if the Sun illuminated new active area. The lack of morphological change in the coma is then more consistent with a global outburst during which the dusty crust is blown away.

## 3.5 C/2013 R1 (Lovejoy)

The results presented in this Section are based on Opitom et al. (2015b). Minor differences between the production rates presented here and those from Opitom et al. (2015b) might exist, since we updated our calibration and dust subtraction procedure. However, it does not impact any of the results we presented.

Comet C/2013 R1 (Lovejoy) is a dynamically old long-period comet discovered on September 7, 2013 at 1.97 au from the Sun (Guido et al. 2013). It was first detected by the Australian amateur astronomer Terry Lovejoy at magnitude 14.4 and brightened up to magnitude 4.5. The comet reached perihelion on December 22, 2013 at 0.8 au from the Sun. It follows an inclined and highly eccentric orbit ($i = 64°$ and $e = 0.9924$). After the disintegration of the bright comet ISON in late November 2013, comet Lovejoy became an ideal backup target, and

it has been extensively observed with a variety of instruments at different wavelengths around its perihelion passage. Thanks to the fast response possible with TRAPPIST, we were able to already observe the comet a few days after its discovery. Since the comet was also observable post-perihelion, it was an extremely interesting target for the study of its activity and chemical composition, and we started an intensive monitoring with narrow band filters.

### 3.5.1 Activity

We collected about 400 images over eight months. We started the observations on September 12, 2013 when the comet was at 1.91 au from the Sun. We observed once or twice a week until November 16, when it was too close to the Sun. Just after perihelion, the comet was too far north to be observed from La Silla, and we recovered it on February 13, 2014. We kept observing with narrow band filters as long as the comet was bright enough, until July 6, 2014 ($r$ = 3.10 au). After April 25 ($r$ = 2.20 au) the signal was too low in the OH and NH filters to derive reliable production rates. Exposure times ranged from 15 to 120 seconds for broad band filters and from 60 to 900 seconds for narrow band filters. Most nights were photometric, and we discarded cloudy nights.

For each image in the narrow band filters, we computed the $A(\theta)f\rho$ value (in the BC filter) or the production rate, depending on the filter. The results are given in Table 3.16, where we give the normalized $A(0)f\rho$ value and the production rates for each image. Gas species are also represented all together in Fig. 3.40. Figure 3.41 shows the evolution of the OH, NH, CN, $C_3$, and $C_2$ production rates and the $A(0)f\rho$ as a function of the heliocentric distance along with the fitted slope for the evolution of pre- and post- perihelion activity. From both the gas and the dust production evolution, we see that the comet activity evolves quite regularly. We could not detect any major outburst or sudden change of the comet activity with the heliocentric distance.

We immediately notice that the five gas species and the dust display an asymmetry about perihelion, since the rate of brightening is steeper than the rate of fading. The asymmetry does not have the same amplitude for the gas and the dust. Indeed, the $A(0)f\rho$ values are higher after perihelion than before at the same heliocentric distance by at least a factor two, while the gas production rates do not display such a strong difference between pre- and post-perihelion values. This of course implies that the dust-to-gas ratio is higher after perihelion.

We adopted a power-law fit to represent the heliocentric dependence of the production rates and the $A(0)f\rho$ both pre- and post-perihelion. The values of the slopes are given in Table 3.17. The rate of brightening is steeper than the rate of fading, which confirms the asymmetry about perihelion observed in Figure 3.41. The slopes have similar values for OH, NH, and $C_2$ and are consistent within the error bars with the slope observed for the dust heliocentric dependence. However, the slopes for CN and $C_3$ are different from the other gas species and the dust. This difference is visible on both sides of perihelion.

Table 3.16: OH, NH, CN, $C_3$, and $C_2$ production rates and $Af\rho$ for comet C/2013 R1 (Lovejoy)

| UT date | r | Δ | Production rates ($10^{25}$ mol/s) | | | | | $A(0)f\rho$ |
|---|---|---|---|---|---|---|---|---|
| | (au) | (au) | Q(OH) | Q(NH) | Q(CN) | Q($C_3$) | Q($C_2$) | ($10^2$ cm) |
| 2013 Sep 12.38 | 1.91 | 1.81 | 870±135 | | | 0.61±0.04 | 2.35±0.13 | |
| 2013 Sep 16.39 | 1.85 | 1.71 | | | 3.14±0.12 | | 2.84±0.20 | 3.79±0.28 |
| 2013 Sep 21.33 | 1.79 | 1.59 | 823±144 | 4.24±1.47 | 3.17±0.14 | 0.67±0.06 | 3.10±0.21 | 4.37±0.37 |
| 2013 Sep 24.39 | 1.75 | 1.52 | | | 3.67±0.12 | | | |
| 2013 Sep 25.35 | 1.73 | 1.50 | | | 3.70±0.14 | | 4.32±0.15 | 4.04±0.39 |
| 2013 Oct 04.35 | 1.61 | 1.28 | | 8.57±0.99 | 3.93±0.12 | | | |
| 2013 Oct 05.33 | 1.60 | 1.25 | 1120±180 | | 4.28±0.13 | 0.96±0.04 | 5.29±0.15 | 6.30±0.18 |
| 2013 Oct 08.33 | 1.56 | 1.18 | 1520±180 | | 3.74±0.12 | | 4.49±0.16 | 6.85±0.24 |
| 2013 Oct 10.31 | 1.53 | 1.13 | 1470±210 | | 5.02±0.16 | | 5.26±0.42 | 7.52±0.24 |
| 2013 Oct 20.29 | 1.40 | 0.89 | 2160±330 | | 5.67±0.23 | | 7.45±0.34 | 10.00±0.50 |
| 2013 Oct 21.33 | 1.38 | 0.87 | 2380±250 | 13.90±1.52 | 6.38±0.19 | 1.08±0.04 | 7.63±0.21 | |
| 2013 Oct 24.32 | 1.34 | 0.80 | 2720±290 | 17.00±1.52 | 6.96±0.21 | 1.72±0.08 | 9.10±0.34 | 13.10±0.30 |
| 2013 Oct 26.30 | 1.32 | 0.75 | 2860±330 | 17.30±1.67 | 7.20±0.31 | 1.78±0.07 | 9.62±0.39 | 14.20±0.40 |
| 2013 Nov 02.35 | 1.23 | 0.61 | | | 7.97±0.27 | 1.58±0.07 | 12.20±0.30 | |
| 2013 Nov 03.37 | 1.21 | 0.59 | 3010±350 | 20.80±1.38 | | | | |
| 2013 Nov 13.34 | 1.09 | 0.43 | 3240±790 | 23.70±3.45 | 10.10±0.70 | | 16.10±0.50 | 22.60±0.80 |
| 2013 Nov 16.34 | 1.06 | 0.41 | | 29.90±5.69 | 12.90±1.20 | 3.08±0.31 | 20.60±0.09 | 28.50±2.10 |
| 2014 Feb 13.39 | 1.26 | 1.56 | | | 8.76±0.44 | | 13.70±0.50 | 42.00±1.70 |
| 2014 Feb 15.40 | 1.28 | 1.56 | 1630±320 | 15.50±2.68 | | | 11.30±0.40 | 34.90±1.40 |
| 2014 Feb 16.40 | 1.30 | 1.57 | | | 6.12±0.36 | | | |
| 2014 Feb 21.39 | 1.36 | 1.58 | 1380±230 | 13.60±2.09 | 5.97±0.26 | 1.74±0.11 | 8.63±0.31 | 28.30±0.90 |
| 2014 Feb 22.39 | 1.37 | 1.58 | | | | | 9.59±0.27 | 29.10±1.00 |
| 2014 Feb 28.39 | 1.45 | 1.59 | | | | | | 21.70±0.90 |
| 2014 Mar 01.39 | 1.47 | 1.59 | | | | | | 24.00±0.90 |
| 2014 Mar 06.39 | 1.54 | 1.59 | 1320±160 | 11.40±1.41 | 5.10±0.17 | 1.40±0.06 | 7.10±0.17 | 21.80±0.60 |
| 2014 Mar 13.39 | 1.63 | 1.58 | 1160±130 | 9.70±1.28 | 4.45±0.16 | 1.21±0.06 | 5.87±0.17 | 17.80±0.60 |
| 2014 Mar 17.39 | 1.68 | 1.57 | | | | | | 15.20±1.20 |
| 2014 Mar 18.38 | 1.70 | 1.57 | 939±115 | 7.54±1.53 | 3.99±0.17 | 1.17±0.08 | 5.97±0.26 | 12.50±0.70 |
| 2014 Mar 20.34 | 1.72 | 1.56 | | | 4.01±0.14 | | | |
| 2014 Mar 25.39 | 1.79 | 1.55 | | | 3.80±0.12 | | 4.66±0.21 | 13.20±0.50 |
| 2014 Mar 26.38 | 1.80 | 1.55 | 859±91 | 7.36±1.00 | 3.95±0.14 | 1.05±0.05 | 4.43±0.29 | 13.10±0.40 |
| 2014 Apr 10.38 | 2.00 | 1.50 | 627±68 | | 3.40±0.14 | 0.82±0.04 | 3.26±0.19 | 9.35±0.35 |
| 2014 Apr 14.42 | 2.06 | 1.49 | | | 2.84±0.15 | | 2.72±0.23 | 8.92±0.48 |
| 2014 Apr 15.25 | 2.07 | 1.48 | 561±56 | | | 0.88±0.03 | | |
| 2014 Apr 16.42 | 2.08 | 1.48 | | 2.33±2.04 | | | | |
| 2014 Apr 18.38 | 2.11 | 1.48 | 512±60 | | 2.72±0.15 | | 2.91±0.24 | 7.56±0.45 |
| 2014 Apr 19.34 | 2.12 | 1.47 | | 3.14±1.40 | | 0.59±0.07 | | |
| 2014 Apr 22.30 | 2.16 | 1.47 | 476±56 | | 2.93±0.13 | | 3.07±0.30 | 7.21±0.40 |
| 2014 Apr 25.38 | 2.20 | 1.47 | 413±65 | | 2.50±0.13 | | 2.03±0.29 | 6.70±0.33 |
| 2014 May 14.16 | 2.44 | 1.50 | | | 2.22±0.23 | | 1.72±0.40 | 4.54±0.76 |
| 2014 May 24.34 | 2.57 | 1.57 | | | 1.80±0.21 | | | 3.96±0.39 |
| 2014 May 27.32 | 2.61 | 1.60 | | | 1.72±0.18 | 0.50±0.05 | 1.97±0.45 | 3.66±0.39 |
| 2014 May 31.18 | 2.66 | 1.64 | | | 1.91±0.14 | 0.50±0.07 | 1.98±0.30 | |
| 2014 Jun 07.21 | 2.74 | 1.73 | | | | | | 3.61±0.26 |
| 2014 Jun 30.21 | 3.02 | 2.15 | | | | | | 3.01±0.41 |
| 2014 Jul 04.03 | 3.07 | 2.23 | | | | | | 3.05±0.35 |
| 2014 Jul 06.99 | 3.10 | 2.30 | | | | | | 2.62±0.59 |

$r$ and Δ are respectively the heliocentric and geocentric distances. The date given in the first column is the mid-time of the observations.

We have a few observations of comet Lovejoy with the RC and GC continuum filters in addition to the ones regularly performed with the BC filter. The comparison of the $A(\theta)f\rho$ values in these three filters allows the colour of the dust and its evolution to be studied. The dust colour is usually computed as the normalized gradient of $A(\theta)f\rho$ from two continuum filters:

$$\text{colour}[\lambda_1,\lambda_2] = \frac{Af\rho_1 - Af\rho_2}{\lambda_1 - \lambda_2}\frac{2000}{Af\rho_1 + Af\rho_2}. \tag{3.7}$$

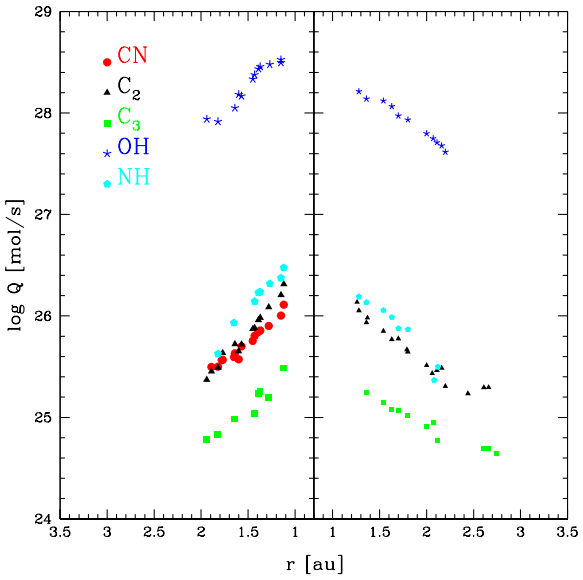


Figure 3.40: Logarithm of comet C/2013 R1 (Lovejoy) OH, NH, CN, $C_3$, and $C_2$ production rates as a function of the heliocentric distance $r$ (au). The $r$-axis is interrupted at perihelion (0.8 au).

Table 3.17: Pre- and post-perihelion fitted power-law slopes for comet C/2013 R1 (Lovejoy) OH, NH, CN, $C_3$, and $C_2$ production rates and $A(0)f\rho$ heliocentric dependences.

| Species | r-dependence | |
|---|---|---|
| | pre-perihelion | post-perihelion |
| OH | -3.28±0.33 | -2.62±0.19 |
| NH | -3.19±0.34 | -2.49±0.34 |
| CN | -2.60±0.17 | -1.84±0.09 |
| $C_3$ | -2.66±0.47 | -1.83±0.40 |
| $C_2$ | -3.56±0.16 | -2.76±0.12 |
| $A(0)f\rho$ | -3.92±0.19 | -3.01±0.07 |

The normalized reflectivity gradient is expressed as the percentage of reddening by 1000 Å. We measured values between 6 % and 14 %/1000 Å. This is in the range of what is usually observed for comets (see for example Lin et al. 2013; Lin et al. 2012; Lara et al. 2004). The dust colour stayed constant during our observations.

### 3.5.2 Composition

We monitored several production rate ratios to study the evolution of the coma composition. In Fig. 3.42 we show the evolution of comet Lovejoy gas production rate ratios to CN. We fitted

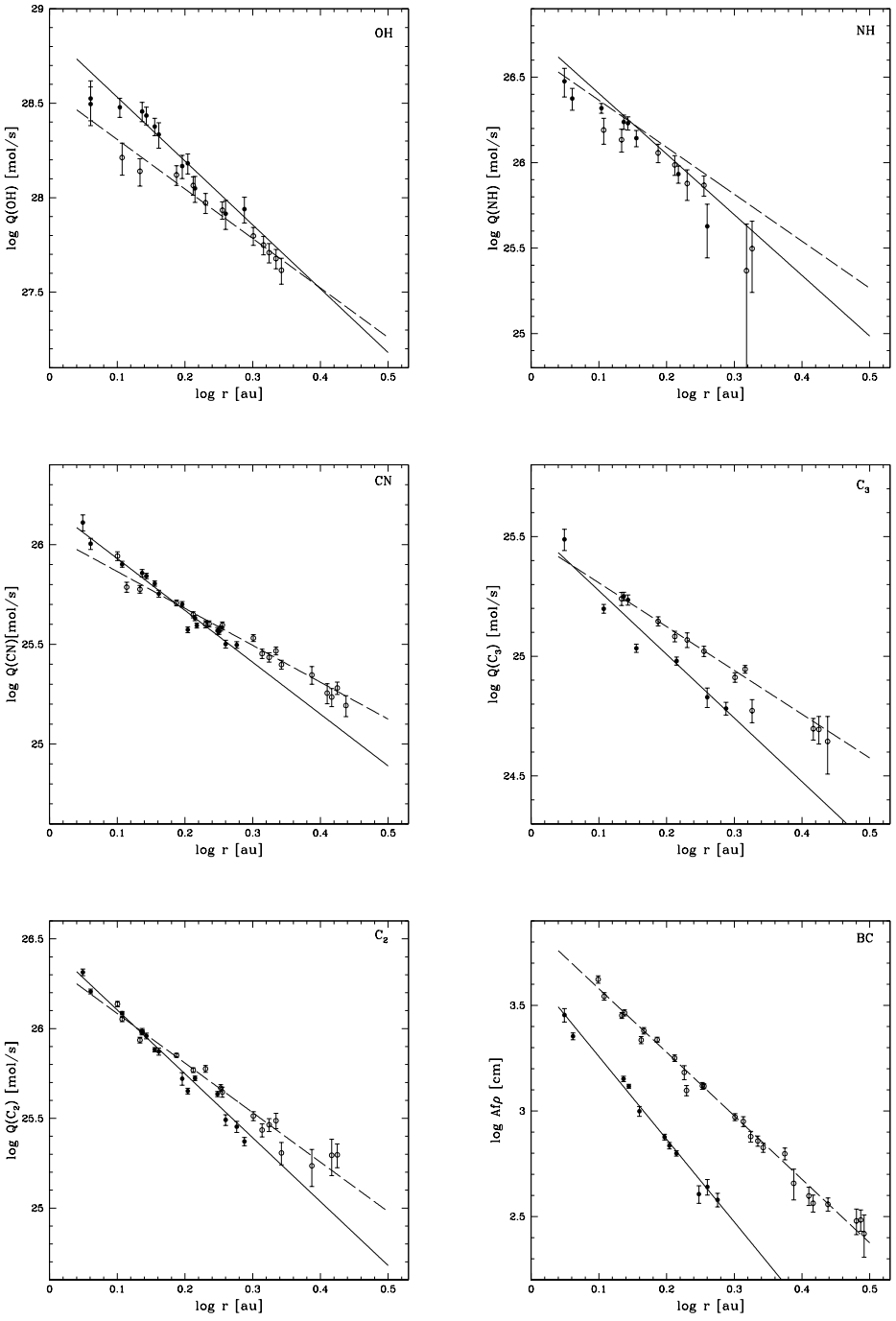


Figure 3.41: Comet C/2013 R1 (Lovejoy) OH, NH, CN, $C_3$, and $C_2$ production rates and $A(0)f\rho$ as a function of the heliocentric distance ($r$). Pre-perihelion data points are represented with filled symbols, and post-perihelion data points are represented with open symbols. Full lines represent power-law fits of the production rates and $A(0)f\rho$ variation with the heliocentric distance pre-perihelion. Dashed lines are the same for post-perihelion values.

power-law slopes to represent the evolution of these ratios with the heliocentric distance, see Tab. 3.18. The $C_2$ to CN ratio decreases with the heliocentric distance by almost a factor two between 1.1 and 2.5 au. At large heliocentric distances, the ratio does not seem to vary any more, but the error bars are larger. Pre- and post-perihelion ratios match within the error bars, and both display the same trend. The $C_2$ production rate is rising faster than the CN production rate as the comet approaches the Sun and decreasing faster after perihelion. Despite the evolution of the $C_2$ to CN ratio, comet Lovejoy can be classified as a typical comet in terms of carbon-chain species as defined by A'Hearn et al. (1995). However, around 2.5 au, the $C_2$ to CN ratio almost reaches the lower limit for a typical comet. This shows that the composition of the coma evolves during the orbit and that a comet could be classified as typical or depleted depending on the heliocentric distance at which it is observed. We must then treat this kind of classification with caution.

Table 3.18: Fitted power-law slopes for the heliocentric dependence of C/2013 R1 (Lovejoy) OH, $C_3$, $C_2$, and $A(0)f\rho$ to CN ratios pre- and post-perihelion.

| Species | r-dependence | |
|---|---|---|
| | pre-perihelion | post-perihelion |
| log[Q(OH)/Q(CN)] | -0.93±0.53 | -1.07±0.20 |
| log[Q(NH)/Q(CN)] | -0.42±0.31 | -0.77±0.27 |
| log[Q($C_3$)/Q(CN)] | +0.04±0.59 | -0.20±0.13 |
| log[Q($C_2$)/Q(CN)] | -0.90±0.15 | -0.84±0.14 |
| log[Q($A(0)f\rho$)/Q(CN)] | -1.26±0.22 | -1.21±0.09 |

Table 3.19: Fitted power-law slopes for the heliocentric dependence of comet C/2013 R1 (Lovejoy) CN, $C_3$, $C_2$, and $A(0)f\rho$ to OH ratios pre- and post-perihelion.

| Species | r-dependence | |
|---|---|---|
| | pre-perihelion | post-perihelion |
| log[Q(CN)/Q(OH)] | +0.93±0.53 | +1.07±0.20 |
| log[Q($C_3$)/Q(OH)] | +0.96±0.72 | +0.77±0.33 |
| log[Q($C_2$)/Q(OH)] | -0.36±0.43 | -0.17±0.23 |
| log[Q($A(0)f\rho$)/Q(OH)] | -0.20±0.38 | -0.44±0.20 |

In Fig. 3.43 we show the evolution of the CN, $C_3$, $C_2$ production rates, and $A(0)f\rho$ compared to the OH production rate. We did not represent the evolution of the NH/OH ratio since simultaneous measurements of these two species were scarce. The dispersion of the ratios is mainly due to the dispersion of the OH production rates caused by the lower signal-to-noise ratio in these images. We fit two separated slopes for pre- and post-perihelion data, which are given in Table 3.19. All the ratios display a slight asymmetry about perihelion, post-perihelion values are higher than pre-perihelion values owing to the asymmetry of the OH production rates about perihelion. The asymmetry is stronger for $A(0)f\rho$ since, as already noticed, the

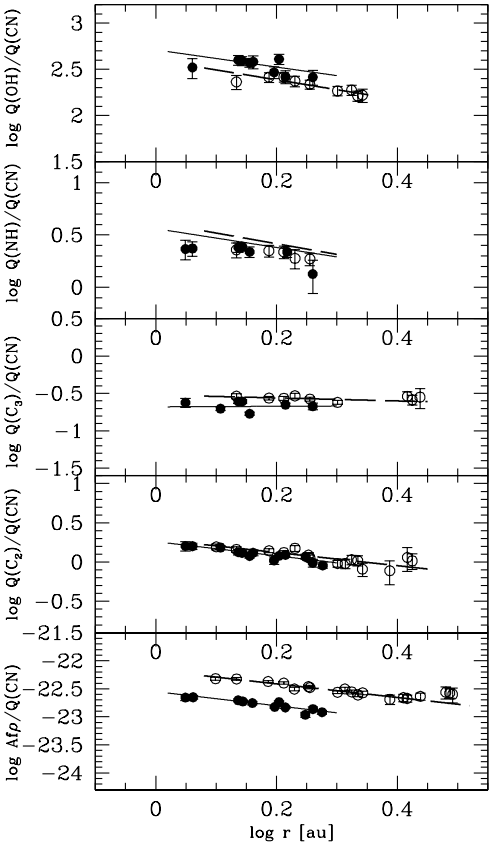


Figure 3.42: Comet C/2013 R1 (Lovejoy) OH, NH, $C_3$, $C_2$, and $A(0)f\rho$ to CN production rate ratios as a function of the heliocentric distance. Pre-perihelion values are represented with filled symbols and post-perihelion values with open symbols. Full lines represent power-law fits of the ratio variations with the heliocentric distance pre-perihelion. Dotted lines are the same for post-perihelion values.

comet is dustier post-perihelion. Except for the asymmetry about perihelion, the $A(0)f\rho$ to OH and $C_2$ to OH ratios are almost constant with the heliocentric distance. For these two ratios, the slopes given in Table 3.19 are approximately consistent with 0. In contrast, the slopes of the CN to OH and, to a lesser extent, $C_3$ to OH ratios are different from zero. This means that the evolution of $C_2$, OH, and the dust are correlated, while $C_3$ and CN are likely not, as suggested by the analysis of the heliocentric dependences of gas and dust production rates.

### 3.5.3 Morphology

In this section, we describe the dust and gas coma morphologies of comet Lovejoy. We tested several techniques to improve the contrast between the coma and the specific features: subtraction and division of an azimuthal median profile, rotational filter, and Larson-Sekanina

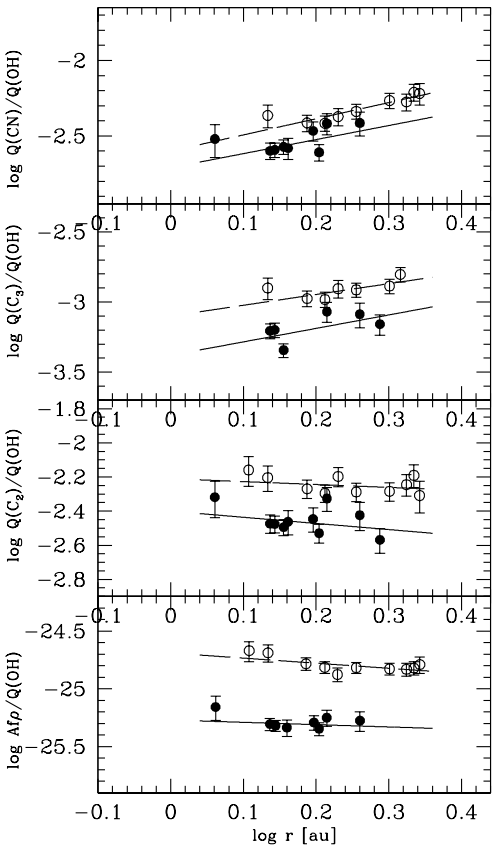


Figure 3.43: Comet C/2013 R1 (Lovejoy) NH, CN $C_3$, $C_2$, and $A(0)f\rho$ to OH production rate ratios as a function of the heliocentric distance. Pre-perihelion values are represented with filled symbols and post-perihelion values with open symbols. Full lines represent power-law fits of the ratios variation with the heliocentric distance pre-perihelion. Dotted lines are the same for post-perihelion values.

filter (see Schleicher and Farnham 2004; Larson and Sekanina 1984). All these techniques give approximately the same results, but the removal of the azimuthal median profile allows fainter large scale structures to be detected, and we thus present the images obtained with this technique.

We first discuss the observations obtained before perihelion between September 12 and November 16, 2013. We detected features in all the filters, indicating that the nucleus of comet Lovejoy has several active regions. The first CN feature was detected around September 21, 2013, while the dust, $C_3$, and $C_2$, features were only detected later, around October 6, 2013. The OH and NH features do not appear in all the images, owing to the high airmass of some observations and the lower signal-to-noise ratio in these bands. We present in Fig. 3.44 the results of the subtraction of the azimuthal median profile for $C_2$, $C_3$, CN, NH, and OH images,

and also for the dust in RC filter for images taken on November 2 and 3, 2013. The RC image shows an enhancement of the coma in the tail direction around PA 280°. There is a broad and slightly curved feature centred on PA 100°. The $C_2$ image shows two jets around PA 100° and 280°, at the same position as the dust features mentioned above. We also see a broad feature around PA 15° and a fainter one around PA 190° that are not visible in the dust images. The features around PA 100° and 280° visible in both $C_2$ and dust images seem to indicate that at least part of the $C_2$ originates in the same region(s) as the dust, or maybe that the $C_2$ is released from dust grains. The CN morphology is different from the $C_2$ morphology. CN displays a roughly hourglass shape with two main fans around PA 15° and 175°. Features were also visible in the $C_2$ images at approximately the same position as the CN jets but were much weaker. The $C_3$ morphology is rather similar to the $C_2$ morphology, with one feature around PA 280° and a large fan around PA 5°. However, the $C_2$ feature around PA 100° and the weak one around PA 190° are not observed in the $C_3$ image. To summarize, $C_2$ and, to a lesser extent, $C_3$ images are the sum of dust and CN features. In the NH and OH filters, we do not detect jets but only an enhancement of the coma centred on the tail direction, around 280°. Since the comet was only visible one or two hours at the end of the night during this period, we could not detect variations in the feature's shape and position during the night caused by the nucleus rotation. The position and the shape of the features described above for November 2 and 3 varied slightly between late September and mid-November because of changes in the viewing geometry. We also have images of the comet post-perihelion. Unfortunately, we could only identify clear features for CN. The morphology is almost the same as in November 2013: an hourglass shape with two main fans around PA 15° and 205°.

### 3.5.4 Discussion

The study of the evolution of comet Lovejoy activity with the heliocentric distance revealed a significant asymmetry about perihelion. This asymmetry is visible from $C_2$, $C_3$, CN, NH, and OH production rates but also from the dust, even if the amplitude of the asymmetry varies depending on the species. The $A(0)f\rho$ values are at least a factor two higher after perihelion than before at the same heliocentric distance. Asymmetries of the activity about perihelion seem to be a common phenomenon among comets (see, for example, A'Hearn et al. 1995, Schleicher et al. 1998, Knight and Schleicher 2013, Opitom et al. 2015a). It remains difficult to know if such asymmetries happen for all comets or to understand their origin, because large datasets with sufficient temporal coverage and with observations on both sides of perihelion are still too scarce. A possible cause often mentioned is a thermal inertia effect. One other probable cause is a seasonal effect on a nucleus with several active regions. Indeed, for comets on highly eccentric orbits, changes in the nucleus illumination can happen close to perihelion. If the illuminated percentage of the active region(s) rises, this will also impact the evolution of the comet gas and dust production rates. Some regions might also need more heat to be activated, for instance if they are buried deeper, or there might be some delay before they start to outgas. The study of comet Lovejoy coma morphology revealed gas and dust jets coming out of the nucleus. This strongly suggests the existence of one or several

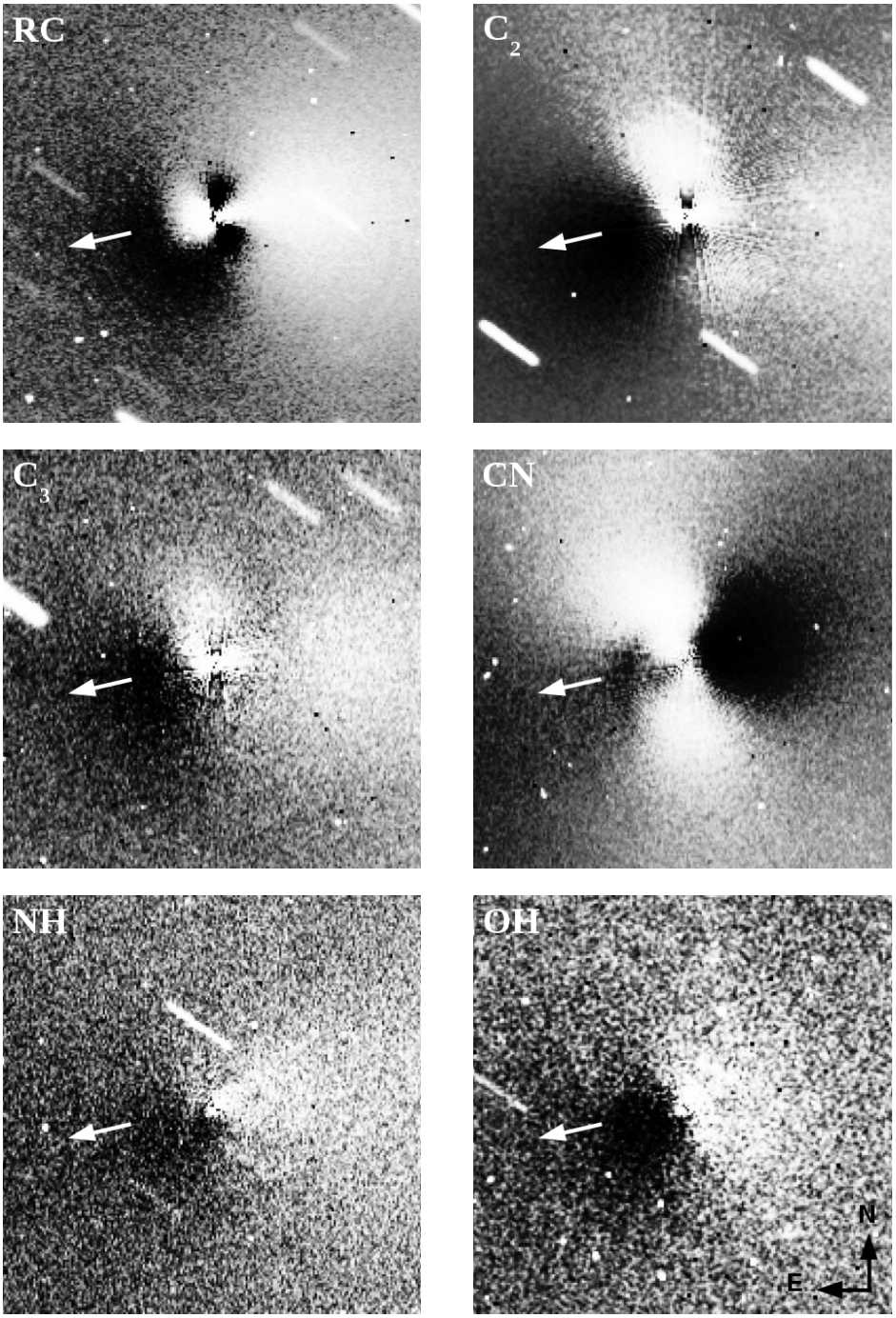


Figure 3.44: C/2013 R1 (Lovejoy) RC, $C_2$, $C_3$ CN, NH, and OH images from November 2 and 3, 2013 processed by subtracting an azimuthal median profile. All images are oriented with north up and east left. The field of view is 4.3' × 4.3'. The arrow indicates the direction of the Sun.

active region(s) on the nucleus. This is consistent with a seasonal effect being the cause of the

observed asymmetry. We also noted that the dust to gas ratio changed; the comet is dustier after perihelion than before. This may bring us important clues about the heterogeneity level of the nucleus. More precisely, this could be explained by different ice and dust mixing in the active regions. However, we must be cautious while drawing conclusions since we do not completely understand the mechanism that causes such asymmetries.

While looking at the evolution of the comet activity with the heliocentric distance, we noticed a correlation between some of the radicals and the dust. The slopes of the $C_2$, NH, OH, and the dust heliocentric dependence presented in Table 3.17 are consistent with each other within the error bars, while the CN slope is shallower. The $C_3$ slope is close to the CN slope. This correlation between some radicals and the dust is also observed after perihelion. It is even more obvious looking at the evolution of the $C_2$, $C_3$, CN, NH, and dust production rates relative to OH. Except for the asymmetry about perihelion, the $C_2$/OH and $A(0)f\rho$/OH ratios do not significantly vary with the heliocentric distance. On the other hand, a power-law fit of the CN/OH and the $C_3$/OH ratio with the heliocentric distance gives a slope different from zero. Once again, these trends are identical on both sides of perihelion.

All this evidence suggests that the radicals we observe in the coma of comet Lovejoy may not all come from the same source. The issue of gas coming from icy or carbonaceous grains in the coma of comets has been debated for a long time. $C_2H_2$, $C_2H_6$, and HCN are usually thought to be the primary parents of $C_2$ and CN (Helbert et al. 2005, Weiler 2012). However, discrepancies between the parent and daughter production rates observed for some comets seem to indicate that we need other parents to explain the abundances of some radicals in the coma (Fray et al. 2005; Dello Russo et al. 2009; Kobayashi et al. 2010; McKay et al. 2014). It has been suggested that $C_2$ and/or CN can come -at least partially- from carbonaceous grains or another unknown source. In the case of comet Lovejoy, we see a strong correlation between the evolution of the dust production and the evolution of some radicals such as $C_2$, NH, and OH. This suggests that at least part of the $C_2$, on one hand, and also part of the NH and OH, on the other hand, could be produced by organic-rich and icy grains, respectively. Since the evolution of the CN production is different from the $C_2$ and does not seem correlated with the dust, most CN would be produced directly by the photodissociation of HCN.

This hypothesis is further reinforced by the study of the coma morphology. Indeed, Fig. 3.44 shows that the dust and $C_2$ morphologies have some similarities. $C_2$ is enhanced in the tail direction, and we see a jet in the sunward direction at the same position as the dust jet. We also notice features around the same position as the CN fans. In contrast, the CN morphology is completely different from the dust. It has an hourglass shape with two jets around PA 15° and 175°. The $C_3$ morphology is similar to the $C_2$ morphology. Since HCN, $C_2H_2$, and $C_2H_6$ usually have the same spatial distribution (Dello Russo et al. 2009, Villanueva et al. 2011), this could indicate that, while most of the CN is the product of HCN photodissociation, only part of the $C_2$ is produced by the photodissociation of $C_2H_2$ (and $C_2H_6$ but $C_2H_6$ is not very efficient to release $C_2$, see Weiler 2012). The rest of the $C_2$ is probably coming from organic-rich grains. This would explain the enhanced $C_2$ regions around PA 15° and 175 ° while the most

Table 3.20: Comparison of mother and daughter species production rates.

| Date | Q(OH)[a] | Q($H_2O$)[b] | Q(CN)[a] | Q(HCN)[b] | Q($C_2$)[a] | Q($C_2H_2$)[b] | Q($C_2H_6$)[b] |
|---|---|---|---|---|---|---|---|
| 2013-Oct-21 | 2380±250 | | 6.38±0.19 | | 7.63±0.21 | | |
| 2013-Oct-22 | | 1850±190 | | 5.9±1.2 | | <9.2 | 13.80±1.70 |
| 2013-Oct-24 | 2720±290 | 1530±250 | 6.96±0.21 | | 9.10±0.34 | | |
| 2013-Oct-25 | | 2320±330 | | 6.8±0.6 | | <1.5 | 21.70±3.50 |
| 2013-Oct-26 | 2860±330 | | 7.20±0.31 | | 9.62±0.39 | | |
| 2013-Oct-27 | | 1560±250 | | 3.6±0.1 | | <2.2 | 17.40±3.70 |
| 2013-Oct-29 | | 1450±410 | | 4.7±0.6 | | <1.7 | 10.80±2.50 |
| 2013-Nov-2 | | | 7.97±0.27 | | 12.20±0.30 | | |
| 2013-Nov-3 | 3010±350 | | | | | | |
| 2013-Nov-7 | | 3680±260 | | 8.7±0.7 | | <1.6 | 21.80±2.50 |
| 2013-Nov-8/12 | | 5000 [d] | | 7.4±0.1 [d] | | | |
| 2013-Nov-13 | 3024±790 | | 10.10±0.70 | 6.0 [c] | 16.10±0.50 | | |
| 2013-Nov-16 | | | 12.90±1.20 | 6.1 [c] | 20.60±0.90 | | |

All production rates are expressed in units of $10^{25}$ mol/s. [a] This paper [b] Paganini et al. (2014b) [c] Agúndez et al. (2014) [d] Biver et al. (2014)

contrasted features are similar to the dust. We mentioned earlier that NH and OH parents could be released from icy grains. If this is the case, we would expect the NH and OH coma to be enhanced in the tail direction since the icy grains are pushed away from the Sun by the radiation pressure. This is exactly what we see in Fig. 3.44. Both NH and OH are enhanced in the anti-solar direction, strongly reinforcing the hypothesis of water and ammonia (the most likely parent of NH) being released by icy grains.

To better understand the relationship between parent and daughter species, we can compare measurements of the parent species production rates made in the IR and the radio domains to the radicals production rates we derived here. Only a few results have been published so far about comet C/2013 R1 (Lovejoy). We summarize the results reported in Paganini et al. (2014b), Agúndez et al. (2014), and Biver et al. (2014) in Table 3.20, along with our daughter species production rates. From this table, we notice that there is a significant dispersion between production rates measured almost simultaneously with different instruments and from different wavelength ranges. This dispersion is probably due in part to the different fields of view (less than 10 arcseconds in the millimeter range and 24 arcseconds in the IR) and models used but also maybe to the rotational variation.

We first compare the OH and $H_2O$ production rates. Our values agree within the error bars with the ones reported by Biver et al. (2014) and Paganini et al. (2014b) for early November. In October, however, the OH production rates we derived are slightly higher than the water production rates measured by Paganini et al. (2014a).

Since measurements of the HCN production rate of comet Lovejoy have also been published by Paganini et al. (2014b) and Agúndez et al. (2014), the comparison with our CN measurements is of great interest for determining the origin of the CN in the coma of comet Lovejoy. In October, the CN and HCN production rates are consistent with each other (except for October 27 and 29 for which HCN production rates reported by Paganini et al. (2014b) are almost a

factor two lower than those measured a few days before and a few days after, maybe because of rotational variation very close to the nucleus). In November, our CN production rates agree with those reported by Paganini et al. (2014b) and Biver et al. (2014), especially if we take the rise in comet activity into account. The HCN production rates reported by Agúndez et al. (2014) are lower than our CN production rates, but they are also lower than those derived by Paganini et al. (2014b) and Biver et al. (2014) only a few days earlier.

Finally, we can also compare the $C_2$ production rates to the production rates of two possible parents, $C_2H_6$ and $C_2H_2$, reported by Paganini et al. (2014b). For all dates except one, the $C_2H_2$ production rate upper limit is lower than the $C_2$ production rate. For some dates the $C_2H_2$ production rate upper limit is almost a factor ten lower than the $C_2$ production rate. The $C_2H_6$ is of the same order of magnitude as the $C_2$ production rate.

The comparison of parent and daughter species production rates seems to confirm our interpretation of the origin of daughter species in the coma of comet Lovejoy. Most of the HCN production rates reported are of the same order of magnitude as our CN production rates, the ones reported by Paganini et al. (2014b) are even in good agreement with our CN production rates. This suggests that HCN is probably the main parent of CN in the coma of comet Lovejoy. For $C_2$, there are large discrepancies between the most likely parent abundance and the $C_2$ abundance. Indeed most of the upper limits of the $C_2H_2$ production rates are much lower than the $C_2$ production rates. This indicates that we need another parent to explain the $C_2$ abundance in the coma or that $C_2$ comes in part from organic-rich grains. Another possible parent of $C_2$ is $C_2H_6$. Paganini et al. (2014b) detected $C_2H_6$ in the coma of comet Lovejoy, and its abundance is of the same order of magnitude as the $C_2$. However, it has been reported that the release of $C_2$ from $C_2H_6$ is not really efficient (Weiler 2012) and makes it a poor candidate for $C_2$ parentage.

Nevertheless, we must remain cautious when comparing parent molecules production rates measured from the infrared to daughter molecules production rates from the optical. The models used and the parameters in these models are different, making any direct comparison difficult. As an example, in this paper we used an outflow velocity of 1 km/s, as in A'Hearn et al. (1995). However, in most infrared and radio studies, including those from Paganini et al. (2014b) and Biver et al. (2014) mentioned earlier, an outflow velocity of $v = 0.8r^{-0.5}$ km/s is assumed. To assess the importance of the outflow velocity used in the model on the derived daughter molecules production rates and then on the comparison between daughter and parent species production, we computed the gas production rates presented in Table 3.20 again using the expansion velocity law: $v = 0.8r^{-0.5}$ km/s. These results are shown in Table 3.21. A comparison of Tables 3.20 and 3.21 shows that the impact of the outflow velocity is significant. The production rates derived from optical data are lower if we use the same velocity law as for the infrared data (lower by a factor 1.8 in October and by a factor 1.5 in mid-November). However, the agreement between the observed profile and the Haser model is much better for constant expansion velocities of 1 km/s. This is not surprising since the Haser scalelengths we use (A'Hearn et al., 1995) have been fitted using an expansion velocity

Table 3.21: Comparison of mother and daughter species production rates using a gas outflow velocity $v = 0.8r^{-0.5}$ km/s to compute daughter species production rates.

| Date | Q(OH)[a] | Q($H_2O$)[b] | Q(CN)[a] | Q(HCN)[b] | Q($C_2$)[a] | Q($C_2H_2$)[b] | Q($C_2H_6$)[b] |
|---|---|---|---|---|---|---|---|
| 2013-Oct-21 | 1280±130 | | 3.53±0.11 | | 4.20±0.12 | | |
| 2013-Oct-22 | | 1850±190 | | 5.9±1.2 | | <9.2 | 13.80±1.70 |
| 2013-Oct-24 | 1500±160 | 1530±250 | 3.95±0.12 | | 5.15±0.19 | | |
| 2013-Oct-25 | | 2320±330 | | 6.8±0.6 | | <1.5 | 21.70±3.50 |
| 2013-Oct-26 | 1610±190 | | 4.16±0.18 | | 5.52±0.22 | | |
| 2013-Oct-27 | | 1560±250 | | 3.6±0.1 | | <2.2 | 17.40±3.70 |
| 2013-Oct-29 | | 1450±410 | | 4.7±0.6 | | <1.7 | 10.80±2.50 |
| 2013-Nov-2 | | | 4.90±0.17 | | 7.46±0.16 | | |
| 2013-Nov-3 | 1810±210 | | | | | | |
| 2013-Nov-7 | | 3680±260 | | 8.7±0.7 | | <1.6 | 21.80±2.50 |
| 2013-Nov-8/12 | | 5000 [d] | | 7.4±0.1 [d] | | | |
| 2013-Nov-13 | 2090±510 | | 6.88±0.44 | 6.0 [c] | 10.90±0.40 | | |
| 2013-Nov-16 | | | 8.97±0.84 | 6.1 [c] | 14.30±0.60 | | |

All production rates are expressed in units of $10^{25}$ mol/s. [a] This paper [b] Paganini et al. (2014b), from observations with the Near InfraRed SPECtrometer at the Keck observatory [c] Agúndez et al. (2014), from Nancay OH observations [d] Biver et al. (2014), from observations with the IRAM 30m telescope

of 1 km/s.

Examination of Table 3.21 shows that given the variability of water production rates measurements, there are no significant differences between OH production rates and those of $H_2O$ for most of the dates. Some of the CN production rates measured are lower than those of HCN reported in the literature, but they are consistent with the lower HCN production rates measured in late October and mid-November. In early November, $C_2$ production rates are still almost a factor five higher than the $C_2H_2$ production rates upper limits.

Another question is the dependence of both scalelengths and fluorescence efficiencies on the heliocentric distance. This of course influences the daughter production rates we derive and then the comparison between daughter and parent molecules production. In our case, we only compare daughter and parent molecules for observations made between 1.4 and 1 au from the Sun so that variations from the $r^2$ scaling used for both scalelengths and g factors should not have a strong influence on our results. For example, if we use a $r^3$ scaling law for the scalelengths, the maximum variation in the production rates over this range heliocentric distances is 20%. Finally, the $C_2$ fluorescence efficiencies we used only consider the $C_2$ in triplet state since the ratio of $C_2$ in triplet and singlet state and its heliocentric dependence are not understood well. We thus underestimate the $C_2$ total production rates, which reinforces our conclusion about $C_2$ parentage.

### 3.5.5 Summary

We performed a photometry and imaging monitoring of the Oort Cloud comet C/2013 R1 (Lovejoy) during several months with TRAPPIST at La Silla observatory. We observed the comet on both sides of perihelion with good temporal coverage. We derived production rates

and $Af\rho$ values and studied the evolution of its activity. We also performed a morphological analysis of the coma.

The morphological analysis revealed several features in the coma, both for the dust and the gas species. This indicates that the nucleus has one or several active region(s). The comparison of the comet activity pre- and -post perihelion shows an asymmetry of the gas and dust production rates about perihelion, the rate of brightening is steeper than the rate of fading. We estimated that it is likely to be a seasonal effect caused by changing system geometry and insolation of the active region(s). The dust production rate is at least two times higher after perihelion than before at the same heliocentric distance, which suggests a certain degree of heterogeneity of the nucleus.

The evolution of the comet activity and production rates ratios with the heliocentric distance, the comparison of parent and daughter species production rates, as well as the coma morphology all indicate that the $C_2$, NH, and OH productions are strongly correlated to the dust production, while the CN production is not. The case of $C_3$ is more complicated and quite intermediate between these two behaviours. We then suggested that an important part of the $C_2$ could be released from organic-rich grains and that water and ammonia (the parents of OH and NH) could be released from icy grains. CN and some $C_2$ would be produced by the photodissociation of HCN and $C_2H_2$, which usually display the same spatial distribution. $C_3$ would also be produced partly from the organic-rich grains and by the photodissociation of a parent molecule.

## 3.6 C/2013 US10 (Catalina)

Comet C/2013 US10 (Catalina) is a dynamically new comet discovered on October 31, 2013 by the Catalina sky survey. The comet reached perihelion on November 15, 2015 at 0.82 au from the Sun. We observed the comet during several months in 2014 and 2015 with TRAPPIST. Simultaneously, we obtained low-resolution spectra with the FORS 2 instrument at the VLT on 4 epochs between May and September 2015. We discuss the consistency of both data sets by comparing simultaneous observations, study the slow evolution of comet Catalina gas and dust activity between 6.6 and 1.4 au from the Sun pre-perihelion, and from 1.00 to 1.18 au post-perihelion, and study its coma composition and morphology.

### 3.6.1 Activity

We were able to follow the evolution of comet C/2013 US10 (Catalina) activity over more than 5 au pre-perihelion. We started to observe the comet on May 16, 2014 ($r$ = 6.65 au) and we first observed only with broad band filters, as the comet was faint. As soon as the comet was bright enough, we started to observe with narrow band dust filters. We could not observe from mid-January to early April due to solar conjunction. When we recovered the comet in April, we observed continuously until mid-September, after what the comet was too close to the

Sun again. We were able to recover it for a brief period of time after perihelion in December and January, before it went too far north. We computed $Af\rho$ values from both broad band and narrow band filters. The long-term dust production evolution is illustrated in Fig. 3.45. The trend is similar for the broad band Rc filter and the three narrow band filters. The $Af\rho$ slowly rises from 6.6 to 3 au pre-perihelion. We then observe a slow decrease or a plateau from 3 to 1.4 au. More precisely, from the broad band Rc filter, it seems that the $Af\rho$ first decreases between 3 and 2 au, and rises between 2 and 1.4 au. Overall, the increase of the dust production between 6.6 and 1.4 au is small. This behaviour is typical of dynamically new comets, making their first entrance into the inner solar system. It not unusual to observe a decrease of the dust activity of a dynamically new comet inside 3 au. It was for example the case of comet C/2009 P1 (Garradd) (see section 3.2.1) and comet C/2013 A1 (Siding Spring) (see section 3.4.1). We were only able to observe the comet for a couple weeks after its perihelion passage. During this time, we observe a rapid decrease of the $Af\rho$. The dust production of comet C/2013 US10 (Catalina) is then very asymmetric about perihelion, with a slow increase as the comet is approaching the Sun and a fast decrease after perihelion.

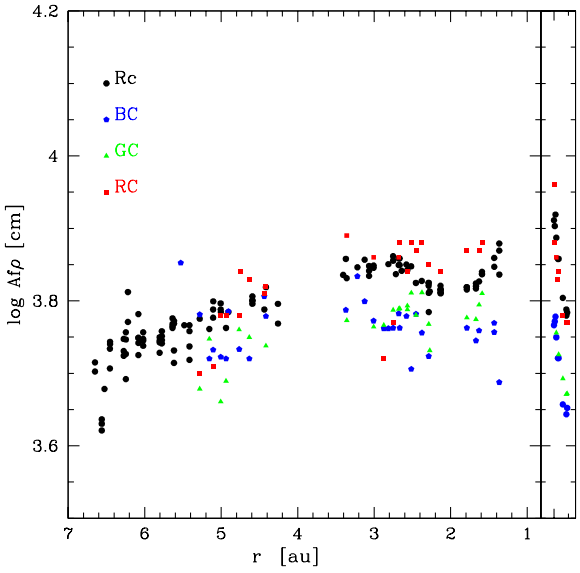


Figure 3.45: Evolution of comet C/2013 US10 (Catalina) $Af\rho$ corrected from the phase angle with the heliocentric distance pre- and post-perihelion from broad band and narrow band continuum filters. The vertical line indicates perihelion ($r$ = 0.82 au).

We monitored the gas activity of the comet from 3.4 to 1.4 au pre-perihelion. We also have a few measurements after the perihelion passage. In addition to narrow band images with TRAPPIST, we obtained low resolution spectra at four epochs. These observations were performed at 2.87 (May 21, 2015), 2.30 (July 7, 2015), 1.84 (August 11, 2015), and 1.47 au (September 7, 2015) pre-perihelion. We used the 300V grism. For each epoch, we performed one short exposure to ensure non-saturated observations of the inner coma, three longer exposures with a small offset to place the comet on one edge of the CCD and sample the gas emission

as far away from the nucleus as possible, and finally one very long exposure with the same offset to increase the gas S/N far from the nucleus. This sequence was repeated two times for each epoch, once with the slit positioned along the tail, and once with the slit in the direction perpendicular to the tail. We do not have observations with the slit perpendicular to the tail direction for the first epoch. We used observations of Ceres with the same grism to subtract the continuum emission. We compare TRAPPIST and VLT/FORS 2 observations to ensure they are consistent. The first spectroscopic observations are those made on May 21, 2015, and the closest TRAPPIST observations are those performed the next day. Figure 3.46 shows the comparison between TRAPPIST and FORS 2 profiles for CN and $C_2$. As it was the case for comet C/2013 A1 (Siding Spring), profiles derived from narrow band imaging and low resolution spectroscopy are a good match for both CN and $C_2$. Figures 3.48 and 3.47 show the evolution of comet Catalina production rates. On these figures, we overplotted gas production rates derived from spectroscopic observations to those derived from TRAPPIST narrow band images. For three dates, spectroscopic values agree within the error bars with the general trend from TRAPPIST observations. The FORS 2 observations from July 7, 2015 give production rates higher than expected from the TRAPPIST trend, even considering the error bars and the variability of the comet. TRAPPIST production rates measured one day later fit well within the trend, so we do not think these higher CN and $C_2$ production rates are due to an outburst. For now, we are still unable to identify the source of this discrepancy.

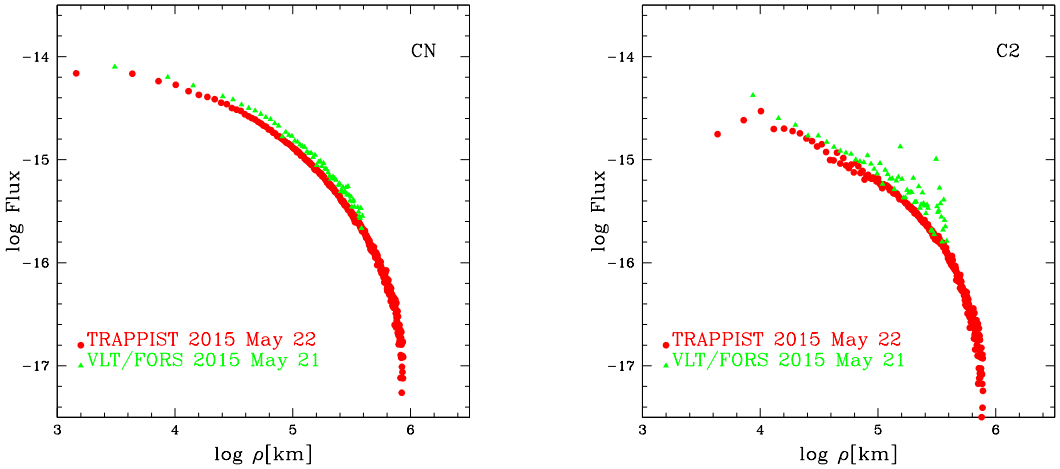


Figure 3.46: CN (left) and $C_2$ (right) brightness profiles from May 21 and 22, 2015. TRAPPIST data are represented with red circles and the closest VLT data is overplotted with green triangles.

Figures 3.47 and 3.48 show the evolution of production rates of comet C/2013 US10 with the heliocentric distance pre- and post-perihelion. Firstly, all gas production rates increase slowly as the comet approaches the Sun. The shapes of the OH and CN lightcurves are very similar. Both these production rates increase from 3.5 to about 2.3 au and we then observe a plateau between 2.3 and 1.5 au. This plateau is not observed for NH, $C_3$, or $C_2$. As for

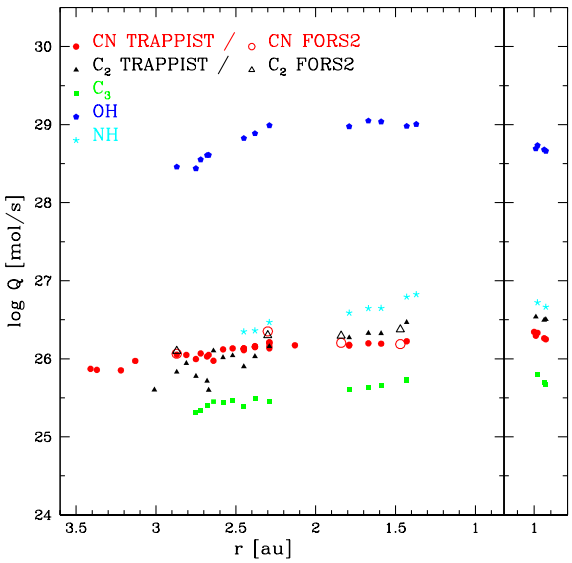


Figure 3.47: Evolution of comet C/2013 US10 (Catalina) OH, NH, CN, $C_3$, and $C_2$ production rates with the heliocentric distance pre- and post-perihelion. The vertical line indicates perihelion ($r = 0.82$ au). Gas production rates derived from spectroscopic observations are represented with open symbols.

the dust, gas production rates are asymmetric about perihelion, they decrease much faster after the perihelion passage. However, the asymmetry is not as strong as for the $A(0)f\rho$. OH production rates are lower after the perihelion passage. We fitted power-law slopes to represent the evolution of production rates with the heliocentric distance. The evolution of most gas production rates is not well represented by a simple slope. This is for example the case of the OH production rates pre-perihelion, for which we observe a plateau between 2.3 and 1.5 au. If we fit a slope only between 2.9 and 2.3 au pre-perihelion, when the OH production rate is increasing, we would obtain a much steeper slope for the evolution of the OH production rate with the heliocentric distance than the one we report here. However, all species do not shown a plateau of gas production rates prior to the perihelion passage. In order to facilitate the comparison of species between each other and with the dust, we thus decided to fit a simple slope over the whole range of pre-perihelion data for all gas species and the dust, but we must keep in mind that a simple slope is not a good representation of the evolution of the gas production rates with the heliocentric distance for all species. The slopes are summarized in Table 3.22. As expected from Fig. 3.45, the dust slope between 3.4 and 1.4 au pre-perihelion is almost consistent with zero, confirming that the dust production do not increase between 3.4 and 1.4 au pre-perihelion. Post-perihelion slopes have large uncertainties, since we only have a few production rate measurements after the perihelion passage. We were not able to derive slopes post-perihelion for $C_3$ and NH, due to the insufficient number of observations. CN has a lower slope than other production rates and is strongly asymmetric. To the contrary, pre-perihelion $C_2$ slope is steeper, but pre- and pot-perihelion slopes are consistent within

the error bars. However, pre-perihelion gas production rates heliocentric trends are poorly represented by simple slopes, especially OH and CN, and we must then interpret these slopes with caution.

Table 3.22: Fitted power-law slopes for comet C/2013 US10 (Catalina) OH, CN, $C_3$, and $C_2$ production rates and $A(0)f\rho$ heliocentric dependences pre- and post-perihelion.

| Species | r-dependence | |
|---|---|---|
| | pre | post |
| OH | -1.45±0.35 | -1.79±1.11 |
| NH | -1.84±0.12 | - |
| CN | -0.74±0.14 | -2.88±0.75 |
| $C_3$ | -1.16±0.09 | - |
| $C_2$ | -1.35±0.13 | -1.59±0.59 |
| $A(0)f\rho$ | +0.06±0.05 | -1.89±0.18 |

### 3.6.2 Composition

We computed gas production rate ratios to study the evolution of comet Catalina composition with the heliocentric distance. The OH, NH, $C_3$, $C_2$, and $A(0)f\rho$ to CN production rate ratios are shown in Fig. 3.49. $C_2$ to CN, $C_3$ to CN, NH to CN, and OH to CN ratios increase with decreasing heliocentric distances. To the contrary, the dust to gas ratio decreases with decreasing heliocentric distances. The OH to CN ratio is lower after perihelion, because the OH production rate is strongly asymmetric about perihelion. We fitted power-law slopes to represent the heliocentric trend of these ratios (see Table 3.23). We could not fit slopes for post-perihelion ratios, owing to the lack of observations after the perihelion passage. The $C_2$ to CN, NH to CN, and OH to CN ratio slopes are similar within the error bars while the $C_3$ to CN slope is lower.

Table 3.23: Fitted power-law slopes for the heliocentric dependence of C/2013 US10 (Catalina) OH, $C_3$, $C_2$, and $A(0)f\rho$ to CN ratios pre-perihelion.

| Species | r-dependence |
|---|---|
| log[Q(OH)/Q(CN)] | -1.08±0.31 |
| log[Q(NH)/Q(CN)] | -1.48±0.09 |
| log[Q($C_3$)/Q(CN)] | -0.57±0.19 |
| log[Q($C_2$)/Q(CN)] | -1.24±0.32 |
| log[Q($A(0)f\rho$)/Q(CN)] | +0.91±0.23 |

We also monitored comet Catalina dust colour, from the RC and BC narrow band filters. The result is shown in Fig. 3.50. Even though there is a large dispersion, we observe an increase of the dust colour as the comet approaches the Sun. The dust becomes redder at

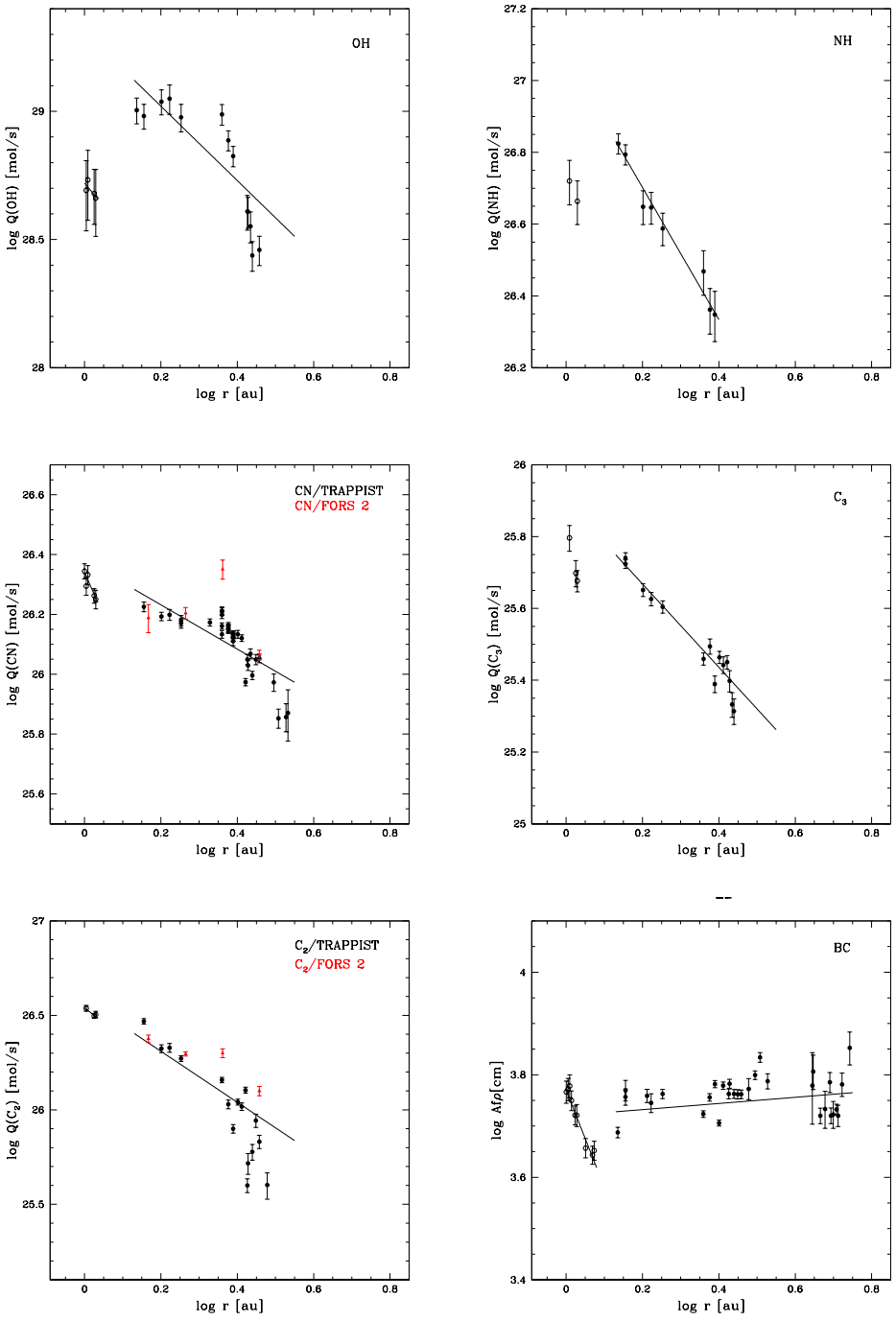


Figure 3.48: Comet C/2013 US10 (Catalina) OH, CN, $C_3$, and $C_2$ production rates and $A(0)f\rho$ as a function of the heliocentric distance ($r$). Filled symbols represent pre-perihelion data and open symbols post-perihelion data. Full lines represent power-law fits of the production rates and $A(0)f\rho$ variation with the heliocentric distance. Gas production rates derived from spectroscopic observations are represented with red triangles.

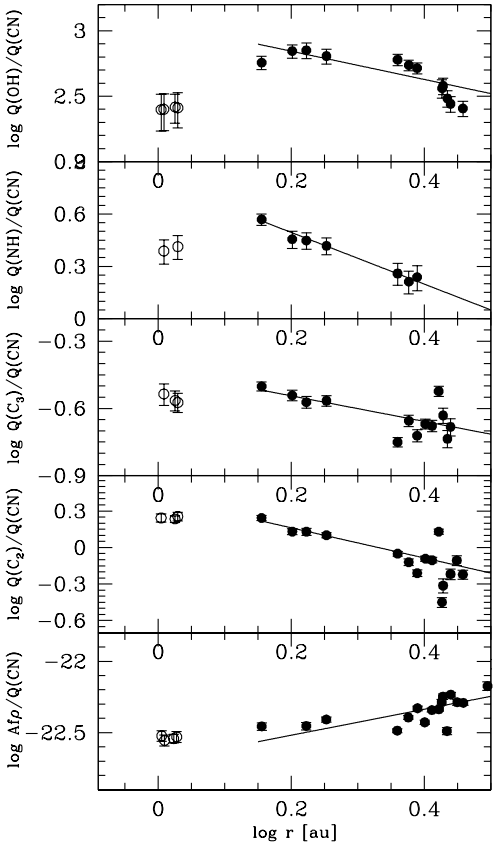


Figure 3.49: Comet C/2013 US10 (Catalina) OH, NH, $C_3$, $C_2$, and $A(0)f\rho$ to CN production rate ratios as a function of the heliocentric distance. Full lines represent power-law fits of the ratios variation with the heliocentric pre-perihelion distance. Filled symbols represent pre-perihelion data and open symbols post-perihelion data.

smaller heliocentric distances. Changes of the dust colour usually reflect changes of the dust properties: size distribution, or composition of the dust grains. However, since we only have optical observations, it is difficult to interpret the trend in the dust colour we observe in terms of changing dust properties. We do not observe an asymmetry of the dust colour about perihelion.

### 3.6.3 Morphology

We processed narrow band images by subtracting an azimuthal median profile to study the morphology of comet C/2013 US10 (Catalina) coma. Figure 3.51 shows the results for observations made on December 22, 2015 ($r$ = 1.07 au) for CN, $C_3$, $C_2$, and the dust in RC filter. We could not detect any morphological features in the OH and NH filters at any time.

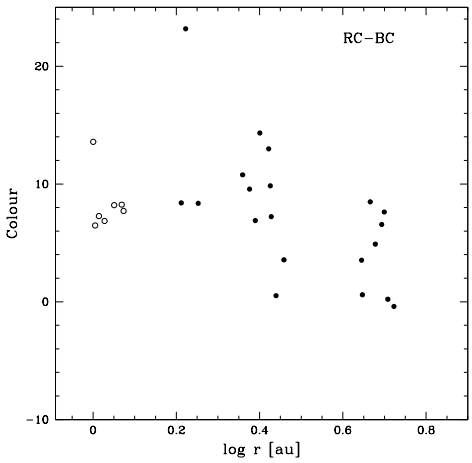


Figure 3.50: Evolution of comet C/2013 US10 (Catalina) dust colour as a function of the heliocentric distance. Filled symbols represent pre-perihelion data and open symbols post-perihelion data.

We first notice that gas and dust morphologies are different. CN and $C_2$ are enhanced in the direction orthogonal to the Sun-tail line. The direction of the $C_3$ feature is more difficult to determine but it could be consistent with what we observe for the CN and the $C_2$. As expected, the dust is enhanced in the tail direction and we observe a dust jet in the sunward direction. The morphological features we observe indicate that there are probably several active zones on the nucleus. CN, $C_3$, and $C_2$ are probably released from the same areas, which might be different from the dust. We started to observe CN features in mid-June, 2015. At that time, the CN has an hourglass shape, which is observed until September 2015. We do not observe strong $C_3$ and $C_2$ features prior to December, 2015. Finally, the dust morphology we describe here is similar to what we observe from July to September, 2015, taking into account the changing viewing geometry.

### 3.6.4 Summary

We observed comet Catalina during several months before its perihelion passage, while the comet was between 6.6 and 1.4 au, and also during a few weeks post-perihelion. Low resolution spectra of comet Catalina were obtained at 4 heliocentric distances pre-perihelion. Both the CN and $C_2$ radial profiles and the gas production rates we derived from these observations are mostly in good agreement with the TRAPPIST observations, allowing the comparison between those data sets.The $A(0)f\rho$ increases between 6.6 and 3 au pre-perihelion and then goes through a standstill period between 3 and 1.4 au. Similarly, the NH, $C_3$, and $C_2$ production rates increase slowly as the comet approaches the Sun and we observe a plateau of the OH and CN production rates between 2.3 and 1.5 au. After perihelion, the activity decreases faster. This behaviour is similar to what we observed for comets C/2009 P1 (Garrad) and C/2013 A1 (Siding Spring) and typical of dynamically new comets. We discuss this further in Chapter 4.

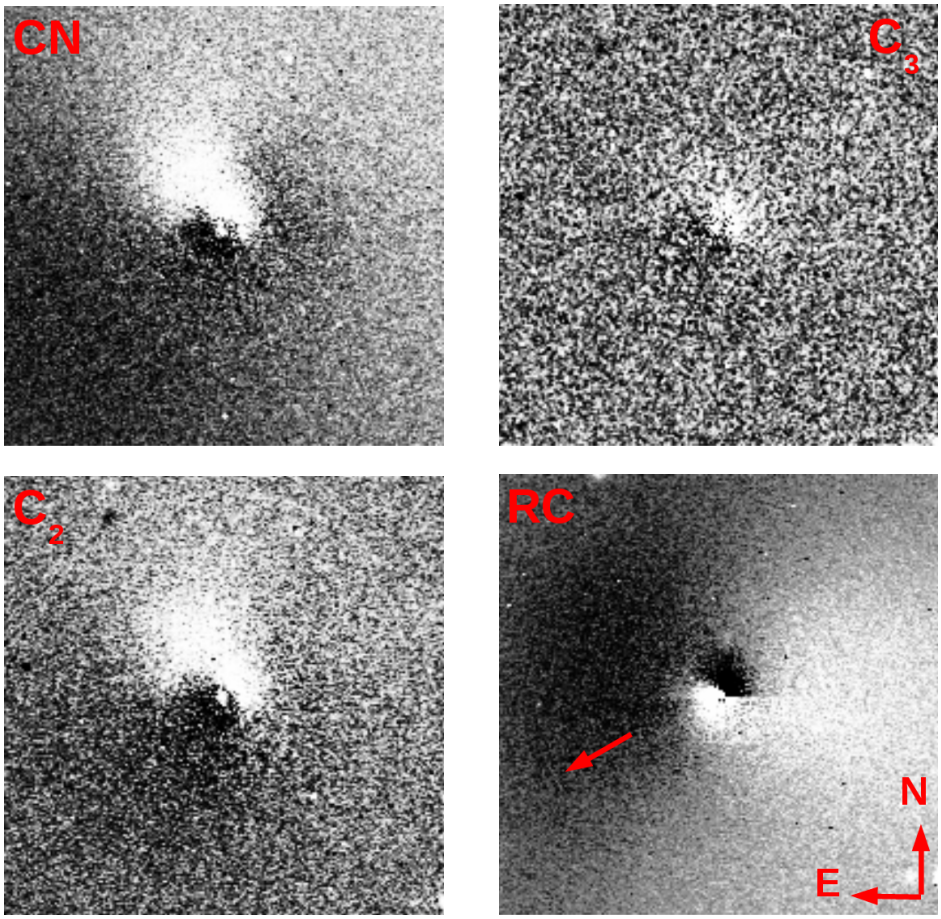


Figure 3.51: C/2013 US10 (Catalina) CN, $C_3$, $C_2$, and dust from RC filter images from December 22, 2015 ($r$ = 1.07 au) processed by subtracting an azimuthal median profile. All images are oriented with north up and east left. The field of view is 4.3′ × 4.3′. The arrow indicates the direction of the Sun.

We observed an increase of the $C_2$, $C_3$, NH and OH to CN ratios with decreasing heliocentric distances pre-perihelion, while the dust to gas ratio is decreasing.

## 3.7 C/2014 Q2 (Lovejoy)

Comet C/2014 Q2 (Lovejoy) is a long period comet originating from the Oort Cloud. It was discovered on 17 August 2014 by Terry Lovejoy at 2.8 au from the Sun (Lovejoy et al., 2014). Comet Lovejoy has a period of about 14,000 years, and is a dynamically old long period comet. This means it was not its first entry in the inner solar system. The comet moves on a 80°-inclined orbit. It reached perihelion on 30 January 2015 at 1.29 au from the Sun. The comet reached naked-eye brightness in January and February 2015 and was observed by numerous telescopes.

### 3.7.1 Activity

We started to observe comet C/2014 Q2 on October 11, 2014 ($r$ = 1.80 au), less than two months after its discovery. At that time, the comet was bright enough to be observed with narrow band filters. First, the only gas species we were able to detect was the CN, but we detected OH, NH, $C_3$, and $C_2$ in the course of November 2014. We observed continuously until January 23, 2015 ($r$ = 1.3 au). After that, the comet was too far north to be observed with TRAPPIST. In late December 2014 and January 2015, we observed the comet for several hours during the same night to attempt measuring the nucleus rotation period.

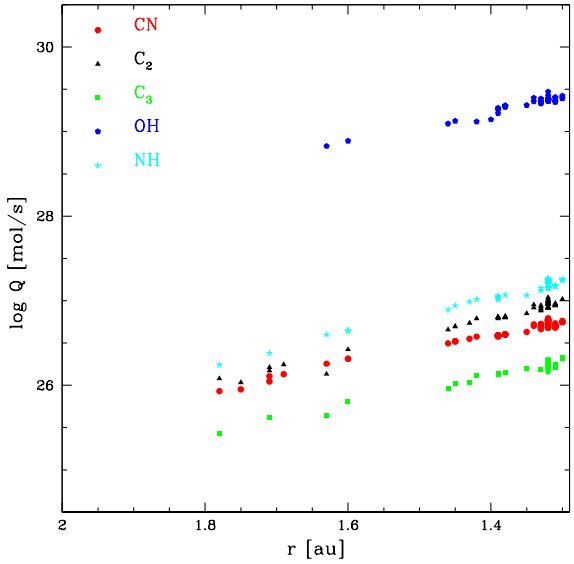


Figure 3.52: Evolution of comet C/2014 Q2 (Lovejoy) OH, NH, CN, $C_3$, and $C_2$ production rates with the heliocentric distance pre-perihelion. The origin of the $r$-axis is perihelion ($r$ = 1.29 au).

We present the evolution of comet Lovejoy gas production rates between 1.8 and 1.3 au pre-perihelion in Fig. 3.52. All gas production rates are rising regularly as the comet approaches the Sun. We fitted power-law slopes to represent the evolution of OH, NH, CN, $C_3$, and $C_2$ production rates and the $Af\rho$ from BC filter with the heliocentric distance pre-perihelion. The resulting slopes are given in Table 3.24 and represented in Fig. 3.53. Slopes derived for gas species are steep, indicating that gas production rates rise fast as the comet approaches the Sun. The dust slope is shallower but it can still be considered as steep compared to the other comets presented in this section. Since we do not have observations post-perihelion, we can not tell whether the activity of this comet was asymmetric about perihelion or not. Amateur astronomers observations of the comet on both sides of perihelion seem to indicate that the activity of the comet peaked before perihelion and that the activity decrease is slower than the increase (see e.g. Seiichi Yoshida's web page[4]). In Fig. 3.53, we observe a rather large

[4] http://www.aerith.net/comet/catalog/2014Q2/2014Q2.html

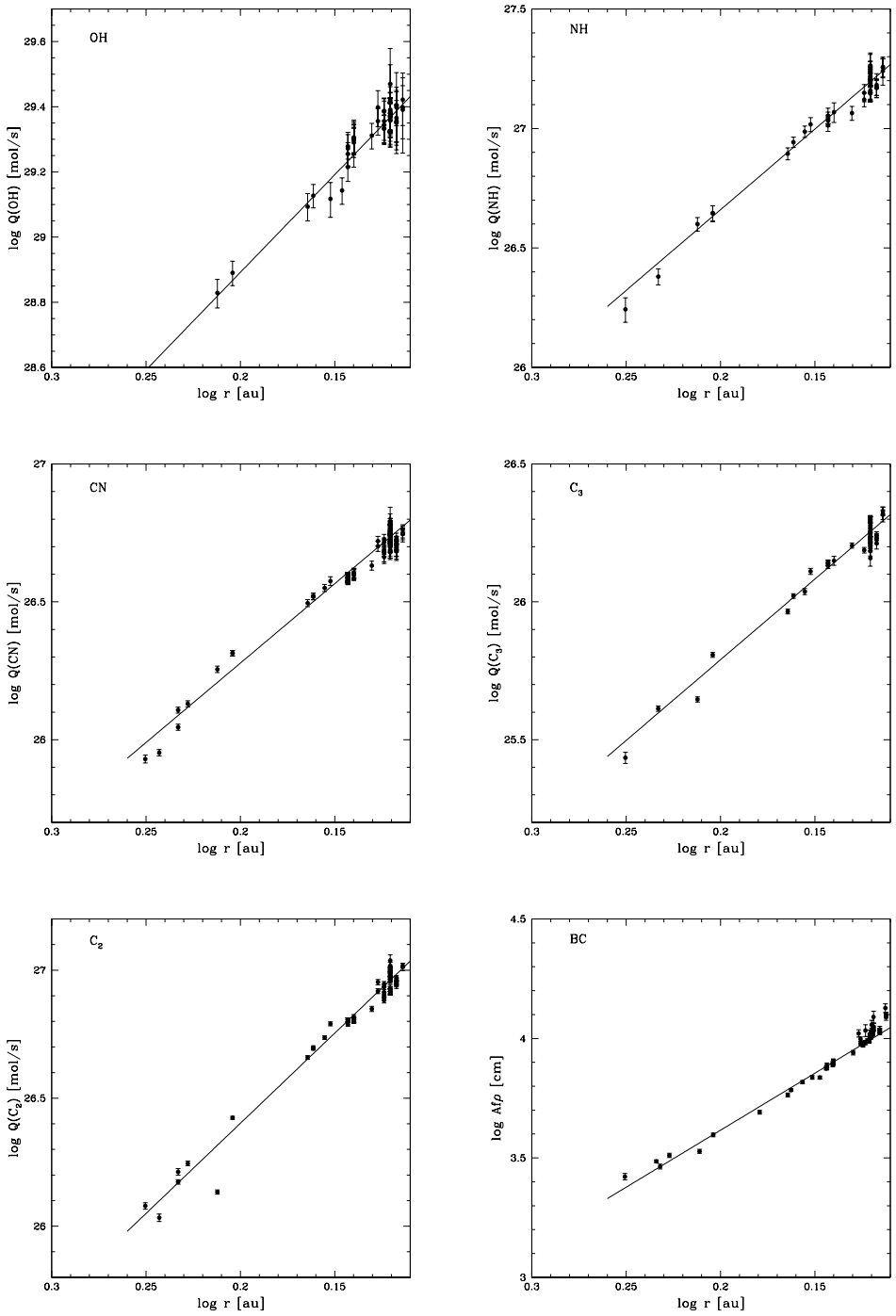


Figure 3.53: Comet C/2014 Q2 (Lovejoy) OH, CN, $C_3$, and $C_2$ production rates and $A(0)f\rho$ as a function of the heliocentric distance ($r$). Filled symbols represent pre-perihelion data and open symbols post-perihelion data. Full lines represent power-law fits of the production rates and $A(0)f\rho$ variation with the heliocentric distance.

dispersion of gas production rates derived from observations made at different times during the same night. We interpret this dispersion as being due to the rotation of comet C/2014 Q2 nucleus. We applied periodograms on the CN lightcurve trying to constrain comet Lovejoy rotation period. However, we were not able to determine the nucleus period from the analysis of the CN lightcurve alone. This might be due to an insufficient time coverage or to an excited rotation state making the determination of the period complicated.

Table 3.24: Fitted power-law slopes for comet C/2014 Q2 (Lovejoy) OH, CN, $C_3$, and $C_2$ production rates and $A(0)f\rho$ heliocentric dependences pre-perihelion.

| Species | r-dependence |
|---|---|
| OH | -5.99±0.26 |
| NH | -6.75±0.24 |
| CN | -5.76±0.17 |
| $C_3$ | -5.85±0.24 |
| $C_2$ | -7.04±0.26 |
| $A(0)f\rho$ | -4.77±0.12 |

### 3.7.2 Composition

Comet C/2014 Q2 (Lovejoy) was observed by numerous observers at different wavelengths. Biver et al. (2015) report water production rates $Q(H_2O) = 5 \times 10^{29}$ mol/s and $Q(H_2O) = 6 \times 10^{29}$ mol/s for the periods 13-16 and 23-26 January 2015 respectively, from observations with the Nancay radio telescope and the Odin satellite. From TRAPPIST observations made on 13-14 January, we measure a mean value of the vectorial-equivalent water production rate $Q(H_2O) = (2.90 \pm 0.18) \times 10^{29}$ mol/s. Our value is lower than the one from Biver et al. (2015), even if we take into account the rotational variation, but the size of the field of view is different. In addition, water production rates measured from radio and optical observations have already been shown to disagree in several cases. The cause of this discrepancy is no well understood but might be linked to the size of the field of view or the models and parameters used to derive gas production rates. Biver et al. (2015) also report a mean value of the HCN production rate $Q(HCN) = 4.95 \times 10^{26}$ mol/s for the 13-25 January period. On January 17, we measure $Q(CN) = (4.99 \pm 0.15) \times 10^{26}$ mol/s from TRAPPIST observations. HCN and CN production rates agree within the error bars, indicating that HCN is probably the main parent of CN in the coma of this comet. This is consistent with the lack of extended sources noticed by Biver et al. (2015).

We computed production rate ratios to study the evolution of comet Lovejoy composition with the heliocentric distance. Fig. 3.54 shows the evolution of OH, NH, $C_3$, and $C_2$ production rates and the $A(0)f\rho$ to CN production rate as a function of the heliocentric distance. We fitted power-law slopes to evaluate the evolution of production rate ratios as the comet approaches the Sun. The slopes are given in Table 3.25. The OH, NH, $C_3$, and $C_2$ to CN production rate

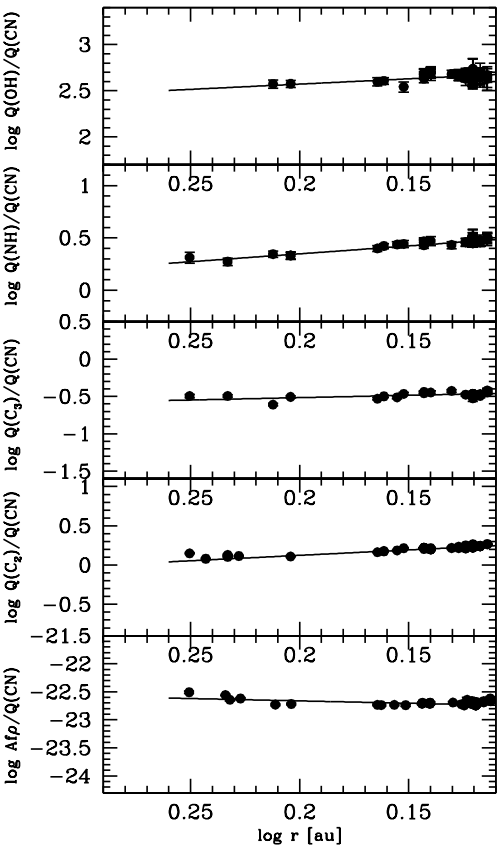


Figure 3.54: Comet C/2014 Q2 (Lovejoy) OH, NH, $C_3$, $C_2$, and $A(0)f\rho$ to CN production rate ratios as a function of the heliocentric distance. Full lines represent power-law fits of the ratio variations with the heliocentric distance.

ratios increase as the comet approaches the Sun. The OH, NH, and $C_2$ to CN ratios have similar slopes, while the $C_3$ to CN slope is shallower. The dust to gas ratio decreases with decreasing heliocentric distances.

Table 3.25: Fitted power-law slopes for the heliocentric dependence of comet C/2014 Q2 (Lovejoy) OH, NH, $C_3$, $C_2$, and $A(0)f\rho$ to CN ratios pre-perihelion.

| Species | r-dependence |
|---|---|
| log[Q(OH)/Q(CN)] | -1.14±0.24 |
| log[Q(NH)/Q(CN)] | -1.51±0.11 |
| log[Q($C_3$)/Q(CN)] | -0.63±0.24 |
| log[Q($C_2$)/Q(CN)] | -1.38±0.29 |
| log[Q($A(0)f\rho$)/Q(CN)] | +0.84±0.24 |

We computed the dust colour from the RC and BC narrow band filters and followed its evolution with the heliocentric distance. The result is presented in Fig. 3.55. The dust colour has a mean value of $7.95 \pm 0.69$ % per 1000 Å. We do not observe any strong variation of the dust colour with the heliocentric distance.

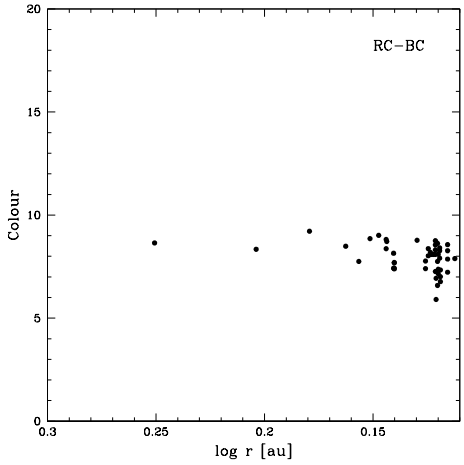


Figure 3.55: Evolution of comet C/2014 Q2 (Lovejoy) dust colour as a function of the heliocentric distance.

### 3.7.3 Morphology

We enhanced TRAPPIST narrow band images by subtracting an azimuthal median profile to study coma features. The result is shown in Fig. 3.56 for images taken on January 17, 2015. We observe an enhancement of the dust in the sunward direction. The gas morphology looks very different from the dust. In the CN image, we observe at least three different jets in various direction. Two of these jets are curved. The $C_3$ morphology is very similar to the CN morphology. We can see the same three jets, even though their relative intensity is different. The jet oriented toward the east is brighter while the one oriented toward the Sun is fainter. The $C_2$ image looks slightly different. The jet oriented towards the east is very bright while the two other jets we observed for CN are barely visible. We do not observe any of the three jets in the OH or NH filter, but an enhancement of the coma towards the south east.

### 3.7.4 Rotation

The gas morphology of the comet is varying from night to night, and between observation made hours apart during the same night. The number, position, and relative intensity of the jets is changing. We then attempted to use the morphology of the coma to determine the rotation period of comet C/2014 Q2 (Lovejoy). From December 2014 to January 2015, the general morphology of the coma varies due to the changing system geometry. Because of this, it is easier to use only January 2015 data to search for the rotation period. We use

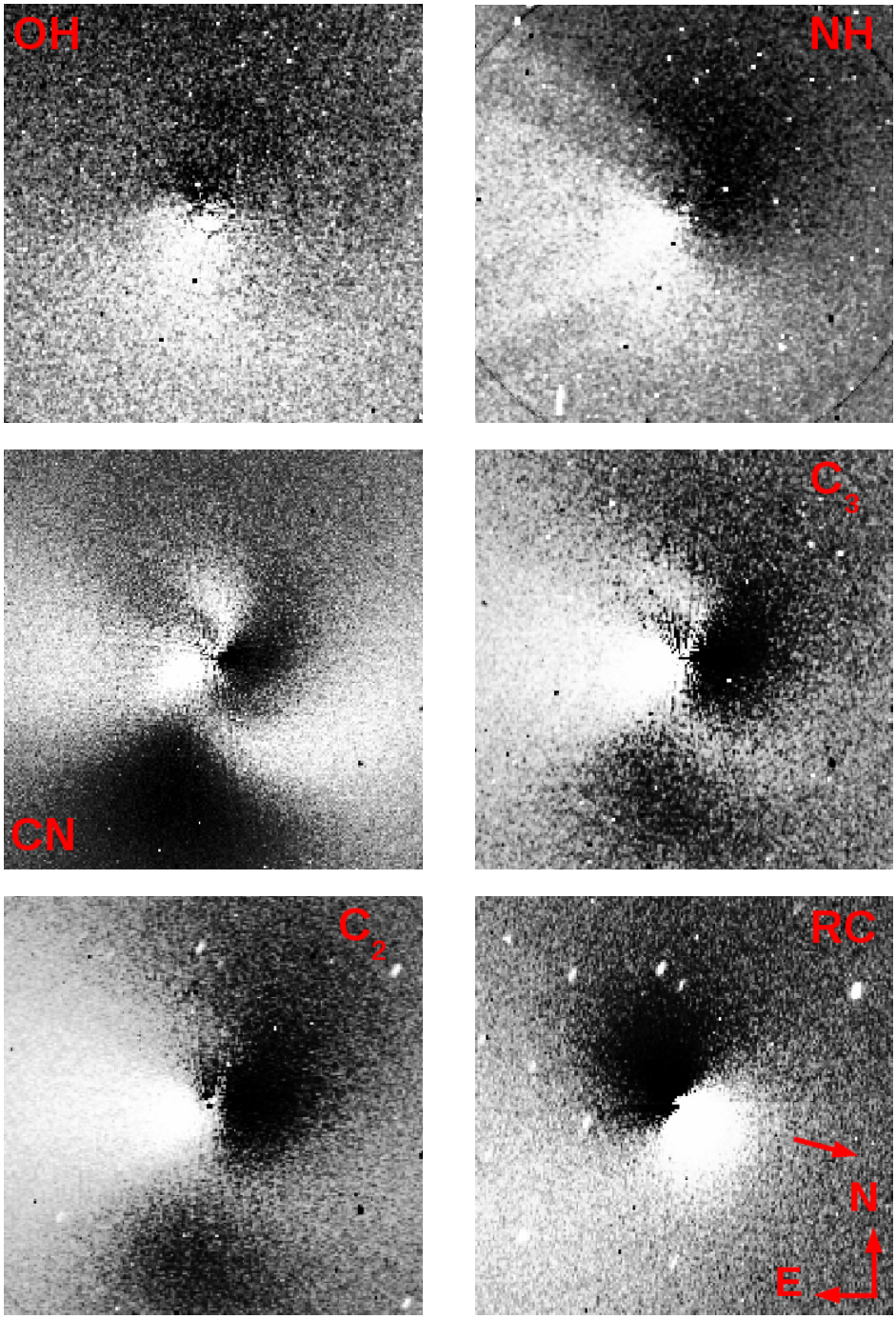


Figure 3.56: C/2014 Q2 (Lovejoy) OH, NH, CN, $C_3$, $C_2$, and RC images from January 17, 2015 processed by subtracting an azimuthal median profile. All images are oriented with north up and east left. The field of view is 4.3' × 4.3'. The arrow indicates the direction of the Sun.

CN images for the period search, because we observe several features in the CN images and this filter is less contaminated by the dust than the $C_3$ and $C_2$ filters. This reduces the risk

of introducing artefacts while subtracting the dust contribution. Serra-Ricart and Licandro (2015) measure a rotation period of $17.89 \pm 0.17$ hr from the analysis of coma morphological features in observations obtained between January 21 and February 11, 2015. If we phase our data using this period, we notice that it is not matching, jets are suddenly jumping from one position to another. It thus seems that a $17.89 \pm 0.17$ hr rotation period is not consistent with our data. Biver et al. (2016) observe a periodic pattern repeating every 22.56 hours within the water production rates they derived from observations with Odin between January 13 and 26, 2015. This period is not consistent with our data either.

We noticed that enhanced CN images taken 3 days apart look very similar. Figure 3.57 shows CN enhanced images phased using a 3 days period. Since this period is a multiple of one day, and since the comet was not visible during the whole night a that time, our phase coverage is not complete. We have several large gaps in phase and this makes the determination of the exact rotation period difficult. As can be seen in Fig. 3.57, a 3 days rotation period seems to work with our data. From our observation we can only determine an approximate of the period and we can not give reliable error bars. We also investigated multiples of this period. A 1.5 days period could also be consistent with our data but shorter periods can be ruled out. Due to the lack of phase coverage, it is difficult to decipher between the 1.5 days and 3 days rotation periods.

Trying to decipher between the two possible rotation periods, we re-analysed the CN production rates lightcurve from January 2015. We de-trended the data using a power-law slope, normalised the de-trended values to arbitrary units, and then phased the production rates using 1.5 and 3 days periods. The results are shown in Fig. 3.58 and 3.59. The dispersion is large but it confirms that the comet rotation period could be 1.5 or 3 days. The lack of phase coverage makes it difficult to decide which period is the best. However, we notice that for the 1.5 days phase curve, we would need a very fast decrease of CN production rates between the maximum at phase 0.5 and the minimum at phase 0.65. This could make the 1.5 days period less likely than the 3 days period. Only more data could allow the determination of the exact rotation period of comet C/2014 Q2 (Lovejoy).

### 3.7.5 Summary

We observed comet Lovejoy regularly between October 11, 2014 and January 23, 2015 and studied the evolution of its activity while the comet was appraoching the Sun. Gas and dust production rates increase fast as the comet approaches the Sun. We observed an increase of the $C_2$, $C_3$, NH, and OH to CN ratios with decreasing heliocentric distances pre-perihelion, while the dust to gas ratio is decreasing. We measured a mean value of the dust colour of about 8 %/1000Å and we did not observe any strong variation of the dust colour with the heliocentric distance. We gathered long series of observation during several nights in December and January. During these nights, the coma morphology and gas production rates vary over the course of several hours due to the rotation of the nucleus. By combining the analysis of the

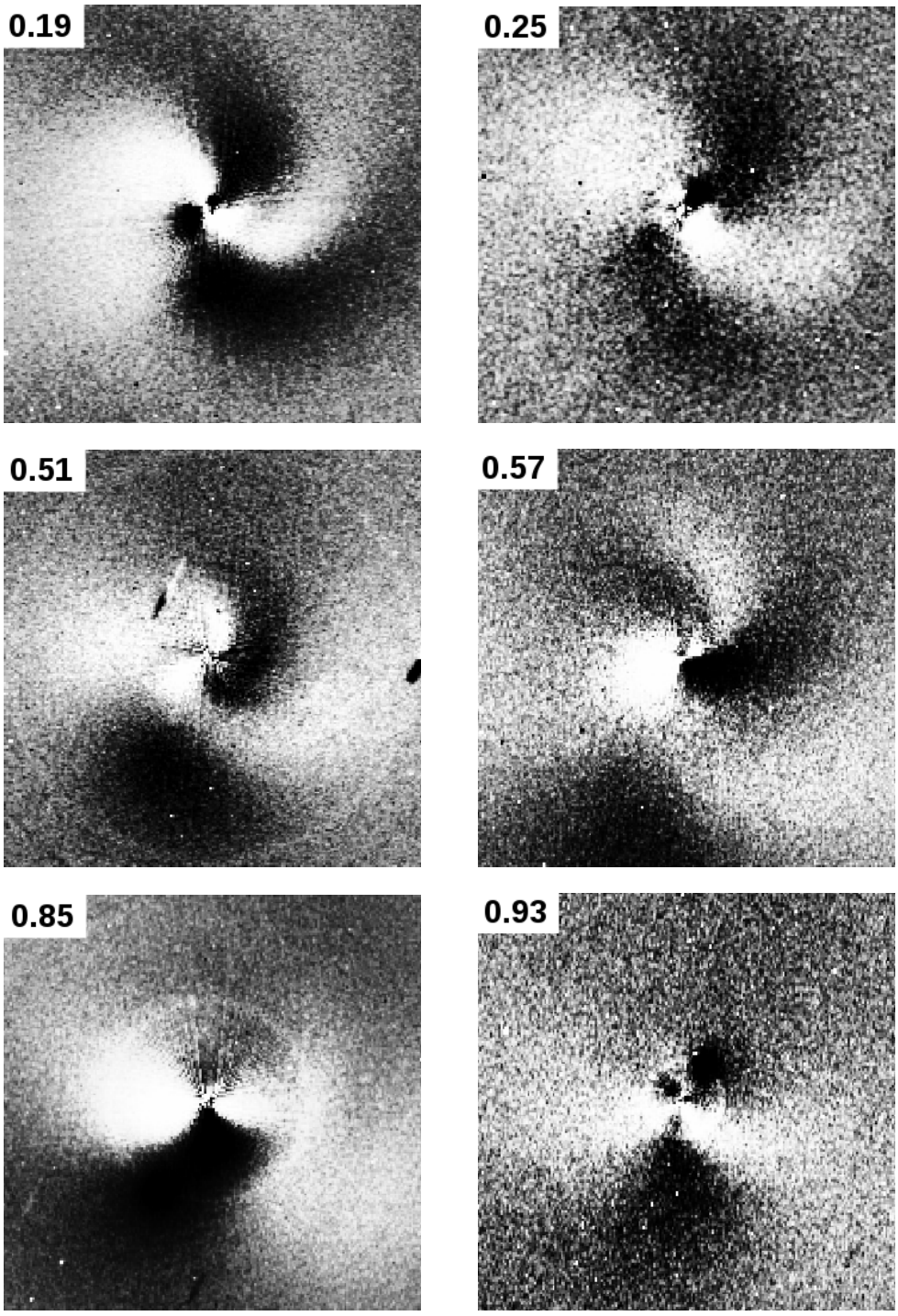


Figure 3.57: C/2014 Q2 (Lovejoy) CN images acquired in January 2015 processed by azimuthal median profile subtraction. The images have been sorted out by rotational phase assuming a rotation period of 3 days. All images are oriented with north up and east left. The field of view is 4.3' × 4.3'.

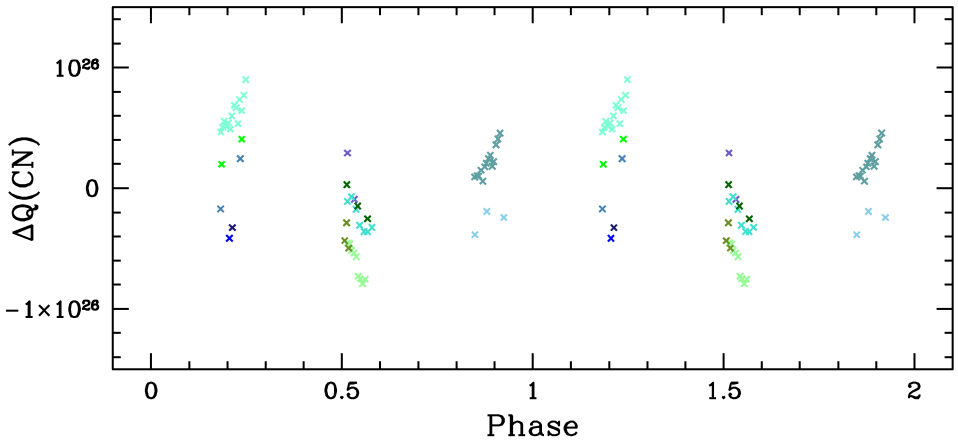


Figure 3.58: C/2014 Q2 (Lovejoy) CN phase curve using a 3 days rotation period. Each night is represented with a different colour.

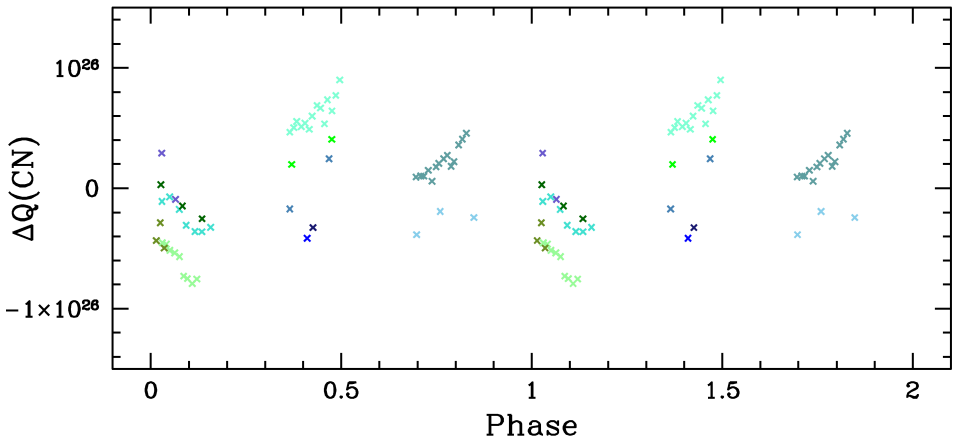


Figure 3.59: C/2014 Q2 (Lovejoy) CN phase curve using a 1.5 days rotation period. Each night is represented with a different colour.

CN coma morphology variation and the CN production rates lightcurve, we determined that the rotation period of the nucleus is probably either 1.5 or 3 days, with a preference for the 3 days period.

## 3.8 Conclusion

In this Chapter, we performed a thorough study of several individual comets. For three of these comets -103P/Hartley 2, C/2012 F6 (Lemmon), and C/2014 Q2 (Lovejoy)- we were able to determine, or at least constrain, the rotation period of the nucleus. The rotation period of a comet nucleus is difficult to determine because we can not usually detect the nucleus directly. Only about two dozen rotation periods are known so far. We have demonstrated

that for comets observable several hours per night, we are able to determine their rotation period from TRAPPIST observations. By applying image enhancement techniques on the TRAPPIST images, we revealed morphological features in the coma. We observed several types of features in TRAPPIST images: jets, spirals, hour-glass shapes, simple enhancement in one direction. Depending on the location of the active area(s), the orientation of the rotation axis of the nucleus, and the observing geometry, we could sometimes see the position and shape of the morphological features vary because of the rotation of the nucleus. That was the case for comets C/2012 F6 (Lemmon) and C/2014 Q2 (Lovejoy). We were then able to distinguish the periodic repetition of identical patterns and to determine the rotation period of these comets. In some cases, like comet 103P/Hartley 2, we could not see variations of the coma morphology with time but we observed variations of gas production rates during the night. We then performed a period analysis on the gas production rate lightcurve and determined the rotation period of the nucleus. The dense temporal coverage of comet 103P/Hartley 2 observations over several months even allowed to detect changes of the rotation period of the comet with time. TRAPPIST is thus a powerful tool to determine the rotation period of comet nuclei, combining the analysis of the coma morphology and the gas production rates lightcurve, and we strongly believe that the rotation period of a larger number of nuclei will be determined in the future. Indeed, we now have more experience about the observing strategy to adopt in order to determine the rotation period of comets. Furthermore, a twin of TRAPPIST has been installed in June 2016 at the Oukaimeden observatory in Morocco. For comets observable from both observatories, we will then gather longer uninterrupted series of observations, facilitating the determination of the rotation period of these comets.

In Section 3.4.4, we introduced a new model we developed to reproduce the shape of the radial profiles we observed in the days following the outburst of comet C/2013 A1 (Siding Spring). This model is simple but it allowed us to reproduce the shape of the bump we observed in the CN and $C_2$ radial profiles after the outburst much better than with the Haser model. Using this model, we were able to characterize the outburst, to determine the time at which it occurred, the quantity of CN and $C_2$ released during the outburst, the expansion velocity of the gas following the outburst, and the characteristic time of the outburst. Our model then provides a new way to interpret the gas radial profiles observed consecutively to an outburst in order to characterize it. It could easily be applied to other comets in outburst, as long as observations of the comet during the days following directly the outburst are available. Applying this model to a larger number of comets will allow us to compare the characteristics of several outbursts and maybe help to better understand the mechanisms triggering these outbursts.

In Sections 3.4 and 3.6, we compared observations of two comet performed simultaneously with TRAPPIST and with the FORS 2 instrument of the VLT. These two comets were observed at different heliocentric distances and with different instrumental set up. In both cases, the radial profiles and production rates we derived from TRAPPIST and FORS 2 observations were in good agreement. This demonstrates that observations made with these two instruments and using different techniques can be compared and combined in a single data set. Since TRAPPIST is only a 60-cm telescope, we can not observe comets at very large heliocentric

distances. However, observing comets when they are far away from the Sun is essential to understand the outgassing at these distances and how it evolves while comets approach the Sun. Combining FORS 2 and TRAPPIST observations provides a way to follow the outgassing of comets over large ranges of heliocentric distances and to better understand how some daughter species are released into the coma and what their origin is.

In Section 3.5, we showed how it is possible to combine several techniques to investigate the origin of daughter species in the coma of comets. We compared the evolution of the production rates of several gas daughter species and the dust with the heliocentric distance, we compared the coma morphology observed in different filters, and we compared the daughter species production rates measured from the optical to the production rates of potential parents measured from infrared observations. Combining all these information, we obtained a good picture of the origin of several daughter species in the coma of comet C/2013 R1 (Lovejoy). The same process could be reproduced for other comets in the future, in order to pursue our investigation of the origin of daughter species in the coma and try to answer the long-debated question of species parentage.

In this Chapter, we studied the evolution of the activity, coma composition, and coma morphology of seven comets. If we try to compare what we observed for these comets, we realize that their behaviour is at the same time similar and completely different. For example, the $C_2$ to CN ratio of most of these comets decreases with the heliocentric distance. The dust to gas ratio of comets 103P/Hartley 2, C/2009 P1 (Garrad), C/2014 Q2 (Lovejoy), C/2013 US10 (Catalina), and C/2013 A1 (Siding Spring) increases with the heliocentric distance while the dust to gas ratio of comet C/2013 R1 (Lovejoy) decreases with the heliocentric distance. The two dynamically new comets (C/2013 A1 (Siding Spring) and C/2013 US10 (Catalina)) and the dynamically young comet (C/2009 P1 (Garradd)) have a very similar behaviour. Their activity increases very slowly as they approach the Sun while the activity of the other comets increases faster before perihelion. The three comets we observed on both sides of perihelion all have an asymmetric activity but the activity of comets C/2012 F6 (Lemmon) and C/2013 R1 (Lovejoy) decreases slower after perihelion while the activity of comet C/2013 US10 (Catalina) decreases faster after the perihelion passage. These are only a few examples but they illustrate how some aspects of the behaviour of these comets might be similar while others are not. With only seven comets, it is however difficult to determine what trends might be common to all comets and what trends reflect the intrinsic properties of each comet. In the next Chapter, we perform a global analysis of our sample of 30 comets. Our objective is to distinguish common trends and properties among our sample and to relate our observations to the origin or evolution of the comets.

# 4 Ensemble properties of our sample of comets

In this Chapter, we analyse our sample of 30 comets observed with TRAPPIST as a whole. Before we start the global analysis of our data set, we feel it is important to detail our observing strategy and explore some selection effects that could affect our sample. Our observing strategy is very simple, we observe every comet visible and bright enough that we can detect at least the CN with narrow band filters. Usually, the cut-off for observing with narrow band filters is around magnitude 12. However, it does not only depend on the magnitude of the comet but also on its dust to gas ratio. We might detect the CN emission in the coma of a magnitude 14 comet which has a low dust to gas ratios, while we might not be able to detect it in a comet which has the same magnitude but a much higher dust to gas ratio. We then cannot just fix a magnitude limit at which we start to observe comets. In practice, for every bright comet we attempt to detect the gas with narrow band filters, and if it is detected we start monitoring the comet on a regular basis. We should also note that Jupiter Family Comets are generally weaker than other types of comets. As a consequence, we only have 8 Jupiter Family Comets in the data set presented in this work and we were not able to detect the five gas species for all of these comets. Most JFCs were only bright enough to be observed with TRAPPIST over a short period of time. Finally, we paid particular attention to very bright comets who were targeted by large telescopes, to comets who were observed simultaneously at other wavelengths, or to space mission targets. These comets have been observed more intensively, at least over some part of their orbit. In 6 years of observations with TRAPPIST, we gathered more than 14,000 images of 30 comets observed with narrow band filters. We have observations over a wide range of heliocentric distances, from 0.3 au for comet C/2012 S1 (Ison) to more than 3.5 au for comet C/2013 US10 (Catalina). All comets have not been observed over the same range of heliocentric distances. For some comets, we only have a few observations spanning over a couple days or weeks, while other comets have been observed for months on both sides of perihelion. The five gas radicals we target in this study (OH, NH, CN, $C_3$, and $C_2$) have not been detected for every comet. The NH filter was only mounted on the telescope in October 2012, so we do not have NH production rates for comets observed prior to this date. For faint comets, we could not detect all radicals, and we were sometimes only able to measure CN production rates. As presented in the previous Chapter, some comets have been followed

regularly over wide ranges of heliocentric distances on both sides of perihelion. Our data set then allows us not only to compare the composition of different comets but also to study and compare the evolution of these comets along their orbit.

For the purpose of our study, we divided the comets of our sample in three categories depending on their dynamical origin: Jupiter Family Comets (JFC), Dynamically New Long Period Comets (DNC), and Dynamically Old Long Period Comets (LPC) - this includes any Long Period Comet which is not a Dynamically New Comet. Table 4.1 summarizes the comets we observed, their dynamical type, as well as their orbital elements and the ranges of distances and dates over which the comets were observed. In order to easily identify the type of comets in the figures presented in this Chapter, we established a colour code. Jupiter Family Comets are represented with red symbols, Dynamically New Long Period Comets with green symbols, and Dynamically Old Long Period Comets (LPC) with black symbols. The case of comet C/2009 P1 (Garradd) is peculiar. Comet Garradd is a dynamically young comet, which means that the comet did approach the Sun only a few times. However, since it was not its first passage in the inner solar system, we chose to classify it as LPC. We also needed a direct way to distinguish between pre- and post-perihelion data. Pre-perihelion observations of JFC are then represented with light red symbols while post-perihelion observations are represented with dark red symbols. Pre- and post-perihelion observations of DNC are represented respectively with light green and dark green symbols. Finally, pre-perihelion observations of LPC are represented with dark symbols while post-perihelion observations are represented with grey symbols. In order to easily identify comets in the figures presented in this Chapter, different symbols were attributed to every comet. These symbols are summarised in Fig. 4.1.

Our main goal is to study the evolution of comet activity and coma composition as a whole, try to define taxonomical classes, compare these classes with those defined by other authors, and make a link between properties of comets and their dynamical origin and place of formation. The main advantage of our study compared to previous ones is that we gathered a completely homogeneous sample. Our 30 comets have been observed with the same technique, telescope, instrument, and filters. A standard data reduction procedure, described in Chapter 2, has been applied to all data and we used the same models and parameters to compute gas production rates and the $Af\rho$ parameter. We also computed the gas production rates and the $Af\rho$ at the same physical distance in the coma for all comets. We then avoid introducing trends in the data linked for example to the geocentric distance of the comets at the time of the observations and ensure that any difference from a comet to another is real instead of an artefact of data reduction. We also observed several comets over wide ranges of heliocentric distances, which allows us to disentangle between variations of the coma composition with the heliocentric distance and intrinsic composition differences between comets. In this Chapter, we study the evolution of the activity of these comets with the heliocentric distance, compare their coma composition and its evolution along their orbit. We study the impact of the parameters used in the Haser model (the Haser scalelengths) on the derived production rates and production rate ratios and, finally, we investigate the origin of radicals in the coma of comets.

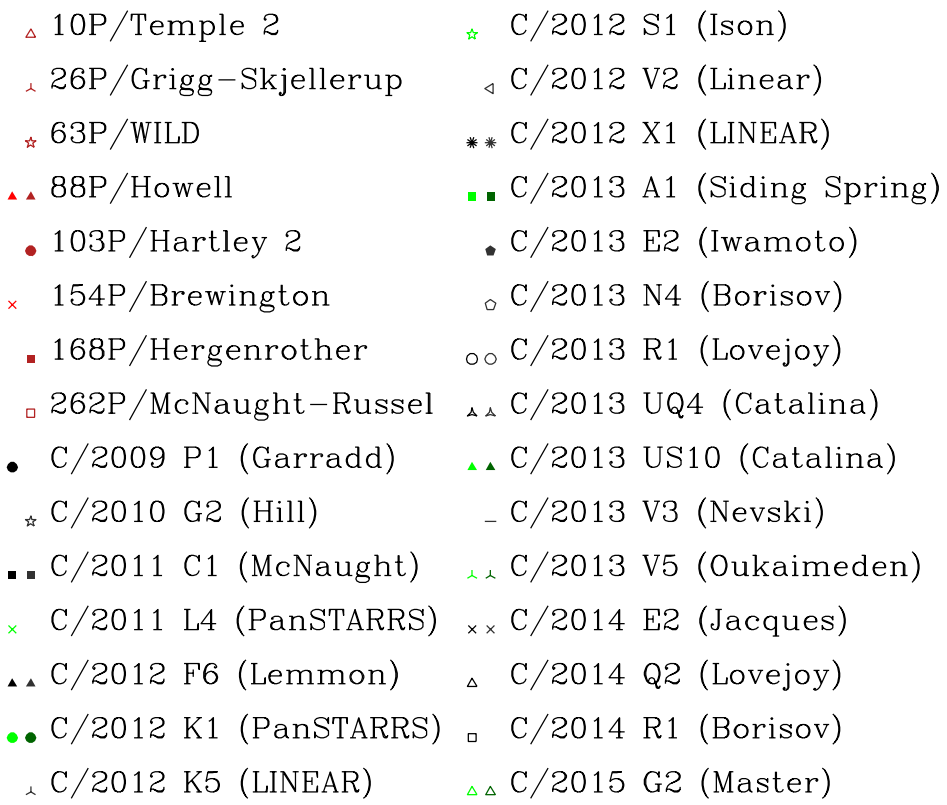


Figure 4.1: Legend of the symbols and colours used to represent the 30 comets of this work. When a comet was observed on only one side of perihelion, only the corresponding symbol is represented.

Table 4.1: Orbital elements and observing circumstances of the comets analysed in this work. $e$ is the eccentricity, $1/a$ the reciprocal semi-major axis ($1/a_0$ for LPCs and DNCs), $q$ the perihelion distance, $i$ the inclination, $t_P$ the time of the perihelion passage in Julian days, $T_J$ the Tisserand parameter relative to Jupiter. Column nine gives the dynamical type of the comet: JFC for Jupiter Family Comets, LPC for dynamically old long period comets, or DNC for Dynamicaly New long period Comets. The last two columns give the range of heliocentric distances and dates over which each comet was observed.

| Comet | $e$ | $1/a$ | $q$ | $i$ | Period | $t_P$ | $T_J$ | Type | $r$ | Dates |
|---|---|---|---|---|---|---|---|---|---|---|
| | | | | | | | | | Pre-/Post-perihelion | Pre-/Post-perihelion |
| 10P/Tempel 2 | 0.5363 | 0.323 | 1.42 | 12.03 | 5.36 | 2457340.76 | 2.964 | JFC | -/0.67-0.79 | -/14.09.2010-11.10.2010 |
| 26P/Grigg-Skjellerup | 0.6401 | 0.331 | 1.08 | 22.44 | 5.24 | 2456479.56 | 2.806 | JFC | -/1.21-1.21 | -/10.07.2013-18.07.2013 |
| 63P/Wild | 0.6507 | 0.179 | 1.95 | 19.78 | 13.19 | 2456393.33 | 2.412 | JFC | -/1.98-2.00 | -/15.05.2013-24.05.2013 |
| 88P/Howell | 0.5631 | 0.322 | 1.36 | 4.38 | 5.48 | 2457118.73 | 2.947 | JFC | 1.38-1.36/1.36-2.51 | 15.03.2015-29.03.2015/14.04.2015-10.11.2015 |
| 103P/Hartley 2 | 0.6945 | 0.288 | 1.06 | 13.62 | 6.47 | 2457863.82 | 2.641 | JFC | -/1.06-1.81 | -/30.10.2010-21.02.2011 |
| 154P/Brewington | 0.6705 | 0.205 | 1.61 | 17.83 | 10.78 | 2456639.40 | 2.431 | JFC | 1.81-1.65/- | 26.09.2013-13.01.2014/- |
| 168P/Hergenrother | 0.6096 | 0.276 | 1.41 | 21.93 | 6.90 | 2456202.46 | 2.663 | JFC | -/1.41-1.43 | -/24.09.2012-17.10.2012 |
| 262P/McNaught-Russel | 0.8154 | 0.144 | 1.28 | 29.08 | 18.25 | 2456265.96 | 1.918 | JFC | -/1.29-1.38 | -/15.12.2012-12.01.2013 |
| C/2009 P1 (Garradd) | 1.0002 | 0.000421 | 1.55 | 106.17 | - | 2455918.76 | -0.432 | DNC | 3.33-1.77/- | 02.05.2011-22.10.2011/- |
| C/2010 G2 (Hill) | 0.9789 | 0.0111 | 1.98 | 103.76 | 906 | 2455806.55 | -0.358 | LPC | -/2.18-2.54 | -/16.11.2011-15.01.2012 |
| C/2011 C1 (McNaught) | 0.9986 | 0.00286 | 0.89 | 16.28 | 6378 | 2455669.50 | 1.130 | LPC | 1.12-0.90/0.88-1.04 | 10.03.2011-09.04.2011/20.04.2011-18.05.2011 |
| C/2011 L4 (PanSTARRS) | 1.00003 | 0.0000295 | 0.30 | 84.12 | - | 2456361.67 | - | DNC | 0.88-0.86/- | 07.02.2013-08.02.2013/- |
| C/2012 F6 (Lemmon) | 0.9984 | 0.00219 | 0.73 | 82.61 | 9457 | 2456376.01 | 0.147 | LPC | 1.95-0.84/1.01-1.61 | 11.12.2012-04.03.2013/29.04.2013-11.06.2013 |
| C/2012 K1 (PanSTARRS) | 1.0004 | 0.0000399 | 1.05 | 142.42 | - | 2456897.16 | - | DNC | 3.09-1.38/1.07-1.18 | 05.02.2014-3.07.2014/06.09.2014-28.09.2014 |
| C/2012 K5 (LINEAR) | 0.9983 | 0.00191 | 1.14 | 92.85 | 17562 | 2456260.19 | -0.059 | LPC | -/1.27-1.59 | -/03.01.2013-08.02.2013 |
| C/2012 S1 (Ison) | 1.0003 | 0.00000852 | 0.01 | 62.19 | - | 2456625.28 | 0.065 | DNC | 1.43-0.33/- | 12.10.2013-23.11.2013/- |
| C/2012 V2 (Linear) | 0.9978 | 0.00236 | 1.46 | 67.18 | 16499 | 2456521.00 | 0.588 | LPC | -/1.48-2.25 | -/04.09.2013-23.01.2014 |
| C/2012 X1 (LINEAR) | 0.9899 | 0.00697 | 1.60 | 44.36 | 1983 | 2456710.15 | 1.151 | LPC | 1.06-1.60/1.60-3.56 | 17.02.2014-19.02.2014/23.02.2014-10.11.2014 |
| C/2013 A1 (Siding Spring) | 0.9999 | 0.0000466 | 1.40 | 129.03 | - | 2456955.82 | -0.919 | DNC | 4.95-1.40/1.40-1.43 | 20.09.2013-20.10.2014/29.10.2014-14.11.2014 |
| C/2013 E2 (Iwamoto) | 0.9937 | 0.00432 | 1.41 | 21.86 | 3383 | 2456360.53 | 1.388 | LPC | -/1.51-2.05 | -/15.04.2013-17.07.2013 |
| C/2013 N4 (Borisov) | 0.9747 | 0.0218 | 1.21 | 37.04 | 332 | 2456526.01 | 1.190 | LPC | -/1.83-2.17 | -/22.11.2013-24.12.2013 |
| C/2013 R1 (Lovejoy) | 0.9985 | 0.00272 | 0.81 | 63.99 | 12442 | 2456649.23 | 0.499 | LPC | 1.85-1.06/1.26-3.10 | 16.09.2013-16.11.2013/13.02.2014-06.07.2014 |
| C/2013 UQ4 (Catalina) | 0.9820 | 0.0172 | 1.09 | 145.11 | 470 | 2456844.46 | -0.969 | LPC | 1.23-1.09/1.08-1.28 | 31.05.2014-30.06.2014/07.07.2014-16.08.2014 |
| C/2013 US10 (Catalina) | 1.0003 | 0.0000379 | 0.82 | 148.88 | - | 2457342.20 | 2.210 | DNC | 6.65-1.36/1.00-1.18 | 16.05.2014-16.09.2015/16.12.2015-01.01.2016 |
| C/2013 V3 (Nevski) | 0.8927 | 0.0783 | 1.39 | 32.01 | 46.8 | 2456595.41 | 1.611 | LPC | -/1.43-1.70 | 16.11.2013-04.01.2014 |
| C/2013 V5 (Oukaimeden) | 0.9986 | 0.0000169 | 0.63 | 154.88 | 9580 | 2456928.72 | -0.877 | DNC | 1.29-0.63/0.63-0.79 | 02.08.2014-26.09.2015/28.09.2014-21.10.2014 |
| C/2014 E2 (Jacques) | 0.9992 | 0.00123 | 0.66 | 156.38 | 22477 | 2456841.02 | -0.919 | LPC | 2.01-0.86/0.81-2.36 | 18.03.2014-05.06.2014/24.07.2014-11.11.2014 |
| C/2014 Q2 (Lovejoy) | 0.9977 | 0.00200 | 1.29 | 80.29 | 13090 | 2457052.57 | 0.246 | LPC | 1.80-1.30/- | 11.10.2014-23.01.2015/- |
| C/2014 R1 (Borisov) | 0.9925 | 0.00689 | 1.35 | 9.93 | 2397 | 2456980.74 | 1.443 | LPC | 1.62- 2.18/- | 20.01.2015-21.03.2015/- |
| C/2015 G2 (Master) | 1.0003 | 0.0000329 | 0.78 | 147.56 | - | 2457166.28 | - | DNC | 1.09-0.79/0.78-0.90 | 13.04.2015-17.05.2015/26.05.2015-15.06.2015 |

## 4.1 Heliocentric evolution of the activity

We first study the evolution of the activity of our comets with the heliocentric distance. We fitted power-law slopes to represent the evolution of OH, NH, CN, $C_3$, $C_2$, and the $Af\rho$ with the heliocentric distance (all $Af\rho$ values have been corrected for the phase angle effect). We were not able to derive slopes for every comet since some comets have not been observed on a sufficient range of heliocentric distances. We only derived a slope when there were at least three measurements of the radical production rate (or the $Af\rho$) over at least 0.3 au, even though in most cases we have many more observations available to derive the slopes. This way, we insured that the slopes derived are representative of the evolution of the activity of the comet. The results of these fits are given in Table 4.2 and represented in Fig. 4.2. Among the comets for which we were able to derive slopes, we have 2 JFC, 5 DNC, and 8 LPC. In numerous cases, the comet activity was departing from a simple slope. This was for example the case for comet C/2012 F6 (Lemmon) $Af\rho$ before perihelion (see Section 3.3), for which we needed to use two different slopes. Four comets from our sample also underwent outbursts: 168P/Hergenrother, C/2010 G2 (Hill), C/2012 S1 (Ison), and C/2013 A1 (Siding Spring). In these cases, we did not include the observations around the time of the outburst in our slope calculations. Even though a single slope is not always a good representation of the evolution of comet gas and dust activity, it provides a simple way to compare the evolution of gas species and dust production between each other, and from one comet to another. For these reasons, we decided to use power-law slopes to study and compare the evolution of the activity of comets. We did not account for pre/post-perihelion asymmetries in the peak of the lightcurve to compute the slopes. Only two comets showed strong asymmetries of the peak about perihelion for all species: comets 103P (Hartley 2) and C/2009 P1 (Garradd). If we would have taken this effect into account, the slope we derived would have been steeper for these two comets. For comet Garradd, the CN slope becomes $-0.92 \pm 0.05$ instead of $-0.77 \pm 0.06$ and for comet Hartley 2 it becomes $-3.14 \pm 0.12$ instead of $-3.12 \pm 0.11$. Since we observed this asymmetry for only two comets and since its effect on the slope is not very strong for these cases, we decided to simply compute pre- and post-perihelion slope for every comet in our data set.

Table 4.2: Power-law slopes of the heliocentric dependence of OH, NH, CN, $C_3$, $C_2$, and $Af\rho$.

| Comet | Type | OH | | NH | | CN | | $C_3$ | | $C_2$ | | $Af\rho$ | |
|---|---|---|---|---|---|---|---|---|---|---|---|---|---|
| | | pre | post | pre | post | pre | post | pre | post | pre | post | pre | post |
| 10P/Tempel 2 | JFC | - | - | - | - | - | - | - | - | - | - | - | - |
| 26P/Grigg-Skjellerup | JFC | - | - | - | - | - | - | - | - | - | - | - | - |
| 63P/WILD | JFC | - | - | - | - | - | - | - | - | - | - | - | - |
| 88P/Howell | JFC | - | -6.72±0.77 | - | -5.60±0.58 | - | -3.92±0.14 | - | -4.24±0.41 | - | -5.05±0.19 | - | -2.51±0.11 |
| 103P/Hartley 2 | JFC | - | -3.81±0.10 | - | - | - | -3.12±0.11 | - | -3.13±0.15 | - | -3.61±0.11 | - | -0.22±0.06 |
| 154P/Brewington | JFC | - | - | - | - | - | - | - | - | - | - | - | - |
| 168P/Hergenrother | JFC | - | - | - | - | - | - | - | - | - | - | - | - |
| 262P/McNaught-Russel | JFC | - | - | - | - | - | - | - | - | - | - | - | - |
| C/2009 P1 (Garradd) | LPC | -0.74±0.12 | - | - | - | -0.80±0.04 | - | -0.76±0.08 | - | -1.75±0.09 | - | 0.22±0.02 | - |
| C/2010 G2 (Hill) | LPC | - | - | - | - | - | - | - | - | - | - | - | - |
| C/2011 C1 (McNaught) | LPC | - | - | - | - | - | - | - | - | - | - | - | - |
| C/2011 L4 (PanSTARRS) | DNC | - | - | - | - | - | - | - | - | - | - | - | - |
| C/2012 F6 (Lemmon) | LPC | -2.48±0.05 | -1.20±0.20 | -2.70±0.09 | -1.97±0.20 | -2.59±0.04 | -1.70±0.11 | -2.82±0.04 | -1.90±0.16 | -3.17±0.04 | -2.32±0.13 | -2.53±0.12 | -1.30±0.08 |
| C/2012 K1 (PanSTARRS) | DNC | - | -1.39±0.23 | - | -3.78±0.15 | -0.77±0.08 | -1.61±0.12 | -1.38±0.21 | -2.22±0.12 | -1.72±0.13 | -2.68±0.08 | -0.01±0.05 | -0.83±0.06 |
| C/2012 K5 (LINEAR) | LPC | - | - | - | - | - | - | - | - | - | - | - | - |
| C/2012 S1 (Ison) | DNC | - | - | - | - | - | - | - | - | - | - | - | - |
| C/2012 V2 (Linear) | LPC | - | -3.81±0.69 | - | -7.66±2.98 | - | -4.07±0.35 | - | -4.27±0.36 | - | -5.16±0.47 | - | -8.73±1.10 |
| C/2012 X1 (LINEAR) | LPC | - | -3.47±0.19 | - | -3.32±0.23 | - | -1.73±0.08 | - | -2.24±0.08 | - | -2.44±0.10 | - | -3.15±0.19 |
| C/2013 A1 (Siding Spring) | DNC | -0.31±0.22 | - | -2.10±0.55 | - | -0.38±0.09 | - | 0.65±0.30 | - | -0.79±0.20 | - | 0.21±0.04 | - |
| C/2013 E2 (Iwamoto) | LPC | - | -2.05±0.39 | - | - | - | -0.61±0.56 | - | - | - | -2.69±0.78 | - | 0.47±0.36 |
| C/2013 N4 (Borisov) | LPC | - | - | - | - | - | - | - | - | - | - | - | - |
| C/2013 R1 (Lovejoy) | LPC | -3.28±0.33 | -2.62±0.19 | -3.19±0.34 | -2.49±0.34 | -2.60±0.17 | -1.84±0.09 | -2.66±0.47 | -1.83±0.40 | -3.56±0.16 | -2.76±0.12 | -3.92±0.19 | -3.01±0.07 |
| C/2013 UQ4 (Catalina) | LPC | - | - | - | - | - | - | - | - | - | - | - | - |
| C/2013 US10 (Catalina) | DNC | -1.45±0.35 | -1.30±1.11 | -1.84±0.12 | - | -0.74±0.14 | -2.88±0.75 | -1.16±0.09 | - | -1.35±0.13 | -1.59±0.59 | 0.06±0.05 | -1.98±0.59 |
| C/2013 V3 (Nevski) | LPC | - | - | - | - | - | - | - | - | - | - | - | - |
| C/2013 V5 (Oukaimeden) | DNC | 1.10±0.33 | - | 0.27±0.30 | - | -1.24±0.28 | - | -0.67±0.24 | - | -0.55±0.32 | - | 2.33±0.23 | - |
| C/2014 E2 (Jacques) | LPC | -1.66±0.17 | -1.27±0.26 | - | - | -1.82±0.10 | -1.78±0.04 | -2.02±0.19 | -3.02±0.06 | -2.86±0.14 | -2.66±0.13 | -1.81±0.12 | -1.23±0.09 |
| C/2014 Q2 (Lovejoy) | LPC | -5.99±0.26 | - | -6.75±0.24 | - | -5.76±0.17 | - | -5.85±0.24 | - | -7.04±0.26 | - | -4.77±0.12 | - |
| C/2014 R1 (Borisov) | LPC | - | - | - | - | - | - | - | - | - | - | - | - |
| C/2015 G2 (Master) | DNC | -1.56±0.18 | - | -2.29±0.23 | - | -2.74±0.32 | - | -1.02±0.70 | - | -1.82±0.35 | - | 2.73±0.29 | - |

We observe a large diversity of slopes among comets, from -8.73 to 2.73. At first sight, the range of slopes we derived is similar for all gas species and the dust. A positive slope means that the activity of the comet is decreasing as it approaches the Sun while a negative slope reflects an activity increasing with decreasing heliocentric distances, as we would expect. Most positive slopes are observed for the dust, even if we derive positive slopes for the OH in comet C/2013 V5 (Oukaimeden) and for the $C_3$ in comet C/2013 A1 (Siding Spring). However, in Section 3.4, we noticed that the positive slope for the $C_3$ for comet Siding Spring is due to a single point above the trend. This slope must then be taken with caution. Generally, the slopes observed for the $Af\rho$ are shallower than for the gas species, independently of the comet dynamical type. The only notable exception is comet C/2012 V2 (Lovejoy), which has a very steep $Af\rho$ slope but the uncertainty of the slope is also much larger than for other comets. The average NH, and to a lesser extent, $C_2$ slopes (respectively $-3.34 \pm 0.60$ and $-2.77 \pm 0.35$ ) are steeper than the average slopes measured for the other gas species (OH, CN, and $C_3$, respectively $-2.34 \pm 0.42$, $-2.13 \pm 0.30$, and $-2.25 \pm 0.35$). We already mentioned earlier in this work that the NH scalelengths and their evolution with the heliocentric distance are poorly known and this could be an effect induced by the Haser scalelengths. For the $C_2$, this trend is more likely to be real, since it is also observed for individual comets (see Table 4.2). This implies that the ratio of $C_2$ to OH and CN should vary with the heliocentric distance. We actually observe such variations and discuss them later in this work.

We try to establish a link between the dynamical origin of comets and the evolution of their activity. From Fig. 4.2, it is clear that dynamically new comets observed pre-perihelion (light green symbols) have shallower slopes than other comets. This correlates with the slow increase of the activity of comets C/2013 A1 (Siding Spring) and C/2013 US10 (Catalina), and the dynamically young comet C/2009 P1 (Garradd), we report in Chapter 3. This shallow evolution the activity of dynamically new (and dynamically young) comets while they approach the Sun for the first time has already been observed from visual magnitudes and other studies of comet gas activity in the optical, see e.g. Whipple (1978); A'Hearn et al. (1995). It is believed that dynamically new comets develop a dust and icy grain halo at large heliocentric distances due to the outgassing of very volatile species. These slow-moving grains sublimate and dominate the coma as the comet approaches the Sun. When it reaches small heliocentric distances, the direct outgassing from the nucleus becomes important as compared to the outgassing from the grains. A halo of icy grains has been invoked to explain the evolution of comet C/2012 S1 (Ison) activity at large heliocentric distances and was confirmed by Knight and Schleicher (2015) who measured an active area larger than the assumed surface of the nucleus, from observations of the comet at large heliocentric distances. Icy grains were also invoked in the coma of the dynamically new comet C/2013 A1 (Siding Spring) (Bodewits et al., 2015) and in the coma of the dynamically young comet C/2009 P1 (Garradd) (Paganini et al., 2012; Combi et al., 2013; Bodewits et al., 2014), as already mentioned in the previous Chapter. The activity of dynamically new comets is also usually highly asymmetric about perihelion. The activity increases slowly as these comets approach the Sun and decreases much faster after the perihelion passage. We could only observe 2 dynamically new comets on both sides of

perihelion: C/2012 K1 (PanSTARRS) and C/2013 US10 (Catalina). Both these comets have steeper slopes after perihelion than before, which confirms this trend. The gas production rates measured for DNCs are then usually lower after the perihelion passage than they were before at the same heliocentric distance. The asymmetry about perihelion observed for DNCs is most probably not due to seasonal effects or to a thermal lag. If the asymmetry was due to a thermal lag, we would expect to observe higher production rates after the perihelion passage than before, while we observe the opposite effect. Seasonal effects would be different from one comet to another. For some comets, the slopes would be steeper after perihelion, while for others the slopes would be shallower. However, steeper slopes after perihelion are observed for all the comets of our sample for which we have data on both sides of perihelion. Two comets are not a sufficient sample to draw conclusions but this effect has also been observed for other dynamically new comets (C/1999 S4 (Mäkinen et al., 2001), C/2002 T7 (Combi et al., 2009), C/2011 L4 (Combi et al., 2014a)). The asymmetry is generally imputed to the halo of grains produced at large heliocentric distances before the comet first perihelion passage, which persists in the coma until the comet comes close to the Sun. After perihelion, normal outgassing dominates, and gas and dust production decreases faster.

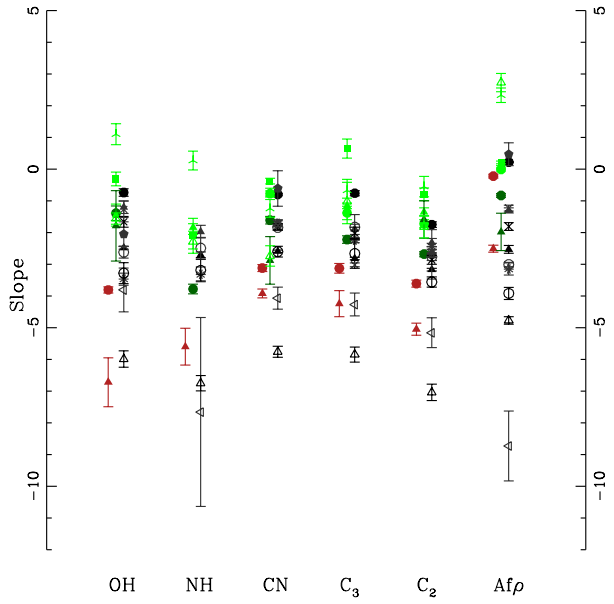


Figure 4.2: Power-law slopes fitted for the evolution of the OH, NH, CN, $C_3$, $C_2$ production rates and the $Af\rho$ with the heliocentric distance.

A'Hearn et al. (1995) reported that Jupiter Family Comets tend to have steeper slopes compared to other comets and large asymmetries about perihelion. According to their study, JFCs also have a smaller fraction of the nucleus which is active. Changes in the illumination of a nucleus which is active only on small areas of its surface and seasonal effects could then explain their observations. Only two JFCs were observed with TRAPPIST over a range of heliocentric

distances sufficient to derive reliable slopes: 88P/Howell and 103P/Hartley 2. Fig 4.2 shows that these comets have steep slopes compared to most comets. For example, the mean CN slope for DNC and LPC is $-1.98 \pm 0.35$ while comets 88P and 103P CN slopes are respectively $-3.92 \pm 0.14$ and $-3.12 \pm 0.11$. Even though these are only two comets, it seems to confirm the trend observed by A'Hearn et al. (1995). Both these comets have been observed only after their perihelion passage, so we do not know whether their activity was symmetric about perihelion or not.

Production rate asymmetries about perihelion are common among comets. In our sample, we observed 5 comets over a sufficient range of heliocentric distances to derive slopes on both sides of perihelion. Out of these 5 comets, 2 were dynamically new comets for which we already discussed the asymmetry and its origin. The other 3 comets are: C/2012 F6 (Lemmon), C/2013 R1 (LoveJoy), and C/2014 E2 (Jacques). They are dynamically old long period comets. Comet Lemmon and comet Lovejoy have steeper slopes before perihelion. Several other cases of long period comets having steeper slope after perihelion are also reported in the literature (comet C/1995 O1 (Biver et al., 1997) and C/2002 V1 (Combi et al., 2011b) for example). Comet Jacques production rates are essentially symmetric, which could indicate that asymmetries about perihelion vary from one comet to another. With only three comets, it is however difficult to investigate the origin of the asymmetry we observe for some comets. With a larger number of comets observed on both sides of perihelion, we will be able to determine whether the asymmetry is different from a comet to another or not, and then decipher if those asymmetries are due to seasonal effects. We do not see any correlations between the morphology of the coma and the slope of brightening or fading, the dynamical type of the comets, or any other quantity. However, we only took a quick look and this should be investigated further in the future.

## 4.2 Outbursts

Of the 30 comets of our sample, 4 underwent outbursts: 168P/Hergenrother, C/2010 G2 (Hill), C/2012 S1 (Ison), and C/2013 A1 (Siding Spring). The evolution of gas production rates of 3 of these comets around the time of the outbursts is shown in Fig. 4.3. In this Section, we will discuss and compare the properties of these outbursts.

Comet 168P/Hergenrother underwent several outbursts in the months before its perihelion passage (Sekanina, 2014). The first one occurred on September 1, 2012 and the visual magnitude of the comet decreased by 1.7 mag. A second outburst, even more important, was observed 21 days later with a decrease of 2.4 mag. Sekanina (2014) also reported a third outburst on October 1. However, the magnitude decrease is much less important and coincides with the comet perihelion passage. We did not observe the comet at the time of the first two outbursts. Our observations of comet 168P only started on September 24, 2012. Because of this, we did not observe the rise of the comet activity characterising the second outburst. We do not clearly detect the third outburst in our observations, even though we observe a

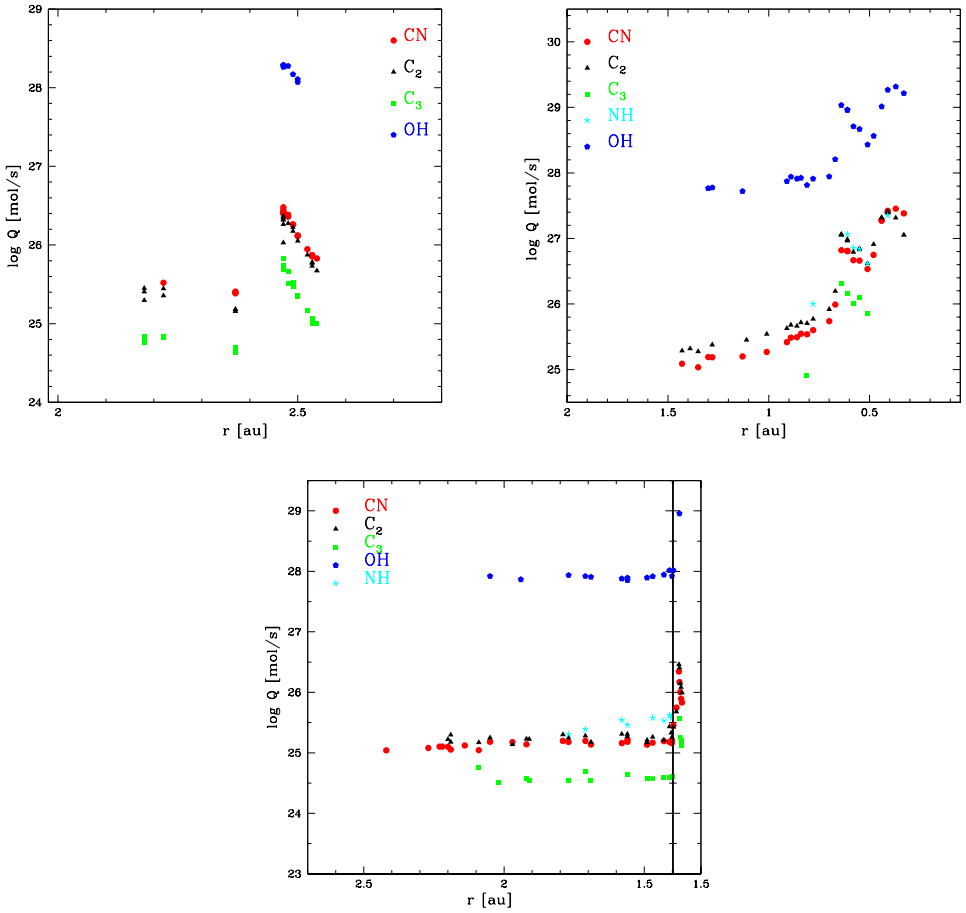


Figure 4.3: Evolution of the logarithm of OH, NH, CN, $C_3$, and $C_2$ production rates as a function of the heliocentric distance for comets C/2010 G2 (Hill) (top left), C/2012 S1 (Ison) (top right), and C/2013 A1 (Siding Spring) (bottom).

smooth increase of the comet activity around the perihelion passage. We examined several gas production rate ratios and were not able to detect strong changes of the coma composition consecutive to the outburst. In that case, the origin of the outburst has been identified. Several nucleus fragments have been detected after the outburst (Sekanina, 2014), indicating that the fragmentation of the nucleus is probably the origin of the outburst. Spectroscopic observations of two fragments with FORS 2 have been performed in the weeks following the fragmentation. The goal of these observations was to detect possible composition differences in the outgassing from the fragments. The reduction and analysis of these observations is still ongoing.

Comet C/2010 G2 (Hill) is a dynamically old long period comet that reached perihelion on September 2, 2011 at 1.98 au from the Sun. We observed the comet in December 2011, while its activity was decreasing. Then, in January 2012 when the comet was around 2.5 au from the

Sun, we observed an outburst of activity. Due to our limited temporal coverage around that time, it is difficult to determine precisely when the outburst occurred but it was sometime between December 30 and January 2. Comet Hill already underwent a major outburst in August 2010 when the comet was at 4.5 au from the Sun but we were not observing at that time (Kawakita et al., 2014). During the January 2012 outburst, gas and dust production rates increase by about a factor 10 and then slowly decrease over the next two weeks. We do not observe changes of the comet composition around the time of the outburst. Kawakita et al. (2014) collected high resolution infrared spectra of comet Hill with NIRSPEC at the Keck II Telescope one week after the outburst. They find that the coma of comet Hill is enriched in organics and highly volatile species. This is why they suggest that the outburst could be driven by the sublimation of CO and/or other highly volatile molecules, even though the energy source powering sublimation remains unknown.

Comet C/2012 S1 (Ison) is a dynamically new comet that reached perihelion at only 2.7 $R_{Sun}$. The activity of the comet increased slowly at large heliocentric distances, as expected for a dynamically new comet (Knight and Schleicher, 2015). Once the comet got closer than 1 au, the activity started to rise faster, as can be seen in Fig 4.3. Around November 12, 2014, 16 days before its perihelion passage, comet Ison underwent a first outburst. From our observations, gas and dust production rates increase by about a factor 10 within 2 days. The activity then decreases until November 18, when a second outburst increases gas and dust production rates by about a factor 5 in two days. A few days after the second outburst peak, the comet became too close to the Sun to be observed with TRAPPIST. We do not observe sudden changes of the coma composition linked to these outbursts. The gas to dust ratio varies, but we think this is caused by the dust moving slower than the gas. The dust emitted during the outburst then takes more time to reach the distance at which we compute gas production rates and Af$\rho$ values. Knight and Schleicher (2015) report a probable important mass loss possibly including a fragmentation event in early November. We think that progressive fragmentation of the nucleus could also be the origin of the two outbursts we observe with TRAPPIST. This is further confirmed by the analysis of SOHO and/or STEREO images by Knight and Battams (2014) and Sekanina and Kracht (2014). Comet Ison did not survive its perihelion passage close to the Sun.

The outburst of comet C/2013 A1 (Siding Spring) is studied in detail in Section 3.4. Gas and dust production rates increase by a factor five within a few days. We do not observe changes of the coma composition during the outburst. We attribute this outburst to the build-up of gas pressure under a dusty crust. When the gas pressure overcomes the cohesive strength of the dust crust, new material is exposed causing a sudden rise of the comet activity.

Some conclusions can be drawn from the observation of 4 comets in outburst with TRAPPIST. First, outbursts happen at different heliocentric distances, for different types of comets, and they can happen before or after the perihelion passage. Since 4 out of our 30 comets underwent an outburst, we can conclude that these sudden increases of the activity are rather frequent. Their intensity varies from one comet to another, and from one event to another for a single

comet. As already mentioned in Section 1.6.1, the origin of an outburst is difficult to identify and differs from a comet to another. Two of our comets underwent fragmentation events (probably of different origin), one outburst is attributed to internal build-up of gas pressure, and the origin of the last one remains unknown. Finally, we could not observe changes of the coma composition linked to these outbursts for any of the 4 comets. Since two of these comets were fragmenting, this indicates that the composition of the nucleus might be homogeneous on large scales. Fragmentation events provide a unique opportunity to probe the inside of the nucleus. If it were composed of an agglomerate of cometesimals formed at different distances from the Sun and having different compositions, we would expect to observe changes of the coma composition during fragmentation events. Since we do not observe such changes, this suggests that the composition of comet nuclei might be homogeneous on large scales. However, the amount of changes observed in the coma would depend on the difference in the composition of the fragments and the area of fresh ice exposed. If only 25% of new surface with different composition is exposed, and if the $C_2$ to CN ratio of the new surface is less than a factor 2 lower, for example, the changes in the composition might be too diluted to produce noticeable variations. The area of fresh ice exposed during an outburst is difficult to estimate because it depends on the number of fragments, the initial size of the nucleus, and the fraction of active surface of the nucleus, which are difficult to estimate in most cases. In the case of comet C/2012 S1 (Ison), a large fraction of new surface might have been exposed, since the comet was disintegrating. Resolved observations of the fragments of comet 73P/Schwassmann-Wachmann 3 at various wavelengths, including optical observations with narrow band filters, do not reveal composition differences between the fragments (Villanueva et al., 2006; Dello Russo et al., 2007; Schleicher and Bair, 2011), which indicates that the composition of the nucleus of this comet is homogeneous on large scales. We are not aware of the existence of systematic studies of a large number of comets in outburst but these kind of studies should be performed in the future to reach a better understanding of the mechanisms producing outbursts, and to confirm the large scale homogeneity of comet nuclei that has been suggested from the study of several comets in outburst.

## 4.3 Composition of comets from the optical

In this Section, we compare the composition of the comets in our data set, trying to define taxonomical classes. We also try to establish links between the composition and activity of comets and their orbital parameters. Finally, we study the evolution of comet composition with the heliocentric distance.

### 4.3.1 Gas

In order to facilitate the comparison between comets, and to allow us to distinguish individual comets in our figures, we computed a mean value for each production rate and each production rate ratio, for every comet. The error bars in this Section do not correspond to the

statistical error on the mean. Instead, we decided to use either the individual error bar when there was only one measurement available, or the standard deviation of the individual values if several measurements were used to compute the mean. These error bars then represent the dispersion of the production rates and production rate ratios around the mean value, due the rotational variability of the comet or the evolution of its activity and composition with the heliocentric distance. Comets C/2012 S1 (Ison) and C/2013 A1 (Siding Spring) both underwent outbursts, implying huge variations of gas and dust production rates over a short period of time. Because of this, we did not compute a mean value of the production rates for comet Ison and for the post-perihelion observations of comet Siding Spring. However, none of these comets was out of the trend described later. We computed mean values of the gas production rate ratios for these comets, since those did not change significantly during the outburst. Mean values do not allow us to study the evolution of the comets composition with the heliocentric distance. For that purpose, we also computed mean values for bins of heliocentric distances. We decided to use bins of 0.5 au when we wanted to gather a significant number of comets in each bin, and bins of 0.1 au when we wanted to study further the evolution of the comet composition with the heliocentric distance. The error bars have been computed the same way as for the mean values.

Figure 4.4 represents the mean values of the logarithm of the NH, CN, $C_3$, and $C_2$ production rates as a function of the logarithm of the OH production rate, for every comet in our data set. In these 4 plots, most comets lie on a diagonal band, meaning that the production of NH, CN, $C_3$, and $C_2$ is correlated to the production of OH. Weakly active comets lie on the lower left end of the diagonal band, and the most active comets lie on the upper right. The diagonal band in which most comets lie is narrow, implying that most comets have a very similar composition, at least regarding the OH, NH, CN, $C_3$, and $C_2$ radicals. We would have expected to observe composition differences between comets, especially between comets from different reservoirs and dynamical origin, but most comets in our data set show a surprisingly uniform composition, while their activity strongly varies. The mean OH, CN, $C_3$, and $C_2$ production rates we measure are spanning over more than two orders of magnitudes. The NH production rates show an even wider range of values (more than three orders of magnitude).

From Fig. 4.4, we notice that Jupiter Family Comets (red symbols) tend to lie on the lower left part of the band. This means that JFCs are generally less active than other comets. The application of a Kolmogorov-Smirnov test on the OH and CN production rates of JFCs on one side, and of the other comets on the other side, confirms that the two populations are significantly different. We do not believe it is due to a selection effect since we would then be biased towards observing the brightest JFCs instead of weakly active comets. A'Hearn et al. (1995) already noticed that JFCs tend to have smaller active areas than other types of comets. Since JFCs have made numerous passages in the inner solar system, a crust could build-up on the surface of the nucleus, hence reducing its active surface and the activity of the comet. A'Hearn et al. (1995) also argue that the build up of a crust both explains the lower activity and the large asymmetries about perihelion. The smaller active area of JFCs could also be explained if their nuclei were in average smaller than those of other types of comets but it

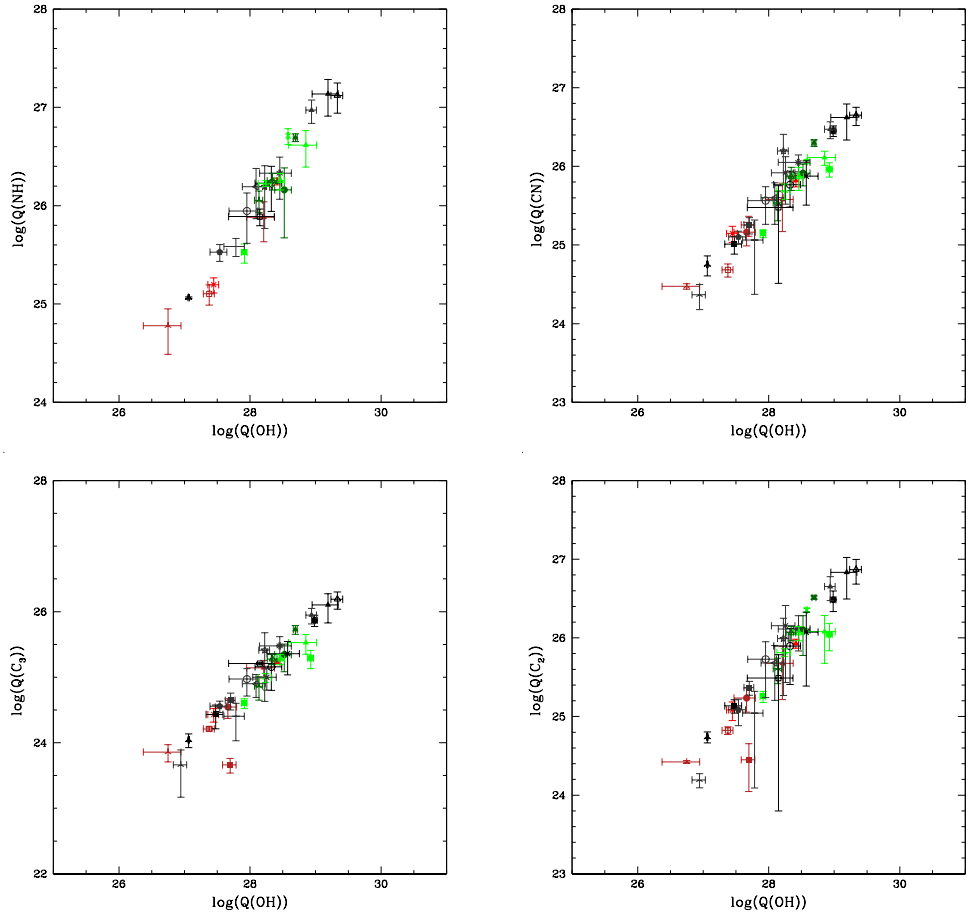


Figure 4.4: Logarithm of the NH, CN, $C_3$, and $C_2$ production rates as a function of the logarithm of the OH production rate for every comet in our data set.

is difficult to confirm given the difficulty to estimate nucleus sizes. We have to be cautious while interpreting this trend in comet activity, since we only observed 8 JFCs. We would need a larger sample, and especially a larger number of JFCs, to confirm this observation.

The $C_3$ over OH and $C_2$ over OH plots look extremely similar, indicating that these two carbon chain species are strongly linked to each other. On these two plots, one comet is located far below the diagonal band, while it lies within that band in the CN over OH plot. This comet is 168P/Hergenrother (red filled squares). This comet is strongly depleted in the carbon chain species $C_3$ and $C_2$. As mentioned in the previous Section, 168P underwent an outburst following the disruption of its nucleus in several pieces. Consecutively to this outburst, we observed the comet with the FORS 2 spectrograph at the VLT, to obtain spectra of the fragments of the comet. These data are still under reduction and are not presented here. However, a first look at the spectra do not show any sign of the $C_3$ and $C_2$ emissions, while the CN was clearly detected. This confirms the conclusion from the TRAPPIST observations presented

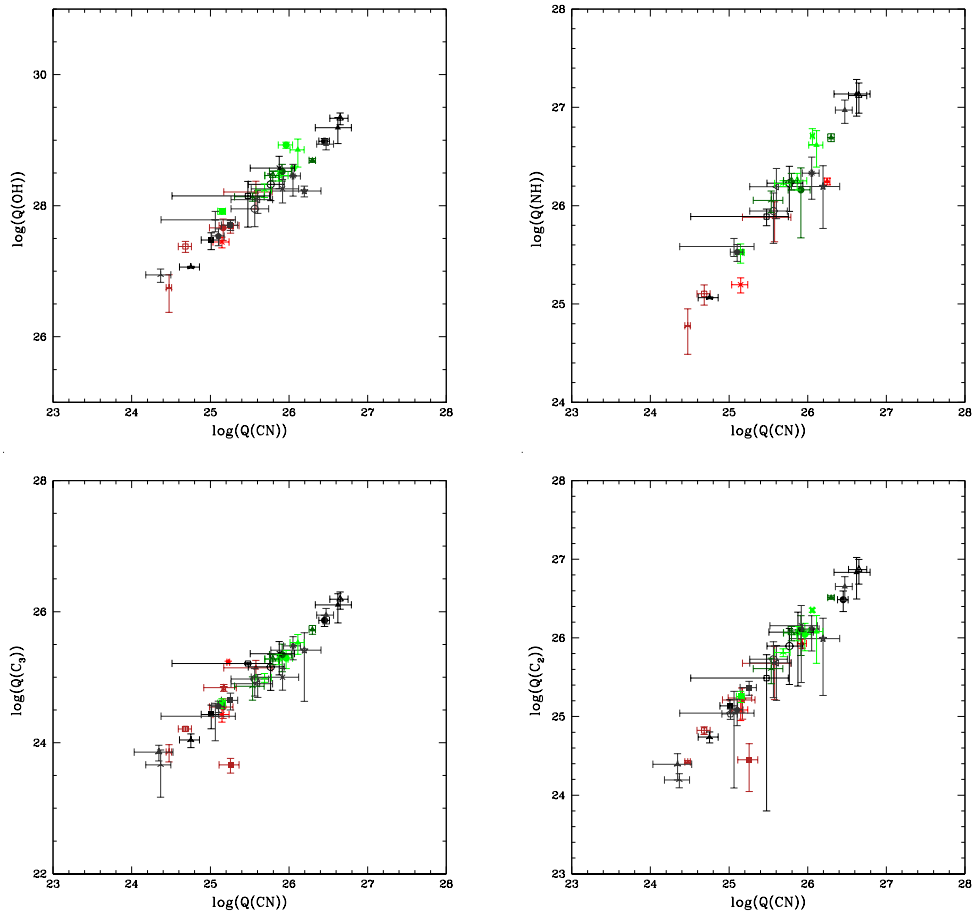


Figure 4.5: Logarithm of the OH, NH, $C_3$, and $C_2$ production rates as a function of the logarithm of the CN production rate for every comet in our data set.

here: comet 168P/Hergenrother is depleted in $C_3$ and $C_2$. This is the only comet strongly depleted in carbon chain species in our data set. There is some dispersion within the diagonal band of the $C_3$ over OH and $C_2$ over OH plots but no other comet really stands out of the trend.

Figure 4.5 shows the logarithm of the OH, NH, $C_3$, and $C_2$ production rates as a function of the logarithm of the CN production rate for every comet in our data set. As for the OH, most comets lie on a narrow diagonal band. This confirms that most of the comets we observed have a remarkably similar composition and that the production of the five radicals we observe is well correlated. Comet 168P/Hergenrother is located below the band in the $C_3$ over CN and $C_2$ over CN plots, since it has been found to be depleted in carbon chain species.

In Fig. 4.6, we show the logarithm of the ratio of the $C_2$ to OH production rates of each comet as a function of the logarithm of the ratio of CN to OH, as it was done in A'Hearn et al. (1995). We first present the plot made using a mean value for each comet. Then, we wanted to study the

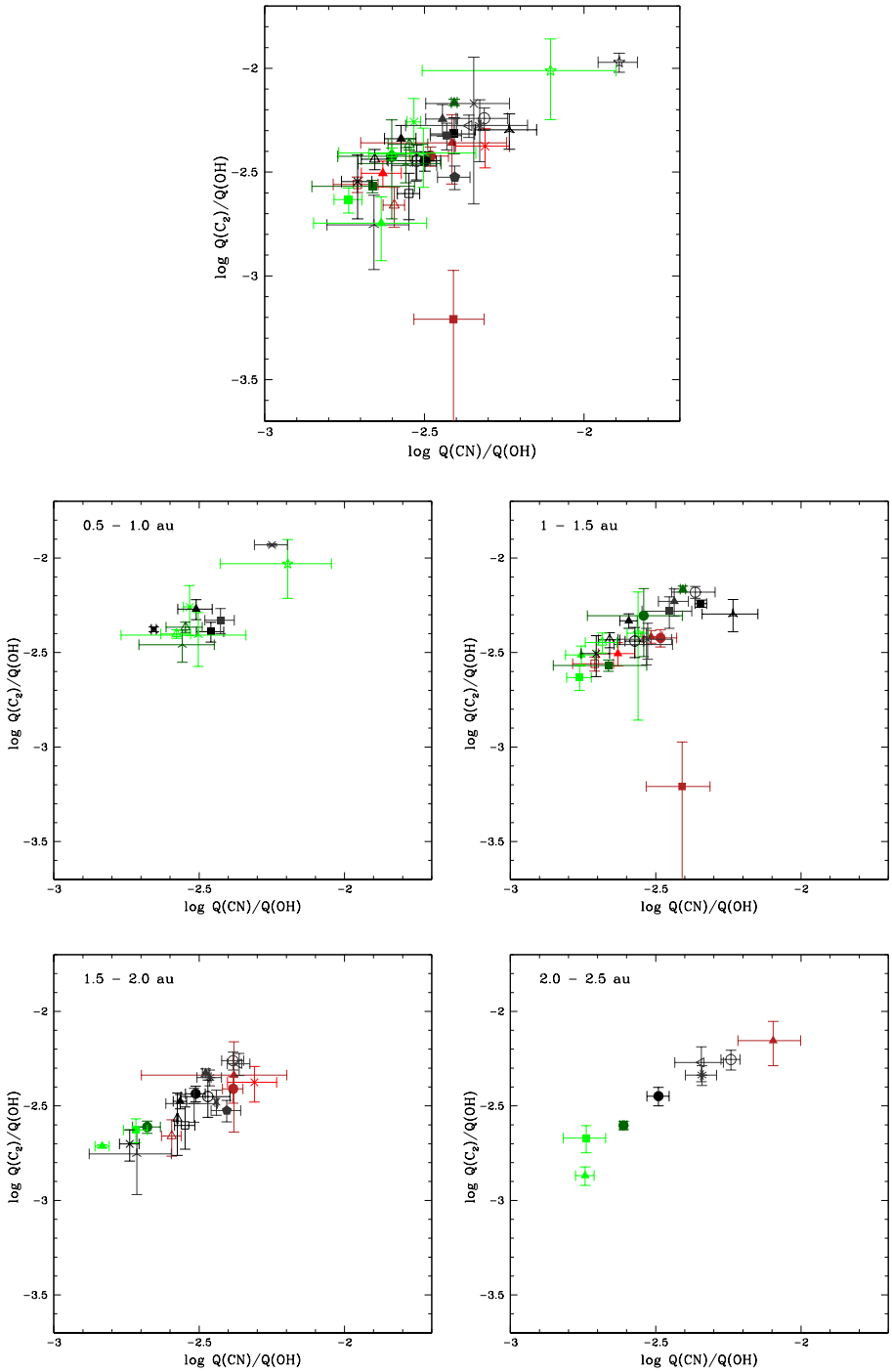


Figure 4.6: Logarithm of the ratio of $C_2$ to OH production rates against the logarithm of the ratio of CN to OH. The first plot has been made using a mean value for each comet. The other plots have been made for 0.5 au-wide bins of heliocentric distance.

changes in this plot with the heliocentric distance, to investigate whether some differences we observe between comets are a bias due to the distance at which they were observed. We thus define four bins of heliocentric distance (0.5 to 1.0 au, 1.0 to 1.5 au, 1.5 to 2.0 au, and 2.0 to 2.5 au) and compute a mean value for each comet in each bin. Some comets have been observed in only one bin while others have been observed over two or three bins. We limit our study to these bins since only a few comets have been observed at either smaller or larger heliocentric distances. In this plot, most comets lie on a diagonal band, as they have similar compositions. Comets C/2012 S1 (Ison) and C/2010 G2 (Hill) are located at the upper right part of the band. These comets have been observed respectively very close and very far from the Sun. Comet 168P/Hergenrother is located below the band because it is depleted in $C_2$ compared to CN, as we already noticed from Fig. 4.4 and 4.5. If we bin all pre-perihelion ratios and compare them to all post-perihelion ratios, we do not see any significant difference between pre- and post-perihelion data. We then examine the evolution of this plot as a function of the heliocentric distance. The plots in the four bins of heliocentric distance have the same general aspect as the one made using a mean value for each comet (first plot at the top). Most comets lie on a diagonal band, except for comet 168P/Hergenrother. In the second bin (from 1.0 to 1.5 au), comet C/2013 UQ4 (Catalina) is located below the diagonal band, which could indicate that this comet is depleted in $C_2$, but only slightly compared to comet 168P/Hergenrother. In the last bin (from 2.0 to 2.5 au), comet C/2013 US10 (Catalina) is also located below the main band, even though at this distance we only observed 8 comets and it is difficult to define whether this comet is typical or whether it really stands out of the main trend. In the 1.0-1.5 au and 1.5-2.0 au bins, comet C/2013 US10 (Catalina) is located within the diagonal band, which indicates that this comet is probably not really depleted in $C_2$. At large heliocentric distances, the $C_2$ images of comet Catalina are heavily contaminated by the dust and the uncertainty due to the dust removal could be higher than estimated.

Figure 4.7 represents the logarithm of the ratio of the $C_3$ to OH production rates of each comet as a function of the logarithm of the ratio of CN to OH, first using a mean value for each comet and then in four bins of heliocentric distance. The first plot of the figure is similar to what we observed for the $C_2$. Most comets lie on a diagonal band. Comets C/2012 S1 (Ison) and C/2010 G2 (Hill) are located to the upper right part of the band, and comet 168P/Hergenrother lies below the band because it is depleted in $C_3$ in addition to being depleted in $C_2$. Since comets C/2013 UQ4 (Catalina) and C/2013 US10 (Catalina) might have a lower $C_2$ abundances, we checked whether these comets also have lower $C_3$ abundances. We do not have simultaneous measurements of comet C/2013 UQ4 (Catalina) $C_3$ and CN production rates, so that we cannot confirm that this comet also has a low $C_3$ abundance. Comet C/2013 US10 (Catalina) has a normal $C_3$ abundance and is located well within the diagonal band. In the 2.0-2.5 au bin, comet C/2012 V2 (Linear) is located below the diagonal band but, as in the case of comet C/2013 US10 (Catalina) for the $C_2$, we did not observe a lot of comets at these distances to make a comparison. If we bin all pre-perihelion ratios and compare them to all post-perihelion ratios, we do not see any significant difference between pre- and post-perihelion data.

Figure 4.8 represents the logarithm of the ratio of the NH to OH production rates of each

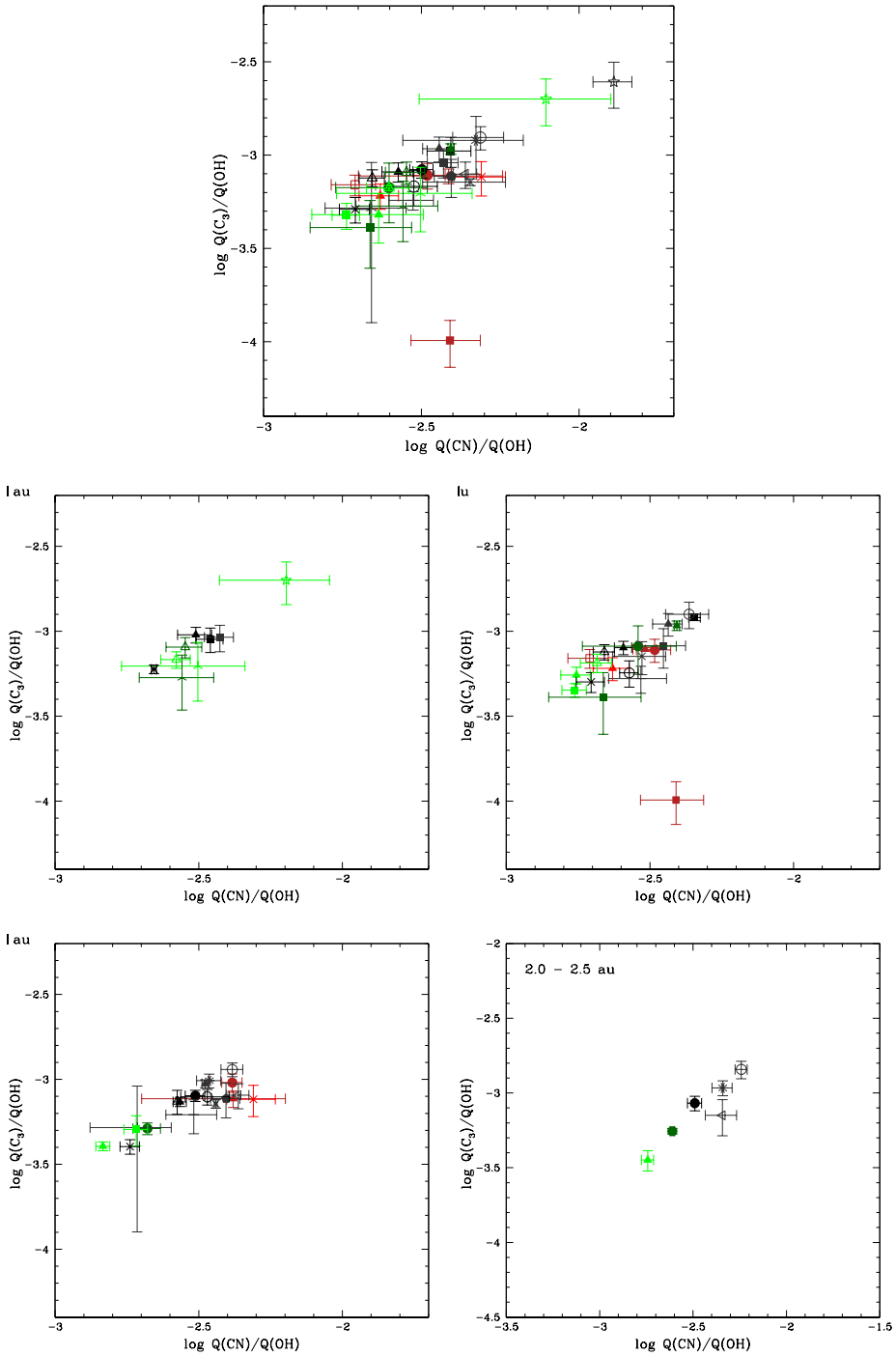


Figure 4.7: Logarithm of the ratio of $C_3$ to OH production rates against the logarithm of the ratio of CN to OH. The first plot has been made using a mean value for each comet. The other plots have been made for 0.5 au-wide bins of heliocentric distance.

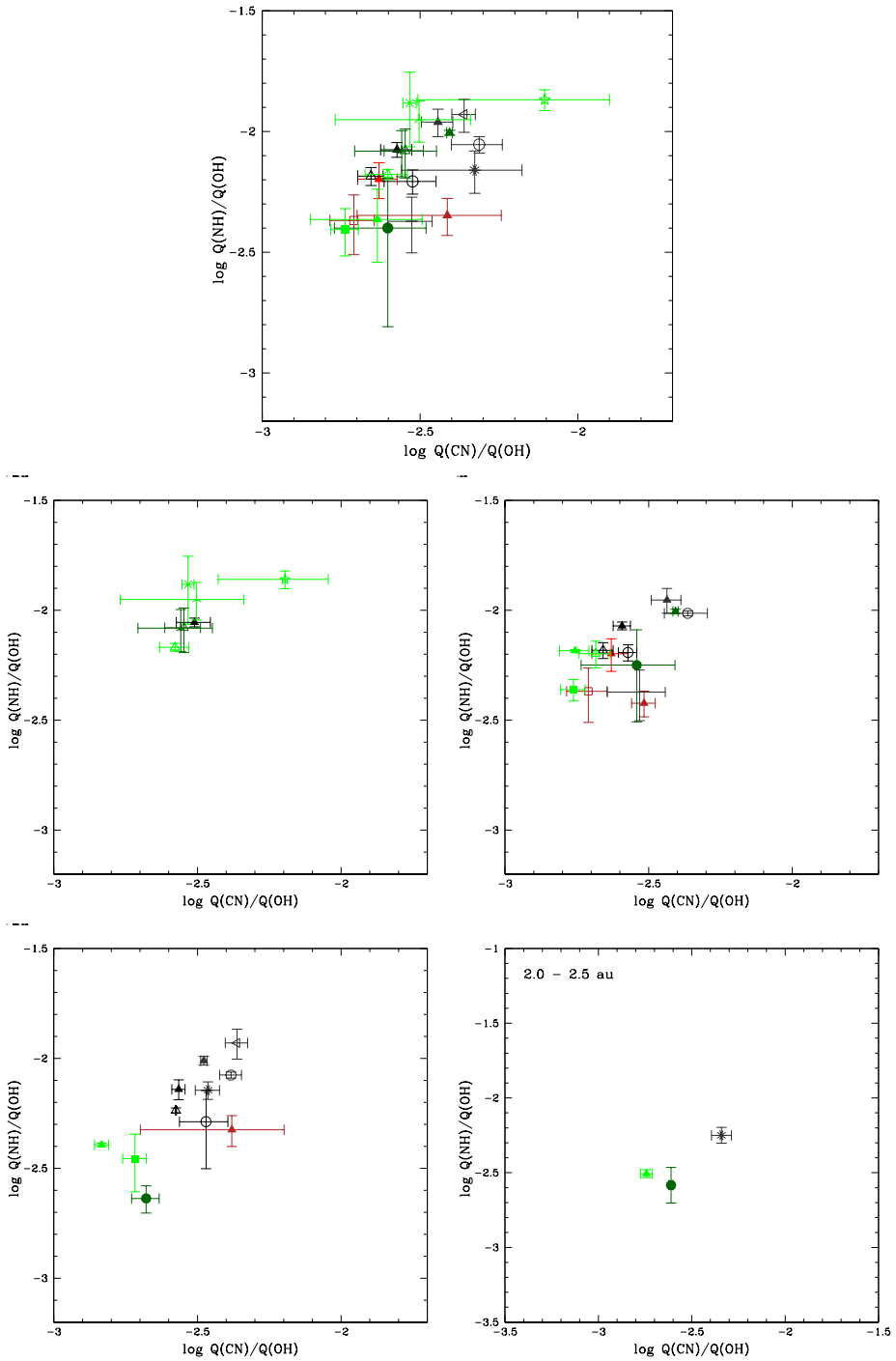


Figure 4.8: Logarithm of the ratio of NH to OH production rates against the logarithm of the ratio of CN to OH. The first plot has been made using a mean value for each comet. The other plots have been made for 0.5 au-wide bins of heliocentric distance.

comet as a function of the logarithm of the ratio of CN to OH, first using a mean value for each comet and then in four bins of heliocentric distance. We did not measure NH production rates for every comet in our data set, since the NH filter was only mounted on the telescope in October 2012. Because of this, our sample to study the NH abundance in comets is smaller than for the $C_3$ and the $C_2$. In the first plot (using a mean value for every comet), most comets lie on a diagonal band, as it was the case for the $C_3$ and the $C_2$. One comet seems to be located above the band: comet C/2011 L4 (PanSTARRS). However, this comet has been observed for a few days in the twilight at high airmass and we only have a couple of NH production rate measurements, so the uncertainty is high. We do not observe comets strongly depleted in NH. If we bin all pre-perihelion ratios and compare them to all post-perihelion ratios, we do not see any significant difference between pre- and post-perihelion data.

The study of the composition of 30 comets observed with TRAPPIST reveals that most comets in our data set are remarkably similar in composition. The only true outlier is comet 168P/Hergenrother. This comet has a very low $C_2$ and $C_3$ abundance compared to other species. From our data set we are not able to identify compositional classes and to establish a taxonomical classification of comets. Previous studies defined two main classes of comets based on their composition: typical comets and carbon-chain depleted comets (A'Hearn et al., 1995; Fink, 2009; Langland-Shula and Smith, 2011; Cochran et al., 2012). The definition of carbon-chain depleted comets varies depending on the author. Some require both $C_2$ and $C_3$ to be depleted (Cochran et al., 2012) while others only require $C_2$ to be under a threshold value (A'Hearn et al., 1995; Fink, 2009). A'Hearn et al. (1995) find that 29% of the comets in their restricted data set are depleted (using only a criterion for $C_2$, $\log(Q(C_2)/Q(CN)) < -0.18$), almost all depleted comets being JFCs. Using a different criterion based on the $C_2$ to $H_2O$ ratio ($\log(Q(C_2)/Q(H_2O)) < -0.3$), Fink (2009) finds 22% of comets depleted in $C_2$, and 6% of comets depleted in $C_2$ and $NH_2$. This is very similar to what is found by A'Hearn et al. (1995). Finally, Cochran et al. (2012) find that 9% of the comets in their data set are depleted in both $C_2$ and $C_3$, while 25% of comets are depleted in $C_2$ only ($\log(Q(C_2)/Q(CN)) < 0.22$).

In Fig. 4.9, we show the evolution of the logarithm of the $C_2$ to CN ratio as a function of the heliocentric distance for all comets in our data set (we used mean values in 0.1 au-wide bins). The horizontal black line represents the limit defined by A'Hearn et al. (1995) to distinguish between typical and depleted comets. However, the understanding of the $C_3$ and $C_2$ emission bands evolved since 1995. This resulted in new fluorescence coefficients for these two species and a re-evaluation of the limit defined by A'Hearn et al. (1995): $\log(Q(C_2)/Q(CN)) < -0.11$ (Schleicher et al., 2003; Farnham and Schleicher, 2005; Schleicher, 2006). We decided to plot the modified limit from (A'Hearn et al., 1995) in Fig. 4.9 instead of the limits defined by Fink (2009) and Cochran et al. (2012), since we used the same model parameters to compute gas production rates. Comet 168P/Hergenrother clearly falls below the separation line, confirming its depletion in $C_2$. A few other comets also have values of the $\log(Q(C_2)/Q(CN))$ smaller than the limit for typical comets, like comets C/2009 P1 (Garradd), C/2013 E2 (Iwamoto), or C/2013 US10 (Catalina). However, all these comets have been observed at large heliocentric distances. Most of these have also been observed at smaller heliocentric distances and have higher $C_2$ to

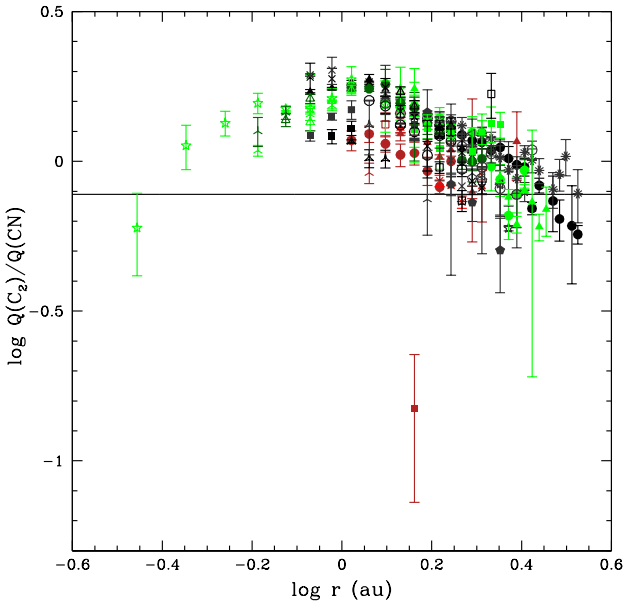


Figure 4.9: Evolution of the logarithm of the $C_2$ to CN production rate ratio with the logarithm of the heliocentric distance. The black line represents the limit of $\log(Q(C_2)/Q(CN)) < -0.11$ from A'Hearn et al. (1995) to distinguish typical and depleted comets, updated by Schleicher (2006).

CN ratios closer to the Sun, so that they can no longer be classified as depleted. In conclusion, most of the comets that could be classified as depleted according to the limit defined by A'Hearn et al. (1995) might actually be typical. This is caused by the variation of the $C_2$ to CN ratio with the heliocentric distance, instead of being an intrinsic depletion of carbon-chain species, the only really depleted comet being 168P/Hergenrother. We then observe only 3% of comets depleted in $C_2$ in our data set while most studies find between 25% and 30% of depleted comets. The reason of the difference between our study and previous ones is still unclear. It is important to notice that we used a completely homogeneous data set, hence avoiding biases introduced by the use of different instruments and data reduction procedures. Furthermore, most our comets have been observed over a range of heliocentric distances, which allows us to discriminate between the low $C_2$ to CN ratios due to the variation of this ratio with the heliocentric distance and intrinsically low $C_2$ to CN ratios. If some of the comets of our sample had only been observed at large distances, we could have classified five other comets as depleted, in addition to 168P/Hergenrother, which would make 27% of the comets of our sample. This amount of depleted comet is within the rage of what is observed in other studies. In addition, all comets observed at heliocentric distances larger than 1.8 au by A'Hearn et al. (1995) are classified as depleted, reinforcing the hypothesis that the evolution of the $C_2$ to CN ratio with the heliocentric distance might affect the classification of comets. Among the 30 comets we observed, only 8 are Jupiter Family Comets. Both A'Hearn et al. (1995) and

Cochran et al. (2012) find that a larger part of JFCs are depleted compared to Long period Comets. In our sample, one out of eight JFCs is depleted while Cochran et al. (2012) observe 37% of depleted JFCs. However, with only 8 JFCs in our sample, we do not have enough comets for significant statistics. Cochran et al. (2012) also find that 18.5% of their LPCs are depleted. We observed 24 Long Period Comets and none is depleted while we could have expected to observe at least 4 of them to be depleted. In conclusion, we might observe differences between our study and previous ones, but our sample is not large enough to determine if these differences are statistically significant. Other composition classes have also been observed in previous studies, such as comets with higher $C_2$ abundances or lower NH abundances, for example. These classes contain fewer comets than the carbon-chain depleted class, and we do not observe any of these peculiar comets in our data set.

Some of the comets we observed with TRAPPIST are also part of previous studies. We do not compare directly gas production rates with those published by other authors, since the parameters used for computing gas production rates vary from one study to another. Instead, we compare the classifications made from the analysis of a group of comets. A'Hearn et al. (1995) observed comets 26P/Grigg-Skjellerup, 103P/Hartley 2, and 88P/Howell. They classify comets 103P/Hartley 2 and 88P/Howell as typical. The case of comet 26P/Grigg-Skjellerup is more complicated: it is classified as typical or depleted according to the criterion they use. Fink (2009) observed comet 103P/Hartley 2 and classify it as a typical comet. Finally, Cochran et al. (2012) observed comets 10/Tempel 2 and 88P/Howell and find that both comets are typical in terms of carbon-chain species. All comets we have in common with previous studies are JFCs and most of them have been observed at different returns. A'Hearn et al. (1995) do not observe changes of production rate ratios of JFCs observed at different returns. This makes us confident that we can compare the taxonomical classification of JFCs observed at consecutive returns. In all common cases, our classification is consistent with previous studies.

From the study of several individual comets we performed in Chapter 3, we noticed that some gas production rate ratios are changing with the heliocentric distance for most comets. As we have shown, these changes of production rate ratios may strongly bias any attempt of defining compositional classes of comets. We decided to study further the evolution of various production rate ratios with the heliocentric distance. As was done earlier in this work, we decided to compute ratios relatively to CN. We then defined 0.1 au- wide bins of heliocentric distance and computed mean values for each comet in each bin.

Figure 4.10 shows the evolution of the logarithm of the OH to CN ratio with the heliocentric distance. The range of OH to CN ratios we observe is large, spanning over approximately one order of magnitude (from 100 to 1000). Even for comets observed at similar heliocentric distances, the range of OH to CN ratios measured is large. This does not seem to be linked to the dynamical type of the comet, even though Dynamically New Comets might have higher OH to CN ratios at large heliocentric distances. Since these comets are thought to release a halo of icy grains at large heliocentric distances due to the outgassing of highly volatile species, this supplementary source of water could explain why DNCs have higher OH to CN ratios

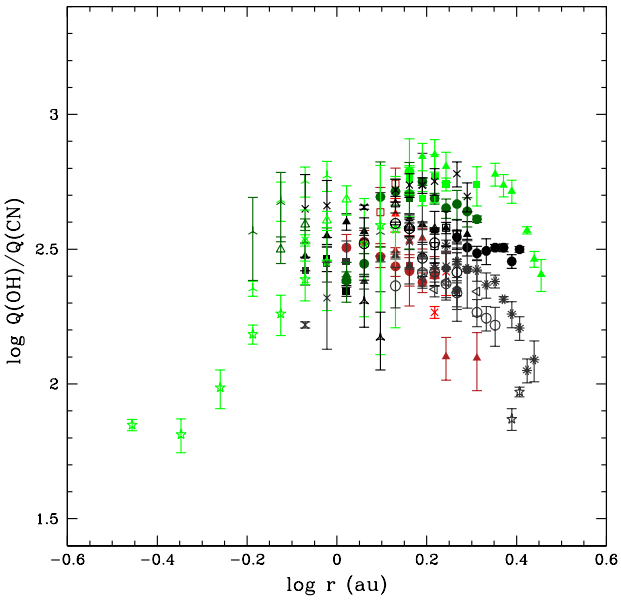


Figure 4.10: Evolution of the logarithm of the OH to CN ratio with the logarithm of the heliocentric distance for all the comets in our sample.

at large heliocentric distances. This effect is not as strong at shorter heliocentric distances, because normal outgassing from the nucleus becomes more important closer to the Sun. Between 0.8 (log r = -0.1) and 2 (log r = 0.3) au, we do not see any general trend for the OH to CN ratio as a function of the heliocentric distance for the comets of our sample. There are trends for individual comets, but we do not see a strong common trend for our whole sample. At heliocentric distances larger than 2 au, the OH to CN ratio decreases with increasing heliocentric distances. The amplitude of this variation is smaller than the dispersion observed among comets. At these distances the water outgassing is becoming less efficient, while the outgassing of more volatile species might still contribute significantly. At heliocentric distances smaller than 0.8 au, the OH to CN decreases as the comets approach the Sun. At such low heliocentric distances, a significant part of the CN could be released from organic-rich grains, as suggested by Dello Russo et al. (2016b). However, only comet C/2012 S1 (Ison) was observed at these distances and we cannot conclude whether this is a general trend or if this behaviour is specific to comet Ison.

A'Hearn et al. (1995) report only small variations of the OH to CN ratio of their comets as a whole but they observe that it is increasing with the heliocentric distance. However, the dispersion in their data at large heliocentric distances is large and the trend is not strong. They also notice that the OH to CN ratio is peaking between 1 and 2 au for individual comets, which is more consistent with what we observe. Overall, the plot of the evolution of the OH to CN ratio with the heliocentric distance they show looks similar to Fig. 4.10. Cochran et al. (2012)

do not find any trend of the OH to CN ratio with the heliocentric distance in their data but we must note they used different scalelengths.

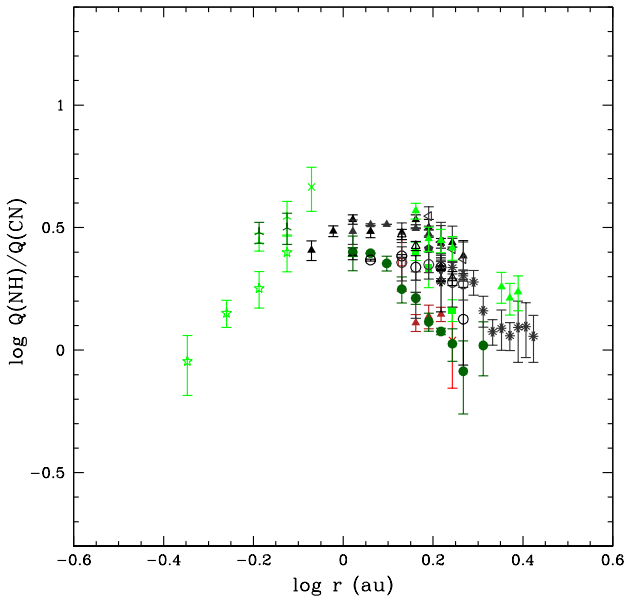


Figure 4.11: Evolution of the logarithm of the NH to CN ratio with the logarithm of the heliocentric distance for all the comets in our sample.

Figure 4.11 shows the evolution of the logarithm of the NH to CN ratio with the heliocentric distance. Values for comets observed at similar heliocentric distances range over a factor 3 approximately, which is narrower than what we observe for OH. We do not see any trend linked to the dynamical type of the comets. Unlike what we observe for the OH, there is a general trend of the NH to CN ratio with the heliocentric distance among the comets of our sample and the amplitude of the trend is larger than the dispersion for comets observed at similar heliocentric distances. The NH to CN ratio peaks around 1 au. At larger heliocentric distances, it decreases with increasing heliocentric distances. At smaller heliocentric distances, it is decreases as comets approach the Sun. However, we only observed a few comets under 1 au and it is difficult to claim this trend is real. The origin of the decrease of the NH to CN ratio at heliocentric distances larger than 1 au is difficult to interpret. Since the turnover point is 1 au, it could point to an effect of the Haser scalelengths we used to derive NH production rates and especially their scaling with the heliocentric distance. We already mentioned that the NH scalelengths and their dependence with the heliocentric distance are poorly known. This could have a large influence on the evolution of the NH to CN ratio with the heliocentric distance. The effect of Haser scalelengths will be studied later in this work (Section 4.3.3). A'Hearn et al. (1995) report an increase of the NH to CN ratio with the heliocentric distance but they mention the trend is not strong and the dispersion of the data is large.

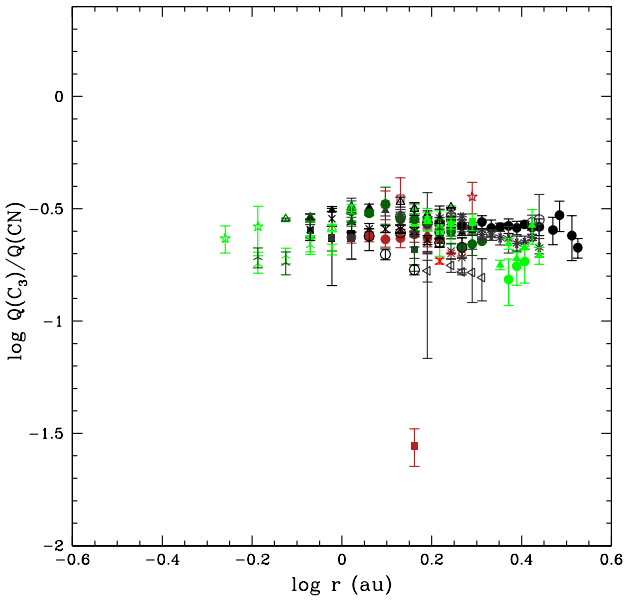


Figure 4.12: Evolution of the logarithm of the $C_3$ to CN ratio with the logarithm of the heliocentric distance for all the comets in our sample.

Figure 4.12 shows the evolution of the logarithm of the $C_3$ to CN ratio with the heliocentric distance. Except for comet 168P/Hergenrother which is depleted in $C_3$, all comets lie on a horizontal band. The band is narrow, indicating that the dispersion of the $C_3$ to CN ratio among comets of our sample is low. We observe variations of about a factor 2 among comets observed at the same heliocentric distance. We do not observe any overall variation of the $C_3$ to CN ratio with the heliocentric distance. There might be variations for individual comets but the amplitude of these variations must be small, since the dispersion among comets if low. The production of $C_3$ is thus well correlated to the production of CN for the comets in our sample. A'Hearn et al. (1995) observe a small decrease of the $C_3$ to CN ratio with the heliocentric distance but this could be biased by a larger number of depleted comets observed at large distances. Cochran et al. (2012) do not observe variations of the $C_3$ to CN ratio with the heliocentric distance below 3 au. They observe higher values of the ratio at larger heliocentric distances but we do not have data at these distances to compare with. Langland-Shula and Smith (2011) do not observe any trend of the $C_3$ to CN ratio with the heliocentric distance either.

Figure 4.9 shows the evolution of the logarithm of the $C_2$ to CN ratio with the heliocentric distance. One comet is located below the others. This is the only carbon-chain depleted comet: 168P/Hergenrother. Except for comet 168P/Hergenrother, we only observe variations of about a factor 2 among comets observed at the same heliocentric distance. We see a clear trend of the $C_2$ to CN ratio with the heliocentric distance, whose amplitude is larger than the

dispersion. At heliocentric distances larger than about 1 au, the ratio decreases with increasing heliocentric distances. The $C_2$ to CN ratio decreases approximately by a factor two between 1 and 2.5 au. At heliocentric distances smaller than about 1 au, the ratio decreases while comets approach the Sun. As it was the case for the OH and the NH, we only observed a few comets close to the Sun and the trend is dominated by comet C/2012 S1 (Ison). More data would be needed to decipher whether this is a general trend among comets or if comet Ison is a peculiar case. Since the trend of the $C_2$ to CN ratio with the heliocentric distance is similar for all comets, it should be possible to define a new limit to separate between typical and depleted comets which varies with the heliocentric distance. This would avoid being biased by the heliocentric distance at which the comet is observed when classifying the comet based on its $C_2$ to CN ratio. However, we are still missing a large number of comets observed at small and large heliocentric distances to reliably define such a limit. We also have only one depleted comet in our sample.

A'Hearn et al. (1995) observe a systematic decrease of the $C_2$ to CN ratio with the heliocentric distance for individual comets, even though they do not see any general trend for their whole sample. The reason why they do not observe a trend for all their comets might be the larger scatter of the data at large heliocentric distances, which they attribute partly to the lower S/N and partly to the greater sensitivity to the assumed scalelengths. Langland-Shula and Smith (2011) observe a steep decrease of the $C_2$ to CN ratio with the heliocentric distance. They argue that it could imply that $C_2$ radicals have release mechanisms different from the other species. Cochran et al. (2012) do not find trends of the $C_2$ to CN ratio with the heliocentric distance. The trend we observe for the $C_2$ to CN ratio might actually indicate that the $C_2$ is released from a different mechanism than the CN, as suggested by Langland-Shula and Smith (2011). In particular, $C_2$ radial profiles of brightness indicate that it could be released from organic-rich grains. However, we must be cautious since other explanations might account for this phenomenon. The Haser scalelengths we used have been determined over a small range of heliocentric distances and we assume they vary with the square of the heliocentric distance for all species. Departures from this scaling law for some species could introduce artificial variations of production rate ratios with the heliocentric distance. Cochran et al. (2012) use different scalelengths from A'Hearn et al. (1995), and they do not observe trends in the $C_2$ to CN ratio. This emphasizes the effect Haser scalengths might have on production rate ratios and their variation with the heliocentric distance. Before concluding that the trend we observe is caused by different release mechanisms for $C_2$ and CN, we have to assess the effect of the Haser scalelengths. This is the object of Section 4.3.3.

### 4.3.2 Dust

Figure 4.13 shows the evolution of the logarithm of the OH, NH, CN, $C_3$, and $C_2$ production rates as a function of the logarithm of the $Af\rho$ for every comet in our data set. For this figure, we used a mean value for each comet. For all gas species, most comets lie on a diagonal band, indicating that the gas and dust releases are correlated. The dispersion is higher than in Fig.

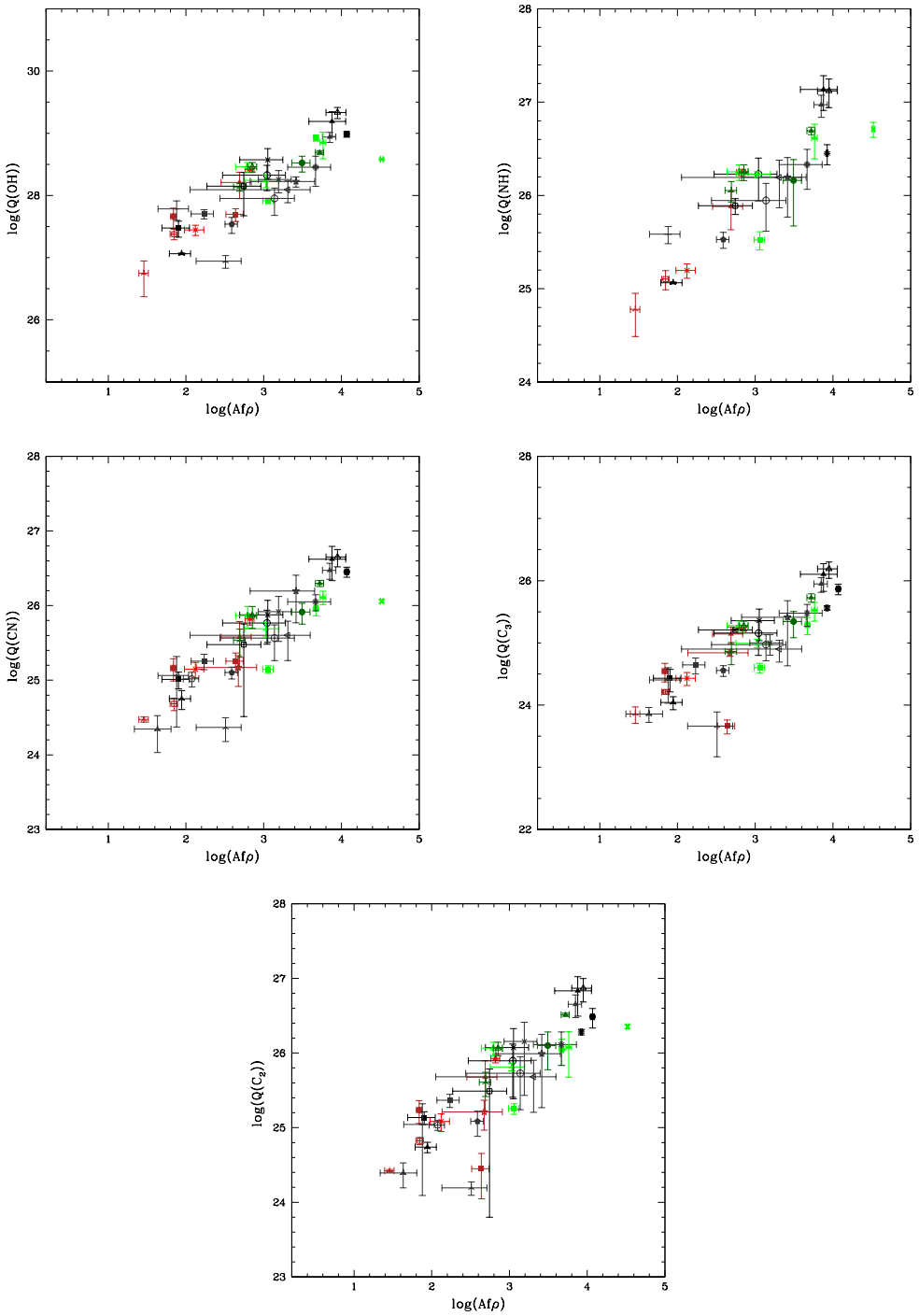


Figure 4.13: Logarithm of the OH, NH, CN, $C_3$, and $C_2$ production rates as a function of the logarithm of the $Af\rho$ for every comet in our data set.

4.5 and 4.4. This means that the correlation between the production of various radicals is better than the correlation between the dust and gas production, at least for the radicals we observe. Several comets come out of the main trend. Comet C/2011 L4 (PanSTARRS) is located to the right of the diagonal band. This comet has an unusually high dust to gas ratio. Comet C/2012 K5 (Linear) also has a dust to gas ratio higher than the trend.

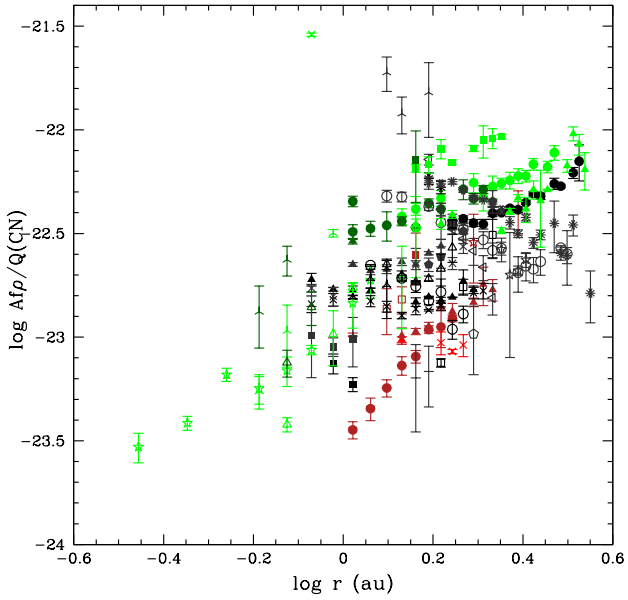


Figure 4.14: Evolution of the logarithm of the $Af\rho$ to CN ratio with the logarithm of the heliocentric distance.

We then study the evolution of the gas to dust ratio with the heliocentric distance for our sample of comets. Figure 4.14 shows the evolution of the logarithm of the $Af\rho$ to CN ratio with the logarithm of the heliocentric distance while Fig. 4.15 shows the evolution of the $Af\rho$ to OH ratio. For these plots, we computed a mean value for each comet in 0.1 au-wide bins of heliocentric distance. From Fig. 4.14, we observe a strong trend for the ensemble of comets: the $Af\rho$ to CN ratio increases with increasing heliocentric distances. Individual comets behave in a different way. For some comets, such as C/2013 R1 (Lovejoy), the $Af\rho$ to CN ratio decreases with the heliocentric distance while for others like C/2012 K1 (PanSTARRS), the ratio increases with the heliocentric distance. There are also comets for which we do not observe clear trends of the $Af\rho$ to CN ratio. Comet C/2011 L4 (PanSTARRS) has much higher $Af\rho$ to CN and $Af\rho$ to OH ratios than other comets observed at the same heliocentric distance. Despite different individual trends, the general trend for the comets in our data set is clear, the dust to gas ratio increases with the heliocentric distance. The $Af\rho$ to OH ratio shown in Fig. 4.15 also increases with the heliocentric distance, even though the trend is not as clear as for the $Af\rho$ to CN ratio. Small heliocentric distances are dominated by comet Ison, which has a low OH abundance. This explains why the $Af\rho$ to OH ratio at low heliocentric distances

looks higher compared to the $Af\rho$ to CN ratio. As for the $Af\rho$ to CN ratio, individual comets have different trends but the general tendency remains the same. From both Fig. 4.14 and 4.15, we see that JFCs tend to have smaller dust to gas ratios. However, since we only observed 8 JFCs, the sample is not large enough to draw significant conclusions. The range of $Af\rho$ to CN and $Af\rho$ to OH ratios for comets observed at similar distance is larger than a factor 10 for some distances. This prevents us to define a law allowing us to reliably infer the OH or CN production rate of a comet from the measurement of its $Af\rho$ value.

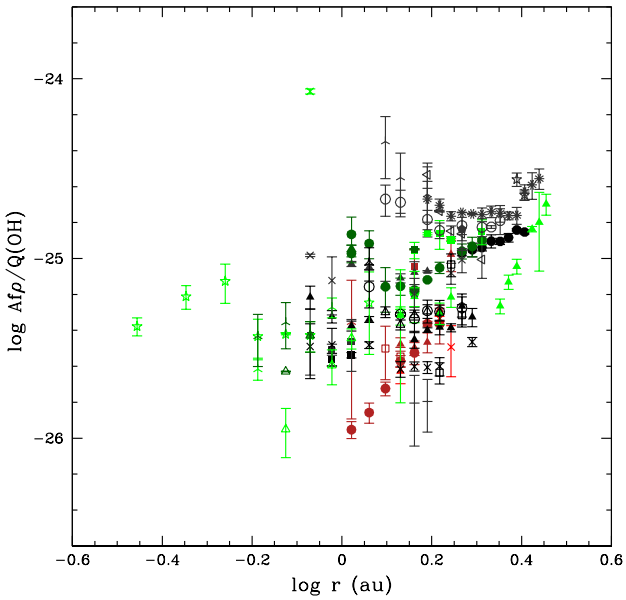


Figure 4.15: Evolution of the logarithm of the $Af\rho$ to OH ratio with the logarithm of the heliocentric distance.

A'Hearn et al. (1995) observe an increase of the $Af\rho$ to CN ratio and of the $Af\rho$ to OH ratio with the heliocentric distance for their sample of comets. They also observe a flattening of the $Af\rho$ to OH ratio trend at small heliocentric distances, which could be consistent with what we observe for comet C/2012 S1 (Ison). Langland-Shula and Smith (2011) observe an even steeper evolution of the dust to gas ratio with the heliocentric distance for their ensemble of comets. These authors propose several hypothesis to explain the trend of the dust to gas ratio with the heliocentric distance. A selection effect could partly account for the trend. Comets having lower dust to gas ratio have lower visual magnitudes for similar gas production rates. The larger gas lifetimes at large heliocentric distances also make low dust to gas ratio comets appear very diffuse at large heliocentric distances. As the visual magnitude is often used as a selection criterion, dusty comets are preferentially observed at large heliocentric distances. However, even if a selection effect could explain why we observe dustier comets at large heliocentric distances, it does not account for the lower dust to gas ratio we observe at small heliocentric distances. A'Hearn et al. (1995) also postulate that the presence of large

grains less volatile than water might explain this trend. At large heliocentric distances, these grains could be vaporized at larger nucleocentric distances than the one at which we compute the gas production rates. Similarly, the fragmentation of grains could release gas at larger nucleocentric distances.

Several authors proposed an alternative explanation based on the correlation between the dust to gas ratio and the perihelion distance. A'Hearn et al. (1995); Fink (2009); Langland-Shula and Smith (2011) all observe an increase of the dust to gas ratio (either the $Af\rho$ to OH or the $Af\rho$ to CN ratio) with the perihelion distance of the comet. They explain it as the build-up of a dust crust on the surface of the nucleus. Because of the crust, the gas would be released through pores rather than directly from the surface, and it would be more difficult to entrain dust. In order to check this hypothesis, we plotted the logarithm of the $Af\rho$ to CN ratio as a function of the perihelion distance of the comet in Fig. 4.16. The first plot has been made using a mean value for each comet, while the others have been made for 0.5 au-wide bins of heliocentric distance, to avoid being biased by the heliocentric distance at which the comets were observed. Figure 4.17 is the same for the $Af\rho$ to OH ratio. In the plots using only one mean value for every comet, there is indeed a slight trend of increasing dust to gas ratio with increasing perihelion distances. Leaving aside comet C/2011 L4 (PanSTARRS) who has an unusually high dust to gas ratio, we fitted a slope to represent the trend of the $Af\rho$ to CN and $Af\rho$ to OH ratios with the perihelion distance of the comet. If we use a mean value for each comet (first plots in Fig. 4.16 and 4.17), we find a slope of $0.23 \pm 0.13$ for the $Af\rho$ to CN ratios and a slope of $0.27 \pm 0.14$ for the $Af\rho$ to OH ratio. However, this trend is not observed in the various bins of heliocentric distances, for which the fitted slopes are consistent with zero (except for the $2-2.5$ au bin for the $Af\rho$ to OH ratio). This indicates that the trend of dust to gas ratio with the perihelion distance of the comet could be an artefact caused by the variation of the dust to gas ratio with the heliocentric distance. The sample of comets observed in the bins of distance is not very large and may not be significant. We must then be cautious while interpreting these plots. In conclusion, from our observations, the origin of the gas to dust ratio increase with the heliocentric distances is difficult to understand and a larger sample of comets with a wide range of perihelion distances is needed in order to draw firm conclusions.

Finally, we study the dust colour of the comets in our sample. We usually use the RC and BC filters to compute the dust colour, as the GC and BC filters are close in wavelengths and the reddening computed from these filters has higher uncertainties. However, before October 2012, the RC filter was not mounted on the telescope. For the comets observed prior to this date, we use the GC and BC filters to compute the colour. Figure 4.18 shows the evolution of the dust colour of the comets in our sample as a function of the heliocentric distance. We used mean values in 0.1 au-wide bins of heliocentric distance. In the left part of the Figure, we only show the comets for which we have almost simultaneous observations in the RC and BC filters. In the right part, we added colours measured from the GC and BC filters when there were no observations in the RC filter. These two plots are very similar. We observe a wide range of colour values among our sample of comets, from 0 to 20%/1000 Å, but all comets have dust colours redder than the Sun (indicating that the efficiency of the scattering of the

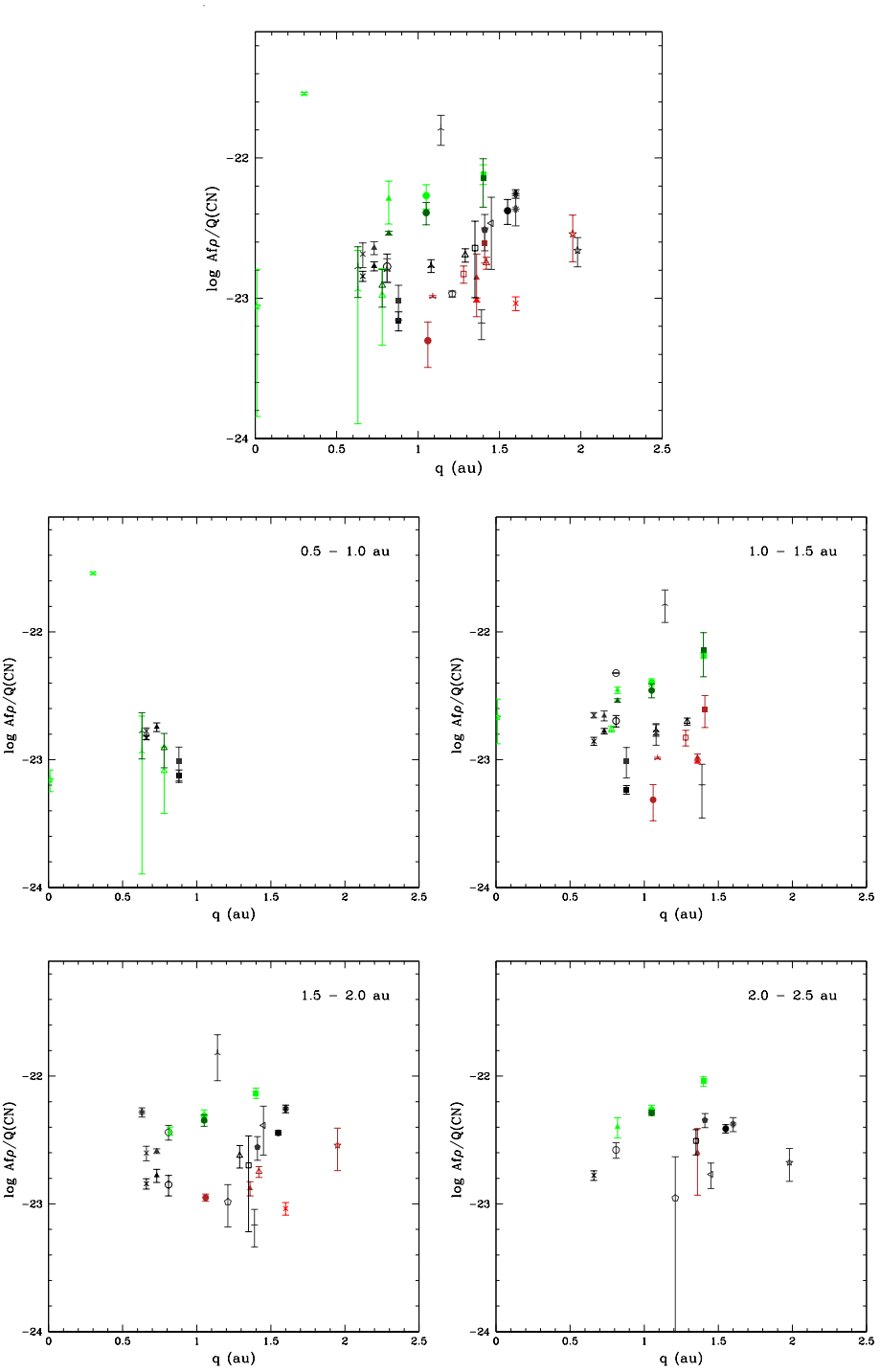


Figure 4.16: Logarithm of the ratio of $Af\rho$ to CN ratio against the perihelion distance of the comets. The first plot has been made using a mean value for each comet. The other plots have been made for 0.5 au-wide bins of heliocentric distance.

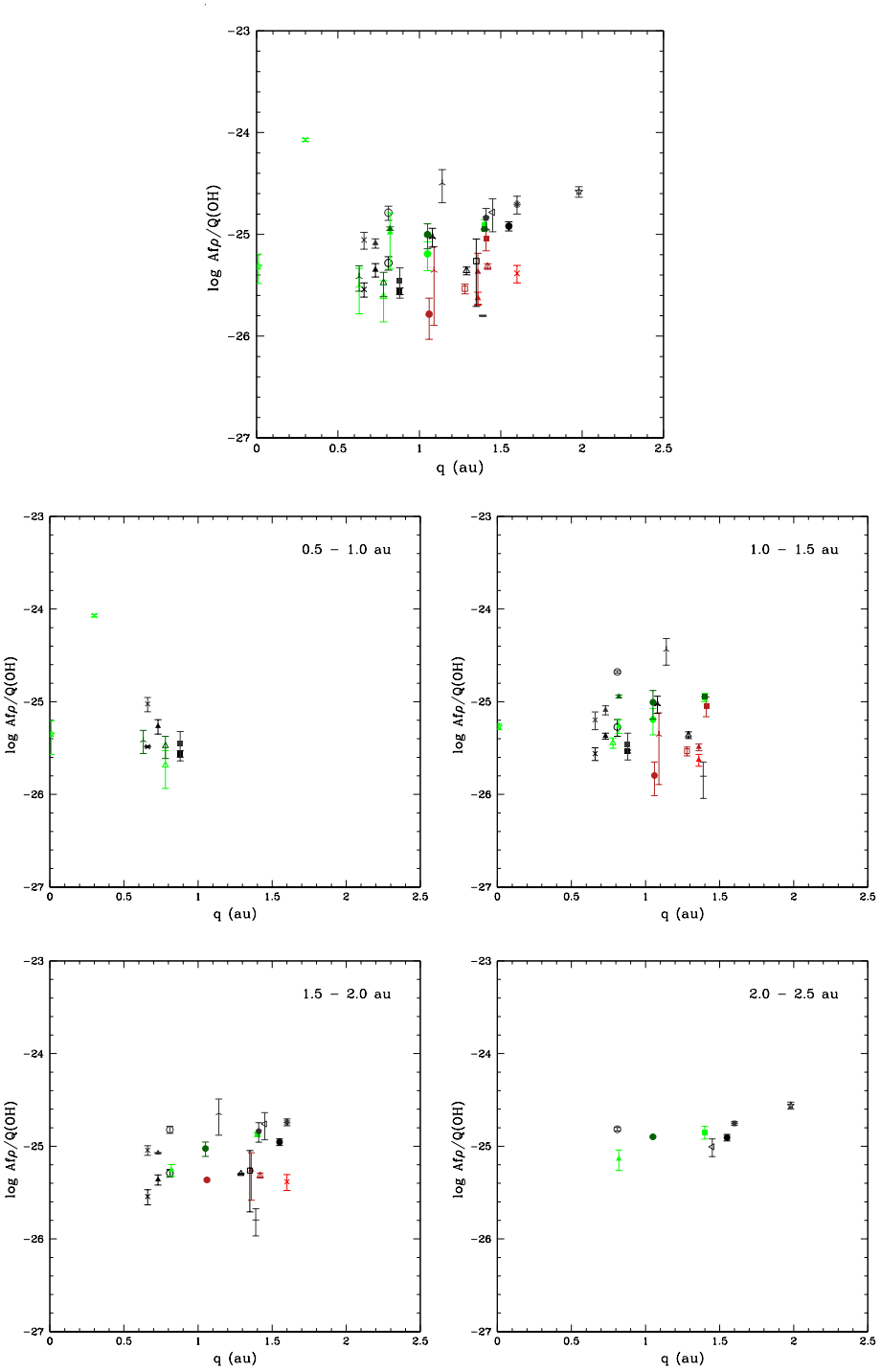


Figure 4.17: Logarithm of the $Af\rho$ to OH ratio against the perihelion distance of the comets. The first plot has been made using a mean value for each comet. The other plots have been made for 0.5-au wide bins of heliocentric distance.

solar light by the dust grains increases with the wavelength), which is consistent with previous studies (Solontoi et al., 2012; Mazzotta Epifani et al., 2014; Lin et al., 2013, 2012; Lara et al., 2004). We do not see any differences in the dust colour linked to the dynamical type of the comets. If we fit a slope to represent the evolution of the colour from the RC and BC filters as a function of the heliocentric distance, there is a slight trend of increasing reddening with decreasing heliocentric distances. However, this trend is dominated by comets observed at very small and large heliocentric distances. Since we only observed a few comet at these distances and the dispersion of the colour measurements is large, we cannot claim there is a trend of dust colour variation with the heliocentric distance for our ensemble of comets. If we only consider comets observed between 0.5 and 2.3 au, which is the range of heliocentric distance over which most comets were observed, there is no significant trend of dust colour variation with the heliocentric distance. We then need to observe a larger number of comets at very large and small heliocentric distances to confirm if there is a trend of dust colour with the heliocentric distance. Solontoi et al. (2012) do not observe systematic variations of the dust colour with the heliocentric distance from the study of 31 comets observed by the Sloan Digital Sky Survey (SDSS) and they do not observe correlations between the colour and the dynamical parameters of their comets either. This indicates that the optical properties of the dust in the coma of comets are similar and, for most comets, do not vary with their distance to the Sun. We do not observe any correlation between the colour and the dust production or the dust to gas ratio of the comets.

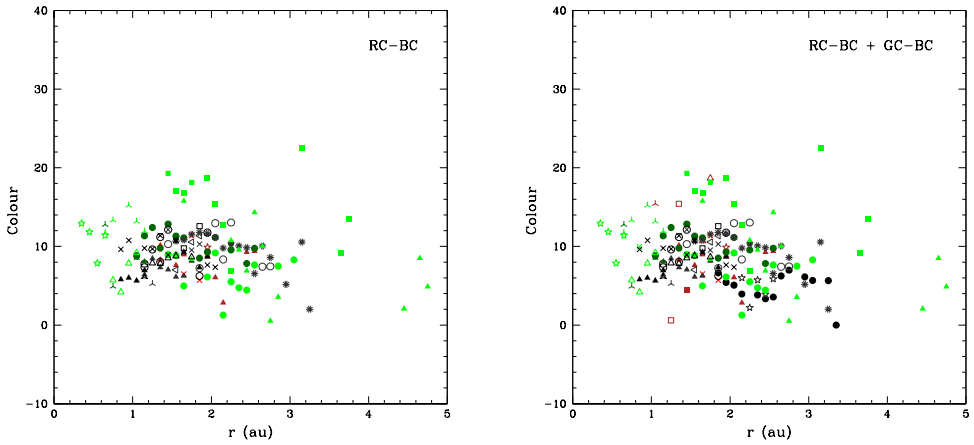


Figure 4.18: Evolution of the dust colour of the comets in our sample with the heliocentric distance from the RC-BC filters (left) and from the RC-BC and GC-BC filter (right).

### 4.3.3 Effect of the scalelengths

In this Section, we analyse the effect of the scalelengths on the computation of gas production rates. Comparing observed radial profiles and the Haser model we fit for several comets, we noticed that the agreement between the observations and the model is not always good. Since

the shape of the Haser model profile depends on the scalelengths, and since the scalelengths used have an influence on the production rates we derive, we decided to study this in more details. We used the observations of comet C/2012 F6 (Lemmon) for that purpose because we have high quality radial profiles for OH, NH, CN, $C_3$, and $C_2$ over a wide range of heliocentric distances. In order to derive reliable daughter scalelengths, especially, we need radial profiles with high S/N at large nucleocentric distances which is the case for comet Lemmon observations. We derived scalelengths in all filters and studied their variation with the heliocentric distance. To find the best scalelengths, we used a Levenberg-Marquardt method, with the parent scalelength, the daughter scalelength, and the gas production rate as free parameters. We fixed the velocity at 1 km/s, as what was done to derive the scalelengths we used for this work, in order to facilitate the comparison with the initial scalelengths. The purpose of this Section is not to define a new set of scalelengths that should be used for all comets in the future. Instead, we want to assess the effect of the scalelengths of the gas production rate and gas production rate ratios we derive and their evolution with the heliocentric distance.

In Fig. 4.19, we show examples of radial profiles observed for comet C/2012 F6 (Lemmon) on February 7, 2013 while the comet was at 1.14 au from the Sun. The black triangles represent the observed radial profiles, while the blue and red lines are respectively the Haser model fitted using the scalelengths introduced in Chapter 2 and those we adjusted on the observed profiles. Table 4.3 gives the values of the scalelengths for both models. The scalelengths from Chapter 2 have been scaled as $r^2$. From Fig. 4.19, we see that the red model is in every case an improvement compared to the blue one. This indicates that, for this comet and at this heliocentric distance, the Haser scalelengths we usually use do not provide a good representation of the observed profile. The two models are closer to each other and closer to the observed profile for the OH and the NH than for the other three species. For the same comet at other heliocentric distances, the original Haser model is a better match for the CN but is doing much worse for the NH, for example. Table 4.3 confirms these observations. The fitted scalelengths for NH and OH are closer to the original scalelengths than for the CN, $C_3$, and $C_2$.

We derived new scalelengths for every gas image of comet C/2012 F6 (Lemmon). In Fig. 4.20, we represent the evolution of the OH parent and daughter scalelengths with the heliocentric distance. First, the dispersion is higher for the daughter scalelengths than for the parent. Daughter scalelengths strongly depend on the quality of the radial profile at large nucleocentric distances. Since the OH is strongly absorbed by the atmosphere, it is difficult to obtain high quality profiles at large nucleocentric distances and this explains the high dispersion of the OH daughter scalelengths. Pre- and post-perihelion scalelengths follow the same trend. At small heliocentric distances (until approximately 1.2 au), parent scalelengths are consistent with the original scalelengths but they diverge at larger heliocentric distances. The increase of comet Lemmon OH parent and daughter scalelengths is shallower than $r^2$. The OH daughter scalelengths are consistent with the original scalelengths until approximately 1.5 au, accounting for the dispersion. At larger distances, the derived values are smaller than the original ones. This might be due to the difficulty to observe the edges of the radial profile

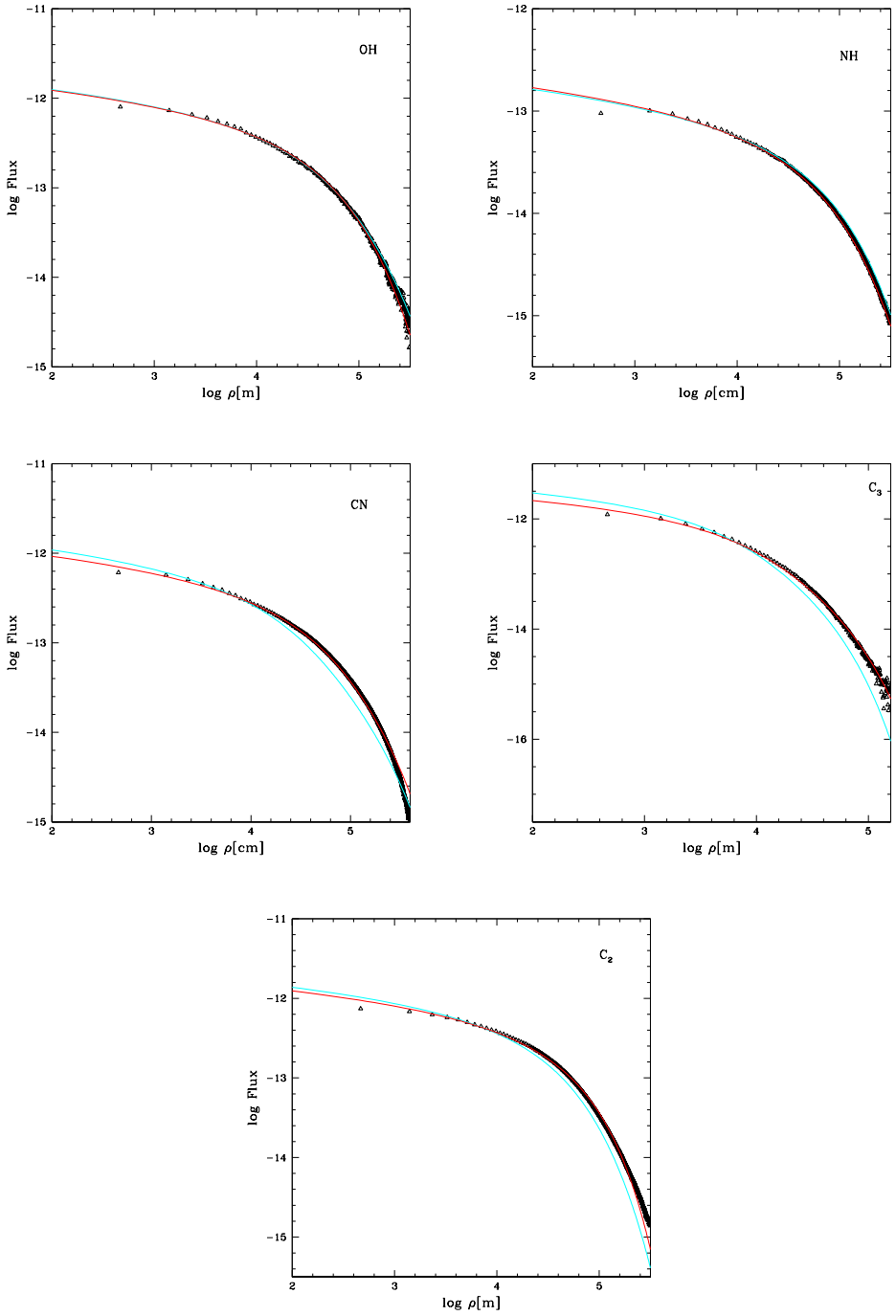


Figure 4.19: Comet C/2012 F6 (Lemmon) OH, NH, CN, $C_3$, and $C_2$ radial profiles for observations performed on February 7, 2013 ($r$ = 1.14 au). The black triangles represent the observed gas profile. The blue line represents the Haser model profile obtained using the scalelengths from A'Hearn et al. (1995). The red line represents the Haser model obtained using the scalelengths we derived in this work.

Table 4.3: Parent ($L_P$) and daughter ($L_D$) OH, NH, CN, $C_3$, and $C_2$ Haser scalelengths for observations of comet C/2012 F6 (Lemmon) on February 7, 2013 as defined in Chapter 2 and fitted on the observed radial profiles.

| Species | $L_P$ (km) | $L_D$ (km) | Reference |
|---|---|---|---|
| OH | $3.10 \times 10^4$ | $2.06 \times 10^5$ | Cochran and Schleicher (1993) |
| | $3.82 \times 10^4$ | $1.42 \times 10^5$ | This work |
| NH | $6.45 \times 10^4$ | $1.94 \times 10^5$ | Randall et al. (1992) |
| | $4.96 \times 10^4$ | $1.98 \times 10^5$ | This work |
| CN | $1.68 \times 10^4$ | $2.71 \times 10^5$ | Randall et al. (1992) |
| | $3.30 \times 10^4$ | $2.40 \times 10^5$ | This work |
| $C_3$ | $3.61 \times 10^3$ | $3.48 \times 10^4$ | Randall et al. (1992) |
| | $5.39 \times 10^3$ | $5.40 \times 10^4$ | This work |
| $C_2$ | $2.84 \times 10^4$ | $8.52 \times 10^4$ | Randall et al. (1992) |
| | $6.34 \times 10^4$ | $6.35 \times 10^4$ | This work |

when the comet is at large heliocentric distances, and then fainter.

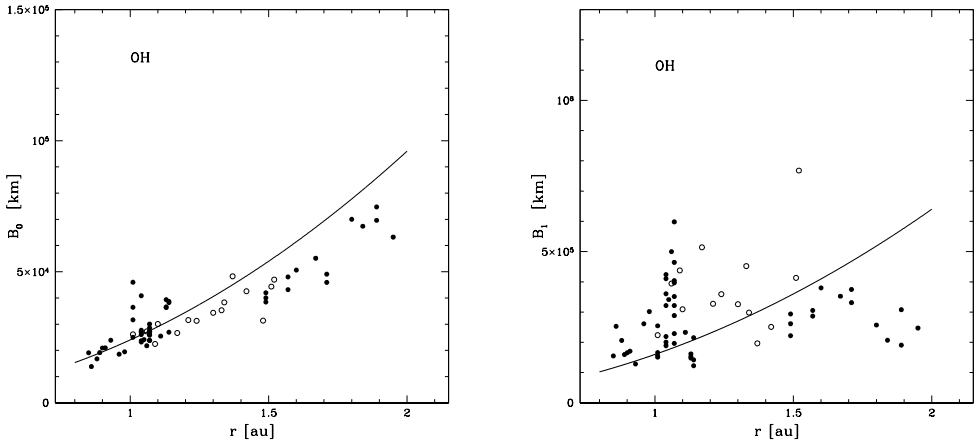


Figure 4.20: Comet C/2012 F6 (Lemmon) OH parent (left) and daughter (right) fitted scalelengths. Pre-perihelion scalelengths are represented with filled circles and post-perihelion scalelengths are represented with open circles. The black line represents the original scalelengths we used for this work, scaled as $r^2$.

Figure 4.21 shows the evolution of the NH parent and daughter scalelengths with the heliocentric distance. In this case too, the dispersion is larger for the daughter than for the parent scalelengths. For the parent scalelengths, pre- and post-perihelion values follow the same trend. The fitted scalelengths are lower than the original ones over the whole range of heliocentric distances. For the daughter scalelengths, the fitted values are higher than the original ones until 1.5 au. At larger heliocentric distances, the fitted scalelengths are much

lower. This is probably explained by the difficulty to get the edges of the radial profile when the comet is at large heliocentric distances. As expected, the NH scalelengths are difficult to constrain, and those we used for this work do not seem to be appropriate to reproduce the shape of the radial profile. This introduces large uncertainties in the computation of NH production rates.

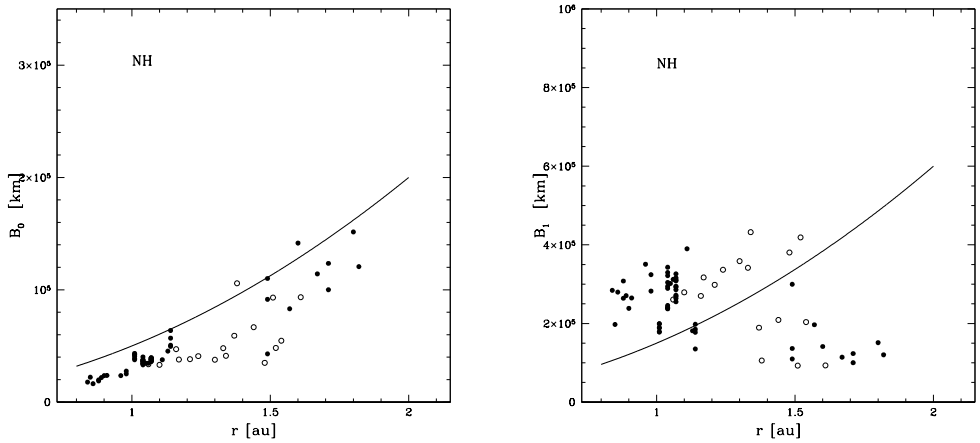


Figure 4.21: Comet C/2012 F6 (Lemmon) NH parent (left) and daughter (right) fitted scalelengths. Pre-perihelion scalelengths are represented with filled circles and post-perihelion scalelengths are represented with open circles. The black line represents the original scalelengths we used for this work, scaled as $r^2$.

Figure 4.22 shows the evolution of the CN parent and daughter scalelengths with the heliocentric distance. CN parent scalelengths follow the same trend pre- and post-perihelion and they are higher than the original scalelengths but their trend with the heliocentric distance could be consistent with a $r^2$ increase. The daughter scalelengths, however, seem to behave differently. At first sight, it seems that the daughter scalelengths drop for heliocentric distances larger than about 1.5 au. This is similar to what we observe for the OH and the NH because of the poor S/N but this should not be the case for CN. However, the lower values are observed only before the perihelion passage and they actually follow the trend of parent scalelengths derived closer to the Sun before the perihelion passage. The scalelengths derived after the perihelion passage are higher than those derived before, even for observations made at the same heliocentric distance, which leads us to believe there is a drop of the parent scalelengths at larger distances. This could suggest different release mechanisms for the CN, like gas coming from grains, even though we would expect it to affect mainly the parent scalelengths rather than the daughter scalelengths. We would need to fit Haser scalelengths on more comets to determine which values are the most commonly observed among comets and to better understand this effect and its origin. Daughter scalelengths derived pre- and post-perihelion both increase slower with the heliocentric distance than the $r^2$ law we assumed earlier.

Figure 4.23 shows the evolution of the $C_3$ parent and daughter scalelengths with the heliocen-

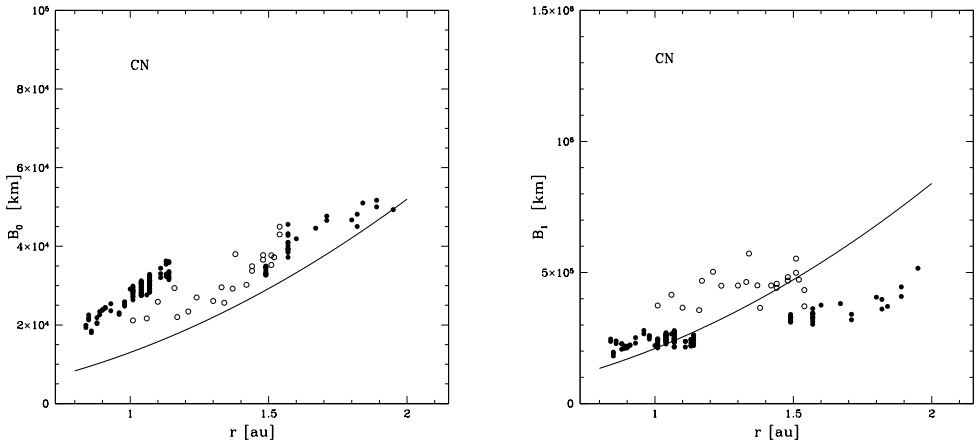


Figure 4.22: Comet C/2012 F6 (Lemmon) CN parent (left) and daughter (right) fitted scalelengths. Pre-perihelion scalelengths are represented with filled circles and post-perihelion scalelengths are represented with open circles. The black line represents the original scalelengths we used for this work, scaled as $r^2$.

tric distance. Parent and daughter scalelengths follow the same trend pre- and post-perihelion. Both scalelengths are larger than the original scalelengths we used for this work but their trend with the heliocentric distance is consistent with the $r^2$ law.

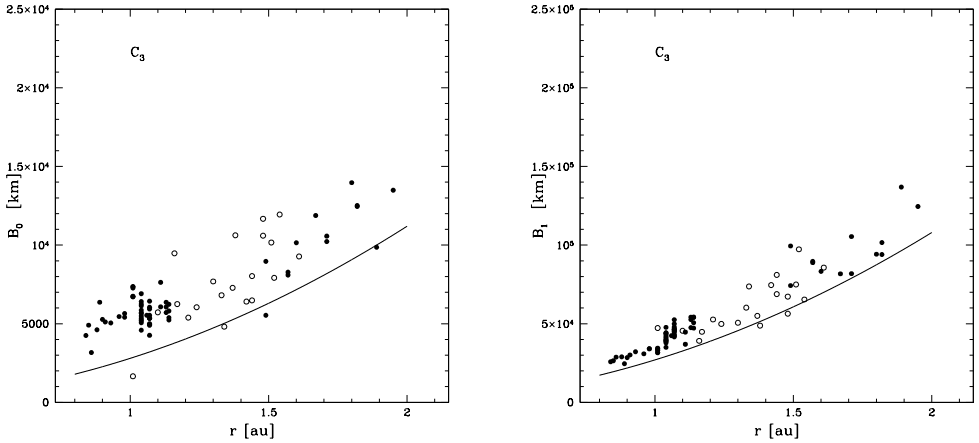


Figure 4.23: Comet C/2012 F6 (Lemmon) $C_3$ parent (left) and daughter (right) fitted scalelengths. Pre-perihelion scalelengths are represented with filled circles and post-perihelion scalelengths are represented with open circles. The black line represents the original scalelengths we used for this work, scaled as $r^2$.

Figure 4.24 shows the evolution of the $C_2$ parent and daughter scalelengths with the heliocentric distance. For pre-perihelion values, the dispersion of both parent and daughter scalelengths we derived is very low. The values are different from the original values we used

for the other parts of this work. Parent scalelengths are larger than the original values while daughter scalelengths are smaller. Actually, for pre-perihelion profiles, the best fit is obtained using almost identical parent and daughter scalelengths. Combi and Fink (1997), among others, already mentioned that the flat shape of the $C_2$ radial profiles is better reproduced using equal parent and daughter scalelengths. These results are thus consistent with previous observations. Combi and Fink (1997) discussed the possibility that the flat $C_2$ profile could be explained if the $C_2$ is released by a halo of CHON grains. For post-perihelion values, the dispersion is larger and the trend is different from pre-perihelion values, since parent and daughter scalelengths are no longer similar. The values are actually closer to the original values, with smaller parent scalelengths and larger daughter scalelengths. This could be explained if the $C_2$ is released from CHON grains before the perihelion passage while it is mainly released from nucleus ices after the perihelion passage. However, we do not have sufficient information to confirm this hypothesis. This analysis should be performed on a larger number of comets, in order to investigate whether comet Lemmon has a peculiar behaviour or if this is observed for other comets too.

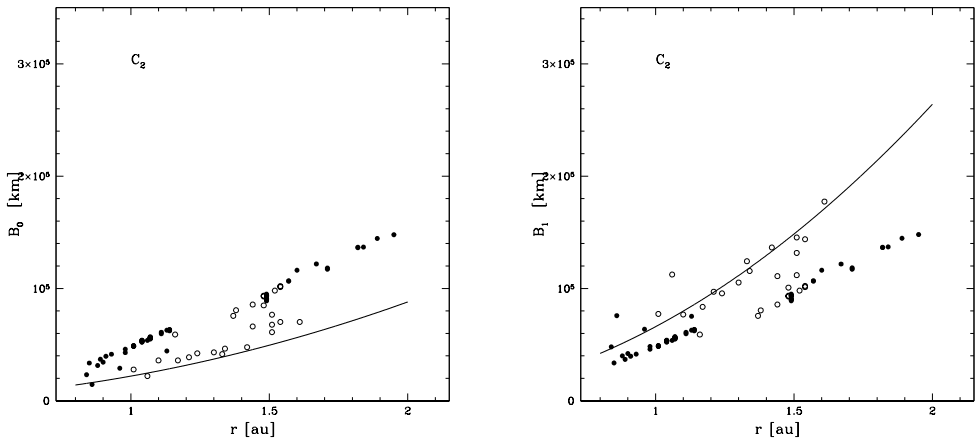


Figure 4.24: Comet C/2012 F6 (Lemmon) $C_2$ parent (left) and daughter (right) fitted scalelengths. Pre-perihelion scalelengths are represented with filled circles and post-perihelion scalelengths are represented with open circles. The black line represents the original scalelengths we used for this work, scaled as $r^2$.

Now that we established that the scalelengths we fitted to match the observed gas radial profiles can be different from the original scalelengths we used for the main part of this work, we compare the production rates we obtain using both sets of scalelengths. Figure 4.25 shows the comparison between gas production rates computed using the original scalelengths in black and those computed fitting the Haser scalelengths on the observed profiles in red. The dispersion is higher for the gas production rates computed using fitted scalelengths since we used different scalelengths for every image. We are then more sensitive to variations of the spatial distribution of radicals due to the rotation of the nucleus, for example. We have not implemented the computation of the error bars on the new production rates yet, so these are

shown without error bars, just to allow assessing the influence of the Haser scalelengths on the gas production rates. The OH production rates computed using both sets of scalelengths are in good agreement with each other over the whole range of heliocentric distances. This is consistent with the fact that the Haser scalelengths we derived are close to the original ones and seem to follow the same trend with the heliocentric distance. Similarly, the new $C_3$ production rates are slightly higher but close to the original ones. As for the OH, the scalelengths we derived are close to the original scalelengths and are consistent with a $r^2$ scaling with the heliocentric distance. We then believe that the production rates we derived for these two species are reliable, as well as their evolution with the heliocentric distance.

The new NH production rates are about 30% lower than the original production rates. This was expected, as the NH scalelengths we derived are different from those we assumed in the rest of the work. The largest differences are observed for $C_2$. The $C_2$ production rates derived using similar scalelengths for the parent and daughter species are up to a factor two higher than those derived using the original scalelengths. The influence of the scalelengths on the $C_2$ production rates is thus very important and should be taken into account. After the perihelion, the scalelengths we derived are consistent with the original scalelengths and the $C_2$ production rates we derived using these scalelengths are mostly consistent with the previous production rates, even though the dispersion is higher. Finally, the new CN production rates are mostly consistent with the original values beyond 1.5 au while they diverge at smaller heliocentric distances. When the comet is closer to the Sun, the new CN production rates are up to 30% higher than the original values. Since CN production rates agree at large heliocentric distances but not at small distances, the slope of the CN gas production rate increase with the heliocentric distance must vary and we expect that the gas production rate ratios relative to CN will vary too.

Figure 4.26 shows the evolution of the OH, NH, $C_3$, $C_2$, and $A(0)f\rho$ to CN ratios as a function of the heliocentric distance. In this Figure, we can compare the trend of these ratios for both sets of Haser scalelengths. The trend of the OH to CN ratio is mostly similar for both data sets, even though the values computed using new scalelengths are lower at heliocentric distances smaller than 1.5 au. The OH to CN ratio pre-perihelion is now slightly increasing with the heliocentric distance (power-law slope=$0.55 \pm 0.09$) while there was no strong trend found using the original scalelengths. There is a strong shift of the NH to CN ratio since both NH and CN production rates change significantly using fitted scalelengths. In addition to a simple shift mostly caused by the shift of the NH values, the trend with the heliocentric distances changes too. As for the OH, the NH to CN ratio is now increasing with the heliocentric distance pre-perihelion (power-law slope=$1.02 \pm 0.11$). The changes in the $C_3$ to CN ratio are not strong and are caused by the changes in the CN production rates at small heliocentric distances. Using original scalelengths, the $C_3$ to CN ratio was slightly decreasing with the heliocentric distances while it is now slightly increasing (power-law slope=$0.36 \pm 0.04$). The $C_2$ to CN ratio is particularly interesting since earlier in this Chapter we noticed that the $C_2$ to CN ratio of the comets in our sample was decreasing with the heliocentric distance. As for most comets we observed, the $C_2$ to CN ratio of comet Lemmon computed using the original scalelengths

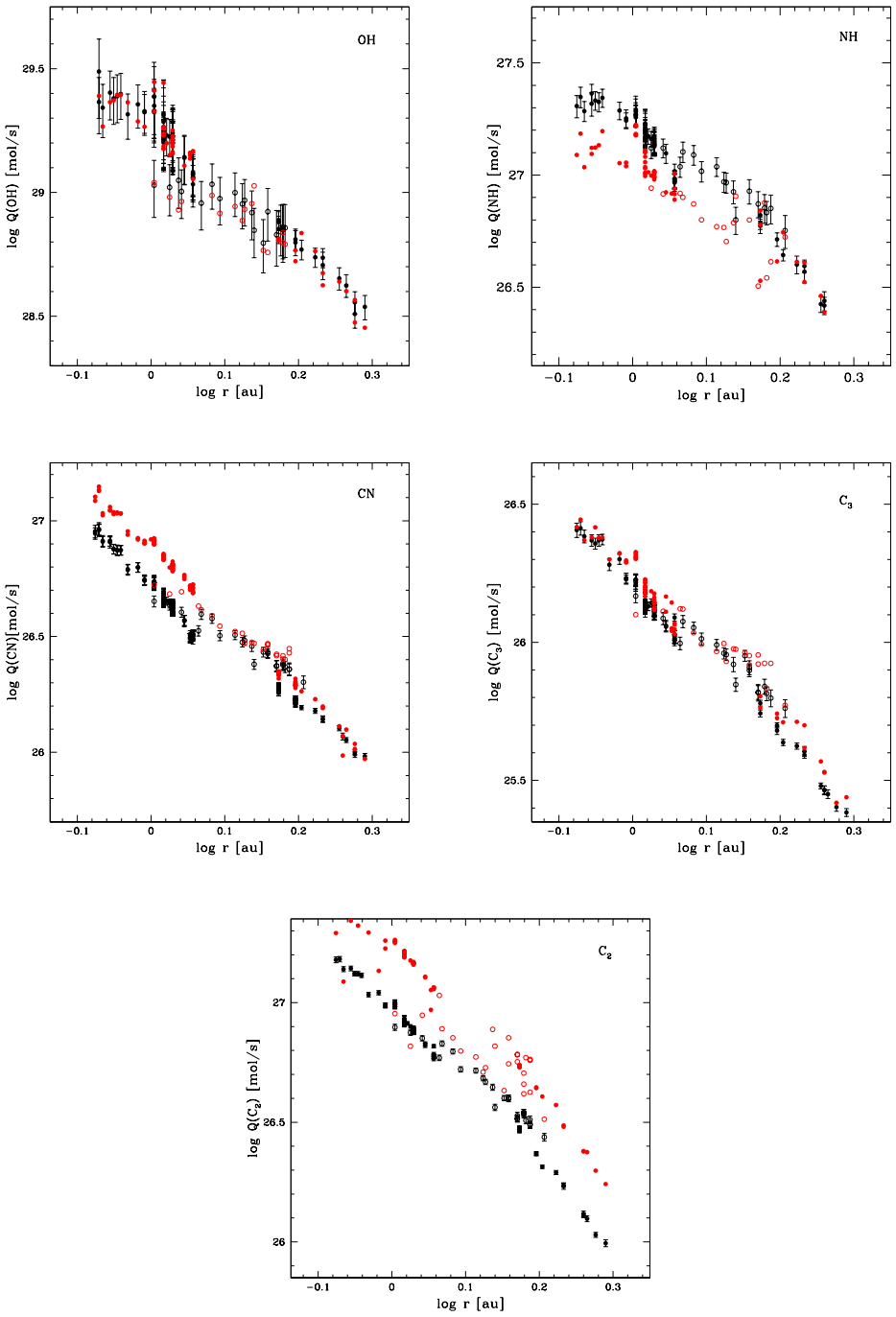


Figure 4.25: Comet C/2016 F6 (Lemmon) OH, NH, CN, $C_3$, and $C_2$ gas production rates computed using the original scalelengths given in Chapter 2 (black symbols) and scalelengths fitted to match the shape of the observed radial profiles (red symbols). Pre-perihelion values are represented using filled circles and post-perihelion values are represented using open circles.

was decreasing with the heliocentric distance. Using our new scalelengths, we do not see the trend of the $C_2$ to CN ratio any more. The $A(0)f\rho$ to CN ratios using both scalelength sets are consistent at heliocentric distances larger than 1.5 au. At smaller distances, the ratio computed using fitted scalelengths for the CN is lower than the ratio computed using original scalelengths. Except for the NH to CN and $C_2$ to CN ratios, the changes in the gas production rate ratio trends are not very important.

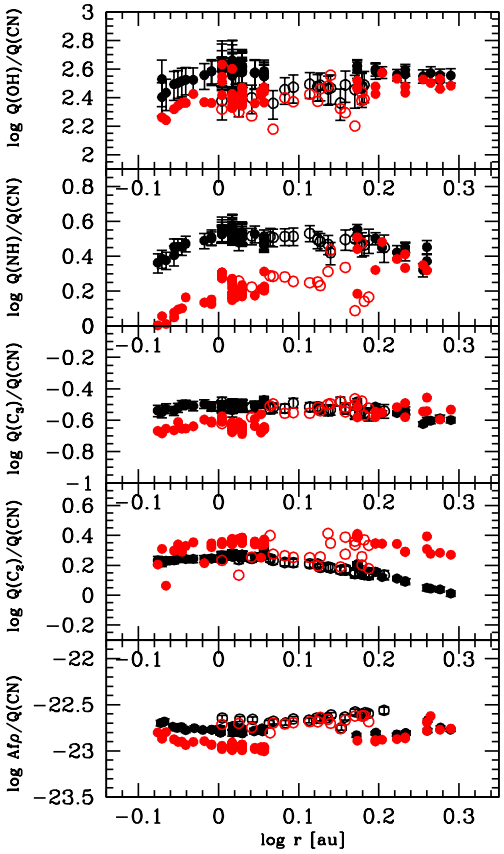


Figure 4.26: Ratio of comet C/2012 F6 (Lemmon) OH, NH, $C_3$, and $C_2$ production rates and the $A(0)f\rho$ to CN production rate as a function of the heliocentric distance. Black symbols are used for ratios computed using the original scalelengths while red symbols are used for ratios computed using scalelengths fitted on the observed profiles. Pre-perihelion values are represented using filled circles and post-perihelion values are represented using open circles.

In conclusion, we studied the effect of the scalelengths as parameters of the Haser model on the gas production rates derived using this model. First, we find that the scalelengths we derived by adjusting the Haser model on the observed profile are usually different from those we used in the rest of this work, especially for NH, CN, and $C_2$. The scaling of the scalelengths with the heliocentric distance is also different from the $r^2$ scaling for some species and seems to vary from one radical to another. The $C_3$ scalelengths are consistent with a $r^2$ scaling as a function

of the heliocentric distance for both parent and daughter scalelengths. The evolution of the CN scalelengths with the heliocentric distance is shallower and seems different for parent and daughter scalelengths. The discrepancy of the fitted scalelengths compared to the ones we first assumed induces changes of the production rates derived using these scalelengths. There is no strong changes for the OH and the $C_3$, but the changes are more significant for the other three species. They can be as high as a factor two in the case of the $C_2$, for example. The trends of the production rate ratios are also modified by the use of fitted scalelengths, especially the NH to CN and $C_2$ to CN ratios. The trend of decreasing $C_2$ to CN ratios with increasing heliocentric distances disappears if we use the fitted scalelengths. We observe a similar trend for the $C_2$ to CN ratio for our sample of comets. This trend could then be an artefact produced by the use of inadequate Haser scalelengths instead of a real change of the $C_2$ to CN ratio as the heliocentric distance changes. We also noticed that the evolution of the parent and daughter scalelengths with the heliocentric distance was different from the $r^2$ scaling we assumed for some species. This probably explains the symmetry of the $C_2$ to CN and NH to CN ratio about 1 au we observed earlier. In the light of the results we presented in this Section, we must be cautious while interpreting changes of gas production rate ratios with the heliocentric distance. A larger number of comets observed with the same instrument, and for which we can derive reliable Haser scalelengths would be needed to confirm the results we presented here and to attempt deriving new Haser scalelengths who better match the observed profiles of the gas species, as well as their evolution with the heliocentric distance.

## 4.4 The origin of species

In this Section, we gather the information we have about the link between parent and daughter species for several comets and try to draw general conclusions about species parentage in the coma of comets. In Chapter 3, we used different techniques to investigate the origin of species in the coma of comet C/2013 R1 (Lovejoy). First, we compared the daughter and parent production rates derived from optical and radio or infrared observations. We also compared the spatial distribution of species and the dust in the coma and we analysed the evolution of production rates with the heliocentric distance for various species and the dust to constrain the origin of species. We perform a similar analysis for several other comets, in order to better understand species parentage in the coma of comets in general.

First, we discuss the OH radical. Even though the parent of OH, water, has been known for a long time, we feel it is important to discuss it here, as it will allow us to point out the difficulty of comparing observations made with different instruments at different wavelengths. Measurements of the water production rate in the coma of a comet can be made at various wavelengths, by detecting the water directly, or some of its dissociation products. Water production rates can thus be estimated from the observations of the H Ly$\alpha$ emission, from the hydroxyl radical that can be observed at optical wavelengths or in the radio domain, and from the forbidden oxygen lines detected at optical wavelengths. Finally, the water molecule can be directly detected at infrared wavelengths. For some comets, such as comet C/2013 A1 (Siding

Spring), the water production rates we derived from the observations of the hydroxyl radical are in agreement with the measurements made at other wavelengths, like the observation of the hydroxyl radical at radio wavelengths (Crovisier et al., 2014). For some other comets, our measurements do not agree with those made at other wavelengths. It is the case of comet C/2014 Q2 (Lovejoy), for which observations of water in the infrared were performed by Biver et al. (2015). There are also comets for which we agree with the measurements made from infrared observations but not with the measurements made from the observation of the Ly$\alpha$ emission (Opitom et al., 2015a). Some examples of water and OH production rates derived from observations of 8 comets at different wavelengths are summarized in Table 4.4. The discrepancies between simultaneous measurements have several possible origins. First, the size of the field of view (FOV) varies depending on the type of observations. FOVs in the infrared are usually small (less than 1 $'$) while the FOV of the SWAN instrument onboard SOHO is much larger (resolution of 1° by 1°). Then, at some wavelengths, only water dissociation products can be observed, such as O, H, or OH. Models are needed to derive water production rates from the observations of these radicals. Depending on the kind of observations, the models used usually differ and this complicates the comparison of the water production rates derived. The parameters used in the models are also crucial. In the previous Section, we have seen that the scalelengths used in the Haser model have a strong influence on the gas production rates we derive. Finally, it is believed that water can also be released from icy grains in the coma instead of directly sublimating from the nucleus. If these icy grains sublimate in the coma, water can be released at larger nucleocentric distances. This could partially explain differences in water production rates measured from very small FOVs versus those measured with larger FOVs, as it was the case for comet C/2009 P1 (Garradd), see for example (Combi et al., 2013; Paganini et al., 2012; Bodewits et al., 2014). Icy grains in the coma of comets seem to be a rather common phenomenon. They have either been detected directly or have been invoked to account for the observations and the behaviour of several comets from our sample: 103P/Hartley 2 (Kelley et al., 2013), C/2009 P1 (Garradd) (Combi et al., 2013; Paganini et al., 2012; Bodewits et al., 2014), C/2013 A1 (Siding Spring) (Li et al., 2014; Bodewits et al., 2015), C/2013 R1 (Lovejoy) (Opitom et al., 2015b), and C/2012 S1 (Ison) (Knight et al., 2015). As a summary, the direct comparison of gas production rates derived from measurements at various wavelengths is very difficult, even in the case where the parentage of the species is well known.

We were able to measure CN production rates for all comets in our sample. For 7 comets, simultaneous infrared or radio measurements of the HCN, the most probable CN parent, production rates are available. These measurements are reported in Table 4.4. For comets 103P/ Hartley 2 (Dello Russo et al., 2011; Drahus et al., 2012), C/2009 P1 (Garradd) (Paganini et al., 2012; Villanueva et al., 2012), C/2012 F6 (Lemmon) (Paganini et al., 2014a; Biver et al., 2014), and C/2014 Q2 (Lovejoy) (Biver et al., 2015) the CN and HCN production rates measured at the same epochs are consistent with each other, see Table 4.4. For comet C/2013 R1 (Lovejoy), the HCN production rates measured are consistent with the CN production rates at some epochs but are too low at other epochs (Paganini et al., 2014b; Biver et al., 2014).

Table 4.4: Comparison of mother and daughter species production rates.

| Comet | Date | Q(OH)[a] | Q($H_2O$) | Q(CN) | Q(HCN) | Q($C_2$) | Q($C_2H_2$) |
|---|---|---|---|---|---|---|---|
| C/2013 R1 | 2013-Oct-21 | 2380±250 | | 6.38±0.19 | | 7.63±0.21 | |
| | 2013-Oct-22 | | 1850±190[b] | | 5.9±1.2[b] | | <9.2[b] |
| | 2013-Oct-24 | 2720±290 | 1530±250[b] | 6.96±0.21 | | 9.10±0.34 | |
| | 2013-Oct-25 | | 2320±330[b] | | 6.8±0.6[b] | | <1.5[b] |
| | 2013-Oct-26 | 2860±330 | | 7.20±0.31 | | 9.62±0.39 | |
| | 2013-Oct-27 | | 1560±250[b] | | 3.6±0.1[b] | | <2.2[b] |
| | 2013-Oct-29 | | 1450±410[b] | | 4.7±0.6 [b] | | <1.7[b] |
| | 2013-Nov-2 | | | 7.97±0.27 | | 12.20±0.30 | |
| | 2013-Nov-3 | 3010±350 | | | | | |
| | 2013-Nov-7 | | 3680±260[b] | | 8.7±0.7[b] | | <1.6[b] |
| | 2013-Nov-8/12 | | 5000 [d] | | 7.4±0.1 [d] | | |
| | 2013-Nov-13 | 3024±790 | | 10.10±0.70 | 6.0 [c] | 16.10±0.50 | |
| | 2013-Nov-16 | | | 12.90±1.20 | 6.1 [c] | 20.60±0.90 | |
| C/2013 A1 | 2014-Jul-9 | | 830±130[e] | | | | |
| | 2014-Jul-10 | 833±130 | | | | | |
| | 2014-Aug-19 | | 850±150[e] | | | | |
| | 2014-Aug-20 | 808±143 | | | | | |
| | 2014-Sep-18 | | 875±120[e] | | | | |
| | 2014-Sep-19 | 785±109 | | | | | |
| | 2014-Oct-5/8 | 1300±300[f] | | | | | |
| | 2014-Oct-6 | 879±112 | | | | | |
| | 2014-Oct-13 | 1040±139 | 1190±160[e] | | | | |
| | 2014-Oct-20 | | 960±160[e] | | | | |
| | 2014-Oct-23 | 832±137 | | | | | |
| C/2014 Q2 | 2015-Jan-13/16 | | 50000[g] | | | | |
| | 2015-Jan-13/14 | 24300±3660 | | | | | |
| | 2015-Jan-13/25 | | | | 49.5[g] | | |
| | 2015-Jan-17 | | | 49.9±1.5 | | | |
| | 2015-Jan-23/26 | | 60000[g] | | | | |
| C/2009 P1 | 2011-Jul-24 | 8530±1530 | | | | | |
| | 2011-Jul-25 | | 8500±600[h] | | | | |
| | 2011-Aug-15 | 8920±2170 | 11300±800[j] | | | | |
| | 2011-Sep-9 | | 8620±0.65[k] | | 31±3[k] | | <8.5[k] |
| | 2011-Sep-10 | 10500±1510 | | 31.2±1.3 | | 35.5±1.9 | |
| | 2011-Sep-17/21 | | 8400[h] | | 24.5±4.5[h] | | <11[h] |
| | 2011-Sep-19 | 10000±1800 | | | | 40.7±1.4 | |
| | 2011-Sep-21 | | 14100±3800[i] | | | | |
| | 2011-Oct-10 | 10200±1900 | 16400±9900[i] | | | | |
| | 2011-Oct-17 | | 27000±300[j] | | | | |
| | 2011-Oct-18 | 7720±1900 | | | | | |
| | 2011-Oct-21 | 8220±2500 | | | | | |
| | 2011-Oct-28 | | 19000±300[j] | | | | |
| 103P | 2010-Oct-30 | 626±150 | | | | | |
| | 2010-Oct-31 | | 638±12[l] | | | | |
| | 2010-Nov-04 | | | | 3.06±0.37 - 3.10±0.39[m] 0.73±0.16 - 1.71±0.34[n] | | 1.37±0.23 - 2.21±0.70[m] |
| | 2010-Nov-05 | | | 1.25±0.22 - 1.67±0.25 | | 1.83±0.26 - 2.54±0.28 | |
| | 2010-Nov-16 | | | 1.70±0.16 - 1.93±0.15 | 1.76±0.61[o] | 2.08±0.19 - 2.37±0.18 | 0.69±0.23[o] |
| C/2012 F6 | 2013-Feb-02 | | 19000±1000[p] | | 21±0.8[p] | | |
| | 2013-Feb-04 | | 19000±1000[p] | | | | |
| | 2013-Feb-06 | | 20700±100[q] | | | | |
| | 2013-Feb-07 | 11600±2200 | | 31.7±1.4 | | | |
| | 2013-Apr-06/08 | | | | 127±9[r] | | |
| | 2013-Jun-05 | 7200±240 | 20300±200[q] | | | | |
| | 2013-Jun-11 | | | 20.1±1.3 | | | |
| | 2013-Jun-20 | | 11000±1000[p] | | 23±2[p] | | |
| C/2012 S1 | 2013-Nov-16 | 5210±1780 | 31340±3940[t] | | | | |
| | 2013-Nov-19 | 3670±1580 | 24000±1300[s] | 56.1±5.3 | 71±6[s] | 81.5±3.4 | 72±11[s] |
| | 2013-Nov-20 | 10300±4800 | 41000±2200[s] | 188±19.8 | 106±33[s] | 208±10 | 76±51[s] |
| C/2010 G2 | 2012-Jan-09 | 1230±390 | 610±30[u] | 13.2±0.8 | 7.7±1.1[u] | | |
| | 2012-Jan-10 | | <710[u] | | 6.5±0.8[u] | | |

All production rates are expressed in units of $10^{25}$ mol/s. [b] Paganini et al. (2014b), [c] Agúndez et al. (2014) [d] Biver et al. (2014) [e] Bodewits et al. (2015) [f] Crovisier et al. (2014) [g] Biver et al. (2015) [h] Paganini et al. (2012) [i] McKay et al. (2015) [j] Combi et al. (2013) [k] Villanueva et al. (2012) [l] Combi et al. (2011a) [m] Dello Russo et al. (2011) [n] Drahus et al. (2012) [o] Mumma et al. (2011) [p] Paganini et al. (2014a) [q] Combi et al. (2014a) [r] Biver et al. (2014) [s] Dello Russo et al. (2016a) [t] Combi et al. (2014b) [u] Kawakita et al. (2014)

Kawakita et al. (2014) report HCN production rates for comet C/2012 G2 (Hill) about a factor two smaller than the CN production rates we measure from TRAPPIST observations. However, comet Hill underwent an outburst. Since the size of the FOV used for the CN measurements with TRAPPIST is larger than the infrared FOV, it reflects gas production rates at earlier times, closer to the outburst. This could partly account for the difference observed. Dello Russo et al. (2016a) measured HCN production rates for comet C/2012 S1 (Ison) on November 19 and 20, 2013. Our CN production rates agree well with the HCN production rates they report on November 19, but not on November 20. Comet Ison also underwent an outburst around that time and the gas production rates were highly variable. Dello Russo et al. (2016a) also report that the CN spatial distribution in the coma of comet Ison is consistent with an extended source as CN parent. In our images, the CN morphology is very similar to the dust morphology, reinforcing the hypothesis that CN might be produced from the disintegration of organic-rich grains in the coma of this comet. For the other comets mentioned above, as well as for comets C/2013 A1 (Siding Spring) and C/2013 US10 (Catalina), the CN morphology looks very different from the dust morphology. Another way to investigate the link between CN and HCN is to compare the lifetime of parent molecules we derived by fitting the Haser model on the observed profiles to the theoretical HCN lifetime. Fray et al. (2005) derived a CN parent scalelength from the HCN photodissociation using photodissociation rates from Huebner et al. (1992) and the model of Combi and Delsemme (1980). They obtain a value for the CN parent scalelength at 1 au of $5.82 \times 10^4$ km. At the same heliocentric distance, we derived an effective parent scalelength around $2.9 \times 10^4$ km by fitting a Haser model on comet C/2012 F6 (Lemmon) radial profiles. According to this, the HCN potodissociation alone is not sufficient to explain the spatial distribution of CN in the coma of comet Lemmon and another parent with smaller scalelength is needed. Comparison of effective Haser parent scalelengths derived for other comets are needed to confirm this, but Fray et al. (2005) find similar results combining scalelengths derived at various heliocentric distances for various comets. Rauer et al. (2003) derive CN parent scalelengths for comet Hale Bopp at large heliocentric distances ($r > 3$ au). At these distances, the scalelengths could be consistent with the potodissociation lifetime of HCN. In conclusion, the comparison of CN and HCN production rates, and the morphology of the coma are consistent with HCN being the main CN source for several comets. However, for some comets, like comet C/2012 S1 (Ison), another CN source is needed to explain the observations. Moreover, the spatial distribution of CN in the coma of comet C/2012 F6 (Lemmon) is not consistent with HCN being the only CN parent. Another source of CN with shorter photodissociation lifetime is then needed to explain our observations, even if the importance of this source might vary from one comet to another, and also as a function of the heliocentric distance of the comet.

We were able to compare the $C_2$ production rates derived from TRAPPIST measurements to almost simultaneous measurements of the $C_2H_2$ production rates for 5 comets, see Table 4.4. The $C_2$ production rate in the coma is significantly larger than the $C_2H_2$ production rate (or its upper limit) for comets C/2009 P1 (Garradd) (Paganini et al., 2012; Villanueva et al., 2012), C/2012 F6 (Lemmon) (Paganini et al., 2014a), and comet C/2013 R1 (Lovejoy) (Paganini

et al., 2014b). We have seen in the previous section that the $C_2$ production rates derived using fitted scalelengths are up to a factor two higher than the original production rates. This even reinforces the discrepancy between the $C_2$ and $C_2H_2$ production rates for comet C/2012 F6 (Lemmon). For comet 103P/Hartley 2, the $C_2$ production rates we measure from TRAPPIST observations are consistent with the $C_2H_2$ production rates reported by Dello Russo et al. (2011) but larger than those reported by Mumma et al. (2011). For comet C/2012 S1 (Ison), the $C_2$ abundance is in agreement with the $C_2H_2$ abundance reported by Dello Russo et al. (2016a) on November 19, 2013 but not on November 20. We then compared the $C_2$ morphology to the morphology of the other gas species and the dust. For comets 103P/Hartley 2, C/2013 R1 (Lovejoy), and C/2012 S1 (Ison), the $C_2$ morphology is similar to the dust morphology, while for comets C/2012 F6 (Lemmon), C/2013 US10 (Catalina), and C/2014 Q2 (Lovejoy) it is rather similar to the CN. For comet C/2013 R1 (Lovejoy), we also noticed that the evolution of the $C_2$ production rates with the heliocentric distance is closer to the dust than the CN. As a conclusion, for some comets (but maybe not for all), $C_2H_2$ is probably not the only source of $C_2$ in the coma. Since in some cases the $C_2$ behaviour seems correlated to the dust, a possible source of $C_2$ could be CHON grains in the coma, as already mentioned in the first Chapter of this work. Since the comets we analyse here seem to behave differently, the proportion of $C_2$ released from the photodissociation of $C_2H_2$ and from CHON grains could vary from one comet to another and with the heliocentric distance of the comet.

We were not able to investigate the origin of the other radicals in this work. As we have seen in the previous section, the NH scalelengths are poorly constrained, and the NH production rates we compute might not by reliable. It is then hazardous to compare the NH production rates we measure to $NH_2$ and $NH_3$ production rates. The parents of $C_3$ are not known yet, and the most plausible candidates are difficult to detect, as we mentioned in Section 1.6.3. As a consequence, we were not able to study the $C_3$ parentage in this work.

The results we present here are consistent with a recent study by Dello Russo et al. (2016b). They compiled infrared observations of 30 comets and compare the HCN, $C_2H_2$, and $C_2H_6$ abundances relative to water to the CN and $C_2$ abundances. They conclude that the mixing ratios of parent and daughter species are consistent for some comets but not for others. Some part of the CN and $C_2$ must then be produced from the dissociation of grains in the coma but the importance of this source may vary from one comet to another.

# 5 Conclusions and perspectives

Comets are among the oldest and best conserved remnants of the early stages of the solar system. Depending on the region of formation in the protosolar nebula, comets are now stored into two main reservoirs: the trans-Neptunian scattered disk, probable source of Jupiter Family Comets, and the Oort cloud, believed to be the source of Long Period Comets. By studying comets from different reservoirs, we can probe the environments in which they formed, and better understand their role in the solar system as suppliers of water and organics. When a comet approaches the Sun, the ices contained in the nucleus sublimate, and water and other complex molecules are released, along with dust, to form the coma that can be studied from the ground. The ices released directly from the nucleus are called parent species, and can be detected from the ground mostly in the IR or micro-wave domains. However, these observations usually require large telescopes and bright comets and, as a consequence, parent species have only been observed on a limited number of comets and over a limited range of heliocentric distances. A long-term monitoring of parent species production in the coma has only been performed for a few very bright comets, like C/1995 O1 (Hale-Bopp) and C/2012 S1 (Ison). At optical wavelengths, some of the photodissociation products of parent species by the solar UV light, called daughter species, can be observed. Observations of these radicals in the optical are easier to perform than the observation of parent species, even with smaller telescopes. A larger number of comets of different dynamical types can then be observed and intense monitoring of comets over a wide range of heliocentric distances can be performed to study the evolution of the activity and the composition of comets over the course of their orbit. Statistically significant samples can be gathered to study the properties of comets as a group, and try to establish links between these properties and the formation regions and processes of comets.

The 60-cm TRAPPIST telescope at La Silla observatory is equipped with a set of narrow band filters designed to isolate the emission of several daughter species visible in the optical spectrum of comets as well as several windows of the dust reflected continuum. Since 2010, we gathered more than 14,000 images of 30 bright comets of different dynamical types. We were able to derive the production rates of five radicals, OH, NH, CN, $C_3$, and $C_2$ by applying a coma model

on the images, and to estimate the dust production in the coma through the $Af\rho$ parameter. Using the ratio between several production rates, we estimated the coma composition of these comets. We also applied enhancement techniques on narrow band images to study the morphology of the coma. Our goal was to gather a large and high quality homogeneous sample of comets observed at various heliocentric distances to perform both an analysis of the properties, activity, and composition evolution of individual comets, and an analysis of our whole data set to study and compare the composition and activity evolution of a group of comets and try to make a link between properties of comets and their dynamical origin and place of formation. Furthermore, since we observed comets over wide ranges of heliocentric distances, we are able to disentangle between real composition differences between comets and changes of the composition with the heliocentric distance, for example.

In Chapter 3, we selected seven comets for which we have a large number of observations over a wide range of heliocentric distances, and who were particularly interesting because they were the target of a space mission, because we had simultaneous observations with other telescopes, or because they underwent outbursts, for example. We were able to measure, or at least constrain, the rotation period of three comets (103P/Hartley 2, C/2012 F6 (Lemmon), and C/2014 Q2 (Lovejoy)) by studying the periodic variation of their gas production rates or coma morphology over the course of several hours. This opens new perspectives to derive systematically the rotation period of comets using TRAPPIST in the future, thanks to the large amount of time available to observe comets and also to the new TRAPPIST-North telescope in Morocco, which will allow us to perform much longer series of observations on some targets. We developed a model to reproduce the shape of the radial profiles observed during the days following the outburst of comet C/2013 A1 (Siding Spring). This model provided a tool to determine the time at which the outburst started, the expansion velocity of the gas ejected during the outburst, the characteristic time-scale of the outburst, and the amount of gas released. This model should be tested in the future on the observations of other comets in outburst to gather informations about the characteristics of a large number of outbursts and better understand these phenomena. We followed the evolution of the activity, dust properties, coma composition, and morphology of these seven comets over wide ranges of heliocentric distances and on both sides of perihelion when feasible. We noticed differences among these comets but also a lot of similarities, especially concerning the behaviour of dynamically new comets, which motivated a global analysis of our sample of comets in order to define common trends and point out differences among individual comets, but also among dynamical types of comets.

In Chapter 4, we performed a global analysis of the ensemble properties of the comets of our data set and we present here the main conclusions that emerged from this analysis. We first noticed that the activity of dynamically new comets is increasing at a slower pace than the activity of other comets while they approach the Sun for the first time. The activity of dynamically new comets for which we have observations on both sides of perihelion is also highly asymmetric about perihelion. The decrease of the activity after the perihelion passage is much faster than the increase of the activity while the comet approaches the Sun. These

effects are attributed to the release of a halo of icy grains in the coma at large heliocentric distances pre-perihelion due to the outgassing of highly volatiles species. The grains sublimate while the comet approaches the Sun and strongly contribute to the outgassing in the coma. After the perihelion passage, the outgassing from nucleus ices dominates and the activity decreases fast.

Four comets of our sample underwent outbursts and for three of these comets, we have observations both before and after the outburst. Outbursts provide rare opportunities to probe the composition of the interior of the nucleus, especially when the outburst is caused by the fragmentation of the nucleus. Even when the origin of the outburst is not a fragmentation event, new layers of ice can be exposed and the comparison of the coma composition before and after the outburst provides clues about the heterogeneity of the ices within the nucleus. We did not observe changes of the coma composition related to the outburst of these comets, which would tend to indicate that the nucleus of these comets has a rather homogeneous ice composition. These conclusions could be confirmed in the future by the observation of individual fragments following splitting events. Such observations were performed for comet 73P/Schwassmann-Wachmann 3 and should be conducted again in the future for every suitable target. Since the separation between the fragments has to be sufficient so that they can be resolved and the fragments must be bright enough to be observed using ground-based observatories, suitable targets for these kind of observations are rare and efforts should be made to put together concerted observing campaigns with various instruments at different wavelengths to observe split comets.

We studied the evolution of the coma composition with the heliocentric distance for the ensemble of comets and noticed several trends. Even though individual comets behave in a different way, we do not see a trend in the evolution of the OH to CN ratio within 2 au. At larger distances, the ratio decreases, probably because the water outgassing becomes less efficient at those distances. The dust to gas ratio of our ensemble of comets (measured through the $Af\rho$ to OH and $Af\rho$ to CN ratios) increases with the heliocentric distance. The origin of this trend is still unclear, but it does not seem related to the perihelion distance of the comets, as postulated by previous studies. The strongest trend we observed was for the $C_2$ to CN ratio. At heliocentric distances larger than 1 au, the $C_2$ to CN ratio decreases with the heliocentric distance, by about a factor 2 between 1 and 2.5 au. Because of this trend, comets appear poorer in $C_2$ compared to CN at larger heliocentric distances. We believe this trend is not due to different release mechanisms for the $C_2$ and the CN but that it is instead an artefact of the parameters used in the Haser model. For this work, we used the same scalelengths as in A'Hearn et al. (1995), scaled as $r^2$ with the heliocentric distance. However, in Section 4.3.3, we showed that the radial profiles generated using these scalelengths are not always a good match to the observed profiles. We then adjusted scalelengths for all observations of comet C/2012 F6 (Lemmon) and found discrepancies between the scalelengths we adjusted and those we used for the rest of this work, especially for NH, CN, and $C_2$. As a consequence, the production rates derived using adjusted scalelengths are different from the original ones and are as much as a factor two higher for the $C_2$ for example. Using the new scalelengths,

the trend of decreasing $C_2$ to CN ratio with increasing heliocentric distances disappears for comet Lemmon. This indicates that the trend of $C_2$ to CN ratio we observed for the ensemble of comets might just be an artefact of the model parameters used to derive production rates.

We demonstrated the importance of the Haser scalelengths used to derive gas production rates and the artefacts they can introduce and we strongly believe that this should be investigated further in the future. The best way to derive more reliable production rates would be to simultaneously fit the parent and daughter scalelengths along with the gas production rate on the observed radial profile. However, this requires high quality radial profiles up to large nucleocentric distances. In practice, some instruments do not have fields of view wide enough, most spectrographs have too short slits, and photometers do not allow us to access to spatial information. Getting the edges of the radial profiles for weak comets would also be challenging and would reduce the number of Jupiter Family Comets observed. Fitting Haser scalelengths on every observation is the best solution to derive more reliable production rates but would strongly reduce the number of comets available in optical data bases. Another way to proceed would be to derive Haser scalelengths for a large number of comets over a wide range of heliocentric distances in order to define new reference scalelengths that could be used by most observers. With TRAPPIST, we are able to produce high quality radial profiles for a large number of comets, and we plan in the near future to compile scalelengths derived for all the comets in our data set for which we have good quality data to produce a new set of scalelengths better adapted to the observed radial profiles. We must also keep in mind the limitations of the Haser model. Several hypotheses underlying the model, such as the spherical symmetry, are not physically realistic. Because of this, we may never be able to reliably reproduce the spatial distribution of species in the coma of comets and more sophisticated models should probably be used in the future.

We compared the composition of the comets of our sample using several gas production rate ratios. Despite the effect of the Haser scalelengths we pointed out, comparing comets between each other still makes sense since we used the same scalelengths for all comets. This study revealed that most of the comets we observed are remarkably similar in terms of coma composition while we could have expected to see differences between comets of different dynamical types, maybe formed in different environments. Two of the comets we observed have particularly high dust to gas ratios as compared to other comets: C/2011 L4 (PanSTARRS) and to a lesser extent C/2012 K5 (Linear). The high dust to gas ratio of these comets is not correlated to the heliocentric distance at which they were observed or their perihelion distance and might then be a primordial characteristic of these comets. Comet 168P/Hergenrother is the most peculiar comet of our sample. It has a very low $C_2$ and $C_3$ abundance relatively to the other species compared to the other comets of the sample. Previous studies including large numbers of comets observed in the optical defined two main classes of comets: typical and carbon-chain depleted comets (A'Hearn et al., 1995; Fink, 2009; Langland-Shula and Smith, 2011; Cochran et al., 2012). Most of these studies found that between 25 and 30% of comets are carbon-chain depleted while we only observed one depleted comet out of the 30 comets of our sample. One might then wonder what explains the difference between our study and

previous ones. First, we observed comets over a wide range of heliocentric distances, which allowed us to discriminate between low $C_2$ to CN ratios due to the decrease of the ratio with the heliocentric distance and intrinsically low $C_2$ to CN ratios. Using an arbitrary limit to separate between carbon-chain depleted and typical comets could lead to classify comets observed at large heliocentric distances as depleted while they are not when observed closer to the Sun. Our sample also contains only eight Jupiter Family Comets. Both A'Hearn et al. (1995) and Cochran et al. (2012) noticed that the amount of depleted comets was larger among JFCS compared to other types of comets. If we had observed more JFCs, the proportion of depleted comets in our sample might have been different. We will then have to add more comets to our sample to confirm the origin of the discrepancy between our study and previous ones.

Finally, we investigated the origin of species in the coma. The issue of species parentage in the coma of comets is particularly important to correctly infer nucleus ice abundances from comets optical observations, and then to retrieve information about the composition of the early solar system at the time comets formed. Understanding the link between parent and daughter species is also essential to understand the origin of the difference between taxonomic classifications made from optical, infrared and radio observations. We found that HCN and $C_2H_2$ are probably not the only source of CN and $C_2$ in the coma of comets. Organic-rich grains in the coma have often been mentioned as a possible additional source. From our observations, the existence and the importance of secondary sources probably vary from a comet to another and are different for the CN and the $C_2$. Understanding the link between parent and daughter species in the coma of comets might then be more complicated than first thought and only more observations and investigations will help comprehend the complex issue of species parentage. Important clues can for example be obtained from a systematic comparison of maps of the spatial distribution of parent species in the coma for several comets at different distances from the Sun, combining new facilities such as the radio-interferometer ALMA or new large field of view optical integral field spectrographs.

The analysis of a sample of 30 comets observed with TRAPPIST allowed us to reveal several interesting trends among comets. It also proved the high quality of the sample provided by the TRAPPIST observations to study comets, compare their composition, and understand their evolution. However, several questions still remain unanswered. Some classes of comets are poorly represented in our sample, we lack of comets observed at very large and small heliocentric distances, and we only observed a few comets on both sides of perihelion. A larger sample is then needed to build further our knowledge and understanding of comets at optical wavelengths. A simple solution would be to gather the data from various studies performed at optical wavelengths into a single huge data set. However, this would introduce biases in the data base. Several studies use scalelengths different from the ones we used for this work. Given the impact of the scalelengths on the production rates this could introduce artificial variations of production rate ratios among comets. Most studies also use variable aperture sizes. Since Haser model profiles do not always match the observed profiles, the value of the production rate we derive depends on the aperture size used. In our work, we

use identical parameters for all observations and we compute gas production rates at a fixed physical distance in the coma for all comets. This provides a highly homogeneous sample from which we can study differences among comets. We keep observing comets with TRAPPIST and, with 5 to 10 new comets observed every year, our data base will grow fast. A twin of TRAPPIST has also been installed at the Oukaimeden observatory in Morocco. With this new telescope our data base will grow even faster, since we are now able to observe comets visible only from the Northern hemisphere but also to follow some comets over a wider range of distances. Particular attention should be paid to Jupiter Family Comets and Dynamically New Comets, since these are the types of comets the less represented in our sample. Jupiter Family Comets are usually weaker and may be difficult to observe with a 60-cm telescope. We could then complement TRAPPIST data by spectroscopic observations with larger telescopes such as the VLT/FORS 2 at ESO, even though our data set would no be homogeneous any more. However, two comets were observed simultaneously with TRAPPIST and the FORS 2 low resolution spectrograph of the VLT and we demonstrated that both the radial profiles and the gas production rates derived from these observations were in good agreement. Given that we use the same scalelengths and compute the gas production rates at the same physical distance in the coma, using FORS 2 observations to complement our data set should not introduce artificial differences between comets and that possibility should then be considered. In the next years, we will gather a much more significant sample to study the composition of comets at optical wavelengths and investigate cometary origin and evolution.

Huge advances have been made in the field of cometary science in the past few years. For the first time in history of comet research, the ESA Rosetta mission is following and studying in-situ a comet along a significant part of its orbit. Together with the lander Philae, the Rosetta spacecraft is collecting invaluable information, revealing in great details the nucleus and coma composition of comet 67P/Churyumov-Gerasimenko, as well as the complex shape of its nucleus, revolutionizing our understanding of these bodies. However, the Rosetta mission targeted only one comet and it is difficult to evaluate to which extent the findings of the Rosetta mission are representative of comets in general. Only a detailed study of a large number of comets from the ground will allow us to interpret these observations in the context of what has been learned from Rosetta and reach a more comprehensive understanding of some of the most primitive objects of our solar system.

# A Gas contamination in the broad band filters

In this work, we used narrow band filters (almost) free of gas contamination to study the properties and activity of the dust coma of comets. However, numerous professional and amateur astronomers also use broad band filters to observe comets. These filters are much less expensive than narrow band filters but their bandpasses are larger and contain some gas emission bands. The B filter bandpass encompasses the emissions of CN, $C_3$, and $C_2$ and the V filter is contaminated by the emission of $C_2$, for example. This appendix is thus aimed at assessing the gas contamination in these broad band filters and its consequence for the derivation of $Af\rho$ values. For this purpose, we decided to use the comet Ison data. This comet is an ideal target, since it has a low dust to gas ratio and its activity is rising fast as the comet approached perihelion.

Figure A.1 shows the evolution of comet Ison $Af\rho$ as a function of the distance to the Sun from Johnson cousins B, V, Rc, and Ic broad band filters, and from the BC narrow band filter. These $Af\rho$ have not been corrected from the phase angle effect. Figure A.1 shows the ratio of the $Af\rho$ from the broad band B, V, Rc, and Ic filters to the $Af\rho$ from the narrow band BC filter as a function of the heliocentric distance. At large distances, the values from broad band filters are slightly higher than those from narrow band filters. The B and V filters are already contaminated by the gas emission while the higher values for the Rc and Ic filters are probably due to a colour effect (we do not have regular observations with the narrow band RC filter for comet Ison). As the comet approaches the Sun and becomes more active, we see more important discrepancies between narrow band and broad band filters. The B and V filters show the strongest discrepancies with values derived from narrow band filters. At the time of the first outburst, the activity increases strongly and we see large differences between the filters. The V filter is the most contaminated by gas emissions and the $Af\rho$ values derived from this filter are about a factor five higher than those from narrow band filters. The B filter is slightly less contaminated but the difference with BC is still large. The Rc and Ic filters are less contaminated. The activity of the comet increases again during the second outburst, along with the discrepancy between broad band and narrow band filters. The $Af\rho$ from the Rc filter is 30% higher than the $Af\rho$ from the BC filter at the time of the second outburst.

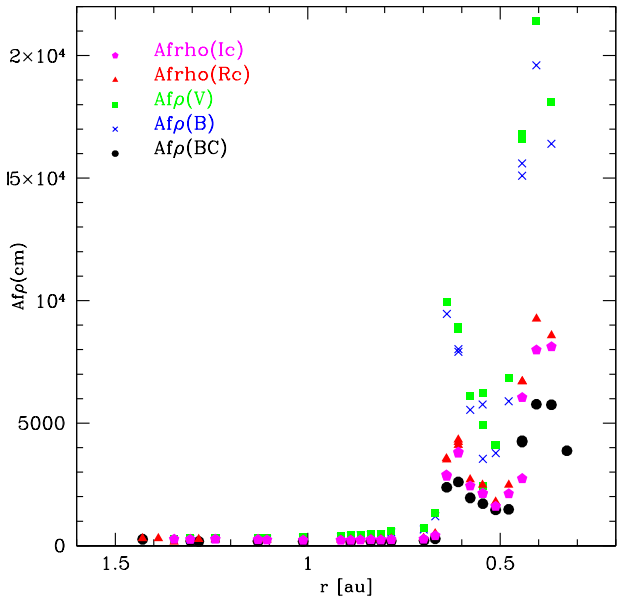


Figure A.1: Comet C/2012 S1 (Ison) $Af\rho$ as a function of the heliocentric distance $r$. The $Af\rho$ was measured from BC narrow band filter and from broad band B, V, Rc, and Ic filters.

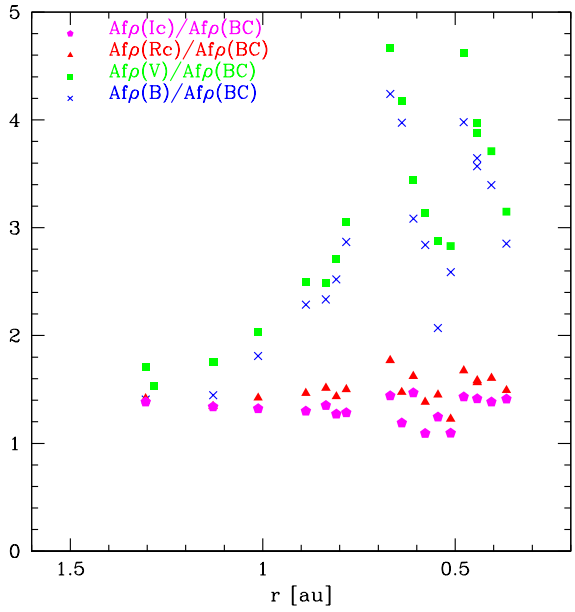


Figure A.2: Ratio of the $Af\rho$ from the broad band B, V, Rc and Ic filters to the $Af\rho$ from the narrow band BC filter as a function of the heliocentric distance $r$.

From the analysis of Fig. A.1, we see that the Ic filter is the less contaminated of the broad band filters while the B and V filters are heavily contaminated. If broad band filters are used to

observe very bright and active comets, we must be aware that these are contaminated by gas emissions and that the $Af\rho$ values we derive are not a good indicator of the dust activity. For fainter or less active comets, however, the broad band Rc and Ic filters are not significantly contaminated and provide good measurements of the $Af\rho$. This is for example the case for comet C/2013 A1 (Siding Spring). Figure 3.32 shows the evolution of comet Siding Spring $Af\rho$ as a function of the distance to the Sun for the narrow band RC and the broad band Rc filters. For this less active comet, the values of the $Af\rho$ from broad band and narrow band filters are in good agreement.

# B The Rosetta ground-based campaign with TRAPPIST

For the first time in history of comet research, the ESA Rosetta mission is following and studying in-situ a comet along a significant part of its orbit. The observations of the nucleus and the coma of comet 67P/Churyumov-Gerasimenko gathered by the orbiter and the lander Philae are currently revolutionizing our understanding of comet composition an structure. Alongside the space mission, a ground-based observing campaign is gathering observations of the comet with dozens of instruments from the ground[1]. These observations are crucial to provide a context to the mission. Measurements of the large-scale activity of the coma, impossible from the orbiter, will indeed provide the link between ground-based and space-borne observations of 67P, and with the comets that have been and will be observed in the future from the ground. Ground-based observations of the gas species allow us to connect the activity observed close to the nucleus to the large scale activity of the comet and to address the long-debated question of species parentage in the coma of comets. The evolution of the comet activity is monitored, trying for example to relate outbursts regularly observed with Rosetta (Tubiana et al., 2015) to large-scale changes observable from the ground. The large-scale gas morphology is also studied, in order to better understand the link between jets observed close to the nucleus (Sierks et al., 2015) and much larger features observed from the ground.

We have been part of the Rosetta ground-based campaign since 2014. We started to observe the comet with TRAPPIST as soon as it was bright enough. Our goal was to observe the comet regularly, so that we can monitor the long-term evolution of its activity and detect sudden changes like outbursts. We observed the comet once or twice a week from April 18, 2015 to June 7, 2016 with broad band filters. Exposure times are ranging from 120 to 240 s. Technical problems and bad weather prevented observations the days around perihelion. Between August 22, 2015 and September 12, 2015 we were able to detect the CN emission using narrow band filters. The $C_2$ was also detected but the SNR in the observations was small and the uncertainty on the $C_2$ is then high. We could not detect the OH, NH, or $C_3$ emissions. We also have observations of the comet with the narrow band continuum filters when it was bright enough.

[1] http:/www.rosettacampaign.net/

Figure B.1 shows the evolution of the $Af\rho$ measured in the broad band Rc filter, corrected from the phase angle effect. We demonstrated in the previous appendix that the broad band Rc filter is contaminated by gas emissions. However, comet 67P is weekly active as compared to comet Ison and the contamination in the Rc filter is negligible, so that we can safely use the observations in this filter to assess the dust production of the comet. The dust production is increasing smoothly as the comet approaches the Sun. It peaks 17 days after the perihelion passage, on August 30, 2015 and decreases after that date. Figure B.2 shows the evolution of the $Af\rho$ as a function of the heliocentric distance. We fitted power-law slopes to represent the evolution of the $Af\rho$ pre- ($-3.39\pm0.20$) and post-perihelion ($-3.28\pm0.04$). The slope is steeper before perihelion than after, which means that the comet dust production is increasing faster when the comet approaches the Sun than it is decreasing after the perihelion passage. The $Af\rho$ measured after perihelion are a factor two higher than those measured at the same distance before perihelion. Schleicher (2006) and Weiler et al. (2004) also observe an asymmetry around perihelion, a peak of the activity after perihelion, lower $Af\rho$ values and shallower slopes after the comet perihelion passage. Since this asymmetry is observed for various species and on different perihelion passages, they attribute this effect to seasonal variations. From the observations of the comet in the BC and RC narrow band filters, we are able to estimate the dust colour: $15\pm7$%/1000 Å. This is consistent with the value of $30\pm42$ %/1000 Å published by Schleicher (2006) and the value of $24\pm1$ %/1000 Å published by Storrs et al. (1992). Our values are also consistent with the values between 11 and 16%/1000 Å measured by Fornasier et al. (2015) and with the spectral slopes between 3.3 and 20%/1000 Å measured by Ciarniello et al. (2015) for the nucleus of comet 67P with the Rosetta spacecraft.

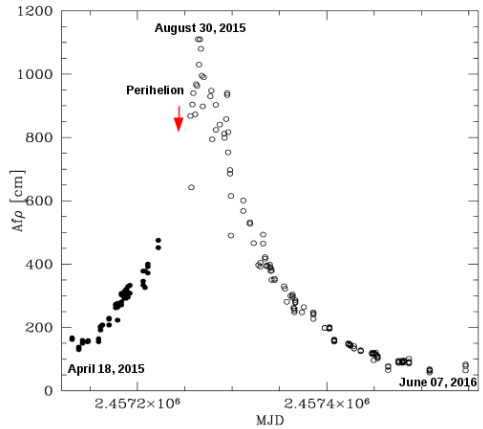


Figure B.1: Comet 67P/Churyumov-Gerasimenko $Af\rho$ evolution with time between April 18, 2015 and June 7, 2016. Pre-perihelion data are represented with full circles and post-perihelion data with open circles.

After the perihelion passage, we were able to detect the emissions of CN and $C_2$. Figure B.3 shows the evolution of the production rates as a function of time between August 22 (9 days after the perihelion passage) and September 12, 2015. The CN production rates first increase, peak on August 29 at the same time as the dust and then decrease. The peak could actually

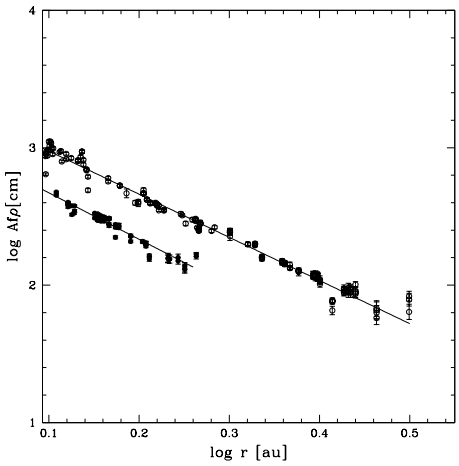


Figure B.2: Comet 67P/Churyumov-Gerasimenko $Af\rho$ evolution as a function of the perihelion distance along with fitted slopes. Pre-perihelion data are represented with full circles and post-perihelion data with open circles. The origin of the x-acis is perihelion.

happen later, since we do not have images in the CN filter between August 29 and September 11. The $C_2$ production rates have larger uncertainties because the comet was weak and the $C_2$ abundance low, which made the dust subtraction very complicated. Because of this, we do not see a clear peak for the $C_2$ production rates. Both our CN and $C_2$ production rates are consistent with those published by Schleicher (2006) for observations at two perihelion passages in 1982 and 1996. This indicates that the activity of the comet does not change from one passage to the next.

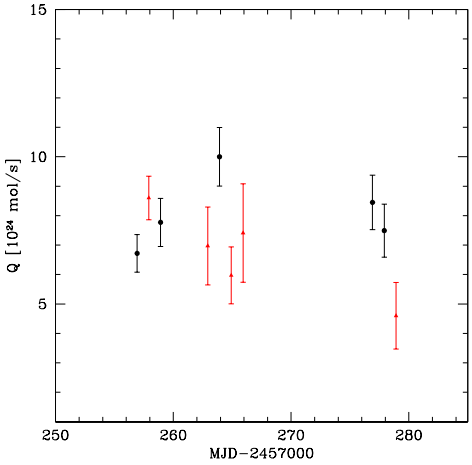


Figure B.3: Comet 67P/Churyumov-Gerasimenko CN and $C_2$ production rates evolution with time between August, 22 2015 and September 12, 2015.

We do not have images of the comet in the $C_2$ and CN filters performed the same day. However,

we wanted to estimate the $C_2$ to CN ratio of the comet to compare it to the other comets of our sample. We then computed ratios whenever we had $C_2$ and CN production rates measurements on consecutive days. These ratios are not as reliable as if the two species were observed almost simultaneously, since rotational variability as strong as a factor 3 was reported by Schleicher (2006). Figure B.4 shows the evolution of the $C_2$ to CN ratio of the comets in our sample as a function of the heliocentric distance, including 67P. The horizontal line represents the limit defined by A'Hearn et al. (1995) to separate the typical and carbon-chain depleted comets (modified by Schleicher (2006)). The $C_2$ to CN ratio of comet 67P is lower than the ratios of comets measured at the same heliocentric distance, but higher than the limit set by A'Hearn et al. (1995). However, we must remember the large rotational variability of the comet and the lack of simultaneous $C_2$ and CN measurements. Schleicher (2006) classify the comet as depleted while Lara et al. (2011) classify it as typical. According to Cochran et al. (1992); Schulz et al. (2004), the comet is slightly depleted. The rotational variability of the comet and the disparity of the results obtained by different authors make it difficult to classify comet 67P but from our data we can say that 67P has a $C_2$ to CN ratio lower than most comets observed at the same distance.

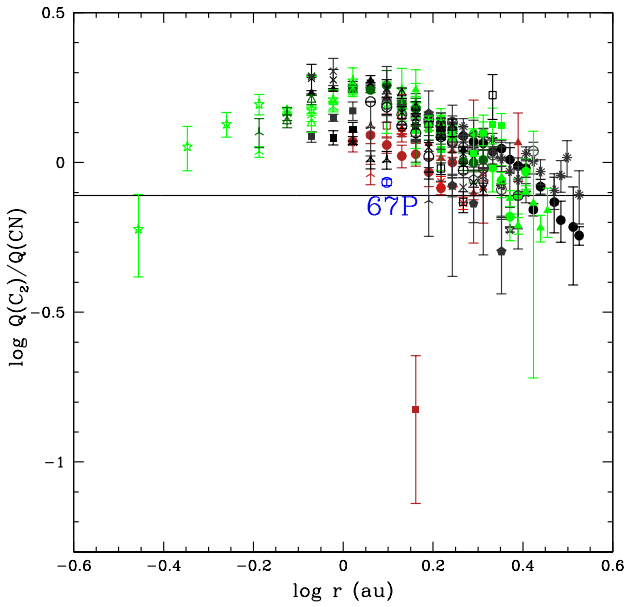


Figure B.4: Evolution of the logarithm of the $C_2$ to CN production rate ratio with the logarithm of the heliocentric distance. The black line represents the limit of $\log(Q(C_2)/Q(CN)) < -0.11$ from A'Hearn et al. (1995) to distinguish between typical and depleted comets, updated by Schleicher (2006). The large blue dot is comet 67/Churyumov-Gerasimenko.

The next step will be to compare these observations with the other observations made from the ground, and with the results from the Rosetta mission, trying to relate in-situ observations to the large-scale activity of the comet. Unfortunately for all ground-based observers, comet 67P

is not a very active comet and it was difficult to observe from the ground during this apparition. The only gas species that could be detected and monitored over a wide range of heliocentric distances is the CN. A long-term monitoring campaign of comet 67P was performed with the FORS 2 instrument of the VLT. Low-resolution spectra of the comet were obtained on a regular basis during almost two years, from 2014 to 2016. In 2014, no gas species could be detected in the spectra (Snodgrass et al., 2016). The CN emission was only detected shortly before perihelion but has been monitored over a much wider range of heliocentric distances after perihelion. The comparison of the dust and CN production rates evolution with the heliocentric distance, their asymmetries, and the implications of these observations will be the subject of a forthcoming paper. Other observations of the CN, and also HCN have been made from the ground, which will allow the comparison between various instruments and between the daughter species and its possible parent. Comparison with the observations of the gas and dust production measurements made in-situ by the Rosetta mission will also be very important to investigate the origin of the asymmetry, confirm the seasonal effect, and understand the production of gas species from the nucleus and the link between species.

# Bibliography


Agúndez, M., Biver, N., Santos-Sanz, P., Bockelée-Morvan, D., and Moreno, R. (2014). Molecular observations of comets C/2012 S1 (ISON) and C/2013 R1 (Lovejoy): HNC/HCN ratios and upper limits to $PH_3$. A&A, 564:L2.

A'Hearn, M. F. (1982). Spectrophotometry of comets at optical wavelengths. In Wilkening, L. L., editor, *IAU Colloq. 61: Comet Discoveries, Statistics, and Observational Selection*, pages 433–460.

A'Hearn, M. F., Belton, M. J. S., Crockett, C. J., Farnham, T. L., Feaga, L., Groussin, O., Mastrodemos, N., Owen, W. M., Sunshine, J. M., and Deep Impact Team (2005). Natural Outbursts by Comet Tempel 1. In *American Astronomical Society Meeting Abstracts*, volume 37 of *Bulletin of the American Astronomical Society*, page 1483.

A'Hearn, M. F., Belton, M. J. S., Delamere, W. A., Feaga, L. M., Hampton, D., Kissel, J., Klaasen, K. P., McFadden, L. A., Meech, K. J., Melosh, H. J., Schultz, P. H., Sunshine, J. M., Thomas, P. C., Veverka, J., Wellnitz, D. D., Yeomans, D. K., Besse, S., Bodewits, D., Bowling, T. J., Carcich, B. T., Collins, S. M., Farnham, T. L., Groussin, O., Hermalyn, B., Kelley, M. S., Kelley, M. S., Li, J.-Y., Lindler, D. J., Lisse, C. M., McLaughlin, S. A., Merlin, F., Protopapa, S., Richardson, J. E., and Williams, J. L. (2011). EPOXI at Comet Hartley 2. *Science*, 332:1396–.

A'Hearn, M. F., Birch, P. V., Feldman, P. D., and Millis, R. L. (1985). Comet Encke - Gas production and lightcurve. Icarus, 64:1–10.

A'Hearn, M. F., Campins, H., Schleicher, D. G., and Millis, R. L. (1989). The nucleus of Comet P/Tempel 2. ApJ, 347:1155–1166.

A'Hearn, M. F., Hoban, S., Birch, P. V., Bowers, C., Martin, R., and Klinglesmith, III, D. A. (1986). Cyanogen jets in comet Halley. Nature, 324:649–651.

A'Hearn, M. F., Millis, R. C., Schleicher, D. O., Osip, D. J., and Birch, P. V. (1995). The ensemble properties of comets: Results from narrowband photometry of 85 comets, 1976-1992. Icarus, 118:223–270.

A'Hearn, M. F., Schleicher, D. G., Millis, R. L., Feldman, P. D., and Thompson, D. T. (1980). Comet bowell 1980b. *The Astronomical Journal*, 89:579–591.

A'Hearn, M. F., Schleicher, D. G., Millis, R. L., Feldman, P. D., and Thompson, D. T. (1984). Comet Bowell 1980b. AJ, 89:579–591.

Altwegg, K., Balsiger, H., Bar-Nun, A., Berthelier, J. J., Bieler, A., Bochsler, P., Briois, C., Calmonte, U., Combi, M., De Keyser, J., Eberhardt, P., Fiethe, B., Fuselier, S., Gasc, S., Gombosi, T. I., Hansen, K. C., Hässig, M., Jäckel, A., Kopp, E., Korth, A., LeRoy, L., Mall, U., Marty, B., Mousis, O., Neefs, E., Owen, T., Rème, H., Rubin, M., Sémon, T., Tzou, C.-Y., Waite, H., and Wurz, P. (2015). 67P/Churyumov-Gerasimenko, a Jupiter family comet with a high D/H ratio. *Science*, 347(27):1261952.

Asphaug, E. and Benz, W. (1996). Size, Density, and Structure of Comet Shoemaker-Levy 9 Inferred from the Physics of Tidal Breakup. Icarus, 121:225–248.

Baum, W. A. and Kreidl, T. J. (1986). Volatiles in cometary grains. In Lagerkvist, C.-I., Rickman, H., Lindblad, B. A., and Lundstedt, H., editors, *Asteroids, Comets, Meteors II*, pages 397–402.

Baum, W. A., Kreidl, T. J., and Schleicher, D. G. (1992). Cometary grains. AJ, 104:1216–1225.

Belton, M. J. S., Julian, W. H., Anderson, A. J., and Mueller, B. E. A. (1991). The spin state and homogeneity of Comet Halley's nucleus. Icarus, 93:183–193.

Belton, M. J. S. and Melosh, J. (2009). Fluidization and multiphase transport of particulate cometary material as an explanation of the smooth terrains and repetitive outbursts on 9P/Tempel 1. Icarus, 200:280–291.

Belton, M. J. S., Samarasinha, N. H., Fernández, Y. R., and Meech, K. J. (2005). The excited spin state of Comet 2P/Encke. Icarus, 175:181–193.

Belton, M. J. S., Thomas, P., Li, J.-Y., Williams, J., Carcich, B., A'Hearn, M. F., McLaughlin, S., Farnham, T., McFadden, L., Lisse, C. M., Collins, S., Besse, S., Klaasen, K., Sunshine, J., Meech, K. J., and Lindler, D. (2013). The complex spin state of 103P/Hartley 2: Kinematics and orientation in space. Icarus, 222:595–609.

Belton, M. J. S., Thomas, P., Veverka, J., Schultz, P., A'Hearn, M. F., Feaga, L., Farnham, T., Groussin, O., Li, J.-Y., Lisse, C., McFadden, L., Sunshine, J., Meech, K. J., Delamere, W. A., and Kissel, J. (2007). The internal structure of Jupiter family cometary nuclei from Deep Impact observations: The "talps" or "layered pile" model. Icarus, 191:573–585.

Benna, M., Mahaffy, P. R., Grebowsky, J. M., Plane, J. M. C., Yelle, R. V., and Jakosky, B. M. (2015). Metallic ions in the upper atmosphere of Mars from the passage of comet C/2013 A1 (Siding Spring). Geophys. Res. Lett., 42:4670–4675.

Bessel, M. S. (1990). Ubvri passbands. *Publications of the Astronomical Society of the Pacific*, 102:1181–1199.

Bieler, A., Altwegg, K., Balsiger, H., Bar-Nun, A., Berthelier, J.-J., Bochsler, P., Briois, C., Calmonte, U., Combi, M., de Keyser, J., van Dishoeck, E. F., Fiethe, B., Fuselier, S. A., Gasc, S.,

Gombosi, T. I., Hansen, K. C., Hässig, M., Jäckel, A., Kopp, E., Korth, A., Le Roy, L., Mall, U., Maggiolo, R., Marty, B., Mousis, O., Owen, T., Rème, H., Rubin, M., Sémon, T., Tzou, C.-Y., Waite, J. H., Walsh, C., and Wurz, P. (2015). Abundant molecular oxygen in the coma of comet 67P/Churyumov-Gerasimenko. Nature, 526:678–681.

Biver, N., Bockelée-Morvan, D., Colom, P., Crovisier, J., Germain, B., Lellouch, E., Davies, J. K., Dent, W. R. F., Moreno, R., Paubert, G., Wink, J., Despois, D., Lis, D. C., Mehringer, D., Benford, D., Gardner, M., Phillips, T. G., Gunnarsson, M., Rickman, H., Winnberg, A., Bergman, P., Johansson, L. E. B., and Rauer, H. (1997). Long-term Evolution of the Outgassing of Comet Hale-Bopp From Radio Observations. *Earth Moon and Planets*, 78:5–11.

Biver, N., Bockelée-Morvan, D., Crovisier, J., Davies, J. K., Matthews, H. E., Wink, J. E., Rauer, H., Colom, P., Dent, W. R. F., Despois, D., Moreno, R., Paubert, G., Jewitt, D., and Senay, M. (1999). Spectroscopic Monitoring of Comet C/1996 B2 (Hyakutake) with the JCMT and IRAM Radio Telescopes. AJ, 118:1850–1872.

Biver, N., Bockelée-Morvan, D., Debout, V., Crovisier, J., Boissier, J., Lis, D. C., Dello Russo, N., Moreno, R., Colom, P., Paubert, G., Vervack, R., and Weaver, H. A. (2014). Complex organic molecules in comets C/2012 F6 (Lemmon) and C/2013 R1 (Lovejoy): detection of ethylene glycol and formamide. *ArXiv e-prints*.

Biver, N., Bockelée-Morvan, D., Moreno, R., Crovisier, J., Colom, P., Lis, D. C., Sandqvist, A., Boissier, J., Despois, D., and Milam, S. N. (2015). Ethyl alcohol and sugar in comet C/2014 Q2 (Lovejoy). *Science Advances*, 1:1500863.

Biver, N., Moreno, R., Bockelée-Morvan, D., Sandqvist, A., Colom, P., Crovisier, J., Lis, D. C., Boissier, J., Debout, V., Paubert, G., Milam, S., Hjalmarson, A., Lundin, S., Karlsson, T., Battelino, M., Frisk, U., Murtagh, D., and Odin Team (2016). Isotopic ratios of H, C, N, O, and S in comets C/2012 F6 (Lemmon) and C/2014 Q2 (Lovejoy). A&A, 589:A78.

Bockelée-Morvan, D., Biver, N., Swinyard, B., de Val-Borro, M., Crovisier, J., Hartogh, P., Lis, D. C., Moreno, R., Szutowicz, S., Lellouch, E., Emprechtinger, M., Blake, G. A., Courtin, R., Jarchow, C., Kidger, M., Küppers, M., Rengel, M., Davis, G. R., Fulton, T., Naylor, D., Sidher, S., and Walker, H. (2012). Herschel measurements of the D/H and $^{16}O/^{18}O$ ratios in water in the Oort-cloud comet C/2009 P1 (Garradd). A&A, 544:L15.

Bockelee-Morvan, D. and Crovisier, J. (1985). Possible parents for the cometary CN radical - Photochemistry and excitation conditions. A&A, 151:90–100.

Bockelee-Morvan, D., Crovisier, J., and Gerard, E. (1990). Retrieving the coma gas expansion velocity in P/Halley, Wilson (1987 VII) and several other comets from the 18-cm OH line shapes. A&A, 238:382–400.

Bockelée-Morvan, D., Crovisier, J., Mumma, M. J., and Weaver, H. A. (2004). *The composition of cometary volatiles*, pages 391–423.

Bockelée-Morvan, D., Lis, D. C., Wink, J. E., Despois, D., Crovisier, J., Bachiller, R., Benford, D. J., Biver, N., Colom, P., Davies, J. K., Gérard, E., Germain, B., Houde, M., Mehringer, D., Moreno, R., Paubert, G., Phillips, T. G., and Rauer, H. (2000). New molecules found in comet C/1995 O1 (Hale-Bopp). Investigating the link between cometary and interstellar material. A&A, 353:1101–1114.

Bodewits, D., Farnham, T. L., A'Hearn, M. F., Feaga, L. M., McKay, A., Schleicher, D. G., and Sunshine, J. M. (2014). The Evolving Activity of the Dynamically Young Comet C/2009 P1 (Garradd). ApJ, 786:48.

Bodewits, D., Kelley, M. S. P., Li, J.-Y., Farnham, T. L., and A'Hearn, M. F. (2015). The Pre-perihelion Activity of Dynamically New Comet C/2013 A1 (Siding Spring) and Its Close Encounter with Mars. ApJ, 802:L6.

Boehnhardt, H. (2000). Comet Splitting - Observations and Model Scenarios. *Earth Moon and Planets*, 89:91–115.

Boissier, J., Bockelée-Morvan, D., Groussin, O., Lamy, P., Biver, N., Crovisier, J., Colom, P., Moreno, R., Jorda, L., and Piétu, V. (2013). Millimetre continuum observations of comet C/2009 P1 (Garradd). A&A, 557:A88.

Bonev, B. P., Mumma, M. J., Radeva, Y. L., DiSanti, M. A., Gibb, E. L., and Villanueva, G. L. (2008). The Peculiar Volatile Composition of Comet 8P/Tuttle: A Contact Binary of Chemically Distinct Cometesimals? ApJ, 680:L61–L64.

Braga-Ribas, F., Sicardy, B., Ortiz, J. L., Snodgrass, C., Roques, F., Vieira-Martins, R., Camargo, J. I. B., Assafin, M., Duffard, R., Jehin, E., Pollock, J., Leiva, R., Emilio, M., Machado, D. I., Colazo, C., Lellouch, E., Skottfelt, J., Gillon, M., Ligier, N., Maquet, L., Benedetti-Rossi, G., Gomes, A. R., Kervella, P., Monteiro, H., Sfair, R., El Moutamid, M., Tancredi, G., Spagnotto, J., Maury, A., Morales, N., Gil-Hutton, R., Roland, S., Ceretta, A., Gu, S.-H., Wang, X.-B., Harpsøe, K., Rabus, M., Manfroid, J., Opitom, C., Vanzi, L., Mehret, L., Lorenzini, L., Schneiter, E. M., Melia, R., Lecacheux, J., Colas, F., Vachier, F., Widemann, T., Almenares, L., Sandness, R. G., Char, F., Perez, V., Lemos, P., Martinez, N., Jørgensen, U. G., Dominik, M., Roig, F., Reichart, D. E., Lacluyze, A. P., Haislip, J. B., Ivarsen, K. M., Moore, J. P., Frank, N. R., and Lambas, D. G. (2014). A ring system detected around the Centaur (10199) Chariklo. Nature, 508:72–75.

Britt, D. T., Consolmagno, G. J., and Merline, W. J. (2006). Small Body Density and Porosity: New Data, New Insights. In Mackwell, S. and Stansbery, E., editors, *37th Annual Lunar and Planetary Science Conference*, volume 37 of *Lunar and Planetary Inst. Technical Report*.

Brown, M. E. (2001). The Inclination Distribution of the Kuiper Belt. AJ, 121:2804–2814.

Bus, S. J., A'Hearn, M. F., Schleicher, D. G., and Bowell, E. (1991). Detection of CN emission from (2060) Chiron. *Science*, 251:774–777.

Buzzi, L., Muler, G., Kidger, M., Henriquez Santana, J. A., Naves, R., Campas, M., Kugel, F., and Rinner, C. (2007). Comet 17P/Holmes. IAU Circ., 8886.

Ciarniello, M., Capaccioni, F., Filacchione, G., Raponi, A., Tosi, F., De Sanctis, M. C., Capria, M. T., Erard, S., Bockelee-Morvan, D., Leyrat, C., Arnold, G., Barucci, A., Beck, P., Bellucci, G., Fornasier, S., Longobardo, A., Mottola, S., Palomba, E., Quirico, E., and Schmitt, B. (2015). Photometric properties of comet 67P/Churyumov-Gerasimenko from VIRTIS-M onboard Rosetta. A&A, 583:A31.

Cochran, A. L. (1985). A re-evaluation of the Haser model scale lengths for comets. AJ, 90:2609–2614.

Cochran, A. L. (1987). Another look at abundance correlations among comets. AJ, 93:231–238.

Cochran, A. L., Barker, E. S., and Gray, C. L. (2012). Thirty years of cometary spectroscopy from McDonald Observatory. Icarus, 218:144–168.

Cochran, A. L., Barker, E. S., Ramseyer, T. F., and Storrs, A. D. (1992). The McDonald Observatory Faint Comet Survey - Gas production in 17 comets. Icarus, 98:151–162.

Cochran, A. L., Levasseur-Regourd, A.-C., Cordiner, M., Hadamcik, E., Lasue, J., Gicquel, A., Schleicher, D. G., Charnley, S. B., Mumma, M. J., Paganini, L., Bockelée-Morvan, D., Biver, N., and Kuan, Y.-J. (2015). The Composition of Comets. Space Sci. Rev., 197:9–46.

Cochran, A. L. and Schleicher, D. G. (1993). Observational Constraints on the Lifetime of Cometary H $_2$O. Icarus, 105:235–253.

Combi, M. R., Bertaux, J.-L., Quémerais, E., Ferron, S., and Mäkinen, J. T. T. (2011a). Water Production by Comet 103P/Hartley 2 Observed with the SWAN Instrument on the SOHO Spacecraft. ApJ, 734:L6.

Combi, M. R., Bertaux, J.-L., Quémerais, E., Ferron, S., Mäkinen, J. T. T., and Aptekar, G. (2014a). Water Production in Comets C/2011 l4 (PanSTARRS) and C/2012 F6 (Lemmon) from observations with SOHO/SWAN. AJ, 147:126.

Combi, M. R., Boyd, Z., Lee, Y., Patel, T. S., Bertaux, J.-L., Quémerais, E., and Mäkinen, J. T. T. (2011b). SOHO/SWAN observations of comets with small perihelia: C/2002 V1 (NEAT), C/2002 X5 (Kudo-Fujikawa), 2006 P1 (McNaught) and 96P/Machholz 1. Icarus, 216:449–461.

Combi, M. R. and Delsemme, A. H. (1980). Neutral cometary atmospheres. I - an average random walk model for photodissociation in comets. ApJ, 237:633–640.

Combi, M. R. and Fink, U. (1997). A Critical Study of Molecular Photodissociation and CHON Grain Sources for Cometary $C_2$. ApJ, 484:879–890.

Combi, M. R., Fougere, N., Mäkinen, J. T. T., Bertaux, J.-L., Quémerais, E., and Ferron, S. (2014b). Unusual Water Production Activity of Comet C/2012 S1 (ISON): Outbursts and Continuous Fragmentation. ApJ, 788:L7.

Combi, M. R., Harris, W. M., and Smyth, W. H. (2004). *Gas dynamics and kinetics in the cometary coma: theory and observations*, pages 523–552.

Combi, M. R., Mäkinen, J. T. T., Bertaux, J.-L., Lee, Y., and Quémerais, E. (2009). Water Production in Comets 2001 Q4 (NEAT) and 2002 T7 (LINEAR) Determined from SOHO/SWAN Observations. AJ, 137:4734–4743.

Combi, M. R., Mäkinen, J. T. T., Bertaux, J.-L., Quémerais, E., Ferron, S., and Fougere, N. (2013). Water production rate of Comet C/2009 P1 (Garradd) throughout the 2011-2012 apparition: Evidence for an icy grain halo. Icarus, 225:740–748.

Cordiner, M. A., Remijan, A. J., Boissier, J., Milam, S. N., Mumma, M. J., Charnley, S. B., Paganini, L., Villanueva, G., Bockelée-Morvan, D., Kuan, Y.-J., Chuang, Y.-L., Lis, D. C., Biver, N., Crovisier, J., Minniti, D., and Coulson, I. M. (2014). Mapping the Release of Volatiles in the Inner Comae of Comets C/2012 F6 (Lemmon) and C/2012 S1 (ISON) Using the Atacama Large Millimeter/Submillimeter Array. ApJ, 792:L2.

Crovisier, J. (1997). Infrared Observations Of Volatile Molecules In Comet Hale-Bopp. *Earth Moon and Planets*, 79:125–143.

Crovisier, J., Biver, N., Bockelée-Morvan, D., Boissier, J., Colom, P., and Lis, D. C. (2009). The Chemical Diversity of Comets: Synergies Between Space Exploration and Ground-based Radio Observations. *Earth Moon and Planets*, 105:267–272.

Crovisier, J., Bockelée-Morvan, D., Colom, P., Biver, N., Despois, D., Lis, D. C., and Teamtarget-of-opportunity radio observations of comets (2004). The composition of ices in comet C/1995 O1 (Hale-Bopp) from radio spectroscopy. Further results and upper limits on undetected species. A&A, 418:1141–1157.

Crovisier, J., Colom, P., Biver, N., Bockelée-Morvan, D., and Boissier, J. (2013). Observations of the 18-cm OH lines of Comet 103P/Hartley 2 at Nançay in support to the EPOXI and Herschel missions. Icarus, 222:679–683.

Crovisier, J., Colom, P., Biver, N., Bockelee-Morvan, D., Nakano, S., Mattiazzo, M., Amorim, A., Goiato, M., Camilleri, P., and Yoshimoto, K. (2014). Comet C/2013 A1 (Siding Spring). *Central Bureau Electronic Telegrams*, 4001.

Crovisier, J., Colom, P., Gérard, E., Bockelée-Morvan, D., and Bourgois, G. (2002). Observations at Nançay of the OH 18-cm lines in comets. The data base. Observations made from 1982 to 1999. A&A, 393:1053–1064.

Crovisier, J. and Encrenaz, T., editors (2000). *Comet science : the study of remnants from the birth of the solar system*.

Dello Russo, N., Vervack, R. J., Kawakita, H., Cochran, A., McKay, A. J., Harris, W. M., Weaver, H. A., Lisse, C. M., DiSanti, M. A., Kobayashi, H., Biver, N., Bockelée-Morvan, D., Crovisier, J., Opitom, C., and Jehin, E. (2016a). The compositional evolution of C/2012 S1 (ISON) from ground-based high-resolution infrared spectroscopy as part of a worldwide observing campaign. Icarus, 266:152–172.

Dello Russo, N., Vervack, R. J., Kawakita, H., Kobayashi, H., Weaver, H. A., Harris, W. M., Cochran, A., Biver, N., Bockelée-Morvan, D., and Crovisier, J. (2014). The volatile composition of 81P/Wild 2 from ground-based high-resolution infrared spectroscopy. Icarus, 238:125–136.

Dello Russo, N., Vervack, R. J., Weaver, H. A., Biver, N., Bockelée-Morvan, D., Crovisier, J., and Lisse, C. M. (2007). Compositional homogeneity in the fragmented comet 73P/Schwassmann-Wachmann 3. Nature, 448:172–175.

Dello Russo, N., Vervack, Jr., R. J., Lisse, C. M., Weaver, H. A., Kawakita, H., Kobayashi, H., Cochran, A. L., Harris, W. M., McKay, A. J., Biver, N., Bockelée-Morvan, D., and Crovisier, J. (2011). The Volatile Composition and Activity of Comet 103P/Hartley 2 During the EPOXI Closest Approach. ApJ, 734:L8.

Dello Russo, N., Vervack, Jr., R. J., Weaver, H. A., Kawakita, H., Kobayashi, H., Biver, N., Bockelée-Morvan, D., and Crovisier, J. (2009). The Parent Volatile Composition of 6p/d'Arrest and a Chemical Comparison of Jupiter-Family Comets Measured at Infrared Wavelengths. ApJ, 703:187–197.

Dello Russo, R. J., Kawakita, H., Vervack, R. J., and Weaver, H. A. (2016b). Emerging trends and a comet taxonomy based on the volatile chemistry measured in thirty comets with high-resolution infrared spectroscopy between 1997 and 2013. Icarus.

DiSanti, M. A., Villanueva, G. L., Paganini, L., Bonev, B. P., Keane, J. V., Meech, K. J., and Mumma, M. J. (2014). Pre- and post-perihelion observations of C/2009 P1 (Garradd): Evidence for an oxygen-rich heritage? Icarus, 228:167–180.

Divine, N. (1981). A simple radiation model of cometary dust for P/Halley. In Battrick, B. and Swallow, E., editors, *The Comet Halley. Dust and Gas Environment*, volume 174 of *ESA Special Publication*, pages 47–53.

Dones, L., Brasser, R., Kaib, N., and Rickman, H. (2015). Origin and Evolution of the Cometary Reservoirs. Space Sci. Rev., 197:191–269.

Dones, L., Weissman, P. R., Levison, H. F., and Duncan, M. J. (2004). *Oort cloud formation and dynamics*, pages 153–174.

Donn, B., Daniels, P. A., and Hughes, D. W. (1985). On the Structure of the Cometary Nucleus. In *Bulletin of the American Astronomical Society*, volume 17 of *Bulletin of the American Astronomical Society*, page 520.

Drahus, M., Jewitt, D., Guilbert-Lepoutre, A., Waniak, W., and Sievers, A. (2012). The Sources of HCN and $CH_3OH$ and the Rotational Temperature in Comet 103P/Hartley 2 from Time-resolved Millimeter Spectroscopy. ApJ, 756:80.

Eddington, A. S. (1910). c 1908 (Morehouse), the envelopes of. MNRAS, 70:442–458.

Edgeworth, K. E. (1949). The origin and evolution of the Solar System. MNRAS, 109:600–609.

Fanale, F. P. and Salvail, J. R. (1984). An idealized short-period comet model - Surface insolation, H2O flux, dust flux, and mantle evolution. Icarus, 60:476–511.

Farnham, T., Bodewits, D., A'Hearn, M. F., and Feaga, L. M. (2012). Deep Impact MRI Observations Of Comet Garradd (C/2009 P1). In *AAS/Division for Planetary Sciences Meeting Abstracts*, volume 44 of *AAS/Division for Planetary Sciences Meeting Abstracts*, page 506.05.

Farnham, T., Schleicher, D., and A'Hearn, M. (2000). The **HB** narrowband comet filters : Standard stars and calibrations. *Icarus*, 147:180.

Farnham, T. L. and Schleicher, D. G. (2005). Physical and compositional studies of Comet 81P/Wild 2 at multiple apparitions. Icarus, 173:533–558.

Feaga, L. M., A'Hearn, M. F., Farnham, T. L., Bodewits, D., Sunshine, J. M., Gersch, A. M., Protopapa, S., Yang, B., Drahus, M., and Schleicher, D. G. (2014). Uncorrelated Volatile Behavior during the 2011 Apparition of Comet C/2009 P1 Garradd. AJ, 147:24.

Feldman, P. D., Cochran, A. L., and Combi, M. R. (2004). *Spectroscopic investigations of fragment species in the coma*, pages 425–447.

Festou, M. C. (1981). The density distribution of neutral compounds in cometary atmospheres. i - models and equations. *Astronomy and Astrophysics*, 95:69–79.

Festou, M. C., Keller, H. U., and Weaver, H. A. (2004). *A brief conceptual history of cometary science*, pages 3–16.

Fink, U. (2009). A taxonomic survey of comet composition 1985-2004 using CCD spectroscopy. Icarus, 201:311–334.

Fink, U., Combi, M. R., and Disanti, M. A. (1991). Comet P/Halley - Spatial distributions and scale lengths for C2, CN, NH2, and H2O. ApJ, 383:356–371.

Fink, U. and Hicks, M. D. (1996). A survey of 39 comets using CCD spectroscopy. ApJ, 459:729–743.

Fornasier, S., Hasselmann, P. H., Barucci, M. A., Feller, C., Besse, S., Leyrat, C., Lara, L., Gutierrez, P. J., Oklay, N., Tubiana, C., Scholten, F., Sierks, H., Barbieri, C., Lamy, P. L., Rodrigo, R., Koschny, D., Rickman, H., Keller, H. U., Agarwal, J., A'Hearn, M. F., Bertaux, J.-L., Bertini, I., Cremonese, G., Da Deppo, V., Davidsson, B., Debei, S., De Cecco, M., Fulle, M., Groussin, O., Güttler, C., Hviid, S. F., Ip, W., Jorda, L., Knollenberg, J., Kovacs, G., Kramm, R., Kührt, E., Küppers, M., La Forgia, F., Lazzarin, M., Lopez Moreno, J. J., Marzari, F., Matz, K.-D., Michalik, H., Moreno, F., Mottola, S., Naletto, G., Pajola, M., Pommerol, A., Preusker, F., Shi, X., Snodgrass, C., Thomas, N., and Vincent, J.-B. (2015). Spectrophotometric properties of the nucleus of comet 67P/Churyumov-Gerasimenko from the OSIRIS instrument onboard the ROSETTA spacecraft. A&A, 583:A30.

Fouchard, M., Froeschlé, C., Rickman, H., and Valsecchi, G. B. (2011). The key role of massive stars in Oort cloud comet dynamics. Icarus, 214:334–347.

Fray, N., Bénilan, Y., Cottin, H., Gazeau, M.-C., and Crovisier, J. (2005). The origin of the CN radical in comets: A review from observations and models. Planet. Space Sci., 53:1243–1262.

Gicquel, A., Milam, S. N., Coulson, I. M., Villanueva, G. L., Cordiner, M. A., Charnley, S. B., DiSanti, M. A., Mumma, M. J., and Szutowicz, S. (2015). The Evolution of Volatile Production in Comet C/2009 P1 (Garradd) during Its 2011-2012 Apparition. ApJ, 807:19.

Gombosi, T. I. and Houpis, H. L. F. (1986). An icy-glue model of cometary nuclei. Nature, 324:43.

Gomes, R., Levison, H. F., Tsiganis, K., and Morbidelli, A. (2005). Origin of the cataclysmic Late Heavy Bombardment period of the terrestrial planets. Nature, 435:466–469.

Gronkowski, P. and Wesołowski, M. (2015). A model of cometary outbursts: a new simple approach to the classical question. MNRAS, 451:3068–3077.

Guilbert-Lepoutre, A., Lasue, J., Federico, C., Coradini, A., Orosei, R., and Rosenberg, E. D. (2011). New 3D thermal evolution model for icy bodies application to trans-Neptunian objects. A&A, 529:A71.

Guilbert-Lepoutre, A., Schulz, R., Rożek, A., Lowry, S. C., Tozzi, G. P., and Stüwe, J. A. (2014). Pre-perihelion activity of comet 67P/Churyumov-Gerasimenko. A&A, 567:L2.

Gulkis, S., Allen, M., von Allmen, P., Beaudin, G., Biver, N., Bockelée-Morvan, D., Choukroun, M., Crovisier, J., Davidsson, B. J. R., Encrenaz, P., Encrenaz, T., Frerking, M., Hartogh, P., Hofstadter, M., Ip, W.-H., Janssen, M., Jarchow, C., Keihm, S., Lee, S., Lellouch, E., Leyrat, C., Rezac, L., Schloerb, F. P., and Spilker, T. (2015). Subsurface properties and early activity of comet 67P/Churyumov-Gerasimenko. *Science*, 347(1):aaa0709.

Gundlach, B., Kilias, S., Beitz, E., and Blum, J. (2011). Micrometer-sized ice particles for planetary-science experiments - I. Preparation, critical rolling friction force, and specific surface energy. Icarus, 214:717–723.

Gurnett, D. A., Morgan, D. D., Persoon, A. M., Granroth, L. J., Kopf, A. J., Plaut, J. J., and Green, J. L. (2015). An ionized layer in the upper atmosphere of Mars caused by dust impacts from comet Siding Spring. Geophys. Res. Lett., 42:4745–4751.

Hanner, M. S. and Newburn, R. L. (1989). Infrared photometry of comet Wilson (1986l) at two epochs. AJ, 97:254–261.

Hartmann, W. K. (1993). Physical mechanism of comet outbursts - an experimental result. Icarus, 104:226–233.

Hartogh, P., Lis, D. C., Bockelée-Morvan, D., de Val-Borro, M., Biver, N., Küppers, M., Emprechtinger, M., Bergin, E. A., Crovisier, J., Rengel, M., Moreno, R., Szutowicz, S., and Blake, G. A. (2011). Ocean-like water in the Jupiter-family comet 103P/Hartley 2. Nature, 478:218–220.

Haser, L. (1957). Distribution d'intensité dans la tête d'une comète. *Bulletin de l'Académie Royal des Sciences de Belgique*, 63:739.

Helbert, J., Rauer, H., Boice, D. C., and Huebner, W. F. (2005). The chemistry of $C_2$ and $C_3$ in the coma of Comet C/1995 O1 (Hale-Bopp) at heliocentric distances $r_h > 2.9$ AU. A&A, 442:1107–1120.

Ho, P. Y. (1962). Ancient and mediaeval observations of comets and novae in Chinese sources. *Vistas in Astronomy*, 5:127–225.

Hsieh, H. H., Fitzsimmons, A., Joshi, Y., Christian, D., and Pollacco, D. L. (2010). SuperWASP observations of the 2007 outburst of Comet 17P/Holmes. MNRAS, 407:1784–1800.

Hsieh, H. H., Jewitt, D. C., and Fernández, Y. R. (2004). The Strange Case of 133P/Elst-Pizarro: A Comet among the Asteroids. AJ, 127:2997–3017.

Hubert, B., Opitom, C., Hutsemékers, D., Jehin, E., Munhoven, G., Manfroid, J., Bisikalo, D. V., and Shematovich, V. I. (2016). An inversion method for cometary atmospheres. Icarus, 277:237–256.

Huebner, W. F., Keady, J. J., and Lyon, S. P. (1992). Solar photo rates for planetary atmospheres and atmospheric pollutants. Ap&SS, 195:1–289.

Huggins, W. (1882). On the Photographic Spectrum of Comet (wells) I., 1882. Nature, 26:179–180.

Ipatov, S. I. and A'Hearn, M. F. (2011). The outburst triggered by the Deep Impact collision with Comet Tempel 1. MNRAS, 414:76–107.

Irvine, W. M., Bergin, E. A., Dickens, J. E., Jewitt, D., Lovell, A. J., Matthews, H. E., Schloerb, F. P., and Senay, M. (1998). Chemical processing in the coma as the source of cometary HNC. Nature, 393:547–550.

Jackson, W. M. (1976). Laboratory observations of the photochemistry of parent molecules: A review. *NASA Special Publication*, 393.

Jehin, E., Gillon, M., Chantry, V., and Magain, P. (2010a). Trappist : un télescope liégeois à la découverte des systèmes planétaires. *Le Ciel*, 72:326–338.

Jehin, E., Gillon, M., Queloz, D., Magain, P., Manfroid, J., Chantry, V., Lendl, M., Hutsemékers, D., and Udry, S. (2011). Trappist : Transiting planets and planetesimals small telescope. *The Messenger*, 145:2.

Jehin, E., Manfroid, J., Hutsemekers, D., Gillon, M., and Magain, P. (2010b). Comet 103p/hartley. *Central Bureau Electronic Telegrams*, 2589:1.

Jewitt, D. and Luu, J. (1989). A CCD portrait of Comet P/Tempel 2. AJ, 97:1766–1790.

Jewitt, D. and Luu, J. (1993). Discovery of the candidate Kuiper belt object 1992 QB1. Nature, 362:730–732.

Jewitt, D. C. and Meech, K. J. (1987). Surface brightness profiles of 10 comets. ApJ, 317:992–1001.

Jewitt, D. C., Soifer, B. T., Neugebauer, G., Matthews, K., and Danielson, G. E. (1982). Visual and infrared observations of the distant Comets P/Stephan-Oterma /1980g/, Panther /1980u/, and Bowell /1980b/. AJ, 87:1854–1866.

Kawakita, H., Dello Russo, N., Vervack, Jr., R., Kobayashi, H., DiSanti, M. A., Opitom, C., Jehin, E., Weaver, H. A., Cochran, A. L., Harris, W. M., Bockelée-Morvan, D., Biver, N., Crovisier, J., McKay, A. J., Manfroid, J., and Gillon, M. (2014). Extremely Organic-rich Coma of Comet C/2010 G2 (Hill) during its Outburst in 2012. ApJ, 788:110.

Kawakita, H. and Mumma, M. J. (2011). Fluorescence Excitation Models of Ammonia and Amidogen Radical ($NH_2$) in Comets: Application to Comet C/2004 Q2 (Machholz). ApJ, 727:91.

Keller, H. U., Arpigny, C., Barbieri, C., Bonnet, R. M., Cazes, S., Coradini, M., Cosmovici, C. B., Delamere, W. A., Huebner, W. F., Hughes, D. W., Jamar, C., Malaise, D., Reitsema, H. J., Schmidt, H. U., Schmidt, W. K. H., Seige, P., Whipple, F. L., and Wilhelm, K. (1986). First Halley multicolour camera imaging results from Giotto. Nature, 321:320–326.

Keller, H. U. and Jorda, L. (2002). *The morphology of cometary nuclei*, page 1235. Kluwer Academic Publishers.

Kelley, M. S., Lindler, D. J., Bodewits, D., A'Hearn, M. F., Lisse, C. M., Kolokolova, L., Kissel, J., and Hermalyn, B. (2013). A distribution of large particles in the coma of Comet 103P/Hartley 2. Icarus, 222:634–652.

Kelley, M. S. P., Farnham, T. L., Bodewits, D., Tricarico, P., and Farnocchia, D. (2014). A Study of Dust and Gas at Mars from Comet C/2013 A1 (Siding Spring). ApJ, 792:L16.

Klavetter, J. J. and A'Hearn, M. F. (1994). An extended source for CN jets in Comet P/Halley. Icarus, 107:322–334.

Knight, M. M., A'Hearn, M. F., Biesecker, D. A., Faury, G., Hamilton, D. P., Lamy, P., and Llebaria, A. (2010). Photometric Study of the Kreutz Comets Observed by SOHO from 1996 to 2005. AJ, 139:926–949.

Knight, M. M. and Battams, K. (2014). Preliminary Analysis of SOHO/STEREO Observations of Sungrazing Comet ISON (C/2012 S1) around Perihelion. ApJ, 782:L37.

Knight, M. M., Mueller, B. E. A., Samarasinha, N. H., and Schleicher, D. G. (2015). A Further Investigation of Apparent Periodicities and the Rotational State of Comet 103P/Hartley 2 from Combined Coma Morphology and Light Curve Data Sets. AJ, 150:22.

Knight, M. M. and Schleicher, D. G. (2011). CN morphology studies of comet 103P/Hartley2. *The Astronomical Journal*, 141:183.

Knight, M. M. and Schleicher, D. G. (2013). The highly unusual outgassing of Comet 103P/Hartley 2 from narrowband photometry and imaging of the coma. Icarus, 222:691–706.

Knight, M. M. and Schleicher, D. G. (2015). Observations of Comet ISON (C/2012 S1) from Lowell Observatory. AJ, 149:19.

Kobayashi, H., Bockelée-Morvan, D., Kawakita, H., Dello Russo, N., Jehin, E., Manfroid, J., Smette, A., Hutsemékers, D., Stüwe, J., Weiler, M., Arpigny, C., Biver, N., Cochran, A., Crovisier, J., Magain, P., Sana, H., Schulz, R., Vervack, R. J., Weaver, H., and Zucconi, J.-M. (2010). High-dispersion infrared spectroscopic observations of comet 8P/Tuttle with VLT/CRIRES. A&A, 509:A80.

Krankowsky, D., Lammerzahl, P., Herrwerth, I., Woweries, J., Eberhardt, P., Dolder, U., Herrmann, U., Schulte, W., Berthelier, J. J., Illiano, J. M., Hodges, R. R., and Hoffman, J. H. (1986). In situ gas and ion measurements at comet Halley. Nature, 321:326–329.

Królikowska, M., Sitarski, G., Pittich, E. M., Szutowicz, S., Ziołkowski, K., Rickman, H., Gabryszewski, R., and Rickman, B. (2014). New catalogue of one-apparition comets discovered in the years 1901-1950. I. Comets from the Oort spike. A&A, 571:A63.

Kuiper, G. P. (1951). On the Origin of the Solar System. *Proceedings of the National Academy of Science*, 37:1–14.

Lamy, P. L., A'Hearn, M. F., Toth, I., and Weaver, H. A. (1996). HST Observations of the Nuclei of Comets 45P/Honda-Mrkos-Pajdusakova, 22P/Kopff, and 46P/Wirtanen. In *AAS/Division for Planetary Sciences Meeting Abstracts #28*, volume 28 of *Bulletin of the American Astronomical Society*, page 1083.

Lamy, P. L., Toth, I., Fernandez, Y. R., and Weaver, H. A. (2004). *The sizes, shapes, albedos, and colors of cometary nuclei*, pages 223–264.

Langland-Shula, L. E. and Smith, G. H. (2011). Comet classification with new methods for gas and dust spectroscopy. Icarus, 213:280–322.

Lara, L. M., Boehnhardt, H., Gredel, R., Gutiérrez, P. J., Rodrigo, R., and Vidal-Nuñez, M. J. (2007). Behavior of Comet 9P/Tempel 1 around the Deep Impact event. A&A, 465:1061–1067.

Lara, L. M., Lin, Z.-Y., and Meech, K. (2011). Comet 103p/hartley 2 at perihelion: gas and dust activity. *Astronomy and Astrophysics*, 532:A87.

Lara, L. M., Lin, Z.-Y., Rodrigo, R., and Ip, W.-H. (2011). 67P/Churyumov-Gerasimenko activity evolution during its last perihelion before the Rosetta encounter. A&A, 525:A36.

Lara, L.-M., Tozzi, G. P., Boehnhardt, H., DiMartino, M., and Schulz, R. (2004). Gas and dust in Comet C/2000 WM1 during its closest approach to Earth: Optical imaging and long-slit spectroscopy. A&A, 422:717–729.

Larson, S. M. and Sekanina, Z. (1984). Coma morphology and dust-emission pattern of periodic Comet Halley. I - High-resolution images taken at Mount Wilson in 1910. AJ, 89:571–578.

Leach, S., Stannard, P. R., and Gelbart, W. M. (1978). Interelectronic-state perturbation effects on photoelectron spectra and emission quantum yields. *Molecular Physics*, 36:1119–1132.

Lederer, S. M., Campins, H., Osip, D. J., and Schleicher, D. G. (1997). Gaseous Jets in Comet Hale-Bopp (1995 O1). *Earth Moon and Planets*, 78:131–136.

Lee, S., von Allmen, P., Allen, M., Beaudin, G., Biver, N., Bockelée-Morvan, D., Choukroun, M., Crovisier, J., Encrenaz, P., Frerking, M., Gulkis, S., Hartogh, P., Hofstadter, M., Ip, W.-H., Janssen, M., Jarchow, C., Keihm, S., Lellouch, E., Leyrat, C., Rezac, L., Schloerb, F. P., Spilker, T., Gaskell, B., Jorda, L., Keller, H. U., and Sierks, H. (2015). Spatial and diurnal variation of water outgassing on comet 67P/Churyumov-Gerasimenko observed from Rosetta/MIRO in August 2014. A&A, 583:A5.

Levison, H. F. (1996). Comet Taxonomy. In Rettig, T. and Hahn, J. M., editors, *Completing the Inventory of the Solar System*, volume 107 of *Astronomical Society of the Pacific Conference Series*, pages 173–191.

Levison, H. F. and Morbidelli, A. (2003). The formation of the Kuiper belt by the outward transport of bodies during Neptune's migration. Nature, 426:419–421.

Levison, H. F., Morbidelli, A., Vanlaerhoven, C., Gomes, R., and Tsiganis, K. (2008). Origin of the structure of the kuiper belt during a dynamical instability in the orbits of uranus and neptune. *Icarus*, 196:258–273.

Li, J., Jewitt, D., Clover, J. M., and Jackson, B. V. (2011). Outburst of Comet 17P/Holmes Observed with the Solar Mass Ejection Imager. ApJ, 728:31.

Li, J.-Y., Samarasinha, N. H., Kelley, M. S. P., Farnham, T. L., A'Hearn, M. F., Mutchler, M. J., Lisse, C. M., and Delamere, W. A. (2014). Constraining the Dust Coma Properties of Comet C/Siding Spring (2013 a1) at Large Heliocentric Distances. ApJ, 797:L8.

Lin, Z.-Y., Lara, L. M., and Ip, W.-H. (2013). Long-term Monitoring of Comet 103P/Hartley 2. AJ, 146:4.

Lin, Z.-Y., Lara, L. M., Vincent, J. B., and Ip, W.-H. (2012). Physical studies of 81P/Wild 2 from the last two apparitions. A&A, 537:A101.

Lin, Z.-Y., Lin, C.-S., Ip, W.-H., and Lara, L. M. (2009). The Outburst of Comet 17p/Holmes. AJ, 138:625–632.

Lovejoy, T., Jacques, C., Pimentel, E., and Barros, J. (2014). Comet C/2014 Q2 (Lovejoy). *Central Bureau Electronic Telegrams*, 3934.

Lowry, S., Duddy, S. R., Rozitis, B., Green, S. F., Fitzsimmons, A., Snodgrass, C., Hsieh, H. H., and Hainaut, O. (2012). The nucleus of Comet 67P/Churyumov-Gerasimenko. A new shape model and thermophysical analysis. A&A, 548:A12.

Lyttleton, R. A. (1948). On the Origin of Comets. MNRAS, 108:465.

Mäkinen, J. T. T., Bertaux, J.-L., Combi, M. R., and Quémerais, E. (2001). Water Production of Comet C/1999 S4 (LINEAR) Observed with the SWAN Instrument. *Science*, 292:1326–1329.

Manfroid, J., Hutsemékers, D., Jehin, E., Cochran, A. L., Arpigny, C., Jackson, W. M., Meech, K. J., Schulz, R., and Zucconi, J.-M. (2007). The impact and rotational light curves of Comet 9P/Tempel 1. Icarus, 187:144–155.

Marcus, J. N. (2007). Forward-Scattering Enhancement of Comet Brightness. I. Background and Model. *International Comet Quarterly*, 29:39–66.

Mazzotta Epifani, E., Perna, D., Di Fabrizio, L., Dall'Ora, M., Palumbo, P., Snodgrass, C., Licandro, J., Della Corte, V., and Tozzi, G. P. (2014). Observational results for eight long-period comets observed far from the Sun. A&A, 561:A6.

McKay, A. J., Chanover, N. J., DiSanti, M. A., Morgenthaler, J. P., Cochran, A. L., Harris, W. M., and Russo, N. D. (2014). Rotational variation of daughter species production rates in Comet 103P/Hartley: Implications for the progeny of daughter species and the degree of chemical heterogeneity. Icarus, 231:193–205.

McKay, A. J., Cochran, A. L., DiSanti, M. A., Villanueva, G., Russo, N. D., Vervack, R. J., Morgenthaler, J. P., Harris, W. M., and Chanover, N. J. (2015). Evolution of $H_2O$, CO, and $CO_2$ production in Comet C/2009 P1 Garradd during the 2011-2012 apparition. Icarus, 250:504–515.

McNaught, R. H., Sato, H., and Williams, G. V. (2013). Comet C/2013 A1 (Siding Spring). *Central Bureau Electronic Telegrams*, 3368:1.

Meech, K. J., A'Hearn, M. F., Adams, J. A., Bacci, P., Bai, J., Barrera, L., Battelino, M., Bauer, J. M., Becklin, E., Bhatt, B., Biver, N., Bockelée-Morvan, D., Bodewits, D., Böhnhardt, H., Boissier, J., Bonev, B. P., Borghini, W., Brucato, J. R., Bryssinck, E., Buie, M. W., Canovas, H., Castellano, D., Charnley, S. B., Chen, W. P., Chiang, P., Choi, Y.-J., Christian, D. J., Chuang, Y.-L., Cochran, A. L., Colom, P., Combi, M. R., Coulson, I. M., Crovisier, J., Dello Russo, N., Dennerl, K., DeWahl, K., DiSanti, M. A., Facchini, M., Farnham, T. L., Fernández, Y., Florén, H. G., Frisk, U., Fujiyoshi, T., Furusho, R., Fuse, T., Galli, G., García-Hernández, D. A., Gersch, A., Getu, Z., Gibb, E. L., Gillon, M., Guido, E., Guillermo, R. A., Hadamcik, E., Hainaut, O.,

Hammel, H. B., Harker, D. E., Harmon, J. K., Harris, W. M., Hartogh, P., Hashimoto, M., Häusler, B., Herter, T., Hjalmarson, A., Holland, S. T., Honda, M., Hosseini, S., Howell, E. S., Howes, N., Hsieh, H. H., Hsiao, H.-Y., Hutsemékers, D., Immler, S. M., Jackson, W. M., Jeffers, S. V., Jehin, E., Jones, T. J., de Juan Ovelar, M., Kaluna, H. M., Karlsson, T., Kawakita, H., Keane, J. V., Keller, L. D., Kelley, M. S., Kinoshita, D., Kiselev, N. N., Kleyna, J., Knight, M. M., Kobayashi, H., Kobulnicky, H. A., Kolokolova, L., Kreiny, M., Kuan, Y.-J., Küppers, M., Lacruz, J. M., Landsman, W. B., Lara, L. M., Lecacheux, A., Levasseur-Regourd, A. C., Li, B., Licandro, J., Ligustri, R., Lin, Z.-Y., Lippi, M., Lis, D. C., Lisse, C. M., Lovell, A. J., Lowry, S. C., Lu, H., Lundin, S., Magee-Sauer, K., Magain, P., Manfroid, J., Mazzotta Epifani, E., McKay, A., Melita, M. D., Mikuz, H., Milam, S. N., Milani, G., Min, M., Moreno, R., Mueller, B. E. A., Mumma, M. J., Nicolini, M., Nolan, M. C., Nordh, H. L., Nowajewski, P. B., Odin Team, Ootsubo, T., Paganini, L., Perrella, C., Pittichová, J., Prosperi, E., Radeva, Y. L., Reach, W. T., Remijan, A. J., Rengel, M., Riesen, T. E., Rodenhuis, M., Rodríguez, D. P., Russell, R. W., Sahu, D. K., Samarasinha, N. H., Sánchez Caso, A., Sandqvist, A., Sarid, G., Sato, M., Schleicher, D. G., Schwieterman, E. W., Sen, A. K., Shenoy, D., Shi, J.-C., Shinnaka, Y., Skvarc, J., Snodgrass, C., Sitko, M. L., Sonnett, S., Sosseini, S., Sostero, G., Sugita, S., Swinyard, B. M., Szutowicz, S., Takato, N., Tanga, P., Taylor, P. A., Tozzi, G.-P., Trabatti, R., Trigo-Rodríguez, J. M., Tubiana, C., de Val-Borro, M., Vacca, W., Vandenbussche, B., Vaubaillion, J., Velichko, F. P., Velichko, S. F., Vervack, Jr., R. J., Vidal-Nunez, M. J., Villanueva, G. L., Vinante, C., Vincent, J.-B., Wang, M., Wasserman, L. H., Watanabe, J., Weaver, H. A., Weissman, P. R., Wolk, S., Wooden, D. H., Woodward, C. E., Yamaguchi, M., Yamashita, T., Yanamandra-Fischer, P. A., Yang, B., Yao, J.-S., Yeomans, D. K., Zenn, T., Zhao, H., and Ziffer, J. E. (2011). EPOXI: Comet 103P/Hartley 2 Observations from a Worldwide Campaign. ApJ, 734:L1.

Meech, K. J., Hainaut, O., Weaver, H. A., Snodgrass, C., Pittichova, J., Riesen., T., Vilas, F., A'Hearn, M. F., Licandro, J., Gulbis, A., and Lowry, S. (2009). Characterization of the nucleus of 103p/hartley 2 for the epoxi mission. In *American Astronomical Society/Division for Planetary Sciences Meeting Abstracts*, volume 41 of *American Astronomical Society/Division for Planetary Sciences Meeting Abstracts*, page 20.07.

Meier, R., Wellnitz, D., Kim, S. J., and A'Hearn, M. F. (1998). The NH and CH Bands of Comet C/1996 B2 (Hyakutake). Icarus, 136:268–279.

Miles, R. and Faillace, G. A. (2012). On liquid phases in cometary nuclei. Icarus, 219:567–595.

Millis, R. L., A'Hearn, M. F., and Campins, H. (1985). The Nucleus and Coma of Comet P/Arend-Rigaux. In *Bulletin of the American Astronomical Society*, volume 17 of BAAS, page 688.

Morbidelli, A. and Brown, M. E. (2004). *The kuiper belt and the primordial evolution of the solar system*, pages 175–191.

Mumma, M. J., Bonev, B. P., Villanueva, G. L., Paganini, L., DiSanti, M. A., Gibb, E. L., Keane, J. V., Meech, K. J., Blake, G. A., Ellis, R. S., Lippi, M., Boehnhardt, H., and Magee-Sauer, K. (2011). Temporal and Spatial Aspects of Gas Release During the 2010 Apparition of Comet 103P/Hartley 2. ApJ, 734:L7.

Mumma, M. J. and Charnley, S. B. (2011). The Chemical Composition of Comets: Emerging Taxonomies and Natal Heritage. ARA&A, 49:471–524.

Mumma, M. J., McLean, I. S., DiSanti, M. A., Larkin, J. E., Dello Russo, N., Magee-Sauer, K., Becklin, E. E., Bida, T., Chaffee, F., Conrad, A. R., Figer, D. F., Gilbert, A. M., Graham, J. R., Levenson, N. A., Novak, R. E., Reuter, D. C., Teplitz, H. I., Wilcox, M. K., and Xu, L.-H. (2001). A Survey of Organic Volatile Species in Comet C/1999 H1 (Lee) Using NIRSPEC at the Keck Observatory. ApJ, 546:1183–1193.

Mumma, M. J., Weaver, H. A., Larson, H. P., Williams, M., and Davis, D. S. (1986). Detection of water vapor in Halley's comet. *Science*, 232:1523–1528.

Mumma, M. J., Weissman, P. R., and Stern, S. A. (1993). Comets and the origin of the solar system - Reading the Rosetta Stone. In Levy, E. H. and Lunine, J. I., editors, *Protostars and Planets III*, pages 1177–1252.

Newburn, R. L. and Spinrad, H. (1984). Spectrophotometry of 17 comets. I - The emission features. AJ, 89:289–309.

Newburn, R. L. and Spinrad, H. (1985). Spectrophotometry of seventeen comets. II - The continuum. AJ, 90:2591–2608.

Newburn, R. L. and Spinrad, H. (1989). Spectrophotometry of 25 comets - post-halley updates for 17 comets plus new observations for eight additional comets. AJ, 97:552–569.

Newton, I. (1687). *Philosophiae Naturalis Principia Mathematica. Auctore Js. Newton.*

O'dell, C. R., Robinson, R. R., Krishna Swamy, K. S., McCarthy, P. J., and Spinrad, H. (1988). C2 in Comet Halley - Evidence for its being third generation and resolution of the vibrational population discrepancy. ApJ, 334:476–488.

Oort, J. H. (1950). The structure of the cloud of comets surrounding the Solar System and a hypothesis concerning its origin. Bull. Astron. Inst. Netherlands, 11:91–110.

Ootsubo, T., Kawakita, H., Hamada, S., Kobayashi, H., Yamaguchi, M., Usui, F., Nakagawa, T., Ueno, M., Ishiguro, M., Sekiguchi, T., Watanabe, J.-i., Sakon, I., Shimonishi, T., and Onaka, T. (2012). AKARI Near-infrared Spectroscopic Survey for $CO_2$ in 18 Comets. ApJ, 752:15.

Öpik, E. (1932). Note on Stellar Perturbations of Nearly Parabolic Orbits . *Proceedings of the American Academy of Arts and Sciences*, 67:169–183–110.

Opitom, C., Guilbert-Lepoutre, A., Jehin, E., Manfroid, J., Hutsemékers, D., Gillon, M., Magain, P., Roberts-Borsani, G., and Witasse, O. (2016). Long-term activity and outburst of comet C/2013 A1 (Siding Spring) from narrow-band photometry and long-slit spectroscopy. A&A, 589:A8.

Opitom, C., Jehin, E., Manfroid, J., Hutsemékers, D., Gillon, M., and Magain, P. (2015a). TRAPPIST monitoring of comet C/2012 F6 (Lemmon). A&A, 574:A38.

Opitom, C., Jehin, E., Manfroid, J., Hutsemékers, D., Gillon, M., and Magain, P. (2015b). TRAPPIST photometry and imaging monitoring of comet C/2013 R1 (Lovejoy): Implications for the origin of daughter species. A&A, 584:A121.

Osborn, W. H., A'Hearn, M. F., Carsenty, U., Millis, R. L., Schleicher, D. G., Birch, P. V., Moreno, H., and Gutierrez-Moreno, A. (1990). Standard stars for photometry of comets. Icarus, 88:228–245.

Paganini, L., DiSanti, M. A., Mumma, M. J., Villanueva, G. L., Bonev, B. P., Keane, J. V., Gibb, E. L., Boehnhardt, H., and Meech, K. J. (2014a). The Unexpectedly Bright Comet C/2012 F6 (Lemmon) Unveiled at Near-infrared Wavelengths. AJ, 147:15.

Paganini, L., Mumma, M. J., Villanueva, G. L., DiSanti, M. A., Bonev, B. P., Lippi, M., and Boehnhardt, H. (2012). The Chemical Composition of CO-rich Comet C/2009 P1 (Garradd) AT R $_h$ = 2.4 and 2.0 AU before Perihelion. ApJ, 748:L13.

Paganini, L., Mumma, M. J., Villanueva, G. L., Keane, J. V., Blake, G. A., Bonev, B. P., DiSanti, M. A., Gibb, E. L., and Meech, K. J. (2014b). C/2013 R1 (Lovejoy) at IR wavelengths and the variability of CO abundances among Oort Cloud comets. ApJ, 791:122–129.

Palmer, P., Wootten, A., Butler, B., Bockelee-Morvan, D., Crovisier, J., Despois, D., and Yeomans, D. K. (1996). Comet Hyakutake: First Secure Detection Of Ammonia In a Comet. In *American Astronomical Society Meeting Abstracts #188*, volume 28 of *Bulletin of the American Astronomical Society*, page 927.

Prialnik, D. and Bar-Nun, A. (1987). On the evolution and activity of cometary nuclei. ApJ, 313:893–905.

Prialnik, D. and Bar-Nun, A. (1992). Crystallization of amorphous ice as the cause of Comet P/Halley's outburst at 14 AU. A&A, 258:L9–L12.

Randall, C. E., Schleicher, D. G., Ballou, R. G., and Osip, D. J. (1992). Observational Constraints on Molecular Scalelengths and Lifetimes in Comets. In *AAS/Division for Planetary Sciences Meeting Abstracts #24*, volume 24 of *Bulletin of the American Astronomical Society*, page 1002.

Rauer, H., Helbert, J., Arpigny, C., Benkhoff, J., Bockelée-Morvan, D., Boehnhardt, H., Colas, F., Crovisier, J., Hainaut, O., Jorda, L., Kueppers, M., Manfroid, J., and Thomas, N. (2003). Long-term optical spectrophotometric monitoring of comet C/1995 O1 (Hale-Bopp). A&A, 397:1109–1122.

Reach, W. T., Kelley, M. S., and Vaubaillon, J. (2013). Survey of cometary $CO_2$, CO, and particulate emissions using the Spitzer Space Telescope. Icarus, 226:777–797.

Reach, W. T., Vaubaillon, J., Kelley, M. S., Lisse, C. M., and Sykes, M. V. (2009). Distribution and properties of fragments and debris from the split Comet 73P/Schwassmann-Wachmann 3 as revealed by Spitzer Space Telescope. Icarus, 203:571–588.

Restano, M., Plaut, J. J., Campbell, B. A., Gim, Y., Nunes, D., Bernardini, F., Egan, A., Seu, R., and Phillips, R. J. (2015). Effects of the passage of Comet C/2013 A1 (Siding Spring) observed by the Shallow Radar (SHARAD) on Mars Reconnaissance Orbiter. Geophys. Res. Lett., 42:4663–4669.

Rodgers, S. D. and Charnley, S. B. (1998). HNC and HCN in Comets. ApJ, 501:L227–L230.

Rotundi, A., Sierks, H., Della Corte, V., Fulle, M., Gutierrez, P. J., Lara, L., Barbieri, C., Lamy, P. L., Rodrigo, R., Koschny, D., Rickman, H., Keller, H. U., López-Moreno, J. J., Accolla, M., Agarwal, J., A'Hearn, M. F., Altobelli, N., Angrilli, F., Barucci, M. A., Bertaux, J.-L., Bertini, I., Bodewits, D., Bussoletti, E., Colangeli, L., Cosi, M., Cremonese, G., Crifo, J.-F., Da Deppo, V., Davidsson, B., Debei, S., De Cecco, M., Esposito, F., Ferrari, M., Fornasier, S., Giovane, F., Gustafson, B., Green, S. F., Groussin, O., Grün, E., Güttler, C., Herranz, M. L., Hviid, S. F., Ip, W., Ivanovski, S., Jerónimo, J. M., Jorda, L., Knollenberg, J., Kramm, R., Kührt, E., Küppers, M., Lazzarin, M., Leese, M. R., López-Jiménez, A. C., Lucarelli, F., Lowry, S. C., Marzari, F., Epifani, E. M., McDonnell, J. A. M., Mennella, V., Michalik, H., Molina, A., Morales, R., Moreno, F., Mottola, S., Naletto, G., Oklay, N., Ortiz, J. L., Palomba, E., Palumbo, P., Perrin, J.-M., Rodríguez, J., Sabau, L., Snodgrass, C., Sordini, R., Thomas, N., Tubiana, C., Vincent, J.-B., Weissman, P., Wenzel, K.-P., Zakharov, V., and Zarnecki, J. C. (2015). Dust measurements in the coma of comet 67P/Churyumov-Gerasimenko inbound to the Sun. *Science*, 347(1):aaa3905.

Rubincam, D. P. (2000). Radiative Spin-up and Spin-down of Small Asteroids. Icarus, 148:2–11.

Sagdeev, R. Z., Szabo, F., Avanesov, G. A., Cruvellier, P., Szabo, L., Szego, K., Abergel, A., Balazs, A., Barinov, I. V., Bertaux, J.-L., Blamount, J., Detaille, M., Demarelis, E., Dul'Nev, G. N., Endroczy, G., Gardos, M., Kanyo, M., Kostenko, V. I., Krasikov, V. A., Nguyen-Trong, T., Nyitrai, Z., Reny, I., Rusznyak, P., Shamis, V. A., Smith, B., Sukhanov, K. G., Szabo, F., Szalai, S., Tarnopolsky, V. I., Toth, I., Tsukanova, G., Valnicek, B. I., Varhalmi, L., Zaiko, Y. K., Zatsepin, S. I., Ziman, Y. L., Zsenei, M., and Zhukov, B. S. (1986). Television observations of comet Halley from VEGA spacecraft. Nature, 321:262–266.

Samarasinha, N. H. and Larson, S. M. (2014). Image enhancement techniques for quantitative investigations of morphological features in cometary comae: A comparative study. Icarus, 239:168–185.

Samarasinha, N. H., Mueller, B. E. A., A'Hearn, M. F., Farnham, T. L., and Gersch, A. (2011). Rotation of Comet 103P/Hartley 2 from Structures in the Coma. ApJ, 734:L3.

Scargle, J. D. (1982). Studies in astronomical time series analysis. II - Statistical aspects of spectral analysis of unevenly spaced data. ApJ, 263:835–853.

Schleicher, D. (2007). Comet 8P/Tuttle. *Central Bureau Electronic Telegrams*, 1113.

Schleicher, D. and Bair, A. (2014). Chemical and physical properties of comets in the Lowell database: Results from 35 years of narrow-band photometry. In Muinonen, K., Penttilä, A., Granvik, M., Virkki, A., Fedorets, G., Wilkman, O., and Kohout, T., editors, *Asteroids, Comets, Meteors 2014*.

Schleicher, D., Knight, M., and Skiff, B. (2014). Comet C/2013 A1 (Siding Spring). *Central Bureau Electronic Telegrams*, 4004.

Schleicher, D. G. (2006). Compositional and physical results for Rosetta's new target Comet 67P/Churyumov Gerasimenko from narrowband photometry and imaging. Icarus, 181:442–457.

Schleicher, D. G. (2010). The Fluorescence Efficiencies of the CN Violet Bands in Comets. AJ, 140:973–984.

Schleicher, D. G. and A'Hearn, M. F. (1988). The fluorescence of cometary OH. ApJ, 331:1058–1077.

Schleicher, D. G. and Bair, A. N. (2011). The Composition of the Interior of Comet 73P/Schwassmann-Wachmann 3: Results from Narrowband Photometry of Multiple Components. AJ, 141:177.

Schleicher, D. G. and Farnham, T. L. (2004). *Photometry and imaging of the coma with narrowband filters*, pages 449–469.

Schleicher, D. G., Millis, R. L., and Birch, P. V. (1998). Narrowband photometry of comet p/halley : Variation with heliocentric distance, season, and solar phase angle. *Icarus*, 132:397–417.

Schleicher, D. G., Millis, R. L., Osip, D. J., and Lederer, S. M. (1998). Activity and the Rotation Period of Comet Hyakutake (1996 B2). Icarus, 131:233–244.

Schleicher, D. G. and Osip, D. J. (2002). Long- and Short-Term Photometric Behavior of Comet Hyakutake (1996 B2). Icarus, 159:210–233.

Schleicher, D. G. and Woodney, L. M. (2003). Analyses of dust coma morphology of Comet Hyakutake (1996 B2) near perigee: outburst behavior, jet motion, source region locations, and nucleus pole orientation. Icarus, 162:190–213.

Schleicher, D. G., Woodney, L. M., and Millis, R. L. (2003). Comet 19P/Borrelly at multiple apparitions: seasonal variations in gas production and dust morphology. Icarus, 162:415–442.

Schneider, N. M., Stewart, A. I. F., McClintock, W. E., Mahaffy, P. R., Benna, M., Deighan, J., Jain, S. K., Stiepen, A., Elrod, M., Chaffin, M. H., Crismani, M., Plane, J., Sanchez, J. D. C., Yelle, R. V., Lo, D., Evans, J. S., Stevens, M. H., Combi, M., Clarke, J. T., Holsclaw, G. M., Montmessin, F., and Jakosky, B. M. (2015). MAVEN IUVS Observations of the Aftermath of Comet Siding Spring's Meteor Shower. In *Lunar and Planetary Science Conference*, volume 46 of *Lunar and Planetary Science Conference*, page 2804.

Schorghofer, N. (2008). The Lifetime of Ice on Main Belt Asteroids. ApJ, 682:697–705.

Schulz, R., Hilchenbach, M., Langevin, Y., Kissel, J., Silen, J., Briois, C., Engrand, C., Hornung, K., Baklouti, D., Bardyn, A., Cottin, H., Fischer, H., Fray, N., Godard, M., Lehto, H., Le Roy, L., Merouane, S., Orthous-Daunay, F.-R., Paquette, J., Rynö, J., Siljeström, S., Stenzel, O., Thirkell, L., Varmuza, K., and Zaprudin, B. (2015). Comet 67P/Churyumov-Gerasimenko sheds dust coat accumulated over the past four years. Nature, 518:216–218.

Schulz, R., McFadden, L. A., Chamberlin, A. B., A'Hearn, M. F., and Schleicher, D. G. (1994). Variability in Comet P/Swift-Tuttle. Icarus, 109:145–155.

Schulz, R., Stüwe, J. A., and Boehnhardt, H. (2004). Rosetta target comet 67P/Churyumov-Gerasimenko. Postperihelion gas and dust production rates. A&A, 422:L19–L21.

Schulz, R., Stüwe, J. A., Tozzi, G. P., and Owens, A. (2000). Optical analysis of an activity outburst in comet C/1995 O1 (Hale-Bopp) and its connection to an X-ray outburst. A&A, 361:359–368.

Seabroke, G. M. (1881). Comet b 1881. Nature, 24:431.

Sekanina, Z. (1991). Comprehensive model for the nucleus of Periodic Comet Tempel 2 and its activity. AJ, 102:350–388.

Sekanina, Z. (1997). The problem of split comets revisited. A&A, 318:L5–L8.

Sekanina, Z. (2014). Temporal Correlation Between Outbursts and Fragmentation Events of Comet 168P/Hergenrother. *ArXiv e-prints*.

Sekanina, Z., Chodas, P. W., and Yeomans, D. K. (1994). Tidal disruption and the appearance of periodic comet Shoemaker-Levy 9. A&A, 289:607–636.

Sekanina, Z. and Kracht, R. (2014). Disintegration of Comet C/2012 S1 (ISON) Shortly Before Perihelion: Evidence from Independent Data Sets. *ArXiv e-prints*.

Serra-Ricart, M. and Licandro, J. (2015). The Rotation Period of C/2014 Q2 (Lovejoy). ApJ, 814:49.

Sicardy, B., Ortiz, J. L., Assafin, M., Jehin, E., Maury, A., Lellouch, E., Hutton, R. G., Braga-Ribas, F., Colas, F., Hestroffer, D., Lecacheux, J., Roques, F., Santos-Sanz, P., Widemann, T., Morales, N., Duffard, R., Thirouin, A., Castro-Tirado, A. J., Jelínek, M., Kubánek, P., Sota, A., Sánchez-Ramírez, R., Andrei, A. H., Camargo, J. I. B., da Silva Neto, D. N., Gomes, A. R., Martins, R. V., Gillon, M., Manfroid, J., Tozzi, G. P., Harlingten, C., Saravia, S., Behrend, R., Mottola, S., Melendo, E. G., Peris, V., Fabregat, J., Madiedo, J. M., Cuesta, L., Eibe, M. T., Ullán, A., Organero, F., Pastor, S., de Los Reyes, J. A., Pedraz, S., Castro, A., de La Cueva, I., Muler, G., Steele, I. A., Cebrián, M., Montañés-Rodríguez, P., Oscoz, A., Weaver, D., Jacques, C., Corradi, W. J. B., Santos, F. P., Reis, W., Milone, A., Emilio, M., Gutiérrez, L., Vázquez, R., and Hernández-Toledo, H. (2011). A Pluto-like radius and a high albedo for the dwarf planet Eris from an occultation. Nature, 478:493–496.

Sierks, H., Barbieri, C., Lamy, P. L., Rodrigo, R., Koschny, D., Rickman, H., Keller, H. U., Agarwal, J., A'Hearn, M. F., Angrilli, F., Auger, A.-T., Barucci, M. A., Bertaux, J.-L., Bertini, I., Besse, S., Bodewits, D., Capanna, C., Cremonese, G., Da Deppo, V., Davidsson, B., Debei, S., De Cecco, M., Ferri, F., Fornasier, S., Fulle, M., Gaskell, R., Giacomini, L., Groussin, O., Gutierrez-Marques, P., Gutiérrez, P. J., Güttler, C., Hoekzema, N., Hviid, S. F., Ip, W.-H., Jorda, L., Knollenberg, J., Kovacs, G., Kramm, J. R., Kührt, E., Küppers, M., La Forgia, F., Lara, L. M., Lazzarin, M., Leyrat, C., Lopez Moreno, J. J., Magrin, S., Marchi, S., Marzari, F., Massironi, M., Michalik, H., Moissl, R., Mottola, S., Naletto, G., Oklay, N., Pajola, M., Pertile, M., Preusker, F., Sabau, L., Scholten, F., Snodgrass, C., Thomas, N., Tubiana, C., Vincent, J.-B., Wenzel, K.-P., Zaccariotto, M., and Pätzold, M. (2015). On the nucleus structure and activity of comet 67P/Churyumov-Gerasimenko. *Science*, 347(1):aaa1044.

Smith, J. A., Tucker, D. L., Kent, S., Richmond, M. W., Fukugita, M., Ichikawa, T., Ichikawa, S.-I., Jorgensen, A. M., Uomoto, A., Gunn, J. E., Hamabe, M., Watanabe, M., Tolea, A., Henden, A., Annis, J., Pier, J. R., McKay, T. A., Brinkmann, J., Chen, B., Holtzman, J., Shimasaku, K., and York, D. G. (2002). The u'g'r'i'z' standard-star system. *The Astronomical Journal*, 123:2121–2144.

Snodgrass, C., Jehin, E., Manfroid, J., Opitom, C., Fitzsimmons, A., Tozzi, G. P., Faggi, S., Yang, B., Knight, M. M., Conn, B. C., Lister, T., Hainaut, O., Bramich, D. M., Lowry, S. C., Rozek, A., Tubiana, C., and Guilbert-Lepoutre, A. (2016). Distant activity of 67P/Churyumov-Gerasimenko in 2014: Ground-based results during the Rosetta pre-landing phase. A&A, 588:A80.

Solontoi, M., Ivezić, Ž., Jurić, M., Becker, A. C., Jones, L., West, A. A., Kent, S., Lupton, R. H., Claire, M., Knapp, G. R., Quinn, T., Gunn, J. E., and Schneider, D. P. (2012). Ensemble properties of comets in the Sloan Digital Sky Survey. Icarus, 218:571–584.

Steffl, A. J., Feldman, P. D., A'Hearn, M. F., Bertaux, J.-L., Feaga, L. M., Keeney, B. A., Knight, M. M., Noonan, J., Parker, J. W., Schindhelm, E. R., Stern, S. A., Vervack, R. J., and Weaver, H. A. (2015). Dust Outbursts From Comet 67P/Churyumov-Gerasimenko Observed by Rosetta-Alice. In *AAS/Division for Planetary Sciences Meeting Abstracts*, volume 47 of *AAS/Division for Planetary Sciences Meeting Abstracts*, page 413.08.

Stevenson, R., Bauer, J. M., Cutri, R. M., Mainzer, A. K., and Masci, F. J. (2015). NEOWISE Observations of Comet C/2013 A1 (Siding Spring) as It Approaches Mars. ApJ, 798:L31.

Storrs, A. D., Cochran, A. L., and Barker, E. S. (1992). Spectrophotometry of the continuum in 18 comets. Icarus, 98:163–178.

Swings, P. (1941). Complex structure of cometary bands tentatively ascribed to the contour of the solar spectrum. *Lick Observatory Bulletin*, 19:131–136.

Swings, P., Elvey, C. T., and Babcock, H. W. (1941). The Spectrum of Comet Cunningham, 1940C. ApJ, 94:320.

Trigo-Rodríguez, J. M., García-Melendo, E., Davidsson, B. J. R., Sánchez, A., Rodríguez, D., Lacruz, J., de Los Reyes, J. A., and Pastor, S. (2008). Outburst activity in comets. I. Continuous monitoring of comet 29P/Schwassmann-Wachmann 1. A&A, 485:599–606.

Tseng, W.-L., Bockelée-Morvan, D., Crovisier, J., Colom, P., and Ip, W.-H. (2007). Cometary water expansion velocity from OH line shapes. A&A, 467:729–735.

Tsiganis, K., Gomes, R., Morbidelli, A., and Levison, H. F. (2005). Origin of the orbital architecture of the giant planets of the solar system. *Nature*, 435:459–461.

Tubiana, C., Snodgrass, C., Bertini, I., Mottola, S., Vincent, J.-B., Lara, L., Fornasier, S., Knollenberg, J., Thomas, N., Fulle, M., Agarwal, J., Bodewits, D., Ferri, F., Güttler, C., Gutierrez, P. J., La Forgia, F., Lowry, S., Magrin, S., Oklay, N., Pajola, M., Rodrigo, R., Sierks, H., A'Hearn, M. F., Angrilli, F., Barbieri, C., Barucci, M. A., Bertaux, J.-L., Cremonese, G., Da Deppo, V., Davidsson, B., De Cecco, M., Debei, S., Groussin, O., Hviid, S. F., Ip, W., Jorda, L., Keller, H. U., Koschny, D., Kramm, R., Kührt, E., Küppers, M., Lazzarin, M., Lamy, P. L., Lopez Moreno, J. J., Marzari, F., Michalik, H., Naletto, G., Rickman, H., Sabau, L., and Wenzel, K.-P. (2015). 67P/Churyumov-Gerasimenko: Activity between March and June 2014 as observed from Rosetta/OSIRIS. A&A, 573:A62.

Valk, J. H., O'dell, C. R., Cochran, A. L., Cochran, W. D., Opal, C. B. S., and Barker, E. S. (1992). Near-ultraviolet spectroscopy of Comet Austin (1989c1). ApJ, 388:621–632.

Villanueva, G. L., Bonev, B. P., Mumma, M. J., Magee-Sauer, K., DiSanti, M. A., Salyk, C., and Blake, G. A. (2006). The Volatile Composition of the Split Ecliptic comet 73P/Schwassmann-Wachmann 3: A Comparison of Fragments C and B. ApJ, 650:L87–L90.

Villanueva, G. L., Mumma, M. J., DiSanti, M. A., Bonev, B. P., Gibb, E. L., Magee-Sauer, K., Blake, G. A., and Salyk, C. (2011). The molecular composition of Comet C/2007 W1 (Boattini): Evidence of a peculiar outgassing and a rich chemistry. Icarus, 216:227–240.

Villanueva, G. L., Mumma, M. J., DiSanti, M. A., Bonev, B. P., Paganini, L., and Blake, G. A. (2012). A multi-instrument study of Comet C/2009 P1 (Garradd) at 2.1 AU (pre-perihelion) from the Sun. Icarus, 220:291–295.

Vincent, J.-B., Bodewits, D., Besse, S., Sierks, H., Barbieri, C., Lamy, P., Rodrigo, R., Koschny, D., Rickman, H., Keller, H. U., Agarwal, J., A'Hearn, M. F., Auger, A.-T., Barucci, M. A., Bertaux, J.-L., Bertini, I., Capanna, C., Cremonese, G., da Deppo, V., Davidsson, B., Debei, S., de Cecco, M., El-Maarry, M. R., Ferri, F., Fornasier, S., Fulle, M., Gaskell, R., Giacomini, L., Groussin, O., Guilbert-Lepoutre, A., Gutierrez-Marques, P., Gutiérrez, P. J., Güttler, C., Hoekzema, N., Höfner, S., Hviid, S. F., Ip, W.-H., Jorda, L., Knollenberg, J., Kovacs, G., Kramm, R., Kührt, E., Küppers, M., La Forgia, F., Lara, L. M., Lazzarin, M., Lee, V., Leyrat, C., Lin, Z.-Y., Lopez Moreno, J. J., Lowry, S., Magrin, S., Maquet, L., Marchi, S., Marzari, F., Massironi, M., Michalik, H., Moissl, R., Mottola, S., Naletto, G., Oklay, N., Pajola, M., Preusker, F., Scholten, F., Thomas, N., Toth, I., and Tubiana, C. (2015). Large heterogeneities in comet 67P as revealed by active pits from sinkhole collapse. Nature, 523:63–66.

Waniak, W., Borisov, G., Drahus, M., and Bonev, T. (2012). Rotation-stimulated structures in the CN and $C_3$ comae of comet 103P/Hartley 2 close to the EPOXI encounter. A&A, 543:A32.

Weaver, H. A., Feldman, P. D., A'Hearn, M. F., and Arpigny, C. (1997). The activity and size of the nucleus of comet hale-bopp (c/1995 o1). *Science*, 275:1900–1904.

Weaver, H. A., Mumma, M. J., Larson, H. P., and Davis, D. S. (1986). Post-perihelion observations of water in comet Halley. Nature, 324:441–444.

Weiler, M. (2012). The chemistry of $C_3$ and $C_2$ in cometary comae. I. Current models revisited. A&A, 538:A149.

Weiler, M., Rauer, H., and Helbert, J. (2004). Optical observations of Comet 67P/Churyumov-Gerasimenko. A&A, 414:749–755.

Weissman, P. R. (1986). Are cometary nuclei primordial rubble piles? Nature, 320:242–244.

Weissman, P. R. (1987). POST Perihelion Brightening of Comet p/ Halley - Springtime for Halley. A&A, 187:873.

Weissman, P. R., Asphaug, E., and Lowry, S. C. (2004). *Structure and density of cometary nuclei*, pages 337–357.

Weissman, P. R. and Lowry, S. C. (2008). Structure and density of cometary nuclei. *Meteoritics and Planetary Science*, 43:1033–1047.

Whipple, F. L. (1950). A comet model. i. the acceleration of comet enckle. *Astrophysical Journal*, 111:375–394.

Whipple, F. L. (1951). A Comet Model. II. Physical Relations for Comets and Meteors. ApJ, 113:464.

Whipple, F. L. (1955). A Comet Model. III. The Zodiacal Light. ApJ, 121:750.

Whipple, F. L. (1978). Cometary brightness variation and nucleus structure. *Moon and Planets*, 18:343–359.

Wiegert, P. and Tremaine, S. (1999). The Evolution of Long-Period Comets. Icarus, 137:84–121.